Development of Single Molecule and Particle Detection Techniques for Microfluidic Analysis

Joshua B. Edel

Submitted in partial fulfilment of the requirement for the degree of
Doctor of Philosophy

Imperial College London, University of London
November 2003

Abstract

Big advances in ultra sensitive detection of fluorescent molecules in liquids have been made at room temperature since the first successful optical microscopic observation of small molecules published in 1976. Over the past several years, high sensitivity detection is finding increasing importance in biological and chemical analysis. This is a result for a need for rapid, on-line measurements at low concentrations. This thesis describes the development and applications of single molecule and particle fluorescence detection techniques for microfluidic analysis. The motivation behind this work was to improve the sensitivity and increase the capability of single molecule detection to old and new interesting systems.

A custom built confocal fluorescence detection system for the analysis of fluorescent molecules within microfluidic channels was developed and will be discussed in the initial chapters. With this work we have essentially established a single-molecule detection capability that can be interfaced with miniaturized systems for on-chip detection. A selection of applications that will be discussed in the thesis demonstrating the capabilities of the confocal spectrometer is as follows:

1) A non-invasive, optical technique for measuring particulate flow within microfluidic channels was developed.

2) A simple method was proposed that can be used to size single particles or molecules in free solution.

3) Hydrodynamic focusing in microstructures was demonstrated and combined with confocal microscopy for improved single molecule detection efficiencies with sub femtoliter probe volumes.

4) A statistical method was devised to distinguish between flow velocities of single molecules or particles in a microfluidic channel.

5) A cell counting and cell recognition method was developed using time correlated single photon counting as well as single molecule spectroscopy. This was demonstrated with primarily e. coli cells expressed with green, cyano, and yellow fluorescent protein.

6) Biological molecules, such as HSA and IgG, labeled to single fluorescent particles were found to be distinguishable based on photon burst characteristics. This approach can prove to be useful for separating proteins in continuous real time.

Acknowledgments

I would like to thank and am grateful to my research supervisor Dr Andrew J. de Mello for his commitment and encouragement towards my project as well as for giving me positive and detailed feedback on the preparation of this thesis. Thanks to Steve Jakeway for initially showing me around the labs. Thanks also go to the rest of the de Mello research group and the members of the entire analytical center. It has been a pleasure working and collaborating on projects with all of you. Thanks to Melanie Fennah for teaching me her approach to PDMS microchip fabrication and to Pedro Lahud for preparing E. Coli cells expressed with various types of proteins. I am grateful to Elisabeth Hill for initially going over her instrumental set up. I would also like to thank the people at Rutherford Appleton laboratories for allowing me to use there micro and nanofabrication facilities. I am grateful to Joerg Enderlein for getting me started on the SMD Monte-Carlo simulations.

Contents

ABSTRACT II
ACKNOWLEDGMENTS III
CONTENTS IV
LIST OF FIGURES IX
LIST OF TABLES XVII
SYMBOLS AND ABBREVIATIONS XVIII

Chapter 1 Introduction

1.1 SINGLE MOLECULE DETECTION 2
1.1.1 THE ABSORPTION-EMISSION CYCLE 2
1.1.2 ULTRA-SENSITIVE ANALYSIS: MOTIVATION 3
1.1.3 SINGLE MOLECULE DETECTION USING CONFOCAL MICROSCOPY 4
1.1.4 MICROFLUIDICS: BACKGROUND 5
1.1.5 SINGLE MOLECULE DETECTION: A GENERAL REVIEW 7
1.1.5.1 Dye Selection *7*
1.1.5.2 Single molecule detection: applications *8*
1.1.6. SINGLE MOLECULE DETECTION IN MICROCHANNELS 10
1.2 PROJECT AIM 14
1.3 REFERENCES 14

Chapter 2 Experimental

2.1 CONFOCAL SPECTROSCOPY 21
2.2 INSTRUMENT DESIGN 24
2.2.1 EXCITATION SOURCE 24
2.2.2 BEAM STEERING OPTICS 25
2.2.3 LASER BEAM ATTENUATION (OD) 26
2.2.4 DICHROIC MIRROR (DM 2) 26
2.2.5 MICROSCOPE OBJECTIVE (OBJ) 27
2.2.6 SD 1 DETECTION PATH 28
2.2.7 SD 2 DETECTION PATH 30
2.2.8 OCEAN OPTICS SPECTROMETER 30
2.3 ACQUISITION METHODS 30
2.3.1 MULTI CHANNEL SCALAR 31
2.3.2 TIME CORRELATED SINGLE PHOTON COUNTING 33
2.3.3 LOCK-IN AMPLIFIER BASED MEASUREMENTS 35
2.4 MICROFLUDICS 35
2.4.1 MICROFLUIDIC CHANNEL DESIGN 36
2.4.2 MICROFLUIDIC DEVICE FABRICATION 37
2.4.2.1 Chip substrates *37*
2.4.2.2 Exposure of substrates *37*
2.4.2.3 Developing and etching of exposed substrates *38*
2.4.2.4 Drilling of access holes *38*
2.4.2.5 Device bonding *38*
2.4.3 DEVICE INTEGRATION 39
2.4.3.1 Optical polishing of the top plate *39*

2.4.3.2 Interfacing the devices with capillary tubing *39*
2.4.3.3 Interfacing the microchannels with a syringe pump *40*

2.5 SUMMARY **40**

2.6 REFERENCES **40**

Chapter 3 Statistical analysis methods

3.1 SINGLE MOLECULE SENSITIVITY REQUIREMENTS **43**

3.1.1 SIGNAL TO NOISE 43
3.1.2 BACKGROUND THRESHOLD DETERMINATION 44

3.2 PEAK LOCATING ALGORITHM **47**

3.3 PHOTON BURST STATISTICS: RECURRENCE TIMES **48**

3.3.1 RECURRENCE TIME ANALYSIS 49
3.3.2 CALCULATION OF RECURRENCE TIMES AND THEORETICAL FITS 50

3.4 PHOTON BURST STATISTICS: AUTOCORRELATION ANALYSIS **51**

3.4.1 AUTOCORRELATION: THEORY 51
3.4.2 AUTOCORRELATION: THEORETICAL FIT 52
3.4.3 AUTOCORRELATION: EXAMPLES 53
3.4.4 CALCULATION OF AUTOCORRELATION CURVES 54

3.5 PHOTON BURST HISTOGRAMS **57**

3.5.1 BURST HEIGHT HISTOGRAM 57
3.5.2 BURST AREA HISTOGRAM 58
3.5.3 BURST WIDTH HISTOGRAM 59

3.6 FLUORESCENCE LIFETIMES ANALYSIS **60**

3.6.1 FLUORESCENCE LIFETIMES: THEORY 61
3.6.2 APPROACH FOR THE FITTING OF FLUORESCENCE LIFETIMES 62
3.6.3 FLUORESCENCE LIFETIME FITTING PROGRAM (J-LIFE) 63

3.7 SUMMARY **66**

3.6 REFERENCES **66**

Chapter 4 Hydrodynamic focussing in microstructures

4.1 INTRODUCTION **69**

4.2 EXPERIMENTAL APPROACH **71**

4.2.1 EXPERIMENTAL MATERIALS 71
4.2.2 HYDRODYNAMIC FOCUSSING IN MICROSTRUCTURES 72
4.2.3 FOCUSSING WIDTH VERSUS FLOW RATE 76
4.2.4 FOCUSSING SYMMETRY WITHIN THE MICROCHANNELS 76
4.2.5 MINIMUM FOCUSSING WIDTH 78
4.2.5.1 Theory *78*
4.2.5.2 Theoretical limits of the focussing width *79*

4.3 HYDRODYNAMIC FOCUSSING SIMULATIONS **80**

4.3.1 ANALYTE DIFFUSION IN FOCUSSED SAMPLE STREAMS 80
4.3.1.1 Analyte diffusion *80*
4.3.1.2 Diffusion within microchannels *80*

4.3.1.3 Simulation overview ... *81*
4.3.1.4 Simulation output ... *82*
4.3.2 PARTICLE VELOCITY DEPENDENCE ON DIFFUSION FROM THE ANALYTE STREAM ... 83
4.3.2.1 Improving molecular detection efficiencies ... *83*
4.3.2.2 Rapid mixing ... *85*
4.3.3 QUANTITATIVE DETERMINATION OF ESCAPED PARTICLES FROM THE ANALYTE STREAM ... 86
4.3.4 MONTE CARLO SIMULATION OF A SINGLE PARTICLE FOCUSSING EXPERIMENT ... 88

4.4 EXPERIMENTAL RESULTS ... 89

4.4.1 SHEATH AND ANALYTE FLOW DEPENDENCE ON MOLECULAR DETECTION EFFICIENCY ... 89
4.4.1.1 Single particle counting: Variation in sheath flow rate ... *90*
4.4.1.2 Single particle counting: Variation in analyte flow rate ... *92*
4.4.1.3 Poisson recurrence time analysis ... *93*
4.4.1.4 Autocorrelation analysis ... *95*
4.4.2 PHOTON BURST CHARACTERISTICS ... 96
4.4.2.1 Burst width analysis ... *96*
4.4.2.2 Burst height analysis ... *97*

4.5 SUMMARY ... 98

4.6 REFERENCES ... 99

Chapter 5 Cells & particles: Population and distribution analysis

5.1 INTRODUCTION ... 102

5.2 EXPERIMENTAL ... 103

5.2.1 MATERIALS ... 103
5.2.1.1 Fluorescent microspheres ... *103*
5.2.1.2 Escherichia coli cells ... *104*
5.2.2 MICROFLUIDICS ... 106
5.2.3 EXPERIMENTAL APPROACH ... 106

5.3 BURST CHARACTERIZATION ... 107

5.3.1 PHOTON BURST HEIGHT (PBH) ANALYSIS ... 107
5.3.1.1 PBH analysis for 200, 500, 930 nm fluorescent particles ... *108*
5.3.1.2 PBH analysis for E. coli expressed with GFP, CFP, YFP ... *110*
5.3.2 PHOTON BURST WIDTH (PBW) ANALYSIS ... 112
5.3.2.1 PBW analysis for 200, 500, 930 nm fluorescent particles ... *112*
5.3.2.2 PBW analysis for E. coli expressed with GFP, CFP, YFP ... *114*
5.3.2.2 PBW analysis for E. coli expressed with GFP, CFP, YFP ... *115*
5.3.3 PHOTON BURST AREA (PBA) ANALYSIS ... 116
5.3.3.1 PBA analysis for 200, 500, 1000 nm fluorescent particles ... *116*
5.3.3.2 PBA analysis for E. coli expressed with GFP, CFP, YFP ... *117*
5.3.3.2 PBA analysis for E. coli expressed with GFP, CFP, YFP ... *118*

5.4 BURST WIDTH DECONVOLUTION ... 118

5.4.1 DECONVOLUTION OF E. COLI MIXTURES ... 118
5.4.2 DECONVOLUTION OF PARTICLE - E. COLI MIXTURE ... 119

5.5 TIME CORRELATED SINGLE PHOTON COUNTING ... 121

5.5.1 FLUORESCENT PARTICLE LIFETIMES ... 121
5.5.1.1 Bulk lifetime ... *121*
5.5.1.2 Single particle lifetimes ... *122*
5.5.2 E. COLI EXPRESSED WITH FLUORESCENT PROTEINS ... 123
5.5.2.1 Bulk lifetime ... *123*
5.5.2.2 Single cell lifetimes ... *125*
5.5.3 INTER-PHOTON BURST RECURRENCE TIMES ... 126

5.5.3.1 Experimental approach *126*
5.5.3.2 Recurrence time analysis *128*

5.6 SUMMARY **130**

5.7 REFERENCES **130**

Chapter 6 Determination of bulk particulate flow velocities in microchannels

6.1 INTRODUCTION **134**

6.2 EXPERIMENTAL **136**

6.2.1 MATERIALS 136
6.2.2 MICROFLUIDICS 136
6.2.3 CHIP AND SAMPLE INTEGRATION 137

6.3 RESULTS **138**

6.3.1 PHOTON BURST SCANS: BURST FREQUENCY 138
6.3.2 AUTOCORRELATION DEPENDENCE ON FLOW VELOCITY 140
6.3.3 RECURRENCE TIME DEPENDENCE ON FLOW VELOCITY 142

6.4 SUMMARY **144**

6.5 REFERENCES **145**

Chapter 7 Determination of single particle flow velocities in microchannels

7.1 INTRODUCTION **147**

7.2 EXPERIMENTAL **149**

7.2.1 MATERIALS 149
7.2.2 MICROFLUIDIC DEVICES 151
7.2.3 EXPERIMENTAL PROTOCOL 151

7.3 THEORY **151**

7.3.1 PARTICLE BURST IDENTIFICATION AND ISOLATION 151
7.3.2 MAXIMUM LIKELIHOOD ESTIMATOR 152
7.3.2.1 Peak probability distribution function *152*
7.3.2.2 Autocorrelation distribution function *154*

7.4 RESULTS **156**

7.4.1 PROBABILITY DISTRIBUTIONS 156
7.4.1.1 Peak probability distribution *156*
7.4.1.2 Autocorrelation distribution *157*
7.4.1.3 Theoretical approximation of the PPD *158*
7.4.2 DISTINGUISHING BETWEEN SINGLE PARTICLES TRAVELLING AT 2 DISTINCT FLOW RATES 160
7.4.2.1 Using the peak probability distribution *160*
7.4.2.2 Errors in assignment of flow velocities using the PPD *162*
7.4.2.3 Using the autocorrelation probability distribution *163*
7.4.3 DISTINGUISHING BETWEEN SINGLE PARTICLES TRAVELLING AT MULTIPLE FLOW RATES 164
7.4.3.1 Using the peak probability distribution *164*
7.4.3.2 Using the autocorrelation distribution *166*

7.5 SUMMARY **167**

7.6 REFERENCES **167**

Chapter 8 Identification of single protein molecules in solution

8.1 INTRODUCTION 169

8.2 EXPERIMENTAL 171

8.2.1 MATERIALS 171
8.2.1.1 Labeling of fluorescent spheres with protein 171
8.2.1.2 Characterization of IgG and HSA labeled particles 172
8.2.2 MICROFLUIDIC CHANNEL DESIGN 175
8.2.3 SAMPLE DELIVERY AND MICROCHANNEL ALIGNMENT 175

8.3 STUDIES OF PARTICLES LABELED WITH IGG AND HSA 175

8.3.1 PHOTON BURST SCAN STATISTICS OF IGG AND HSA LABELED PARTICLES 176
8.3.2 BURST WIDTH HISTOGRAM ANALYSIS FOR IGG AND HSA LABELED PARTICLES 177
8.3.2.1 Flow rate dependence on BWH for IgG and HSA labeled particles 177
8.3.2.2 Particle size dependence on BWH for IgG and HSA labeled particles 179
8.3.3 BURST HEIGHT VERSUS AREA ANALYSIS FOR IGG AND HSA LABELED PARTICLES 180
8.3.4 AUTOCORRELATION ANALYSIS FOR IGG AND HSA LABELED PARTICLES 182

8.4 STUDIES OF PARTICLES LABELED WITH IGG AND ANTI IGG CONJUGATES 184

8.4.1 MOTIVATION BEHIND DISTINGUISHING BETWEEN IGG AND ANTI IGG LABELED PARTICLES 184
8.4.2 LABELING OF ANTI IGG ONTO IGG-PARTICLES 185
8.4.3 RESULTS 185
8.4.3.1 Burst width histogram analysis for IgG and anti IgG labeled particles 185
8.4.3.2 Autocorrelation curve analysis for IgG and anti IgG labeled particles 186
8.4.3.3 Height versus area distribution analysis for IgG and anti IgG labeled particles 187

8.5 SUMMARY 188

8.6 REFERENCES 189

Chapter 9 Conclusion

9.1 PROJECT AIM 192

9.2 SUMMARY OF ACHIEVEMENTS 192

9.3 SYSTEM IMPROVEMENTS 195

9.4 OUTLOOK 196

Appendices

A1 REALTIME MONITORING OF QUANTUM DOT SYNTHESIS 197

A2 MATLAB SOURCE CODE 213

A2.1 SMD STATISTICAL ANALYSIS PROGRAM 213
A2.2 TCSPC FITTING PROGRAM (WITHOUT A GUI) 231
A2.3 BINNING OF TIME TAGGED SCANS 236
A2.4 MLE STATISTICS PROGRAM 247
A2.5 SMD MONTE CARLO SIMULATION 252
A2.6 HYDRODYNAMIC FOCUSSING SIMULATIONS 256

A3 LIST OF PUBLICATIONS 259

List of Figures

Chapter 1

Figure 1.1 Schematic illustration of the fluorescence absorption-emission cycle and timescales for a single molecule. Competing processes that may reduce the size of a fluorescence photon burst are also shown....3

Figure 1.2 Injection and detection of λ-DNA molecules in free buffer solution. Channel cross section, 50 μm (width) × 20μm (height); E = 86 V/cm; L = 20 mm. DNA concentration, 41 pM; injection volume, 150 pL; injected amount, 6.1 zmol (~3700 molecules). (Adapted with permission. Copyright 1997, The American Chemical Society). 11

Chapter 2

Figure 2.1 Schematic representation of a confocal microscope 21

Figure 2.2 Schematic of the confocal spectrometer for integration with microfluidic devices. (DM, dichroic mirror, M, mirror, I, adjustable iris, OD, neutral density filter, EXP, beam expander, P, right angled prisms, OBJ, microscope objective, BS, beam splitter, LP, long pass filter, L, lens, PH, confocal aperture, SD, single-photon counting avalanche diode detector)..... 22

Figure 2.3 Photographic images of the spectrometer. 23

Figure 2.4 438 nm laser pulse at a repetition rate of 40 Mhz. The FWHM was 73 ps and a maximum optical power of 100 mW/pulse was possible. The average power was 0.48 mW..... 25

Figure 2.5 Transmission curve for the DM 2 dichroic mirror. 27

Figure 2.6 (a) 1/e2 Gaussian intensity contours plotted for a series of laser beam radii (λ = 488nm, f =1.6mm, n = 1.52). (b) Cylindrical and curved components of the Gaussian probe volume. The curved contribution is more significant for larger beam radii and correspondingly tight beam waists. 28

Figure 2.7 Comparison of typical PMT and SPAD wavelength-dependent quantum efficiencies. 29

Figure 2.8 Schematic layout of the post-detector electronics used for fluorescence collection..... 31

Figure 2.9 GUI of the MCS acquisition program. The photon burst scan shown is that of single E. coli cells expressed with green fluorescent protein. Each burst represents a single cell travelling through the probe volume..... 32

Figure 2.10 GUI of the TCSPC acquisition program. The lifetime decay shown (red) is that of single E. coli cells expressed with green fluorescent protein. The instrument response of the detector is shown in blue. 33

Figure 2.11a Single photon burst scan of E. coli expressed with green fluorescent protein using the TCSPC acquisition card in TTMM mode..... 34

Figure 2.11b Fluorescence lifetime decays for E. coli cells expressed with green fluorescent protein using the TCSPC acquisition card in TTMM mode. Each decay profile represents a single cell burst shown in figure 2.9a. 34

Figure 2.12 A 4 in sq. cad design containing 24 microfluidic chips. The CAD file is used as a mask in the chip fabrication process. 37

Figure 2.13 Photograph of 2 complete microfluidic devices. The G2 chip consisted of 2 Y shaped inputs and 1 output. The T100 has 4 microfluidic channels ranging in widths from 20μm – 100 μm. 39

Chapter 3

Figure 3.1 Photon burst scans originating from 1nM and 500pM R-phycoerythrin buffered solutions. Sample is contained within a 50μm square fused silica capillary. Laser illumination = 5 W, channel width = 1ms. The bottom panel shows a similar burst scan originating from a deionized water sample measured under identical conditions. 45

Figure3.2 Simulated fluorescence and background photocount probability distributions. The vertical dashed line at 2 counts represents an arbitrarily defined threshold value for peak determination. 46

Figure 3.3 A photon counting histogram generated from a 16 second photon burst scan originating from a solution of 1000 nm fluorescent microbeads. The dotted curve shows a least squares fit of early channels to a Poisson distribution, and the dashed vertical line marks the peak threshold (4.47 counts). 47

Figure 3.4 Graphical output of the Matlab program for the threshold as well as peak location determination for E. coli cells labelled with green fiuorescent protein. 48

figure 3.5 Burst interval distribution analysis of photon burst scans. Data originate from 1 μm fluorescent beads moving through 150 μm wide microchannels at flow rates of 200nL min^{-1} (circles) and 1000nL min^{-1} (squares). Least squares fits to a single exponential function are shown by the solid lines. 49

Figure 3.6 Graphical output of the Matlab program for the calculation and analysis of photon recurrence times. A least squares fits to a single exponential function is shown by the solid red lines. 50

Figure 3.7 Autocorrelation analysis of photon burst scans of 1 μm fluorescent beads moving through 150 μm wide microchannels at flow rates of 500nL min^{-1} (diamond) and 1000nL min^{-1} (stars). Solid lines represent fits from equation 3.15. 54

figure 3.8 Graphical output of the Matlab program for the calculation and analysis of autocorrelation curves. A least squares fits to the theoretical function is shown with a solid red lines. 57

Figure 3.9 Burst width, area, and height histograms for a photon burst scan of single cells expressing green fluorescent protein. The histograms were calculated over 128 cell bursts. 60

Figure 3.10 GUI of the TCSPC lifetime fitting program. The program shown can fit up to 3 components. 64

Figure 3.11 Fluorescence lifetime decay (blue) for CdSe Nanocrystalline quantum dots. The green curve is the instrument response function and the red curve is the least squares fit. The lower panel displays the residuals of the fit..... 65

Chapter 4

Figure 4.1 Cartoon representation of hydrodynamic focussing in microstructures. In a focussed flow the analyte stream width can have approximately the same dimensions as the probe volume.70

Figure 4.2 Hydrodynamic focussing in a 60 μm wide microfluidic channel. The sheath stream is represented by a blue dye. The analyte flow rate was 5 μl/min and the sheath flow rate was varied between 11 μl/min (top left) to 0.25 μl/min (bottom right). 73

Figure 4.3 Hydrodynamic focussing in a 60 μm wide microfluidic channel. The sheath stream is represented by a blue dye. The analyte flow rate was 1 μl/min and the sheath flow rate was varied between 2 μ/min (top left) to 0.25μl/min (bottom right). 74

Figure 4.4 Hydrodynamic focussing in a 100 μm wide microfluidic channel. The sheath stream is represented by a blue dye. The analyte flow rate was 3 μl/min and the sheath flow rate was varied between 18 μl/min (top left) to 0.05 μl/min (bottom right). 75

Figure 4.5 a) Focussing width relative to sheath flow rate for a 60 μm wide channel. The analyte flow rates are 1, 3, 5, 7, 9 μl/min. b) Focussing width relative to sheath flow rate for a 100 μm wide channel. The analyte flow rates are 0.25, 0.5, 1, 3, 5 μl/min 76

Figure 4.6 Focussing width profile within a 60 μm wide microfluidic channel. The analyte flow rate was 3 μl/min and the sheath flow was varied between 0.05 μl/min and 5 μl/min. 77

Figure 4.7 Variations of focussing width as a function of α for a variety of sheath and analyte flow rates within a 60 μm wide microfluidic channel. The red curve is a least squares fit governed by Equation 4.3..... 79

Figure 4.8 Simulation of focussing width versus α for a variety of channel dimensions..... 80

Figure 4.9 Simulation of particles diffusing from a hydrodynamically focussed analyte stream with a flow rate of 1 μl/min. The channel width and focussed stream are 60μm and 10 μm respectively..... 83

Figure 4.10 Simulation of 1000 nm particles diffusing from a hydrodynamically focussed analyte stream at flow rate ranging from 0.01 μl/min 5 μl/min. The channel width and focussed stream are 60μm and 10 μm respectively. 84

Figure 4.11 Simulation of 1 nm particles diffusing from a hydrodynamically focussed analyte stream at flow rates ranging from 0.01 μl/min 5 μl/min. The channel width and focussed stream are 60 μm and 10 μm respectively..... 85

Figure 4.12 (left) Percent of particles lost from the analyte stream as a function of the channel length for a particle radius of 0.1 nm and focussing width of 10 μm. (right) Same as left with a particle radius of 1000 nm. 87

Figure 4.13 Fraction of particles lost for a particle radius of 10 nm at a flow rate of 1 µl/min at various analyte focussing widths 87

Figure 4.14 (Left) Simulation of two SMD experiments within hydrodynamically focussed microchannels for 1000 nm particles. The analyte flow rate was 1 µl/min. The sheath flow rate was (top left) 2 µl/min and (bottom left) 0.5 µl/min. The channel width was 60 µm. (Right) Simulated autocorrelation curves produced from the photon burst scans for 1000 nm fluorescent particles. 89

Figure 4.15 Single photon burst scans of 0.93 µm fluorescent particles in a focussed analyte stream at various sheath flow rates. The analyte flow rate is constant at 1000 nl/min. 90

Figure 4.16 Total particles detected from single photon burst scans of 0.93 µm fluorescent particles in a focussed analyte stream at various sheath flow rates. The analyte flow rates were 1 µl/min and 3 µl/min respectively 91

Figure 4.17 Single photon burst scans of 0.93 µm fluorescent particles in a focussed analyte stream taken at a sheath flow rate of 1 µl/min and an analyte flow rate of 1 and 3 µl/min within a 60 µm wide microfluidic channels. 93

Figure 4.18 (a) Recurrence times from single photon burst scans of 0.93 µm fluorescent particles in a focussed analyte stream at various sheath flow rates. The analyte flow rates were 1 µl/min and 3 µl/min respectively. (b) Average interburst time. 94

Figure 4.19 (a) Autocorrelation curves for single photon burst scans of 0.93 µm fluorescent particles in a focussed analyte stream at various sheath and analyte flow rates. (b) Simulated autocorrelation curve for a hydrodynamically focussed analyte stream with linear velocities of 18 and 23 mm/s within a 60 µm wide microfluidic channel. 95

Figure 4.20 Mean particle burst width in a hydrodynamically focussed analyte stream. The analyte flow rate was 1 µl/min (black) and 3 µl/min (blue) respectively. The sheath flow rate was varied between 0.04 – 4 µl/min. 96

Figure 4.21 Burst width histogram for hydrodynamically focussed steams at a constant analyte flow rate of 1 µl/min. The sheath flow rates are 0.2, 0.6, 1.5 µl/min which correspond to focussed analyte stream widths of 32, 19, 12 µm respectively 97

Figure 4.22 Mean burst height as a function of sheath flow rate. The analyte flow rates remained constant and were 1 µl/min (black) and 3µl/min (blue) 98

Chapter 5

Figure 5.1 (Left) A microfluidic cell sorter fabricated by Fu et al. The device shown has channels that are 100 µm wide at the wells, narrowing to 3 µm at the sorting junction. The channel depth is 4 µm, and the wells are 2 mm in diameter. (Right) A sketch of the algorithms that they used for the forward sorting and reverse sorting of cells is shown in the schematic of the T-shaped junction. 102

Figure 5.2 Normalized excitation (dark blue) and emission (green) spectra of 930 nm fluorescent microspheres. The absorption and emission maxima were 505 nm and 515 nm respectively

and the spectra were acquired on a fluorescence/transmission spectrometer. λ_{ex} = 475 nm, λ_{em} = 550 nm. 104

Figure 5.3 Excitation and emission spectra of cyano, green and yellow fluorescent protein. The emission maxima are 470, 504, and 525 nm for the cyano, green and yellow proteins respectively. Taken from Clontech (living colours range). 105

Figure 5.4 Three dimensional bucket structure of GFP showing the 11 β-strands forming a hollow cylinder through which is threaded a helix containing the chromophore. The drawing was obtained from the RCSB protein data bank. 106

Figure 5.5 Representative single-particle fluorescence burst scans for 930 nm, 500 nm, and 200 nm Fluospheres at flow rates of 100, 1000, and 5000 nl/min respectively. 109

Figure 5.6 Peak height relative standard deviation with respect to flow velocity. 110

Figure 5.7 Single-cell fluorescence burst scans for E. coli expressed with GFP. The volumetric flow rates (left – right) are 2, 1, 0.5 µl/min respectively. 111

Figure 5.8 Representative single-cell fluorescence burst scans for E. coli expressed with CFP, GFP, and YFP (left – right). The volumetric flow rates in all the plots was 1.0 µl/min. 112

Figure 5.9 Histogram burst width distributions for 930 nm, 500 nm, and 200 nm Fluospheres at flow rates of 100, 1000, and 5000 nl/min respectively. 114

Figure 5.10 Histogram of burst width distributions for E.-coli expressed with CFP, GFP, and YFP. The flow velocity was 1 µl/min for all measurements. 115

Figure 5.11 Histogram burst area distributions for 930 nm, 500 nm, and 200 nm Fluospheres at flow rates of 100, 1000, and 5000 nl/min respectively. 117

Figure 5.12 (Top) Burst width histogram for a mixture of 33 % of each of CFP, GFP, and YFP (blue diamonds). The deconvolved distribution is represented by a dashed line. (Bottom) Component distributions for CFP, GFP and YFP. 119

Figure 5.13 Deconvolved burst width histograms for a mixture of 10 % E. coli expressed with GFP (blue) and 90 % particles (red). The convolved distribution is represented by a black line. The residual is plotted in the bottom half. 120

Figure 5.14 (Top) Fluorescence decay (blue) for 500 nm fluorescent particles in a 0.1 x TBE buffer solution. Decay fit (red) and IRF (green) are also shown. The lower panel displays the residuals of the fit. 121

Figure 5.15 Fluorescence lifetime decays (blue) for 4 single 500 nm fluorescent particles along with a least squares decay fit (red). 122

Figure 5.16 Lifetime histogram from an accumulation of 130 single fluorescent particle decays. A Gaussian fit is shown in red. 123

Figure 5.17 Lifetime histogram from an accumulation of ~75 single E. coli cells expressed with CFP (left) and GFP (Right). 125

Figure 5.18 Schematic principle of the initial steps of an inter-photon burst recurrence time analysis.127

Figure 5.19 Normalized inter-photon burst frequency versus time for E. coli expressed with GFP. The 1st contribution (left) arises from photons associated with a burst, the 2nd from the inter – burst recurrence time. 128

Figure 5.20 Normalized 1st contribution of the inter-photon burst frequency for E. coli expressed with CFP, GFP, and YFP. 129

Chapter 6

Figure 6.1 FT signals collected when the fluorescent microspheres were introduced into the detection area. Conditions: 0.1 X TBE buffer, pH 8.4; electric field strength 161 V/cm. Courtesy of A. Manz. 135

Figure 6.2 Schematic of "Double-Y" PDMS microchip used for the analyses. The detection volume was positioned at a point midway along the wide (150 μm) channel. 136

Figure 6.3 Component-based confocal detection optics. (M, mirror; I, adjustable iris; OD, neutral density filter; SF, spatial filter; P, right-angled prism; OBJ, 100x microscope objective; DC, dichroic beamsplitter; EF, emission filter; L, lens; AP, confocal aperture; SPAD, detector).138

Figure 6.4 Representative single particle photon burst scans at a variety of flow rates for 0.93 μm fluospheres in TBE buffer. 139

Figure 6.5 Expanded portions of the single particle photon burst scans as a function of volumetric flow rate. 139

Figure 6.6 Average photon burst width for 0.93 μm fluorescent particles travelling at a flow rate of 1 μl/min in TBE buffer. 140

Figure 6.7 Experimental autocorrelation curves for 0.93 μm fluorescent beads flowing thru a microfluidic channel. The dwell time was 2 ms. 141

Figure 6.8 1/FWHM value of the autocorrelation curve as a function of flow rate (gradient 0.75). ... 142

Figure 6.9 Inter burst separation distributions determined for a variety of flow rates for 0.93 μm fluorescent particles. 142

Figure 6.10 Variation in the normalized burst frequency as a function of flow rate for 0.93 μm fluorescent particles (gradient 0.72). The detection region within the PDMS chip was positioned at a point midway along the 150 μm wide channel. 143

Figure 6.11 Variation in the normalized recurrence time as a function of flow rate for 0.93 μm fluorescent particles (gradient 0.78). The detection region within the PDMS chip was positioned at a point midway along the 150 μm wide channel. 144

Chapter 7

Figure 7.1 Cartoon representation of flow velocity dependence on single particle photon burst characteristics 147

Figure 7.2 Fluorescence lifetimes obtained by the MLE for single (a) Cy5-dCTP, (b) MR121-dUTP, (c) Bodipy-dUTP and (d) JA53-dUTP molecules in water against number of detected photons per burst. 149

Figure 7.3 (a) Fluorescence burst scans originating from 0.93 μm Fluospheres flowing through a microchannel at volumetric flow rates of 2000 nL/min and 300 nL/min. (b) Expanded portions of (a). 150

Figure 7.4a Variation of the peak probability distribution function for 0.93 μm fluorescent particles travelling at a flow rate of 2000 nL/min as a function of the number of bursts analysed. .. 153

Figure 7.4b Variation of the peak probability distribution function for 0.93 μm fluorescent particles travelling at a flow rate of 2000 nL/min as a function of the number of bursts analysed. .. 154

Figure 7.5 Variation of the autocorrelation probability distribution function for 0.93 μm fluorescent particles travelling at a flow rate of 2000 nL/min as a function of the number of bursts analysed. 156

Figure 7.6 Peak probability distribution functions for 0.93 μm fluorescent particles travelling at flow rates between (a) 700 – 2000 nL/min and (b) 100 – 600 nl/min. 157

Figure 7.7 Autocorrelation probability distribution functions for 0.93 μm fluorescent particles travelling at flow rates between 100 – 2000 nL/min. 158

Figure 7.8 Experimental and simulated peak probability distribution functions for 0.93 μm fluorescent particles travelling at flow rate of 1000 nl/min (top) and 200 nl/min (bottom)..... 159

Figure 7.9 ε values for an actual particulate flow rate of 2000 nL/min. γ_a PPD had flow rates of 2000 nL/min (a –b), and 500 nl/min (c-d). The γ_b PPD has flow rates ranging from 100 – 2000 nL/min. 161

Figure 7.10 The percent error in assigning correct and incorrect flow velocities to single particles in a system with particles travelling at two distinct flow rates as a function of the PPD flow rate in γ_b. In all cases the γ_a PPD flow rate was defined to be 2000 nL/min. 163

Figure 7.11 (Top) The percent error in assigning correct and incorrect flow velocities to single particles in a system with particles travelling at two distinct flow rates as a function of the APD flow rate in χ_b. In all cases the χ_a APD flow rate was defined to be 2000 nL/min. (Bottom) Difference between assigning velocities using the APD and PPD. 164

Figure 7.12 (a) MLE values calculated with PPD flow rates of 100 – 2000 nL/min for single particles travelling at a flow rate of 2000 nL/min. 165

Figure 7.12 (b) MLE values calculated with PPD flow rates of 100 – 2000 nL/min for single particles travelling at a flow rate of 300 nL/min. 165

Figure 7.13 χ_b values calculated with APD flow rates of 100 – 2000 nL/min for single particles travelling at a flow rate of 2000 nL/min. 166

Chapter 8

Figure 8.1 Model of the HSA and IgG molecules from x-ray diffraction studies..... 170

Figure 8.2 Electropherograms obtained by applying a separation voltage of 15 kV for 500 nm fluorescent particles (top), labeled with IgG (middle) and HSA (bottom) in a 50 mM phosphate buffer (pH 7.4). 173

Figure 8.3 Emission spectra of (a) 500 nm carboxylate modified particles (black) and IgG labeled particles (red) (b) 500 nm carboxylate modified particles (black) and HSA labeled particles (red). An excitation wavelength of 460 nm was used for all measurements. 174

Figure 8.4 Photon burst scans for 500 nm particles (a), HSA labeled particles (b), IgG labeled particles (c) and 50/50 IgG-HSA labeled particles (d). A flow rate and dwell time of 500 nl/min and 100 ìs was used for all scans..... 177

Figure 8.5 Burst width histograms for 500 nm particles (top), HSA labeled particles (middle), IgG labeled particles (bottom). 178

Figure 8.6 Comparison between labeled and unlabeled particle burst width histograms for 200 nm particles (top), 500nm particles (middle), 930 nm particles (bottom). 179

Figure 8.7 Comparison of burst height versus area plot for unlabeled 500 nm particles and for IgG and HSA labeled 500 nm particles. 180

Figure 8.8 Autocorrelation curves for labeled and unlabeled fluorescent particles at flow rates of 1 and 0.5 µl/min. 182

Figure 8.9 Ratio of autocorrelation curves between IgG and HSA labeled particles. The curves were measured for particle sizes of 500 nm (blue) and (930 nm) red. The volumetric flow rate was 500 nl/min..... 183

Figure 8.10 Photon burst scans for 500 nm particles (a) labeled with IgG and (b) anti –IgG. The flow rate was 500 nl/min. 186

Figure 8.11 Burst width histograms for 500 nm particles labeled with IgG and anti –IgG.....186

Figure 8.12 Autocorrelation curves for IgG labeled and anti-IgG labeled fluorescent particles at flow rates of 0.5 µl/min..... 187

Figure 8.13 Area-height plots for IgG labeled and anti-lgG labeled fluorescent particles at flow rates of 0.5 µl/min. 187

List of Tables

Chapter 5

Table 5.1 Fluorescein equivalents in fluorescent particles 108

Table 5.2 Summary of average burst width for 3 particle sizes at 3 flow rates. 113

Table 5.3 Summary of average burst areas for 3 particle sizes at 3 flow rates. 116

Table 5.4 Summary of lifetimes and amplitudes for CFP, GFP, YFP. 124

Table 5.5 Summary of yields and amplitudes for E. coli expressing CFP, GFP, YFP. 124

Chapter 8

Table 8.1 Slopes of burst area versus height plot for a flow rate of 500 nl/min 181

Symbols and Abbreviations

AIT average interburst time

APD autocorrelation probability distribution

BAH burst area histogram

BHH burst height histogram

BSD burst size distribution

BWH burst width histogram

CE capillary electrophoresis

CEF collection efficiency function

χ^2 chi-squared parameter

CM confocal microscope

CMM continuous mode measurement

cps counts per second

CW continuous wave

D diffusion coefficient

Δt burst separation time

DNA deoxyribonucleic acid

DW Durbin Watson

FCS fluorescence correlation spectroscopy

FWHM full width half maximum

λ Laser wavelength

LIF laser induced fluorescence

LSA least squares analysis

M molar concentration

MC Monte-Carlo

MCS multi-channel scalar

MDE molecular detection efficiency

μTAS miniaturized total analysis system

MLE maximum likelihood estimator

$N(\Delta t)$ burst interval distribution

N.A. numerical aperture

NA numerical aperture

P(x) Poisson distribution

PCH photon counting histogram

PDMS poly(dimethylsiloxane)

PIV particle image velocimetry

PLA peak locating algorithm

PMT photomultiplier tube

PPD peak probability distribution

r beam radius

Re Reynolds number

R6G Rhodamine 6G

R-PE R-phycoerythrin

RSD relative standard deviation

S/N signal-to-noise

SERS surface enhanced Raman scattering

SMD single molecule detection

SMFC single molecule flow cytometry

SPAD single-photon counting avalanche photodiode

τ_D characteristic diffusion time

τ_{flow} characteristic flow time

τ_R burst recurrence time

TBE tris borate EDTA buffer (89 mM tris borate, 2 mM EDTA, pH ~8.3)

TCSPC time-correlated single-photon counting

TTMM time-tagged mode measurement

UHQ ultra-high quality

V confocal probe volume

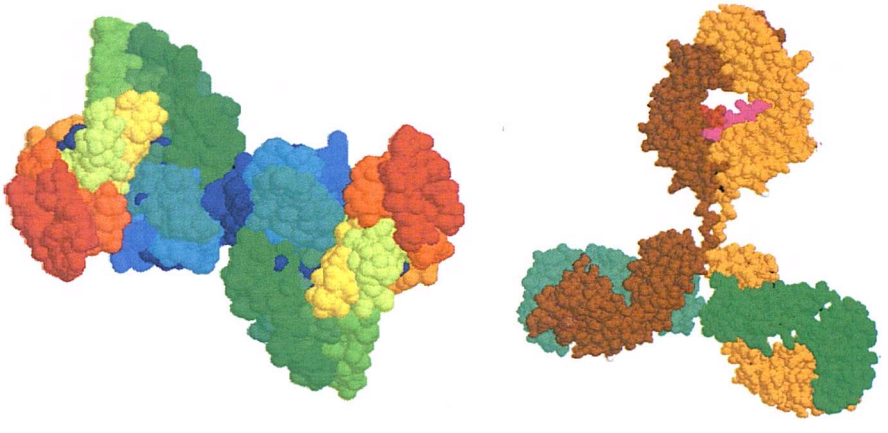
w_0 beam waist radius

WQS weighted quadratic sum

Z' probe depth

- 1 -

An introduction to the concepts and theory of single-molecule fluorescence detection is given. The motivation for ultra sensitive analysis is addressed, as well as a current overview of research relevant to the work in this thesis.



Introduction

1.1 Single Molecule detection

A significant challenge facing experimentalists in the physical and biological sciences is the detection and identification of single molecules in solution. The ability to perform such sensitive and selective measurements is extremely valuable in applications such as DNA analysis, immunoassays, environmental monitoring, and forensics where small sample volumes and low analyte concentrations are the norm. More generally, most experimental observations of physical systems provide a measurement of ensemble averages, and yield information only on average properties. In contrast, single molecule measurements allow the observation of how individual members of a molecular population behave and interact in real-time. This thesis describes the development and application of single molecule and particle fluorescence detection techniques for microfluidic analysis. This represents detection at the ultimate sensitivity level of ~1.66×10^{-24} moles (1.66 yoctomoles). This quantity is equal to the inverse of Avogadro's number *(a 'guacamole').* The motivation behind this work has been to improve and apply single molecule detection to novel analytical problems.

Single molecule spectroscopy in solution is a relatively new field of research and is becoming increasingly popular.[1] Over the past few years a number of techniques with sufficient sensitivity have been developed to detect single molecules in solution. Scanning probe microscopies (most notably scanning tunnelling microscopy and atomic force microscopy) have been used to great effect in the analysis of surface bound species[2], but for the detection of single molecules in liquids optical methods incorporating the measurement of absorption and emission processes have proved most successful.

1.1.1 The Absorption-Emission Cycle

The key concept underlying most optical approaches to single molecule detection in solution is that a single molecule can be cycled repeatedly between its ground state and an excited electronic state to yield multiple photons. The process can be understood by reference to **Figure 1.1**. Fluorescence emission in the condensed phase can be described using a four-step cycle. Excitation from a ground electronic state to an excited state is followed by rapid (internal) vibrational relaxation. Subsequently, radiative decay to the ground state is observed as fluorescence emission and is governed by the excited state lifetime. The final stage is internal relaxation back to the original ground state. Under saturating illumination, the rate-

limiting step for this cycle is governed by the fluorescence lifetime (τ_f), which is typically of the order of a few nanoseconds. If a single molecule diffuses through an illuminated zone (e.g. the focus of a laser beam) it may reside in that region for several milliseconds. The rapid photon absorption-emission cycle may therefore be repeated many times during the residence period, resulting in a burst of fluorescence photons as the molecule transits the beam. The burst size is limited theoretically by the ratio of the beam transit time (τ_r) and the fluorescence lifetime, i.e.

$$N_{photons} = \frac{\tau_r}{\tau_f} \qquad \text{(Equation 1.1)}$$

For typical values of τr (5 ms) and τf (5 ns) up to one million photons may be emitted by the single molecule. In practice, photobleaching and photodegradation processes limit this yield to about 105 photons. Furthermore, advances in optical collection and detection technologies enable registration of about 1% of all photons emitted. This results in a fluorescence burst signature of up to 1000 photons or photoelectrons.

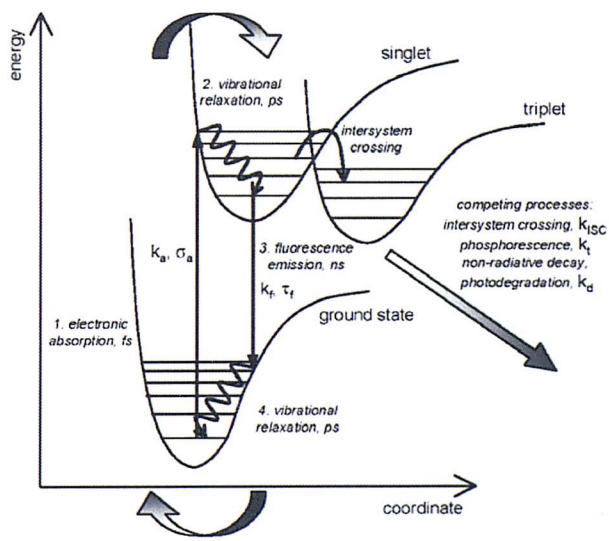


Figure 1.1 Schematic illustration of the fluorescence absorption-emission cycle and timescales for a single molecule. Competing processes that may reduce the size of a fluorescence photon burst are also shown.

1.1.2 Ultra-sensitive analysis: motivation

Big advances in ultra sensitive detection of fluorescent molecules in liquids at room temperature have been made since the first successful optical microscopic observation of

single molecules in 1976.[3] Over the past several years, high sensitivity detection has found increasing importance in biological and chemical analysis. This is a result of a need for rapid, on-line measurements at low concentrations.[4]

The primary challenge in SMD is to ensure sufficient reduction in background levels to enable discrimination between the analyte signal and noise. As an example, in a 1 nM aqueous dye solution each solute molecule occupies a volume of approximately 1 fL.[5] However, within this same volume are contained in excess of 10^{10} solvent molecules. Despite the relatively small scattering cross-section for an individual water molecule ($\sim 10^{-28}$ cm^2 at 488 nm), the cumulative scattering signal from the solvent may swamp the desired fluorescence signal. The principal way of reducing the solvent background is to minimise the optical detection volume: the signal from a single molecule is independent of probe volume dimensions, but the background scales proportionally with the size of the detection region. Alternative background signal reduction methods include optical rejection of Raman and Rayleigh scatter by photobleaching of the solvent[6], and by using time-gated detection.[7] Although, there are several experimental approaches to SMD in solution, a number of factors hold common:

1. Small detection volumes are used to reduce background signals ($\sim 10^{-12} - 10^{-15}$ L).

2. A low analyte concentration ensures that less than one analyte molecule is present in the probe volume at any instant.

3. High-efficiency photon collection and detection maximizes the proportion of fluorescence bursts registered.

4. Background reduction methods are employed to improve signal-to-noise ratios.

1.1.3 Single molecule detection using confocal microscopy

Confocal microscopy (CM) is currently the most widely used method for realizing SMD. In SMD based confocal microscopy, the excitation source is typically a laser. The major benefit in using laser-induced fluorescence (LIF) is in the sensitivity that can be achieved. A laser beam has essentially monochromatic excitation; therefore, the excitation line can be precisely matched to the absorption maximum of the analyte under investigation.

In CM single molecules are detected as they diffuse or move through the probe volume. The diffusion time is directly related to the hydrodynamic radius, the solvent viscosity, and the flow rate of the sample.[8] The hydrodynamic radius is in turn determined by the shape and size of the molecule. Typically for a probe volume in the fL range the diffusion time will be on the order of a few milliseconds. Diffusion times can be mathematically extracted using autocorrelation analysis.[8]

It should be noted that the molecular detection efficiency in CM is extremely low because it is almost impossible to ensure that all analyte molecules pass through such a small probe volume. The larger the probe volume the greater the molecular detection efficiency; however, a compromise with the signal to noise ratio will always exist. To address this issue, it is of interest to use micro capillaries or microchannels to manipulate and deliver analyte molecules to the detection region. This method has great potential in increasing the molecular detection efficiencies in such experiments. Conversely the small volumes associated with microfluidic systems require detection methods which will provide the ultimate limit of detection. It is for this reason that performing SMD within microfluidic systems has recently become a high priority goal.

1.1.4 Microfluidics: background

The first suggestion of downsizing in the physical sciences was mentioned by Richard Feynman at the 1959 meeting of the American Physical Society in a talk entitled "There is plenty of room at the bottom".[9] He opened a discussion on examining the limits set by physical principles on known technology and proposed a variety of new nano-tools including the concept of "atom by atom" fabrication. In the following decades his predictions became reality as microelectronic systems have shrunk to sizes close to the molecular level. With this in mind, it is perhaps surprising that the concept of a miniaturized total analysis system (μ-TAS) for biological and chemical applications was only seriously addressed by Manz and Widmer in 1990.[10]

μ-TAS are microfluidic analytical instruments employing micromachined features (such as channels, electrodes, reactors and filters) that are able to manipulate and process fluid samples with high precision and efficiency. Microfluidic chip devices have been used in a wide variety of applications including nucleic acid separations[11], protein analysis[12], small-molecule organic synthesis[13], DNA amplification[14], immunoassays[15], DNA sequencing[16], and cell manipulations.[17] The benefits of downsizing include enhanced analytical performance, reduced separation and analysis times, reduced reaction times, smaller sample sizes, reduced

reagent waste, high levels of functional integration and automation, and reduced instrument footprints when compared to conventional (larger) analogues. Ideally a μ-TAS contains all the necessary features for sampling, sample pre-treatment, chemical reactions, analyte separartion, analyte isolation and detection. Much of the pioneering work in microfluidics has focussed on transferring successful technologies from conventional systems to microfluidic formats. For example, the miniaturization of column dimensions and creation of fluidic networks on monolithic substrates for capillary electrophoresis has resulted in large improvements in separation efficiency, sample throughput and analysis times.[11, 18-20] The benefits of device downsizing can be clearly seen by considering diffusional motion of small molecules in a solvent. If for example a path length for a diffusing molecule is changed by a factor of 1000 (e.g. from 1 mm to 1 μm) the diffusion time will be decreased by a factor of 1 000 000. Other benefits include the actual size and the scale of the device. Clearly due to the relatively small channel dimensions (< 100 μm), there is potential to have thousands of microfluidic devices on a single chip, which in turn has direct impact on device cost and analytical throughput. The popularity of μ-TAS technology has grown dramatically over the past 10 years and can be justified by the significant growth of original papers in the literature.[21, 22]

Small volumes of samples and reagents are representative of most miniaturized systems. This characteristic has clear advantages associated with cost and analytical throughput, but does pose constraints on appropriate detection methods. Consequently, much research has recently focussed on the development of detection techniques that are highly sensitive, universal, miniaturized, and cost-effective. The majority of microfluidic systems utilize fluorescent based schemes for detection. However, other approaches to "on-chip" detection have been introduced. These include electrochemical[23], electrochemiluminescent[24], absorption[25], indirect fluorescence[26], refractive index[27], and plasma detection.[28]

The most popular materials used to make microfluidic devices are glass, silicon, and polydimethylsiloxane (PDMS).[29] Devices can also be made using a combination of these materials. Microfluidic channels are typically structured using microlithographic techniques. Briefly, methods normally involve exposing a glass substrate coated with a thin layer of photoresist to UV light through a photomask. Subsequent development in an organic solvent allows the removal of exposed portions of photoresist. This resist mask is used to define the pattern of the desired fluidic microstructure. Etching allows the photoresist pattern to be transferred to the substrate material. Etchants are typically aqueous in nature and can act isotropically or anisotropically.[30-32] Anisotropic etching can yield channels with extremely high aspect ratios while isotropic etchants yields sloping walls with low aspect ratios.

Hydrofluoric acid based solutions are most commonly used as they allow for precise control over the etching rate. Once etched a glass-glass microfluidic device must be drilled to obtain access holes to the channels. The final step is to thermally bond the cover glass to the substrate in an oven at 600 °C.[30] If a glass device is to be used for SMD using confocal spectroscopy, the top plate thickness is limited by the working distance of the microscope objective. The short working distance of high NA microscope objectives is a major constraint in successfully performing SMD in microfluidic devices with CM. For a 1.3 NA objective a typical working distance is ~150 μm. Therefore microchip construction must be designed in such a manner that the top plate is no thicker than the actual working distance. This limitation can generally be overcome by optically polishing the top plate to the required thickness. The method described above is time consuming; however, the key benefit is that an extremely rigid structure is made.

An alternative to a glass-glass microdevice is to use a PDMS substrate covered with a thin microscope cover slip. This polymer has several attractive features: it can be easily moulded, is optically transparent, durable, chemically inert, and non toxic. Creation of microstructures using this polymer is easily accomplished. Typically a 10:1 mixture of base and curing agent is degassed under vacuum and poured over a negative mould of the desired structure. Curing can either take place for 1 hr at 90 ^{0}C or overnight for 24 hr. The polymer can then be *peeled off* the master which can be reused. Enclosed channels are created when the PDMS forms a seal with another substrate. A primary advantage in using PDMS is that it forms a natural reversible seal with glass. This means that devices made from PDMS can be cleaned to remove blockages that may form during use. An irreversible seal can also be formed by treatment of the PDMS surface with an oxygen plasma prior to bonding.[33] Chips made from PDMS are much cheaper and generally easier to produce when compared to chips made from glass.[34]

1.1.5 Single molecule detection: a general review

1.1.5.1 Dye Selection

Dye selection plays an important role in SMD applications. Ionic dyes are often well suited to SMD as fluorescence quantum efficiencies can be close to unity and fluorescence lifetimes below 10 nanoseconds. For example, xanthene dyes such as Rhodamine 6G and tetremethyl-rhodamine isothyiocyanate are commonly used in SMD studies.[35, 36] However, other highly fluorescent dyes such as fluorescein are unsuitable for such applications due unacceptably

high photodegradation rate coefficients. Single molecule detection of free fluorescein (to date) has only been reported once.[37] Furthermore, some solvent systems may enhance non-radiative processes, such as intersystem crossing, and yield significant reduction in the photon output. Macromolecules such as R-phycoerythrin (R-PE) containing multiple fluorophores are ideally suited to SMD. R-PE is a naturally occurring molecule, which is derived from cyanobacteria and algae.[38] B-phycoerythrin has been used extensively in the development of SMD techniques.[39] However this molecule like fluorescein exhibits strong photobleaching effects.[40] It is becoming increasingly popular to use naturally occurring fluorescent proteins in SMD studies.[41, 42] For example, Green Fluorescent Protein (or GFP) is very resistant to photo bleaching because its chromophore is located within the interior of its "ß-can" structure and is thus protected from molecular oxygen.

1.1.5.2 Single molecule detection: applications

Due to the extensive range of SMD studies to date, a comprehensive review will not be provided herein. Rather, the reader is directed to excellent review articles covering the field of research.[43-49] A few examples of SMD utilizing CM are described below. Rigler and co-workers pioneered the use of confocal techniques to detect single molecules. They based their initial experiments on detecting single Rhodamine 6G molecules in water diffusing through a 0.24 fL probe volume,[50] and reported a signal to noise ratio of approximately 1000. Other interesting applications of CM include the observations of the dynamics of a single dye molecule interacting with guanine on a DNA strand.[51] Edman et al. report on two possible conformations for tetramethyrhodamine tethered to a short DNA oligomer. Fluorescence correlation spectroscopy under confocal conditions has been used to examine singlet-triplet intersystem crossings in fluorophores.[52] Nie at al have recently devised a system to follow single molecule fluorescence directly in real-time.[52] This approach has been used to study dye molecules in solution as well as fluorescently labelled proteins and DNA fragments. With a low background level and high excitation efficiency, single rhodamine molecules have been detected with a signal to noise ratio of ~20 in 1 ms.

DNA based applications using SMD are also of high current interest. Potential applications include fragment sizing and ultimately DNA sequencing. SMD has also been shown to be of interest in fields as diverse as immunology, and biotechnology.[53] Described below are a few examples of SMD applications used for DNA analysis. Keller et al were the first to propose a novel method for rapid DNA sequencing based on single molecule detection.[54] Their approach requires labeling different nucleotide types with distinguishable fluorophores and polymerase incorporation of the labeled nucleotides into a strand of DNA. The DNA fragment

must then be attached to a suitable support within the microchannel. Movement of the supported DNA into a flow stream then causes the DNA fragment to stretch out into the flow. Exonuclease digestion of the free end of the fluorescently-labeled DNA strand sequentially releases the fluorophore labeled nucleotides into the flow stream and efficient SMD and identification of the fluorophores in the ordered sample stream is obtained. Determination of single DNA molecule fragment lengths has also recently been reported. In these studies, the integrated fluorescence signals of individual fragments are used to calculate the fragment length.[55] Pico green is a fluorescent molecule that is typically used for quantitation of dsDNA in solution. The dye, unbound to DNA, has a very low fluorescence quantum yield and is therefore weakly fluorescent. Upon binding to dsDNA there is a 2000 fold increase in the signal intensity.[56] Dyes of this nature are extremely valuable for SMD due to almost no background fluorescence being created by the free dye itself. Research by members of the de Mello group at Imperial College has shown that a signal to noise ratio of several hundred can be attained when measuring single molecule bursts of lambda DNA labelled with picogreen.[57]

It has become increasingly popular to use single molecule fluorescence resonant energy transfer (SM-FRET) to monitor conformational dynamics of single proteins.[58, 59] In FRET, a short wavelength "donor" fluorophore is pumped by a light source and its energy is transferred to a longer wavelength "acceptor" via a Forster dipole-dipole interaction, whereupon the acceptor fluoresces at a longer wavelength. Recently Rhoades et al. provided direct evidence for heterogeneous folding pathways from single-molecule studies using confocal spectroscopy.[60] Individual fluorophore-labeled molecules of the protein adenylate kinase were trapped within surface-tethered lipid vesicles, thereby allowing spatial restriction without inducing any spurious interactions with the environment. The conformational fluctuations of these protein molecules, were studied using fluorescence resonance energy transfer between two specifically attached labels. Folding and unfolding transitions appeared in experimental time traces as correlated steps in the donor and acceptor fluorescence intensity.

CM is currently the method of choice for SMD applications. However, there are several other methods that have been used to good effect. For example; hydrodynamic focusing of a narrow stream within a sheath flow (orthogonal to excitation) is often used to ensure that an entire sample is delivered to an excitation volume.[61,62] Under appropriate conditions, each molecule within the sample can be detected sequentially and with high efficiency. This approach is conventionally termed single-molecule flow cytometry (SMFC). In SMFC, individual molecules are motivated within the sample stream at the same rate, and experience the same radiation field during their passage through the detection volume. During focusing, the sample

stream accelerates to match the velocity of the sheath stream; this keeps the flow rate constant. By the 'conservation of mass' principle the diameter of the sample stream must be decreased. This method results in sample stream diameters from 1 – 20 μm. A primary disadvantage with this approach is in the large background signal that arises when the probe volume is enlarged to the picoliter scale. This can often be larger than the fluorescence signal from the target molecule.

Another approach to realizing SMD uses levitated microdroplets. When using this technique, volumes between 1 fL – 1 pL can be obtained.[63, 64] SMD is achieved by laser induced fluorescence detection of single molecules dissolved in levitated micro-droplets. For example, Whitten and co-workers electrodynamically levitated microdroplets and detected small numbers of rhodamine-6G molecules. As few as 12 molecules were detected in a single water droplet.[64] A benefit of this approach is that small micro droplet volumes minimize background emission due to solvent Raman and Rayleigh scattering and impurity fluorescence. However, severe problems arise due to position dependent variations of the excitation laser intensity and the fluorescence collection efficiency inside the micro droplet (caused by refraction of incident excitation and emitted fluorescence at the micro droplet surface).[63] Another major drawback of sensitive detection in levitated microdroplets is the very low sample throughput rate. It can take as long as several minutes to measure the bursts arising from a single microdroplet.

1.1.6. Single molecule detection in microchannels

The following section describes a comprehensive review of studies detailing the use of SMD for detection in microchannel environments.

Effenhauser and co-workers reported one of the first examples of SMD in microfludic devices in 1997.[65] In the same publication, the authors also provided the first report of electrophoresis microchips structured in PDMS using soft lithographic techniques. Injection and detection of full length λ-DNA molecules in free buffer yielded fluorescence bursts which were attributed to the passage of a single molecule through the detection volume as is shown in ***Figure 1.2***. This was performed by intercalated λ DNA molecules with YOYO-1. A high signal to noise ratio was achieved as each λ-DNA molecule was labeled with approximately 5000 intercalating dye molecules. At a similar time Mathies and colleagues demonstrated SMD of Rhodamine 6G in simple silicon/glass microstructures.[66] Although, a good signal-to-noise ratio was demonstrated, scattering from the silicon substrate resulted in high background levels.

The first SMD separation within a microfluidic channel was performed by Ramsey et al.[67] They managed to separate Rhodamine 6G (at 15 pM) and Rhodamine B (at 30 pM) by counting fluorescence bursts from individual molecules. They noted that although the molecular detection efficiency was low (~1.75%), reductions in channel dimensions and electrokinetic focusing of sample streams could be use to theoretically increase detection efficiencies to approximately 75%. In 1998 Haab and Mathies detected fragments in a 100-1000 base pair DNA sizing ladder separated by capillary electrophoresis.[68] The authors realised that in order to detect a larger fraction of the intra-capillary sample either the detection volume has to be increased or more sample should pass through the detection volume. As stated previously, an increased detection volume is generally undesirable since background interferences increase. Consequently, the authors adopted an approach incorporating both a physical narrowing (or tapering) of channel dimensions and electrodynamic focusing to deliver more sample through the detection volume. It was shown that both a physical taper and electrokinetic pinching affords superior sample stream restriction. This single molecule counting technique was subsequently used to detect electrophoretic gel separations of a DNA sizing ladder and yielded a greater than three-fold enhancement in detection efficiencies with respect to normal chip-based separations.[68]

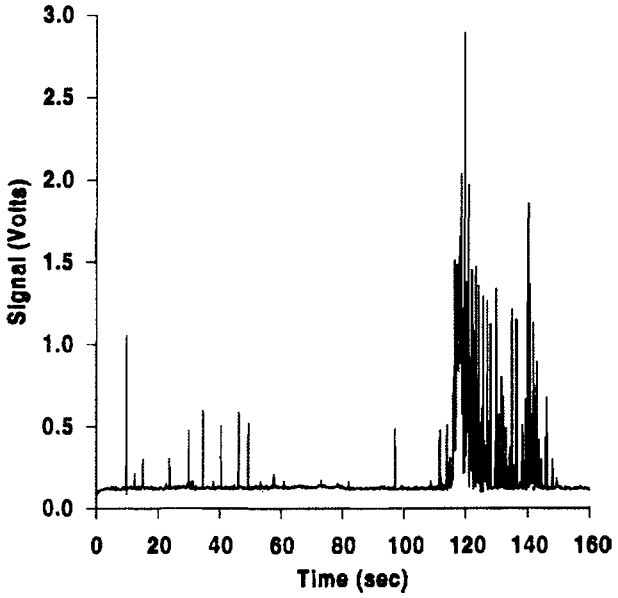


Figure 1.2 Injection and detection of λ-DNA molecules in free buffer solution. Channel cross section, 50 μm (width) × 20μm (height); E = 86 V/cm; L = 20 mm. DNA concentration, 41 pM; injection volume, 150 pL; injected amount, 6.1 zmol (~3700 molecules). (Adapted with permission. Copyright 1997, The American Chemical Society).

Single photon burst techniques have been used by Soper and co-workers to detect double stranded DNA molecules in poly(methylmethacrylate) (PMMA) and polycarbonate (PC) microfluidic devices.[69] A confocal epi-illumination detection system was constructed to monitor the fluorescence signature from single DNA molecules that were multiply labeled with the mono-intercalating dye, TOPRO-5 (having an absorption maximum at 765 nm). Near-IR excitation minimized autofluorescence produced from the polymer substrate, and initial experiments demonstrated efficient detection of single DNA molecules and molecular detection efficiencies of up to 73% were reported for probe volumes of 1 pL and channel widths of 10 μm.

Performing SMD-DNA fragment sizing is becoming increasingly popular within microchannels due to the potential for low detection limits and quick analysis times.[53, 55] For example, Yan et al. developed an efficient and reliable double-stranded DNA (dsDNA) staining protocol for DNA fragment sizing by flow cytometry.[55] The protocol uses PicoGreen to label a range of DNA concentrations (0.5 ng/mL to 10000 ng/mL) without regard to the solution dye/bp ratios and without initial quantification of the DNA analyte concentration. Another approach has been developed by Quake et al.[70] They demonstrated a microfabricated single-molecule DNA sizing device. The device is 100 times faster than pulsed-field gel electrophoresis, and has a resolution that improves with increasing DNA length. It also requires a million times less sample than pulsed-field gel electrophoresis and has comparable resolution for large molecules. The authors demonstrated efficient sizing of DNA molecules ranging from 2000 to 200,000 base pairs. Although this approach was successful, channel dimensions were relatively large with respect to confocal probe volumes. This resulted in reduced detection efficiencies. With this in mind Craighead and co-workers at Cornell University remedied this problem by reducing channel dimensions to the sub-micron scale. With this approach significant advances in DNA fragment sizing have been achieved.[71] Nanochannels were fabricated using sacrificial layer fabrication techniques, allowing for the creation of complex structures with a high degree of structural precision. With this approach DNA sizing and quantification could be performed with as little as 10000 molecules in only a few seconds.

More recently Craighead and colleagues have utilized zero mode waveguides to circumvent the problem of diffraction limited optics and have performed SMD at micromolar concentrations with a microsecond temporal resolution.[72] A similar approach was undertaken by Lyon and Nie.[73] The authors used sub-micrometer capillaries (500-600 nm i.d.) for confinement and detection of single molecules at room temperature. These restrictive channels markedly reduce the Brownian motion of low molecular weight analytes and allow

detailed studies of single molecules in solution. With a confocal fluorescence microscope, single molecules were observed for periods up to 60 ms. This is 50-100 times longer than the bulk diffusion time.

The efficient functioning and integration of processes within microfluidic systems is almost always closely related to the precise control of flow velocities and flow profiles within microchannels. The ability to accurately monitor flow velocities and flow profiles with high spatial resolution in experimental systems is a highly powerful tool. Recently there has been interest in using SMD for high spatial resolution hydrodynamic flow profiling using fluorescence correlation spectroscopy (FCS).[74] Confocal fluorescence microscopy was used to detect single tetramethylrhodamine (TMR-4-dUTP) biomolecules traversing a 1 fL volume element defined by an argon laser. The microchannel was then scanned with a diffraction-limited laser beam thereby demonstrating Poiseuille laminar flow profile. In FCS, fluorescence emission from individual molecules is collected as they move through a diffraction-limited detection volume. Autocorrelation analysis of the emission subsequently yields information relating to molecular diffusion coefficients, flow velocities and rate coefficients.[45, 75-77] Viser et al. used a similar approach to probe flow profiles of pressure-driven flow inside a microcapillary. By using FCS, it was found that bacteria and microspheres are retarded in their flow by optical forces produced by the laser beam. In 2002, Lenne and co-workers also reported on hydrodynamic and electrophoretic flow profiling in microcapillaries using FCS.[75] Capillary electrophoresis resulted in velocity profiles that are dependent on channel dimensions while hydrodynamic flow profiles were found to be Poiseuille like.

A final application worth briefly mentioning is time-resolved detection of single molecules using the principles of time-correlated single-photon counting (TCSPC). This technique has enabled the fluorescence lifetime of a single molecule to be recorded in a confocal system.[78-81] Single molecule lifetime determination offers a useful extra dimension for identification and discrimination at the single-molecule level. A bulk lifetime measurement results in an ensemble averaged fluorescence decay time while accumulation of single molecule decays allows for the construction of a lifetime histogram. This is an ideal method to directly probe system inhomogeneity. As an example, Sauer and colleagues used TCSPC to measure lifetimes of single Cy5-dCTP and MR121- dUTP molecules.[82] They were able to obtain an overall classification probability of about 96% for distinguishing between both molecules via fluorescence decay times. Cy5-dCTP had a fluorescence lifetime of 1.42 +/- 0.21 ns and MR121-dUTP had a lifetime of 2.41 +/- 0.32 ns.

1.2 Project aim

Commercial confocal laser scanning microscopes can be prohibitively costly and complex. Modification of a standard fluorescence microscope may not offer full operator control in optical alignment and optimisation. Hence, the initial aim of this project was to develop a custom built confocal fluorescence detection system for the analysis of fluorescent molecules within microfluidic channels. In order to maximize configurational flexibility, the system was constructed so as to be able to perform SMD, TCSPC, steady-state fluorescence spectroscopy and Raman spectroscopy.

A selection of key applications will be discussed in this thesis that address a number of issues previously described: First, a non-invasive, optical technique for measuring particulate flow within microfluidic channels was developed. Second, a novel method was developed to size single particles or molecules in free solution. Third, hydrodynamic focusing in microstructures was demonstrated and combined with confocal microscopy as a route to improving molecular detection efficiencies within sub femtoliter probe volumes. Fourth, a statistical method using the maximum likelihood estimator was devised to distinguish between flow velocities of single molecules or particles in a microfluidic channel. Fifth, a microfluidic cell counting and cell recognition technique was developed using time correlated single photon counting as well as single molecule spectroscopy. This method was also used to analyse E. coli cells expressed with green, cyano, and yellow fluorescent protein. Finally, biological molecules, such as human serum albumin and immunoglobulin G, labeled to single fluorescent particles were found to be distinguishable based on photon burst characteristics. This approach can prove to be useful for discriminating and identifying proteins in continuous real time.

The motivation behind all the above applications is to demonstrate the benefits of new analysis techniques which can potentially be used at the single molecule level. The approaches undertaken result in lower sample consumption, higher throughput, and ultra-fast analysis times when compared to conventional systems.

1.3 References

(1) Barnes, M. D.; Whitten, W. B.; Ramsey, J. M. *Anal. Chem.* **1995**, 418A-423A.

(2) Vargas, F.; Hollricher, O.; Marti, O.; de Schaetzen, G.; Tarrach, G. *Journal of Chemical Physics* **2002**, *117*, 866-871.

(3) Hirschfeld, T. *Applied Optics* **1976**, *15*, 2965-2966.

(4) Jakeway, S. C.; de Mello, A. J. Russell, E. L. *Fresenius J Anal Chem* **2000**, *366*, 525-539.

(5) Hill, E. K.; de Mello, A. J. *The Analyst* **2000**, *125*, 1033-1036.

(6) Affleck, R. L.; Ambrose, W. P.; Demas, J. N.; Goodwin, P. M.; Keller, R. A. *Analytical Chemistry* **1996**, *68*, 2270-2276.

(7) Harris, T. D.; Macklin, J. J.; Trautman, J. K. *Abstracts of Papers of the American Chemical Society* **1997**, *214*, 122 - ANYL.

(8) Osborne, M. A.; Balasubramanian, S.; Furey, W. S.; Klenerman, D. *Journal of Physical Chemistry B* **1998**, *102*, 3160 - 3167.

(9) Feynman, R., *http://www.zyvex.com/nanotech/feynman.html* **2003**.

(10) Manz, A.; Graber, N.; Widmer, H. M. *Sensors and Actuators B* **1990**, *1*, 244-248.

(11) Zhang, B. L.; Foret, F.; Karger, B. L. *Analytical Chemistry* **2001**, *73*, 2675-2681.

(12) Sanders, G. H. W.; Manz, A. *Trac-Trends in Analytical Chemistry* **2000**, *19*, 364-378.

(13) Freemantle, M. In *Chemistry and Engineering News*, 1999, pp 27-36.

(14) Kopp, M. U.; de Mello, A. J.; Manz, A. *Science* **1998**, *280*, 1046-1048.

(15) Rossier, J. S.; Schwarz, A.; Reymond, F.; Ferrigno, R.; Bianchi, F.; Girault, H. H. *Electrophoresis* **1999**, *20*, 727-731.

(16) Buchholz, B. A.; Doherty, E. A. S.; Albarghouthi, M. N.; Bogdan, F. M.; Zahn, J. M.; Barron, A. E. *Analytical Chemistry* **2001**, *73*, 157-164.

(17) Taylor, M. T.; Belgrader, P.; Furman, B. J.; Pourahmadi, F.; Kovacs, G. T. A.; Northrup, M. A. *Analytical Chemistry* **2001**, *73*, 492-496.

(18) Mitchell, M. C.; Spikmans, V.; de Mello, A. J. *Analyst* **2001**, *126*, 24-27.

(19) Lee, G. B.; Chen, S. H.; Huang, G. R.; Sung, W. C.; Lin, Y. H. *Sensors and Actuators B-Chemical* **2001**, *75*, 142-148.

(20) Krishnan, M.; Namasivayam, V.; Lin, R. S.; Pal, R.; Burns, M. A. *Current Opinion in Biotechnology* **2001**, *12*, 92-98.

(21) Auroux, P. A.; Iossifidis, D.; Reyes, D. R.; Manz, A. *Analytical Chemistry* **2002**, *74*, 2637-2652.

(22) Reyes, D. R.; Iossifidis, D.; Auroux, P. A.; Manz, A. *Analytical Chemistry* **2002**, *74*, 2623-2636.

(23) Wang, J. *Chemistry-a European Journal* **1999**, *5*, 1681-1685.

(24) Arora, A.; Eijkel, J. C. T.; Morf, W. E.; Manz, A. *Analytical Chemistry* **2001**, *73*, 3282-3288.

(25) Zimmermann, B.; Burck, J.; Ache, H. J. *Sensors and Actuators B-Chemical* **1997**, *41*, 45-54.

(26) Munro, N. J.; Huang, Z. L.; Finegold, D. N.; Landers, J. P. *Analytical Chemistry* **2000**, *72*, 2765-2773.

(27) Kameoka, J.; Craighead, H. G. *Sensors and Actuators B* **2001**, *77*, 632-637.

(28) Eijkel, J. C. T.; Stoeri, H.; Manz, A. *Analytical Chemistry* **1999**, *71*, 2600-2606.

(29) McDonald, J. C.; Duffy, D. C.; Anderson, J. R.; Chiu, D. T.; Wu, H. K.; Schueller, O. J. A.; Whitesides, G. M. *Electrophoresis* **2000**, *21*, 27-40.

(30) Stjernstrom, M.; Roeraade, J. *Journal of Micromechanics and Microengineering* **1998**, *8*, 33-38.

(31) Parisi, G. I.; Haszko, S. E.; Rozgonyi, G. A. *Journal of the Electrochemical Society: Solid-state science and Technology* **1977**, *124*, 917-921.

(32) Ulrich, J.; Zengerle, R. *Sensors and Actuators A* **1996**, *53*, 379-385.

(33) Duffy, D. C.; McDonald, J. C.; Schueller, O. J. A.; Whitesides, G. M. *Analytical Chemistry* **1998**, *70*, 4974-4984.

(34) Lorenz, H.; Despont, M.; Fahrni, N.; LaBianca, N.; Renaud, P.; Vettiger, P. *Journal of Micromechanics and Microengineering* **1997**, *7*, 121-124.

(35) Ramsey, J. M.; Whitten, W. B. *Abstracts of Papers of the American Chemical Society* **1989**, *198*, 74 - ANYL.

(36) Wagner, B.; Mathis, H.; Schmidt, K.; Kalusche, G.; McCaskill, J. *Nucleosides and Nucleotides* **1997**, *16*, 635-642.

(37) Lee, Y. H.; Maus, R. G.; Smith, B. W.; Winefordner, J. D. *Analytical Chemistry* **1994**, *66*, 4142-4149.

(38) Molecular Probes, **1998**.

(39) Bunfield, D. H.; Davis, L. M. *Applied Optics* **1998**, *37*, 2315-2326.

(40) Wu, M.; Goodwin, P. M.; Ambrose, W. P.; Keller, R. A. *Journal of Physical Chemistry* **1996**, *100*, 17406 - 17409.

(41) Moerner, W. E. *Journal of Chemical Physics* **2002**, *117*, 10925-10937.

(42) Harms, G. S.; Cognet, L.; Lommerse, P. H. M.; Blab, G. A.; Schmidt, T. *Biophysical Journal* **2001**, *80*, 2396-2408.

(43) Zhuang, X. W.; Rief, M. *Current Opinion in Structural Biology* **2003**, *13*, 88-97.

(44) de Mello, A. J. *Lab on a Chip* **2003**, *3*, 29N-34N.

(45) Michalet, X.; Weiss, S. *Comptes Rendus Physique* **2002**, *3*, 619-644.

(46) Vives-Rego, J.; Lebaron, P.; Nebe-von Caron, G. *Fems Microbiology Reviews* **2000**, *24*, 429-448.

(47) Ishii, Y.; Yanagida, T. *Single Molecules* **2000**, *1*, 5-16.

(48) Uppenbrink, J.; Clary, D. *Science* **1999**, *283*, 1667.

(49) Barnes, M. D.; Whitten, W. B.; Ramsey, J. M. *Analytical Chemistry* **1995**, *67*, 418A-423A.

(50) Mets, U.; Rigler, R. *Journal of Fluorescence* **1994**, *4*, 259-264.

(51) Ambrose, W. P.; Goodwin, P. M.; Jett, J. H.; van Orden, A.; Werner, J. H.; Keller, R. A. *Chemical Reviews* **1999**, *99*, 2929-2956.

(52) Nie, S.; Zare, R. N. *Ann. Rev. Biophys. Biomol. Struct.* **1997**, *26*, 567-596.

(53) van Orden, A.; Keller, R. A.; Ambrose, W. P. *Analytical Chemistry* **2000**, *72*, 37-41.

(54) Keller, R. A. *Research grant proposal* **1998**.

(55) Yan, X.; Grace, W. K.; Yoshida, T. M.; Habbersett, R. C.; Velappan, N.; Jett, J. H.; Keller, R. A.; Marrone, B. L. *Analytical Chemistry* **1999**, *71*, 5470-5480.

(56) Yue, S. T.; Singer, V. L.; Roth, B. L.; Millard, P. J.; Jones, L. J.; Haugland, R. P.; Molecular Probes Inc.: Intl, 1996.

(57) Hill, E. K.; de Mello, A. J. *Unpublished results* **2000**.

(58) Ha, T. *Methods* **2001**, *25*, 78-86.

(59) Ha, T. *Current Opinion in Structural Biology* **2001**, *11*, 287-292.

(60) Rhoades, E.; Gussakovsky, E.; Haran, G. *Proceedings of the National Academy of Sciences of the United States of America* **2003**, *100*, 3197-3202.

(61) Nguyen, D. C.; Keller, R. A.; Jett, J. H.; Martin, J. C. *Analytical Chemistry* **1987**, *59*, 2158-2161.

(62) Demas, J. N.; Wu, M.; Goodwin, P. M.; Affleck, R. L.; Keller, R. A. *Applied Spectroscopy* **1998**, *52*, 755-762.

(63) Ramsey, J. M.; Whitten, W. B. *Abstracts of Papers of the American Chemical Society* **1990**, *199*, 62 - ENVR.

(64) Whitten, W. B.; Ramsey, J. M.; Arnold, S.; Bronk, B. V. *Analytical Chemistry* **1991**, *63*, 1027-1031.

(65) Effenhauser, C. S.; Bruin, G. J. M.; Paulus, A.; Ehrat, M. *Analytical Chemistry* **1997**, *69*, 3451-3457.

(66) Mathis, H. P.; Kalusche, G.; Wagner, B.; McCaskill, J. S. *Bioimaging* **1997**, *5*, 116-128.

(67) Fister, J. C.; Jacobsen, S. C.; Davis, L. M.; Ramsey, J. M. *Analytical Chemistry* **1998**, *70*, 431-437.

(68) Haab, B. B.; Mathies, R. A. *Biophysical Journal* **1998**, *74*, A9.

(69) Wabuyele, M. B.; Ford, S. M.; Stryjewski, W.; Barrow, J.; Soper, S. A. *Electrophoresis* **2001**, *22*, 3939-3948.

(70) Chou, H.; Spence, C.; Scherer, A.; Quake, S. R. *Proceedings of the national academy of sciences of the united states of america* **1999**, *96*, 11-13.

(71) Foquet, M.; Korlach, J.; Zipfel, W.; Webb, W. W.; Craighead, H. G. *Analytical Chemistry* **2002**, *74*, 1415-1422.

(72) Levene, M. J.; Korlach, J.; Turner, S. W.; Foquet, M.; Craighead, H. G.; Webb, W. W. *Science* **2003**, *299*, 682-686.

(73) Lyon, W. A.; Nie, S. M. *Analytical Chemistry* **1997**, *69*, 3400-3405.

(74) Gosch, M.; Blom, H.; Holm, J.; Heino, T.; Rigler, R. *Anal. Chem.* **2000**, *72*, 3260.

(75) Lenne, P. F.; Colombo, D.; Giovannini, H.; Rigneault, H. *Single Molecules* **2002**, *3*, 194-200.

(76) Dittrich, P. S.; Schwille, P. *Analytical Chemistry* **2002**, *74*, 4472-4479.

(77) Foldes-Papp, Z.; Demel, U.; Tilz, G. P. *Proceedings of the National Academy of Sciences of the United States of America* **2001**, *98*, 11509-11514.

(78) Moerner, W. E.; Fromm, D. P. *Review of Scientific Instruments* **2003**, *74*, 3597-3619.

(79) Treussart, F.; Alleaume, R.; Le Floc'h, V.; Roch, J. F. *Comptes Rendus Physique* **2002**, *3*, 501-508.

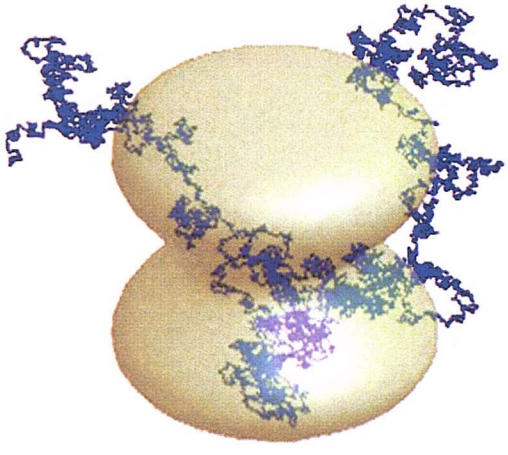
(80) Lee, M.; Tang, J. Y.; Hochstrasser, R. M. *Chemical Physics Letters* **2001**, *344*, 501-508.

(81) Enderlein, J.; Krahl, R.; Ortmann, U.; Wahl, M.; Erdmann, R.; Klose, E. *Proc. SPIE* **1995**, *2388*, 71 - 78.

(82) Sauer, M.; Angerer, B.; Han, K. T.; Zander, C. *Physical Chemistry Chemical Physics* **1999**, *1*, 2471-2477.

- 2 -

This chapter describes the development and implantation of the confocal spectrometer for single molecule analysis. In brief, the system is capable of performing single molecule detection, time correlated single photon counting, time tagged photon counting, steady state fluorescence, and Raman spectroscopy. Design and fabrication procedures for microfluidic devices are also discussed.



Experimental

2.1 Confocal Spectroscopy

Single molecule confocal spectroscopy has emerged as an important tool for the characterization of biological molecules. As previously mentioned, the ability to perform high sensitivity measurements is extremely valuable in many applications, including DNA analysis, immunoassays, environmental monitoring, and forensics. Over the past few years a number of optical techniques with sufficient sensitivity have been developed to detect single molecules. Scanning probe microscopies have been highly successful in the analysis of surface bound species, but for single molecule detection in fluids, fluorescence methods have proved most successful. The key advantage of single-molecule spectroscopy in biophysics is its ability to directly measure the temporal trajectory of a functioning biomolecule. Such a measurement can provide information on functional dynamics which is not typically possible using conventional bulk measurement techniques. The sharp spatial resolution of confocal microscopes allows definition of a distinct and small observation volume that is ideal for single-molecule detection.

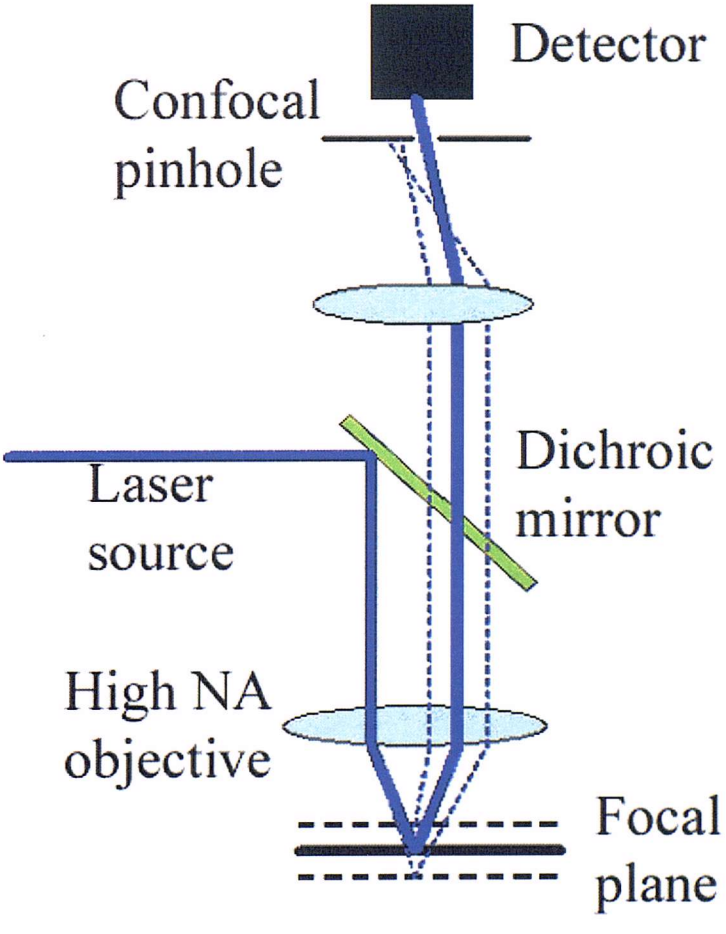


Figure 2.1 Schematic representation of a confocal microscope

In its simplest form, a confocal spectrometer consists of a point light source, a point focus in the object plane and a pinhole detector; all of which are confocal with each other (*Figure 2.1*). In single molecule confocal microscopy (CM), the excitation source is typically a laser. The major benefit in using laser-induced fluorescence (LIF) is in the sensitivity that can be achieved.[1-4] Lasers typically exhibit monochromatic light output, allowing the excitation source to be precisely matched to the absorption maximum of the analyte. In CM, the excitation source is typically reflected at a dichroic beam splitter and focused by a microscope objective to create a micron sized beam waist in the sample. A dichroic mirror is used to allow for discrimination between the excitation source and analyte emission. The objective must posses a high numerical aperture (NA) as this allows for tight focussing of the incident light as well as maximizing the collection of fluorescence photons over a wide solid angle.[5] For example, if an NA of 1.3 is used a collection angle of 68^0 relative to the plane of the objective is possible. Numerical aperture defines the three-dimensional cone angle from which light is collected. Fluorescence emission is isotropic, so selection of a large NA objective will increase the proportion of light collected from the probe volume.

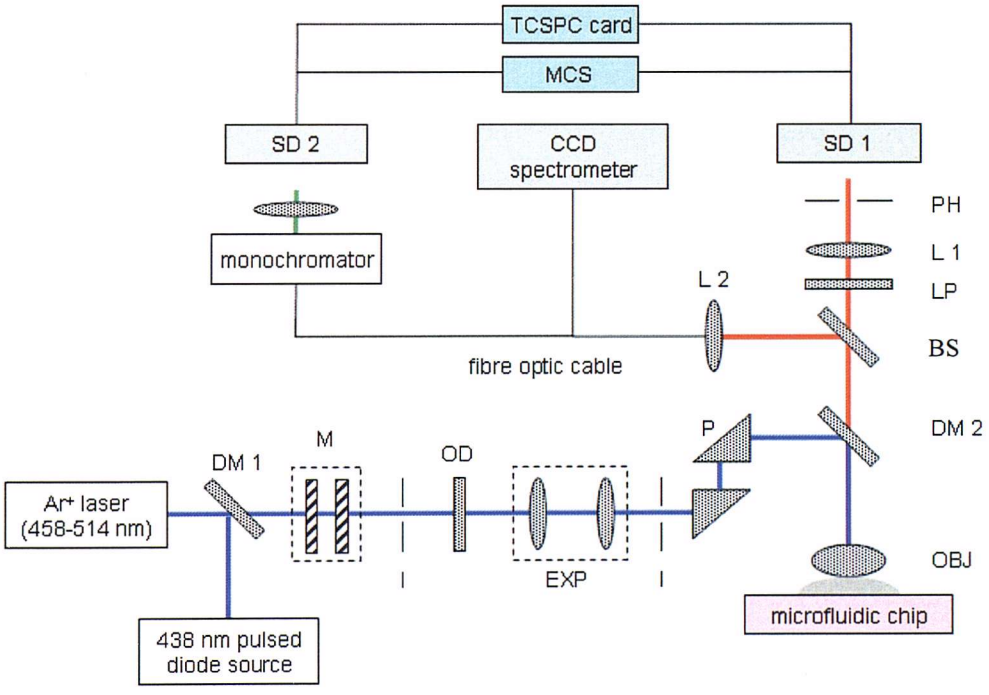
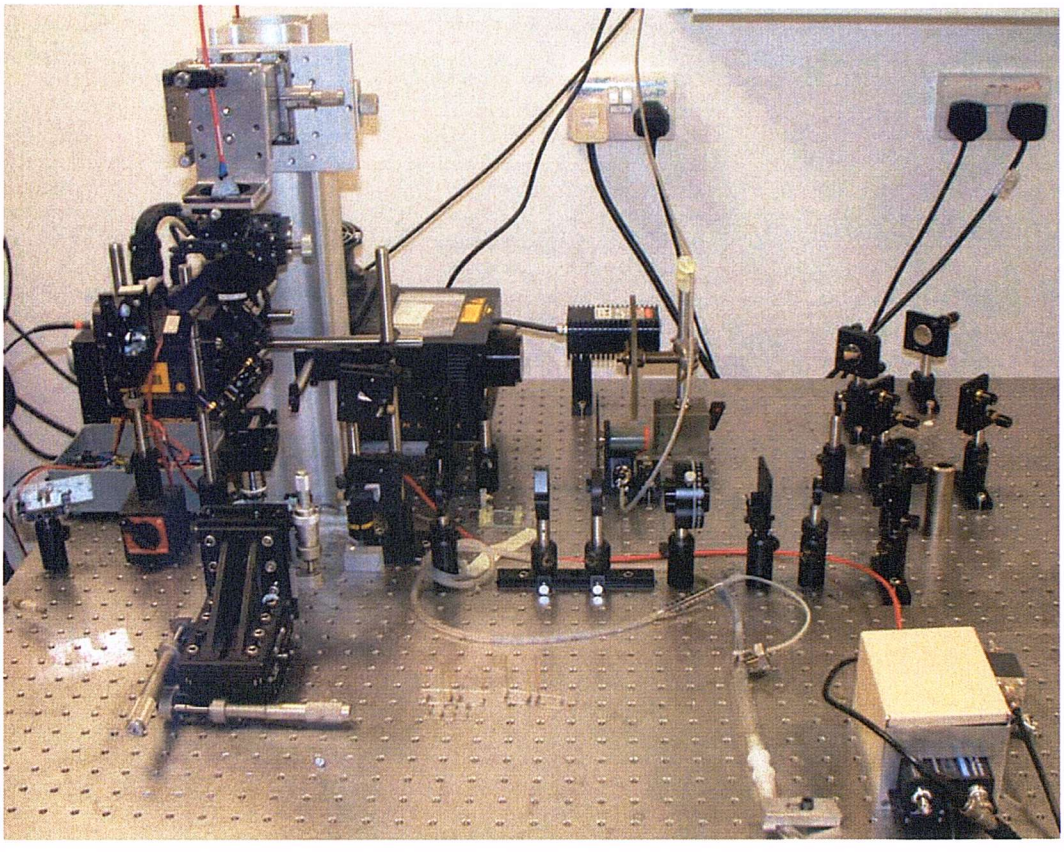


Figure 2.2 Schematic of the confocal spectrometer for integration with microfluidic devices. (DM - dichroic mirror, M - mirror, I - adjustable iris, OD - neutral density filter, EXP - beam expander, P - right angled prisms, OBJ - microscope objective, BS - beam splitter, LP - long pass filter, L - lens, PH - confocal aperture, SD - single-photon counting avalanche diode detector).



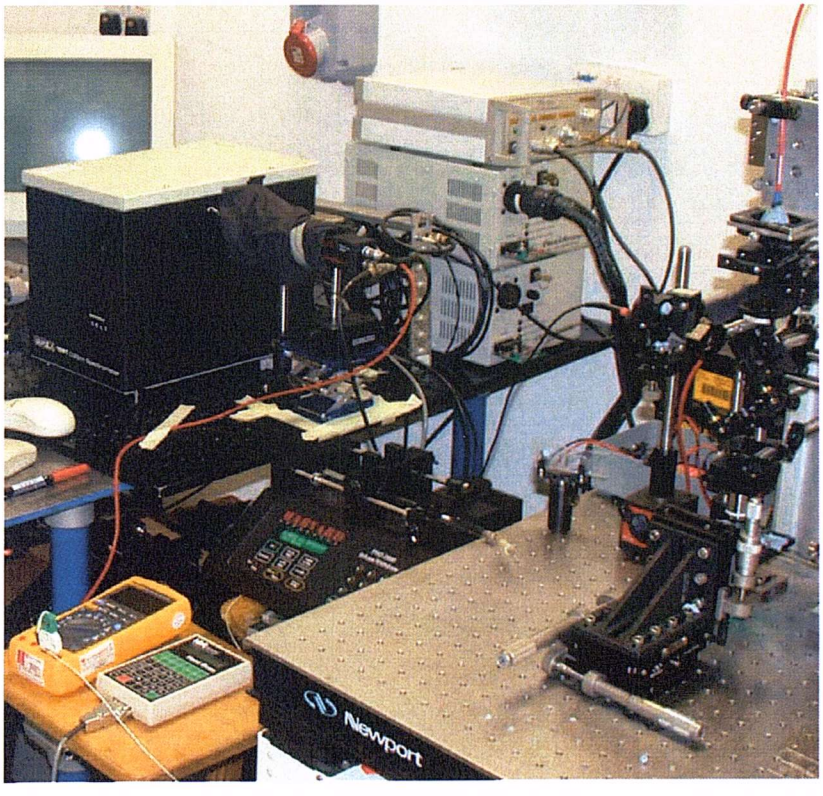


Figure 2.3 Photographic images of the spectrometer.

Fluorescence from the sample is collected by the same microscope objective used to focus excitation light and is passed through the dichroic beam splitter. In the example shown in *Figure 2.1*, fluorescence photons emanating from the focal plane are transmitted towards the confocal detector pinhole, whereas scattered radiation (of higher energy) is reflected through the dichroic back towards the light source. A detector collects the photons that are passed through the pinhole. A pinhole is located precisely in the confocal plane of the objective so that only light emanating from the focal point is transmitted through the pinhole to the detector. Light that does not derive from the focal plane is mostly rejected by the aperture, and therefore is not detected. *Figure 2.1* shows a schematic diagram of a generic confocal fluorescence system. Some sample beam paths are shown, including rays from just above or below the focal plane that are blocked by the pinhole. The optical probe volume is crucial in confocal detection as knowledge of the excitation volume defined by confocal optics is critical for quantitative applications. Both the magnification power of the objective as well as the detection pinhole size governs the detection probe volume.

The confocal spectrometer developed in this thesis for the analysis of single molecules and particles is shown in *Figures 2.2 and 2.3* respectively. The system was built and mounted on an optical bench and breadboard (50 cm x 120 cm; Thorlabs, Elliot Scientific, Harpenden UK) to ensure maximum flexibility in the design and build. Parts of the instrument are developed from a similar spectrometer described by Elisabeth Hill.[6]

2.2 Instrument Design

2.2.1 Excitation source

The spectrometer incorporates two excitation sources; a multi line argon ion laser as well as a pulsed diode laser. The argon ion laser is a continuous wave (CW), air-cooled laser operating in light control mode, with emission lines ranging from 457.9 nm to 514.5 nm (Omnichrome; Melles Griot, Cambridge, UK). A maximum power output at 488 nm is approximately 40 mW. A tuneable laser allowed excitation of a number of common fluorophores used in this thesis. The strongest lasing outputs occur at 514 nm (green) and 488 nm (blue). The appropriate wavelength is controlled by using a tuneable Littrow prism as a wavelength-selecting element. The source was ideal for time-integrated spectral analysis, as well as for obtaining single molecule and particle photon burst scans.

The picosecond pulsed diode laser operates at 438 nm (PicoQuant GmbH). The pulsed diode laser provides the excitation source for time correlated single photon counting experiments. The pulsed diode was driven with a PDL 800-B driver also from PicoQuant. The driver unit contains a built in pulse generator which produces a master frequency of 40 MHz that can be divided by factors of 1, 2, 4, 8, 16 to produce selectable frequencies of 40, 20, 10, 5, 2.5 MHz. An external function generator (TTi, electronics, UK) was coupled to the external trigger input of the driver so that lasing repetition frequencies could be controlled and varied between 100 KHz and 40 Mhz. As will be shown in the following chapter, low repetition frequencies are needed when analyzing species with long fluorescent lifetimes (greater than 10 ns) in order to maximize the potential number of photon counts. ***Figure 2.4*** shows an example of a typical laser pulse obtained at a repetition rate of 40 MHz with a full width half maximum of 73 ps. With the current diode laser head peak powers up to 208 mW/pulse and pulse widths as short as 50 ps were achieved. The average power was 1.24 mW for a repetition rate of 40 MHz. The driver unit was set up to contain a permanently active sync output which allows the PDL-800 to trigger the TCSPC electronics which will be discussed in a later section.

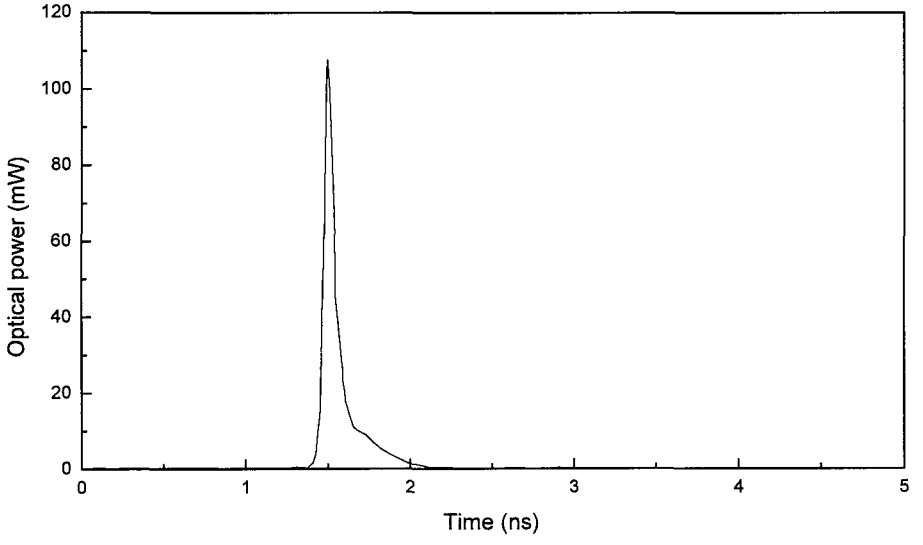


Figure 2.4 438 nm laser pulse at a repetition rate of 40 Mhz. The FWHM was 73 ps and a maximum optical power of 100 mW/pulse was possible. The average power was 0.48 mW.

2.2.2 Beam steering optics

Both lasers were aligned so that the paths taken by each laser beam were identical after the DM 1 dichroic mirror. Combining both beams to follow the same path was achieved using a dichroic mirror positioned at a 45° angle (with respect to the argon ion laser) so that the 438 nm beam would be reflected by the dichroic mirror and the 488 nm line would pass directly

through the mirror. Beamsteering mirrors (BK7 glass, λ/10 surface flatness, reflectivity > 99 %; Comar Instruments, Cambridge, UK) were used to control the beam height as well as beam direction. The beam height and alignment is defined by the use of 5 irises (I) with controllable apertures. The height of all apertures was fixed to be 100 mm above the optical table.

Both laser beams were spatially filtered (5-axis compact filter; Newport Ltd.) to ensure a near-Gaussian intensity profile. This is crucial in defining the shape of the probe volume in SMD experiments.[7] The beam was further expanded 2x using standard Galileian optics (EXP). Beamsteering prisms (P) were used to direct the light into the dichroic mirror (DM 2) of the confocal system. Prior to the prism an optical chopper (Elliot Scientific, UK) was introduced to allow for lock-in amplification if required. The chopper was typically operated at frequencies between 100 and 3500 Hz. In the majority of experiments the chopper was operated at 3500 Hz so that the frequency was much lower than the acquisition dwell times (in the majority of cases this varied between 0.5 – 2 ms).

2.2.3 Laser beam attenuation (OD)

The laser beam must be attenuated, as in SMD based experiments photobleaching often occurs when using high laser powers (> 10 μW).[8-10] Attenuation on the order of 3.0 – 4.0 OD was used in the majority of experiments, to insure a laser power between 100 nW and 7 μW, and achieved using three different methods. 1) A filter wheel was used with variable optical density (0 – 1 OD). This was placed directly in front of the argon ion laser. 2) Glass neutral density filters were used as required (0.2 – 4 OD, Newport Ltd., Newbury, UK) to attenuate both laser beams and were placed directly in front of the beam expander. 3) A polarizer was placed prior the prisms in order to control the plane of polarization. Both lasers had a plane of polarization 90 ° out of phase with respect to each other. Hence, the desired laser could be chosen simply by rotating the filter. This filter was also used for attenuation of the laser beams.

2.2.4 Dichroic mirror (DM 2)

A dichroic mirror (470 DRLP02; Omega Optical, Brattleboro, VT, US) is oriented at 45° to reflect the laser beam radiation and so define a vertical axis, normal to the surface of the optical table. The argon ion lines above 470 nm could still be used as 50 % of the laser power, at these higher wavelengths, could be reflected by the dichroic mirror. The transmission and reflectance characteristics of DM 2 are shown in ***Figure 2.5***. It was also possible to replace

this with a 515 nm dichroic (above that of the 514 nm argon ion line). However, this was deemed non viable as a large proportion of the photons collected from the microscope objective would go undetected due to the lower energy transmission cut-off.

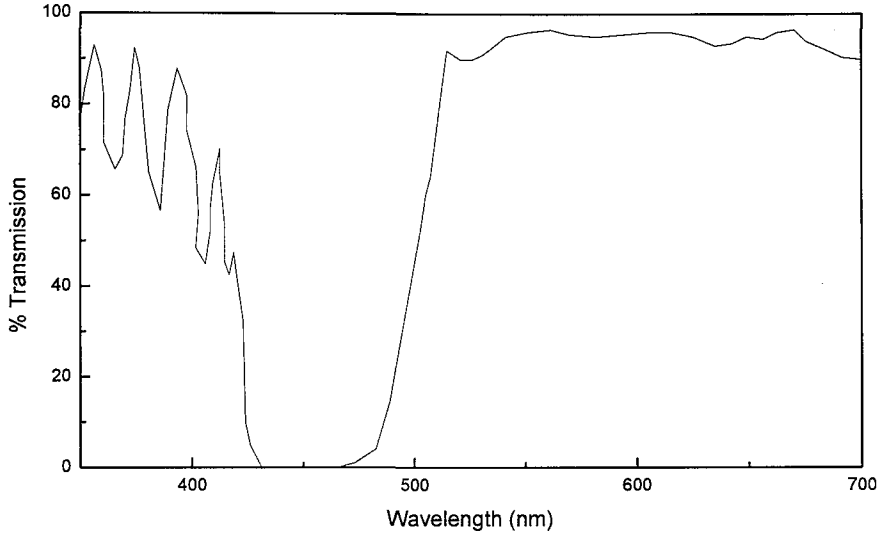


Figure 2.5 Transmission curve for the DM 2 dichroic mirror.

2.2.5 Microscope objective (OBJ)

An infinity corrected, high NA microscope objective (Fluar 100×/1.3 NA, oil immersion; Carl Zeiss Ltd., Welwyn Garden City, UK) brings the laser light to a tight focus within a microfluidic channel. The collimated laser beam has a $1/e^2$ diameter of 2.5 mm. This was determined by using the knife edge approach.[11] The width of the incident beam is selected to nearly fill the back of the microscope objective, and so yield a beam focus estimated to be close to the diffraction limit. The focussed beam diameter (d) is given by the ***Equation 2.1***,

$$d = \frac{1.27\lambda f}{nD} \qquad \text{(Equation 2.1)}$$

where D is the incident diameter of the laser radiation at the objective, n is the refractive index of the focusing medium, f is the focal length of the objective and λ is the lasing wavelength. The focused laser spot defines an approximate probe volume of 0.42 fL and is defined according to the following equation:

$$V = 2\pi\left(\frac{\lambda f}{n\pi D}\right)^2 Z' + \frac{2\lambda^2}{3\pi}\left(\frac{n\pi D}{\lambda f}\right)^2 Z'^3 = \frac{2\lambda^2 f^2}{\pi n^2 D^2} Z' + \frac{2\pi n^2 D^2}{3 f^2} Z'^3 \qquad \text{(Equation2.2)}$$

The volume is expressed in terms of identifiable experimental variables and constants (The probe depth Z' is limited by the diameter of the confocal pinhole). The first term may be correlated with the cylindrical contribution to the overall volume, and the second term is the additional volume due to the curved contour.[6]

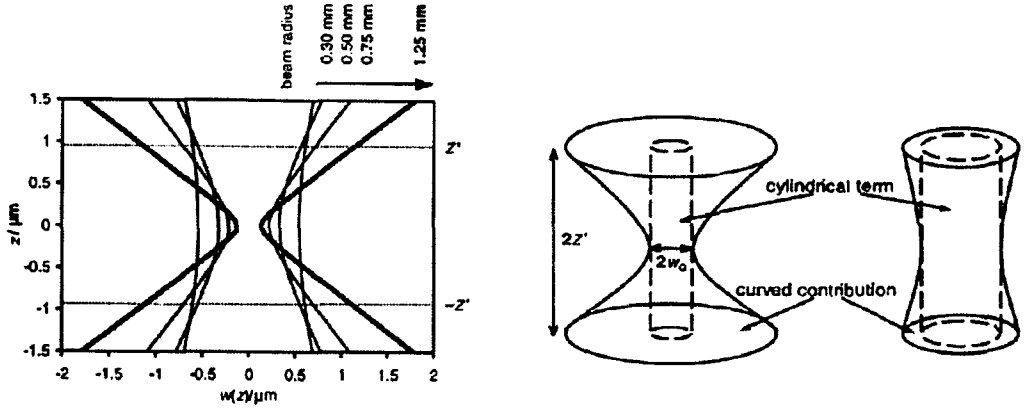


Figure 2.6 (a) $1/e^2$ Gaussian intensity contours plotted for a series of laser beam radii (λ = 488nm, f=1.6mm, n = 1.52). (b) Cylindrical and curved components of the Gaussian probe volume. The curved contribution is more significant for larger beam radii and correspondingly tight beam waists.

In the literature to date, it has been routine to approximate the confocal probe volume as a cylinder with a radius defined by the diffraction limited waist of a Gaussian beam. This is useful when the beam is narrow or not tightly focused. However, Hill and de Mello demonstrated that when the collimated beam is broad the corresponding diffraction limited focus is narrowed, and the probe volume more closely resembles a pair of truncated cones.[6] Examples of $1/e^2$ intensity profiles are shown in ***Figure 2.6.***

Fluorescence emitted by the sample (within a microfluidic channel) placed directly below the objective is collected by the same high NA objective and transmitted through the same dichroic mirror discussed in section 2.1.4. The fluorescence is then passed through a 50:50 beamsplitter so that the collected fluorescence is split into two equal paths (SD 1 and SD 2).

2.2.6 SD 1 detection path

The SD 1 single photon counting avalanche photodiode (SPAD) detector was used for measuring single molecule and particle fluorescent burst scans and consisted of an emission filter (515EFLP; Omega Optical) to remove any residual excitation light. A plano-convex lens

(+50.2F; Newport Ltd.) focuses the fluorescence onto a precision pinhole ranging in size from 25 – 100 μm (Melles Griot) placed immediately in front of a 600 μm fibre optic cable (Elliot Scientific Ltd., UK). The pinhole is positioned in the confocal plane of the microscope objective. This fibre optic cable was coupled directly to the front of the detector and adjustable in the x and y planes. The precision pinhole and fibre optic cable are mounted on XYZ translation stages to allow for fine adjustment of the incoming radiation. The electronic signal from the detector is routed to a multi channel scalar (MCS-PCI; EG&G), running on a Pentium PC as well as to a TimeHarp 100 (PicoQuant) time correlated single photon counting (TCSPC) card running on a separate Pentium PC.

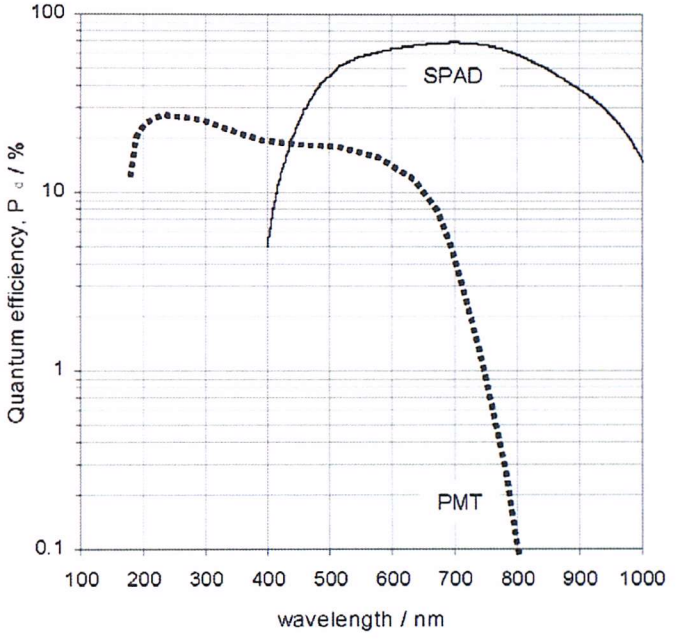


Figure 2.7 Comparison of typical PMT and SPAD wavelength-dependent quantum efficiencies.

The detector used for all measurements is a SPAD operating in single-photon counting mode (SPCM-AQR-131; EG&G Canada, Vaudreuil, Quebec, Canada). The detector dark count rate on average was typically below 100 Hz. Detection plays a crucial part in SMD. A typical photomultiplier tube (PMT) has a low response quantum efficiency; only 5% of photons that fall on the photocathode are typically registered. Furthermore, the quantum efficiency of a PMT generally falls off in the far visible/ near infrared. Consequently it is more appropriate to use low-level light detectors such as SPADs. Quantum efficiencies tend to be a factor of 10 higher than that of standard PMT's in the visible region with a more uniform response over the entire wavelength range (*Figure 2.7*). This is highly beneficial as most fluorophore

emission falls in the region between 400 – 900 nm. Another advantage is that the dark count rate of a SPAD can be as low as 20 Hz.

2.2.7 SD 2 detection path

The fluorescence along the SD 2 detection path was focused onto a 1000 μm fibre optic cable with a transmittable range of 400 – 1000 nm. This was directly coupled to an Ocean Optics s2000 CCD spectrometer (Ocean Optics, Netherlands) which will be discussed in the following section, as well as to a monochromator (SPEX 1681, Jobin Yvone, Middlesex, UK). This single beam scanning monochromator has a minimum resolution of 2 nm. The monochromator has an *f*-number of 4. This was matched to the detection optics in order to ensure, minimum spectral resolution as well as maximum light throughput. The fluorescence output from the monochromator was collected with another silicon avalanche photodiode operating in single-photon counting mode (SPCM-AQ-13; EG&G Canada, Vaudreuil, Quebec, Canada). The dark count rate on average was well below 300 Hz. The electronic signal from the detector was coupled to the same multi channel scalar (MCS-PCI; EG&G) and TCSPC card as described previously. The output signal was also coupled to a lock-in amplifier.

2.2.8 Ocean Optics spectrometer

The Ocean Optics S2000 spectrometer has active range between 200 nm – 1000 nm and was used for microfluidic alignment purposes as well as Raman spectroscopy and acquisition of real time emission spectra. Time-resolved emission spectra can be taken at time scales as low as 10 ms. The time scale is limited to the processor speed of the computer. The S2000 features a high-sensitivity linear CCD array that provides high response and a spectral resolution of 2 nm.

2.3 Acquisition methods

The confocal spectrometer primarily allows for 3 acquisition methods which are as follows: 1) A multi channel scalar was used primarily for real time single molecule photon burst scans. 2) Time correlated single photon counting allows measurements of fluorescence lifetimes. 3) A Picolog acquisition card interfaced with the lock-in amplifier was used to produce amplified photon burst scans. A schematic of the system is shown in ***Figure 2.8***.

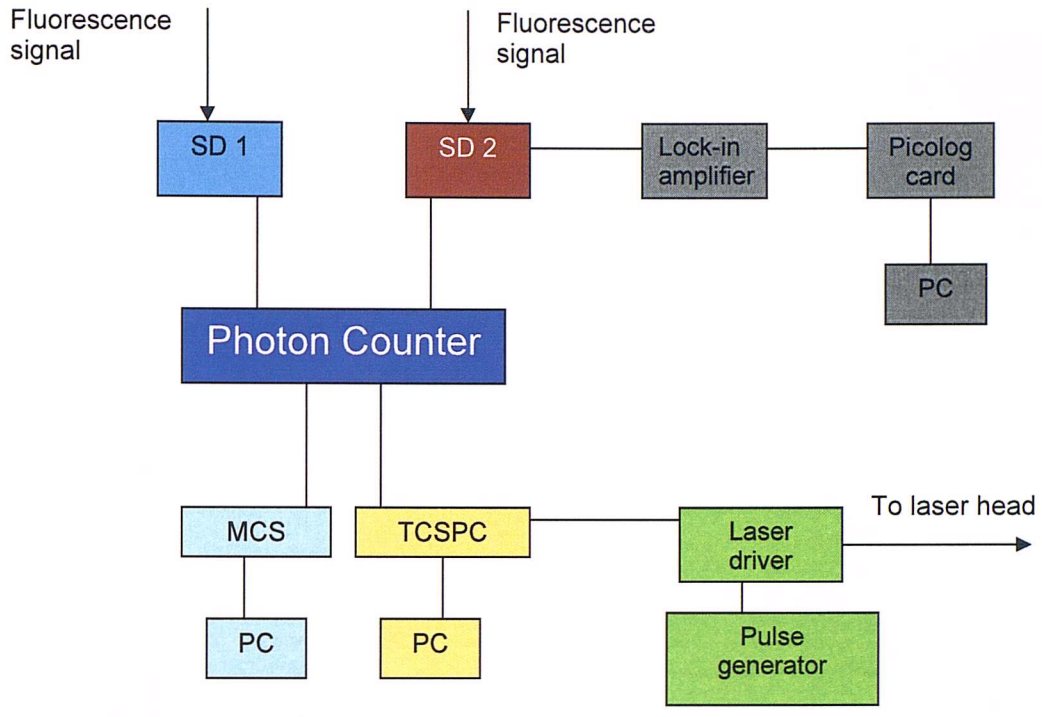


Figure 2.8 Schematic layout of the post-detector electronics used for fluorescence collection.

2.3.1 Multi channel scalar

Signals from either detector SD 1 or SD 2 could be recorded with a multi-channel scalar (MCS-PCI; EG&G, Perkin-Elmer, UK) running on a 266 MHz Pentium PC. For rea-time signal monitoring the detectors were routed *via* a gated photon counter (SRS 400; Stanford Research Systems, Sunnyvale, US). The MCS essentially records the counting rate of events. When a scan is started, the MCS begins counting input events in the first channel of its digital memory. At the end of the pre-selected dwell time, the MCS advances to the next channel of memory to count the events. This '*dwell*' and '*advance*' process is repeated until the MCS has scanned through all the channels in its memory. The MCS employs a crystal-controlled clock with 100-ppm accuracy and high-speed digital electronics to achieve a wide range of accurate operating parameters. With the dwell time per channel variable from 100 ns to 1300 seconds, and a scan length variable from 4 to 65,536 channels, time scans ranging from 400 ns to 2.7 years can be selected. In an SMD experiment it is absolutely essential that there is no dead time between channels in order to guarantee all photons detected will be counted. The card used employs digital circuits to eliminate the dead time between channels that are typically encountered in lower-quality MCS cards. This results in no loss of counts and no double counting as the MCS advances from one time channel to the next. The graphical user interface

for a photon burst scan acquisition is shown in ***Figure 2.9***. In this case a dwell time of 20 µs and a total of 65,000 channels were used. This results in a total acquisition time of 1.3 s.

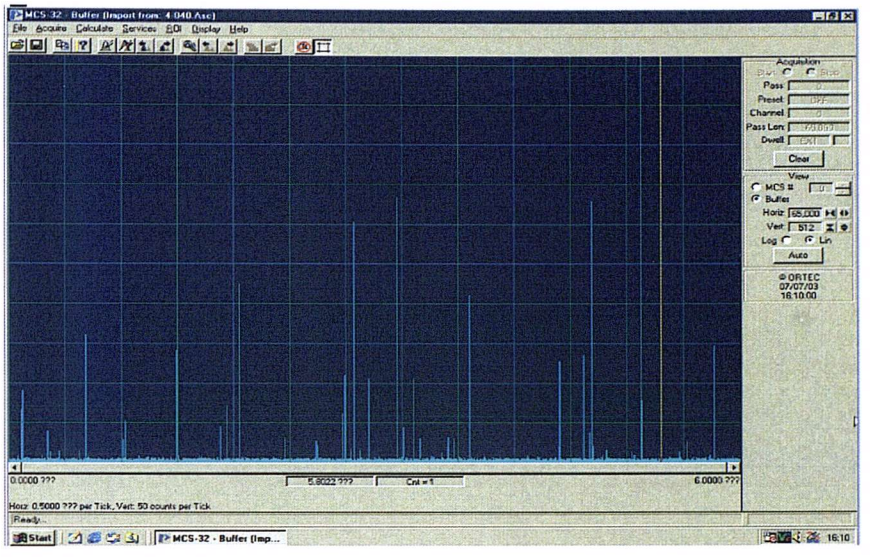


Figure 2.9 GUI of the MCS acquisition program. The photon burst scan shown is that of single E. coli cells expressed with green fluorescent protein. Each burst represents a single cell travelling through the probe volume.

In order to obtain high precision photon burst statistics an accumulation of a greater number of scans is required. The 'Job' command under the 'Services' menu provides an easy way for performing such a task. Once the 'Job Stream' is defined and implemented, data acquisition proceeds automatically under the 'Job Control'. An example of a 'job file' for automating the task of performing and saving 30 scans at a constant dwell time is shown below.

```
SET_DWELL_TIME 100e-6                  //Define the dwell time
SET_PASS_LENGTH 65000                  //Set number of channels
CLEAR                                          //Clears the memory
START                                  //Starts 1st acquisition
LOOP 30
        WAIT
        FILL_BUFFER
        CLEAR
        START
        SET_MCS 0                      //Sends scan to buffer
        EXPORT "c:\1000nm\file-???.Asc"  //Exports data files
        SET_MCS 1
END_LOOP
```

This short program exports the raw data to '*ascii files*' called *file-001,file-002,file-003….., file-030*. A program written in Matlab was used to perform single molecule and particle analysis directly on these files and will be discussed in detail in Chapter 3.

2.3.2 Time correlated single photon counting

TCSPC has proved to be one of the most reliable and sensitive methods of measuring fluorescence decay times since its inception in 1961.[12] The application of TCSPC creates a second dimension for the analysis of single molecules and particles. Determination of single-molecule or particle fluorescence lifetimes increases options for molecular identification and discrimination. TCSPC performed using 'plug and play' computer acquisition cards is a relatively new and promising technique.[13-19] With state-of-the-art TCSPC cards (as used herein), it is even possible to extract fluorescence lifetimes of a single molecule or particle. The acquisition of fluorescence decay curves by TCSPC is done by histogramming arrival times of individual photons over many excitation and fluorescence cycles. The arrival times are in fact relative times between a laser excitation pulse and corresponding fluorescence photon arrival time.

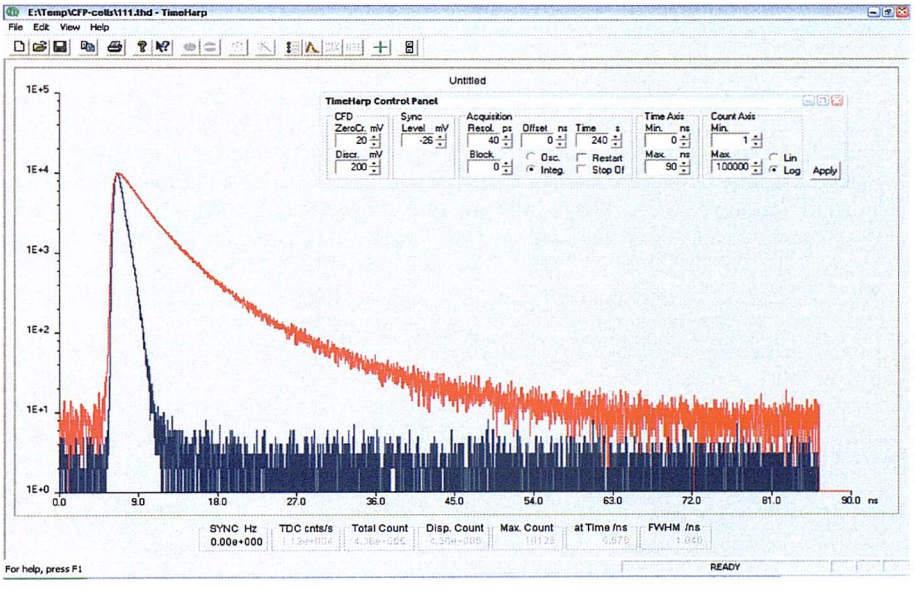


Figure 2.10 GUI of the TCSPC acquisition program. The lifetime decay shown (red) is that of single E. coli cells expressed with green fluorescent protein. The instrument response of the detector is shown in blue.

As with the MCS card, signals from either SD 1 or SD 2 could be recorded with the TimeHarp 100 (PicoQuant) TCSPC card running on a 600 MHz Pentium PC. For real time signal monitoring the detectors were also routed *via* the same gated photon counter. The Timeharp 100 card contains all the components necessary for TCSPC. High measurement rates of up to $3x10^6$ counts/s and a time resolution of less than 40 ps are possible. The card is also designed so that it can be integrated with a SPAD detector which makes the system

ideally suited for single molecule fluorescence lifetime determination. With the current configuration, 2 types of measurements are possible: 1) Continuous mode measurement (CMM). 2) Time-tagged mode measurement (TTMM). With a CMM, normal TCSPC experiments can be performed to determine fluorescence lifetimes of bulk systems. An example of this is shown in ***Figure 2.10*** where the blue curve is the instrument response and the red curve is the fluorescence decay profile. As will be shown in Chapter 3 fluorescence lifetimes can be easily extracted from such data.

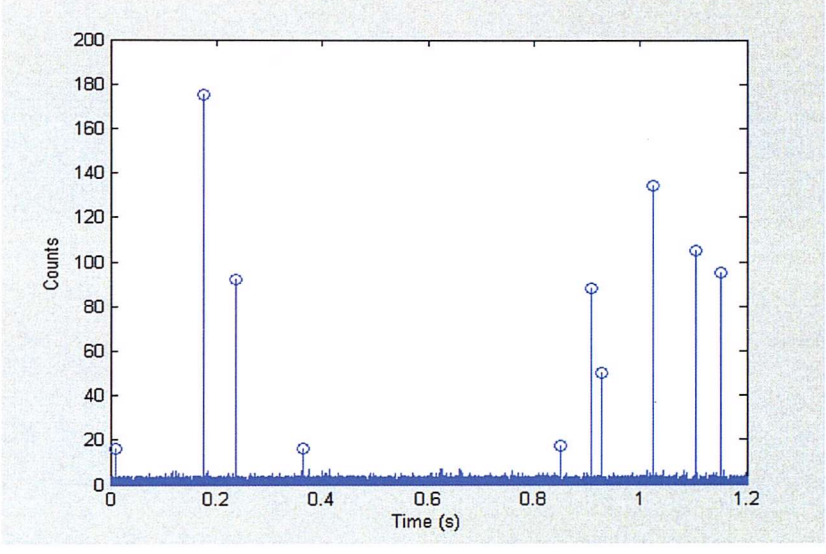


Figure 2.11a Single photon burst scan of E. coli expressed with green fluorescent protein using the TCSPC acquisition card in TTMM mode.

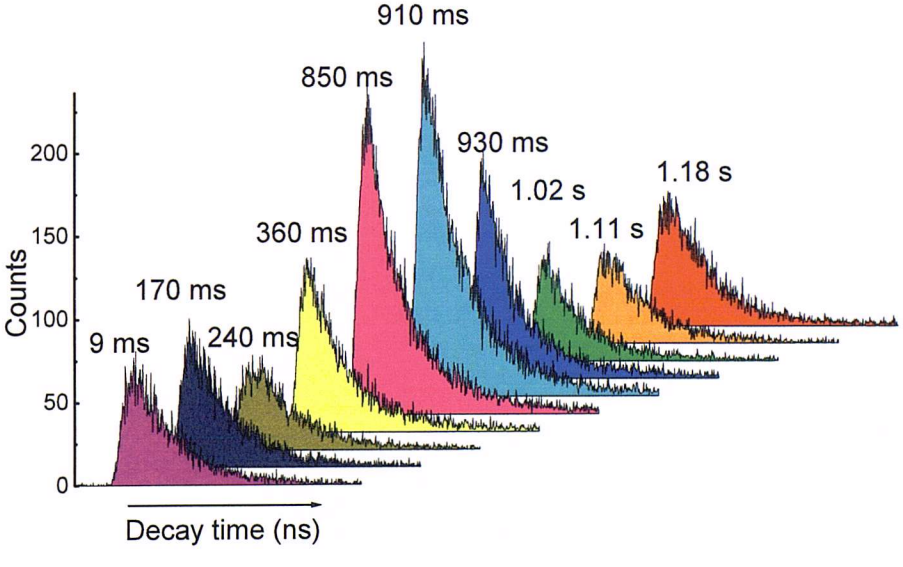


Figure 2.11b Fluorescence lifetime decays for E. coli cells expressed with green fluorescent protein using the TCSPC acquisition card in TTMM mode. Each decay profile represents a single cell burst shown in Figure 2.9a.

The TTMM approach is more suited for extracting single molecule or single particle fluorescence lifetimes. The mode allows for the recording of individual count events without the formation of a histogram. As each event is recorded with a time tag, photon burst identification is possible and is of great value for SMD in liquid flow. In TTMM the internal clock runs at 100 ns per tick. 12 bits are used for the 'stop-start' timing and 20 bits are needed for the time tag. The 20 bits of time-tag along with a 'clock tick' of 100 ns will cover a maximum span of 104.9 ms. In this mode a maximum of $3x10^5$ counts/s is possible. An example of the output of such an acquisition is shown in ***Figure 2.11.*** A program written in Matlab was used to extract the information from TTMM files and is available in Appendix 2.3. The program essentially produces 2 outputs. The first is a photon burst scan and the second is a fluorescence decay profile associated with each burst in the photon burst scan. The fluorescence lifetimes can be extracted by 2 different methods. The first method statistically compares the decay profile to that of the bulk solution and the second method requires a least squares analysis on each fluorescent decay. The former method will be discussed in the following chapter.

2.3.3 Lock-in amplifier based measurements

A lock-in amplifier essentially measures a periodic signal and gives an output in the form of a DC voltage proportional to the value of the signal being measured. It is called an "amplifier" because the DC level at output is usually greater than the AC level at input and is termed "lock-in" because it 'locks-in' to and measures to the modulation frequency. All other frequencies are eliminated; hence, background noise can be minimized using such an approach. This approach was not used for SMD and TCSPC as removing dark current from the detector was not necessary with the dwell times used. An average dwell time was typically 100 μs and hence each bin would have less than a 1 count per second background level; much lower than the total counts from a single molecule burst. Phase sensitive detection was strictly used in the measurement of bulk emission spectra where the time per channel was approximately 1 to 2 s.

2.4 Microfludics

Real challenges for detection arise due to the scale of miniaturized devices. Sample volumes in these devices are in the nL – fL range.[20, 21] As CM is completely insensitive to sample downsizing this is an ideal method for linking with microfluidics. As previously mentioned, microchannels offer several benefits including the minimization of the active volume as well

as the potential for higher throughput and reduced analyte consumption. Unfortunately the short working distance of a high NA microscope objective is a major constraint in linking a microfluidic device with CM. For a 1.3 NA objective a typical working distance is approximately 170 μm. Therefore microchip construction must be designed in such a manner that the top plate is no thicker than this working distance. In order to observe single molecule bursts on microdevices this parameter must be strictly observed so that maximum possible signal intensities can be achieved. In the following sections device fabrication and integration methods will be briefly discussed.

2.4.1 Microfluidic channel design

The majority of microfluidic devices discussed in this thesis were fabricated from soda-lime glass. Although initial devices were fabricated in polydimethyl siloxane (PDMS) covered with a glass microscope cover slide, they proved to be difficult to handle due to the flexibility associated with PDMS. A much more rigid structure is required due to contact between the oil immersion objective and the microfluidic device. The initial motivation behind using PDMS was driven by reduced fabrication times and device complexity. PDMS devices can take as little as 24 hr to make in comparison to 3 – 4 days for a glass device. The following sections will only deal with the fabrication of glass microfluidic chips. Whenever a PDMS chip was used in later chapters, the structures as well as chip design will be discussed where appropriate.

The purpose of integrating microfluidics and confocal SMD is to observe single molecules and particles in flowing systems. For this reason, relatively simple structures were fabricated with multiple or single inputs and a single output. The need for more complicated and sophisticated chips, including micromixers and capillary electrophoresis columns, were not required in the current studies. A mask of several chip designs in a 4 in^2 CAD drawing is shown in *Figure 2.12*.

Channel widths (defined in the mask) were 20 μm, 40 μm, and 100 μm and channel lengths varied from 12 -24 mm. Chips were etched to a depth of 30 μm and reservoir holes were 400 μm in diameter.

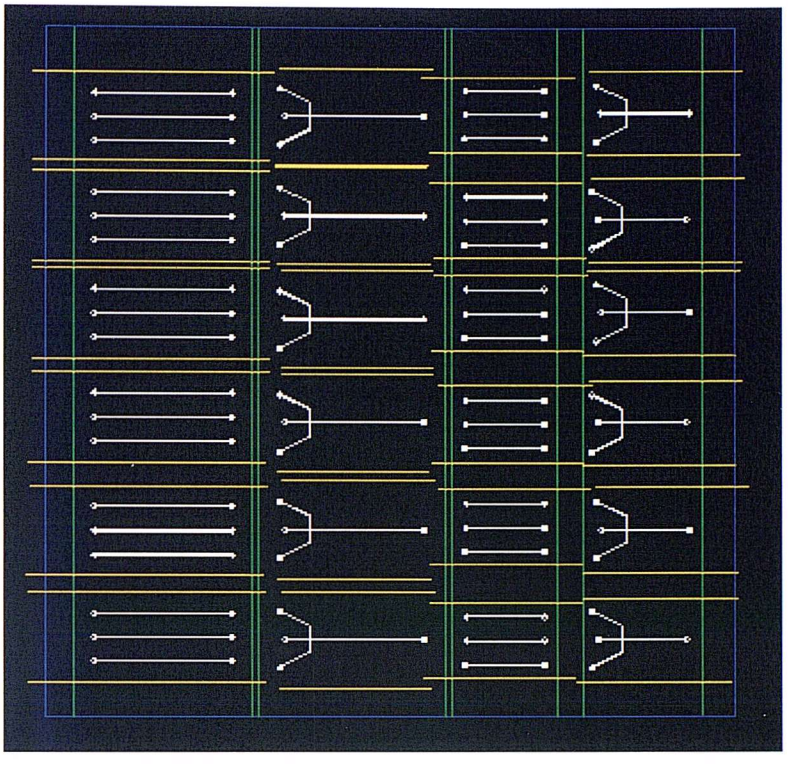


Figure 2.12 A 4 in sq. CAD design containing 24 microfluidic chips. The CAD file is used as a mask in the chip fabrication process.

2.4.2 Microfluidic device fabrication

2.4.2.1 Chip substrates

Soda-lime glass wafers pre-coated with positive photoresist and low reflective chromium were purchased from Nanofilm (Westlake Village, CA, USA). The wafers used varied in size from 2.5 – 4 in^2. The chromium film and photoresist had film thicknesses of 100 nm and 530 nm respectively. The glass wafers were 1.1 mm thick.

2.4.2.2 Exposure of substrates

Microfluidic channel patterns were imprinted into the photoresist using a direct-write photolithographic system (DWL2.0, Heidelberg Instruments, Heidelberg, Germany) incorporating a HeCd 442 nm laser. The DWL system has a minimum resolution of 1 μm and hence the smallest channel dimensions could not be lower than 1 μm. Due to the high resolution needed exposure times could take upwards of 8 hours for a 4 x 4 in sq substrate.

2.4.2.3 Developing and etching of exposed substrates

The exposed photoresist was then removed by immersing the substrate in a 5:1 ratio of developing agent (Microposit, Coventry, UK) to ultra pure water for no more than 3 minutes, followed by a chromium etching procedure (Lodyne etch, Microchem Systems, Coventry, UK) for approximately 1 min. The exposed glass surfaces were then etched using a buffered oxide etching solution (HF/NH_4F) at ambient temperature. Etching rates were on the order of 0.1 μm/min. It should be noted that working with HF requires great care and stringent safety procedures must be followed. Such solutions can cause severe injury and even death. The etching reaction was quenched by removing the substrate from the etching solution and rinsing it with 18 MΩ deionized water. Once complete, the etched substrate was sonicated sequentially in acetone to remove the unexposed photoresist and rinsed in chromium etchant to remove the remaining chromium layer. The substrate was then finally rinsed with water and dried with nitrogen gas.

2.4.2.4 Drilling of access holes

Access holes were drilled where appropriate in the substrate using a 400 μm dental drill bit (Diama, London, UK). In order to minimize substrate fractures the entire substrate was drilled under water. This ensured rapid cooling surrounding the drilling location. Once drilling was complete the substrate was diced using a glass cutting saw and was then washed in pure water followed by sonication in hexane to remove oils and organic materials. This was followed by sonication in methanol. Finally the chip substrates were rinsed for 5 minutes in a 50/50 H_2SO_4/H_2O_2 mixture followed by rinsing in ultra pure water and dried with N_2 gas.

2.4.2.5 Device bonding

Prior to bonding the glass coverplates were cleaned in the same manner as above. When both the top and bottom plates were completely dry, a 100 μl drop of water was placed on the bottom substrate and contacted with the top cover plate. The surface tension provided by the water prevented any relative movement of the two pieces of glass while the chip was heated.

The cover plate was thermally bonded to the substrate by heating the assembly under an applied pressure at 550°C for 1 h, 580°C for 5 h and 555°C for 1 h. The complete device was then allowed to cool for 8 hours. If the bonding cycle resulted in the substrates not being completely bonded, the cycle was repeated. It was rarely necessary to go through more than 2 bonding cycles to achieve complete boding.

2.4.3 Device integration

2.4.3.1 Optical polishing of the top plate

Once bonded, the complete chip thickness was 2.2 mm (the top and bottom halves both being 1.1 mm). Unfortunately 1.1 mm was much thicker than the working distance of the microscope objective and therefore the coverplate was optically polished down to a thickness of 100 μm (the maximum working distance was ~170 μm). Initially the microfluidic devices were polished using a standard polishing technique; however, this resulted in fine glass particulates entering the microfluidic channels. The channels could not be easily cleaned and were rendered useless. A revised approach involved filling the channels with a bees' wax prior to polishing as well as covering the bottom half containing the access holes with a glass wafer also coated in bees' wax to insure particulate matter did not enter the channels. This approach was successful. The wax could easily be removed by putting the chip on a hotplate at 90 ^{0}C followed by application of a vacuum to the reservoir. The channels were then rinsed with hexane and methanol to remove any remaining wax and finally the channels were rinsed with ultra pure water.

2.4.3.2 Interfacing the devices with capillary tubing

Interfacing the 400 μm access holes with tubing was performed as follows: 375 μm o.d., 150 μm i.d. Polymicro tubing (Composite Metals, Worchester, UK) was glued to the access holes using Araldite 2014 (RS Components, UK). The Araldite was allowed to cure on a hot plate set to 90 ^{0}C for 2 hr. The interface proved to be extremely stable to different solvent environments. Araldite 2014 did not dissolve under the application of any organic solvents, or basic and acidic environments. Examples of complete devices are shown in *Figure 2.13*.

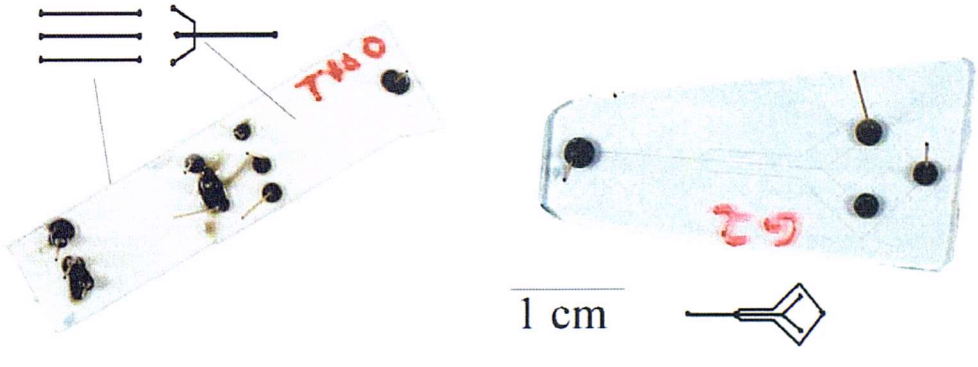


Figure 2.13 Photograph of 2 complete microfluidic devices. The G2 chip consisted of 2 Y shaped inputs and 1 output. The T100 has 4 microfluidic channels ranging in widths from 20 μm – 100 μm.

2.4.3.3 Interfacing the microchannels with a syringe pump

Syringe pumps (Harvard Apparatus, Cambridge, MA, USA) were used to deliver solutions at various flow rates from 1000 μL or 5000 μL gastight syringes (Hamilton) into the capillary tubing. The interface between the syringe needle and the polymicro tubing was affected using standard Peek ® finger tight accessories (VWR International, UK). The complete microfluidic device was finally placed on the XYZ translation stage underneath the microscope objective.

2.5 Summary

This experimental chapter has described the construction and development of a sophisticated confocal spectrometer which is capable of SMD, TCSPC, and steady-state fluorescence spectroscopy as well as Raman spectroscopy. The second part of the chapter has briefly described the fabrication and development of microfluidic devices that were used in experimental studies.

2.6 References

(1) Keller, R. A.; Ambrose, W. P.; Arias, A. A.; Gai, H.; Emory, S. R.; Goodwin, P. M.; Jett, J. H. *Analytical Chemistry* **2002**, *74*, 316a-324a.

(2) Edel, J. B.; Hill, E. K.; de Mello, A. J. *Analyst* **2001**, *126*, 1953-1957.

(3) van Orden, A.; Keller, R. A.; Ambrose, W. P. *Analytical Chemistry* **2000**, *72*, 37-41.

(4) van Orden, A.; Cai, H.; Goodwin, P. M.; Keller, R. A. *Analytical Chemistry* **1999**, *71*, 2108-2116.

(5) Ferris, M. M.; Rowlen, K. L. *Review of Scientific Instruments* **2002**, *73*, 2404-2410.

(6) Hill, E. K.; de Mello, A. J. *The Analyst* **2000**, *125*, 1033-1036.

(7) Enderlein, J.; Ambrose, W. P. *Applied Optics* **1997**, *36*, 5298-5302.

(8) Eggeling, C.; Widengren, J.; Rigler, R.; Seidel, C. A. M. *Analytical Chemistry* **1998**, *70*, 2651-2659.

(9) Daniel, D. C.; Thompson, M.; Woodbury, N. W. *Journal of Physical Chemistry B* **2000**, *104*, 1382-1390.

(10) Affleck, R. L.; Ambrose, W. P.; Demas, J. N.; Goodwin, P. M.; Schecker, J. A.; Wu, J. M.; Keller, R. A. *Analytical Chemistry* **1996**, *68*, 2270-2276.

(11) Izzo, A. D.; Mackanos, M. A.; Beckham, J. T.; Jansen, E. D. *Lasers in Surgery and Medicine* **2001**, *29*, 343-350.

(12) O'Connor, D. V.; Phillips, D. *Time-Correlated Single Photon Counting*; Academic Press: Lonodn, 1984.

(13) Sauer, M.; Angerer, B.; Han, K. T.; Zander, C. *Physical Chemistry Chemical Physics* **1999**, *1*, 2471-2477.

(14) Zander, C.; Drexhage, K. H.; Han, K. T.; Wolfrum, J.; Sauer, M. *Chemical Physics Letters* **1998**, *286*, 457-465.

(15) Enderlein, J. *Chemical Physics Letters* **1999**, *301*, 430-434.

(16) Enderlein, J.; Krahl, R.; Ortmann, U.; Wahl, M.; Erdmann, R.; Klose, E. *Proc. SPIE* **1995**, *2388*, 71 - 78.

(17) Maus, M.; Cotlet, M.; Hofkens, J.; Gensch, T.; De Schryver, F. C.; Schaffer, J.; Seidel, C. A. M. *Analytical Chemistry* **2001**, *73*, 2078-2086.

(18) Kollner, M.; Wolfrum, J. *Chemical Physics Letters* **1992**, *200*, 199-204.

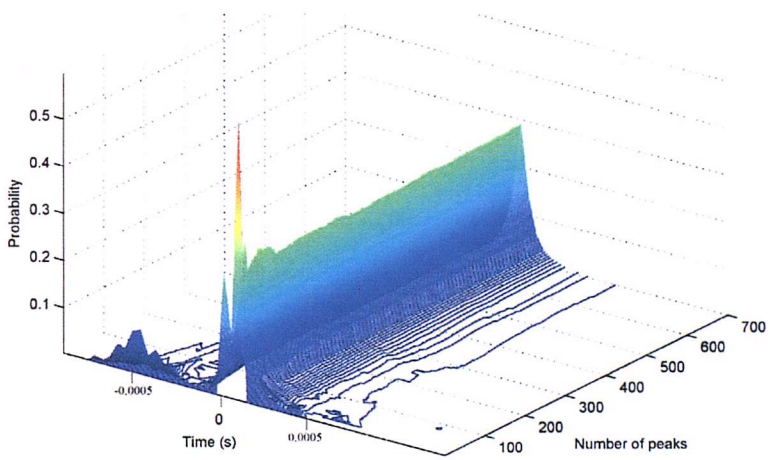
(19) Tellinghuisen, J.; Goodwin, P. M.; Ambrose, W. P.; Martin, J. C.; Keller, R. A. *Analytical Chemistry* **1994**, *66*, 64-72.

(20) Auroux, P. A.; Iossifidis, D.; Reyes, D. R.; Manz, A. *Analytical Chemistry* **2002**, *74*, 2637-2652.

(21) Becker, H.; Manz, A. *Sci. Prog.* **1996**, *79*, 49 - 63.

- 3 -

Approaches for the analysis of single molecule and particle photon burst scans are discussed. These include fluorescence burst threshold analysis, autocorrelation analysis, Poisson recurrence time analysis, peak identification, and computation of burst statistics (e.g. burst areas, heights, and widths). Approaches are also discussed for the analysis of single molecule and particle fluorescence lifetimes using time correlated single photon counting and time tagged based measurements.



Statistical analysis methods

3.1 Single molecule sensitivity requirements

The measurement of fluorescence photons emitted from individual molecules form the basis of SMD. In practice as many as 1000 photons can be collected from a single molecule. In order to extract statistically useful information from these photons it is therefore essential to maximize the detection sensitivity while minimizing the background count rate. In the following sections a detailed analysis is presented on the determination of the background threshold.

3.1.1 Signal to noise

Observing single fluorescent molecules in solution can be considered one of the most challenging experiments in the physical sciences. A single fluorescent molecule is surrounded by billions of solvent molecules and impurities which could potentially all interfere with observation of the single molecule. For this reason, the background as well as the signal must be carefully optimized.[1] A crucial parameter is the signal to noise ratio (SNR) defined by

$$SNR = \frac{s\tau}{\sqrt{(s + bVP + d)\tau}} \qquad \text{(Equation 3.1)}$$

where τ is the measurement duration time, V is the excitation volume, P is the excitation power of laser beam, b is a parameter due to background signal caused from Raman and Raleigh scattering, d is the detector dark count rate, and s is the signal rate (Hz). The denominator is essentially the root mean square of all the contributions related to shot noise. A shot noise limited signal essentially follows a Poissonian distribution.[2] From ***Equation 3.1*** it is obvious that the SNR is highly dependant on both the integration time and the count rate. It is also useful to note that the SNR can be improved by decreasing the detection probe volume. A larger excitation power can theoretically also improve the SNR. However, non reversible photodegredation effects will typically result in a poorer SNR. Fluorescent molecules tend to have a finite life span and emit up to 100,000 photons before irreversible degredation.[3, 4] The background rate, b, can be minimized by using appropriate optical filters as well as pre-treating solvents (e.g. using distilled and de-ionized water).

3.1.2 Background threshold determination

When sampling a small volume within a system that may freely exchange particles with a large surrounding analyte bath, a Poisson distribution of particles is predicted. A Poisson distribution is a discrete series (belonging to a random variable x which can only attain values from a finite set) that is defined by a single parameter μ equating to the mean and variance of the distribution.

$$P(n = x) = \frac{\mu^x e^{-\mu}}{x!} \qquad \text{(Equation 3.2)}$$

Common Poissonian processes include radioactive disintegration, random walks and Brownian motion. Although particle number fluctuations in the excitation volume are Poissonian in nature, the corresponding fluorescence intensity modulation induces a stronger correlation between photon counts. The deviation Q is defined as the scaled difference between the variance and the expectation value of the photon counts, and gives a measure of the broadening of the photon counting histogram (PCH). Q is directly proportional to the molecular brightness factor ε and the shape factor γ of the optical point spread function.[5, 6] (γ is constant for a given experimental geometry.)

$$Q = \frac{\langle \Delta n^2 \rangle - \langle n \rangle}{\langle n \rangle} = \gamma\varepsilon \qquad \text{(Equation 3.3)}$$

A pure Poisson distribution has Q=0, and for super-Poissonian statistics Q>0. Deviation from the Poisson function is maximised at low number density and high molecular brightness.

In an SMD experiment raw data are generally collected with a multi channel scalar and photons are registered in binned intervals.[1, 7-12] ***Figure 3.1*** illustrates typical photon burst scans demonstrating the detection of single molecules (R-phycoerythrin) in solution. Fluorescence photon bursts due to single molecule events are clearly distinguished above a low background baseline (bottom panel) of less than 5 counts per channel in the raw data. It is noticeable that bursts vary in both height and width. This is in part due to the range of possible molecular trajectories through the probe volume, photobleaching kinetics and the non-uniform illumination intensity in the probe region. In addition, it can be seen that the burst frequency decreases as bulk solution concentration is reduced. This effect is expected since the properties of any given single-molecule event are determined by molecular parameters alone

(e.g. photophysical and diffusion coefficients); the concentration simply controls the number of detected events (event frequency).

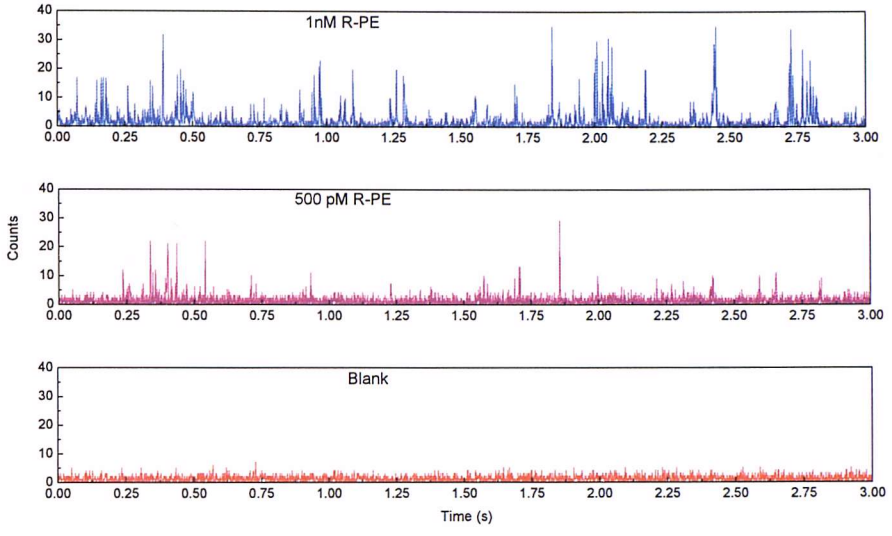


Figure 3.1 Photon burst scans originating from 1nM and 500pM R-phycoerythrin buffered solutions. Sample is contained within a 50μm square fused silica capillary. Laser illumination = 5 W, channel width = 1ms. The bottom panel shows a similar burst scan originating from a deionised water sample measured under identical conditions.

Although many fluorescence bursts are clearly distinguishable from the background it is necessary to set a count threshold for peak discrimination in order to correctly identify fluorescence bursts. A photocount distribution can be used as the starting point for determining an appropriate threshold for a given data set. The overlap between signal and background photocount distributions affects the efficiency of molecular detection. ***Figure 3.2*** shows typical signal and background photocount probability distributions, with a threshold set at approximately 2 photocounts per channel. The probability of false detection resulting from the fluctuation in the background distribution can be quantified by the area under the 'background' curve above the threshold cut-off (shaded area). Hence, counts above the threshold can be defined as true single molecule events with 100 % certainty if there is no overlap above the threshold between the background and fluorescence probability distributions. Counts below the threshold are considered to be indistinguishable from the background fluctuation and hence are not considered to be single molecule events. Selecting a high threshold value will result in reduced single molecule detection events. Conversely, a low threshold will result in counts associated with the background being incorrectly identified as single molecule events. An appropriate algorithm for the threshold determination is crucial in classifying single molecule events in an SMD experiment. The following paragraph discusses an approach based on Poissonian statistics.

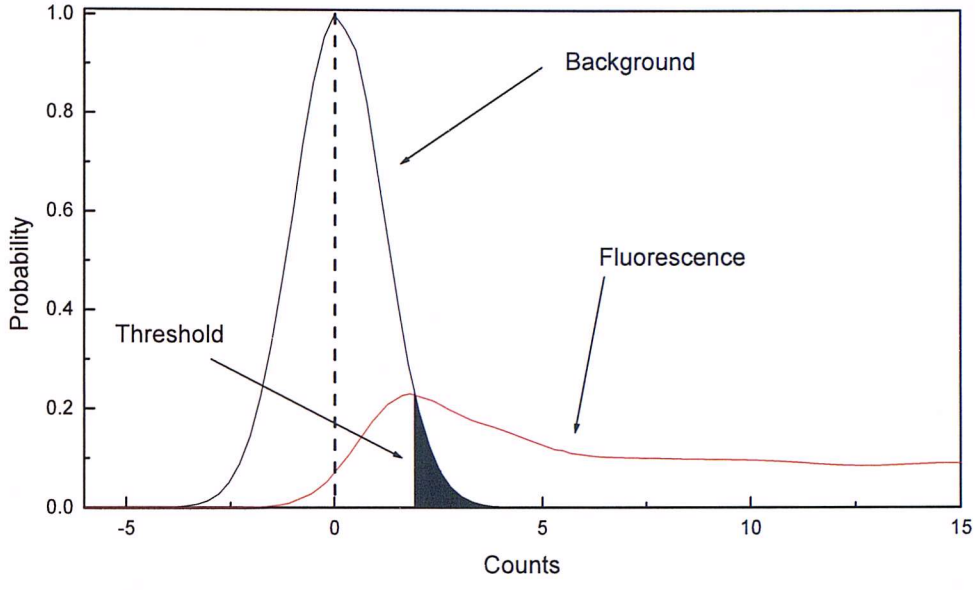


Figure 3.2 Simulated fluorescence and background photocount probability distributions. The vertical dashed line at 2 counts represents an arbitrarily defined threshold value for peak determination.

Since the background shot noise is expected to exhibit Poissonian statistics, the early part of the photocount distribution (*i.e.* the portion that is dominated by low, background counts) can be theoretically fit to a Poisson distribution in order to set a statistical limit for the threshold. Photon counting events above this threshold can be defined as photon bursts associated with the presence of single molecules. The selected peak discrimination threshold can be defined as three standard deviations from the mean count rate, i.e.

$$n_{threshold} = \mu + 3\sqrt{\mu} \qquad \text{(Equation 3.4)}$$

A threshold that lies 3 standard deviations above the mean yields a confidence limit that is typically greater than 99%. ***Figure 3.3*** illustrates an example of a photon counting histogram for a single particle burst scan. A least squares fit to an appropriate Poisson distribution (red curve) can therefore be used in conjunction with ***Equation 3.4*** to extract the calculated threshold (blue dashed line).

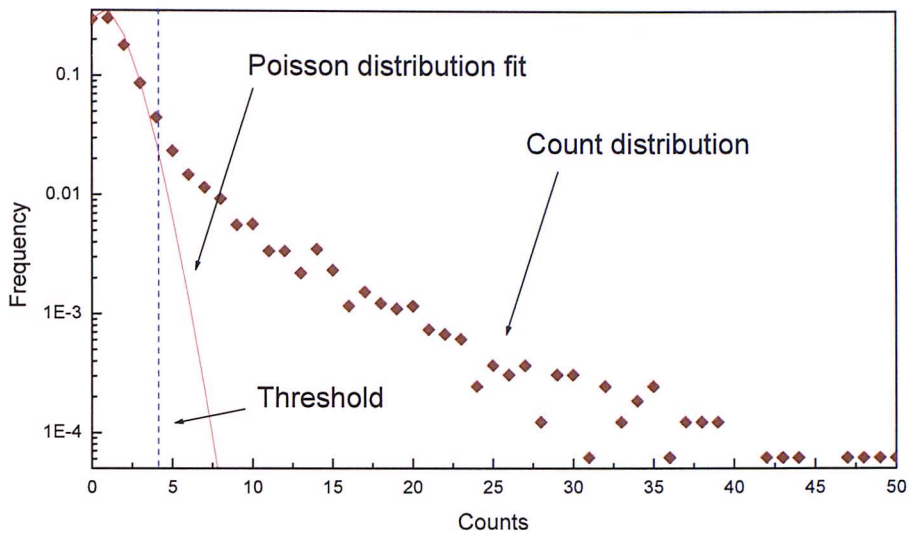


Figure 3.3 A photon counting histogram generated from a 16 second photon burst scan originating from a solution of 1000 nm fluorescent microbeads. The dotted curve shows a least squares fit of early channels to a Poisson distribution, and the dashed vertical line marks the peak threshold (defined as $\mu+3\sqrt{\mu}$ = 4.47 counts).

3.2 Peak locating algorithm

Initially Origin 6.0 was used to determine the peaks, heights and peak locations. The algorithm is based on a simple moving rectangle. If a peak is to be found inside a rectangle, the difference in height between the local data maximum inside the rectangle and the datum values at both rectangle ends has to be no less than the rectangle height. Unfortunately this approach proved to be quite unsuccessful as only a small portion of photon bursts were identified. This was caused by bursts not having a pure Gaussian form. For this reason a modified algorithm written in Matlab 6.5 was used to distinguish bursts from background signal.

The peak-locating algorithm written in Matlab is based on a Toeplitz matrix that determines local peak maxima down a column vector.[13] Briefly, the program searches for a given peak maximum above a specific threshold value which can be defined as three standard deviations from the mean background count rate, i.e. $n_{threshold} = \mu + 3\sqrt{\mu}$. Once a peak is found, the peak area is determined by analyzing a specified number of bins either side of the peak maximum until the background threshold value is reached. Once this is done, the program searches for the next peak and continuously repeats until all peaks are accounted for. Although the peak-locating algorithm used is memory demanding, it appears to be more efficient at extracting single molecule and particle bursts when compared to other

commercially available software packages, as complete customization of the search parameters is possible (i.e. minimum/maximum burst height, area, and width, background threshold). Using a standard desktop PC, equipped with a Pentium 4 processor and 512 Mb of RAM, a maximum of 650,000 data points were analyzed using the Toeplitz approach without the need for splicing the column vector. Once each particle burst was located, the burst was extracted from the raw data and inserted into a matrix with each column associated with a single particle burst, ω(r) (where r is defined as a given particle burst). Typically a given matrix has up to 4000 columns (particle bursts) and 500 rows (250 bins to the left and right of each burst maxima).

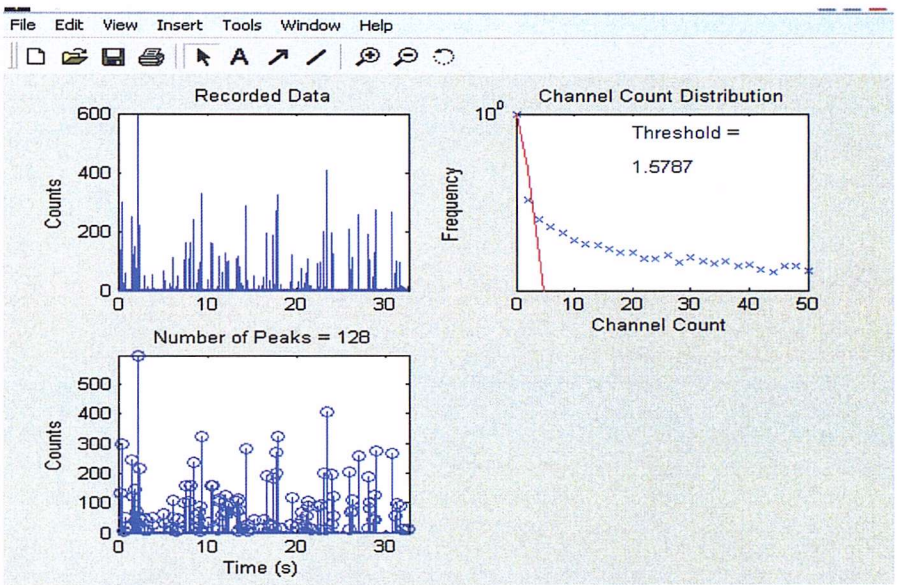


Figure 3.4 Graphical output of the Matlab program for the threshold as well as peak location determination for E. coli cells labelled with green fluorescent protein.

The source code for the program is available in Appendix 2.1; however an example of the output is shown in ***Figure 3.4*** for the analysis of a photon burst scan of *Escherichia coli* cells expressed with green fluorescent protein. In the top left of the Figure, a raw photon burst scan is plotted. In the top right of the Figure a background threshold histogram is plotted and was calculated from the photon burst scan. In this case the background threshold limit is 1.5787 counts at a 99 % confidence interval. Finally, the peak locating algorithm is used and all located peaks above the given threshold are defined with a 'O' at the peak maximum.

3.3 Photon burst statistics: Recurrence times

3.3.1 Recurrence time analysis

Another valuable quantitative analysis method for the analysis of fluorescence bursts utilizes the analysis of Poisson statistics. In this case, burst interval distributions are predicted to follow a Poissonian model, in which peak separation frequencies adopt an exponential form.[14, 15] The probability of a single molecule (or particle) event occurring after an interval Δt is given by *Equation 3.5*

$$N(\Delta t) = \lambda \exp(-\beta t) \qquad \text{(Equation 3.5)}$$

where λ is a proportionality constant and β is a characteristic frequency at which single molecule events occur. The recurrence time τ_R can then be simply defined as,

$$\tau_R = \frac{1}{\beta} \qquad \text{(Equation 3.6)}$$

Equation 3.5 simply states that longer intervals between photon bursts are less probable than shorter intervals at a given flow rate. Furthermore, the recurrence time reflects a combination of factors that control mobility, probe volume occupancy or other parameters in the single molecule regime. Consequently, it is expected that τ_R should be inversely proportional to concentration, flow rate or solvent viscosity in a range of systems. *Figure 3.5* shows frequency N(Δt) versus time plots for two flow rates. A least squares fit to a single exponential function yields values of τ_R = 91 ms for a volumetric flow rate of 200 nL/min and τ_R = 58 ms for a volumetric flow rate of 1000 nL/min.

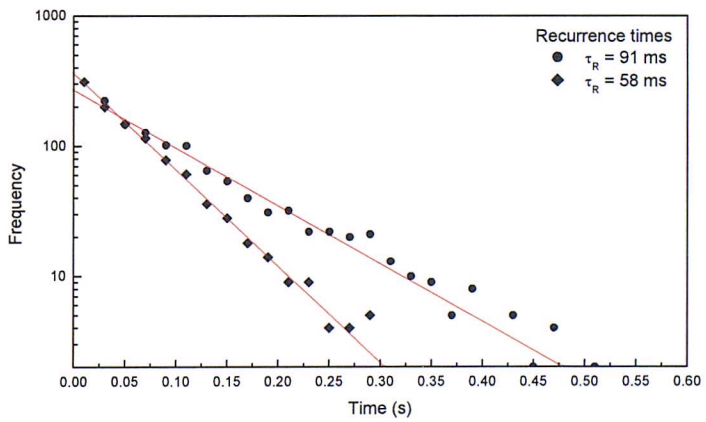


Figure 3.5 Burst interval distribution analysis of photon burst scans. Data originate from 1 μm fluorescent beads moving through 150 μm wide microchannels at flow rates of 200 nL min^{-1} (circles) and 1000 nL min^{-1} (squares). Least squares fits to a single exponential function are shown by the solid lines.

3.3.2 Calculation of recurrence times and theoretical fits

All recurrence times were calculated using a program written in Matlab and its fundamental routine is based on the peak locating algorithm described in section 3.2. The code is available in Appendix 2.1. Briefly, the recurrence times were calculated as follows: '*FTM*' is defined as a unit vector containing all times a photon burst was recorded. From this vector Δt in *Equation 3.5* can be determined simply by taking the difference between all consecutive points in this vector(i.e. *Rec* = *FTM*(i+1)-*FTM*(i)). The vector '*Rec*' was histogramed into 20 evenly spaced time intervals and from this histogram, the recurrence time, [N(Δt)], was determined and plotted. Examples of typical recurrence time decays are shown in *Figure 3.5* for 1 μm fluorescent particles at flow velocities of 1000 and 200 nl/min respectively through a 150 μm wide microfluidic channel.

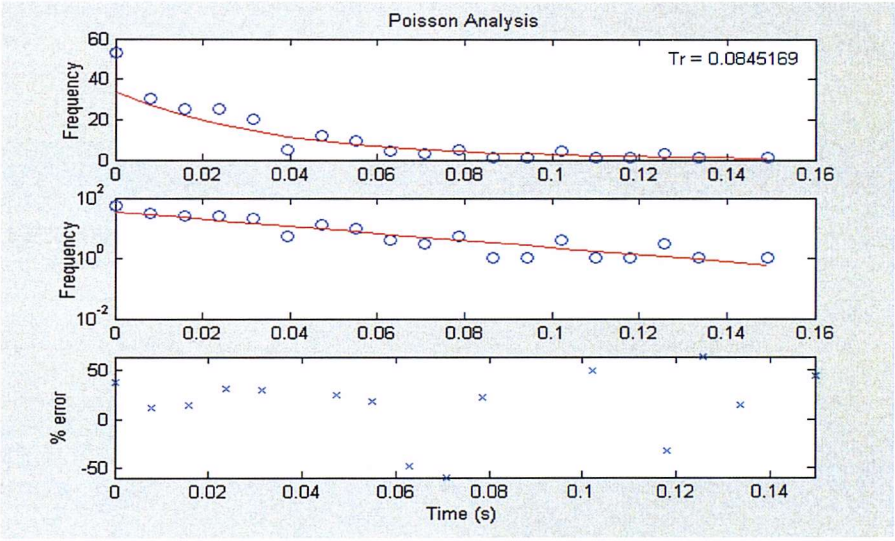


Figure 3.6 Graphical output of the Matlab program for the calculation and analysis of photon recurrence times. A least squares fits to a single exponential function is shown by the solid red lines.

The least squares fitting algorithm used for extracting τ_R, is based on finding the coefficients of a polynomial p(x) of degree n that fits the data, p(x(i)) to y(i). The result p is a row vector of length n+1 containing the polynomial coefficients in descending powers. This was achieved by using the built in function '*polyfit*' in Matlab. *Polyfit*(x,y,n) returns the polynomial coefficients p and a structure S in order to obtain error estimates. An example of the output of the complete program for analysis of single fluorescent particles travelling at a volumetric flow velocity of 1 μl/min within a microfluidic channel is shown in *Figure 3.6*.

In the upper panel of *Figure 3.6* the recurrence time histogram is plotted 'O' along with the linear least squares fit (red line). Below this, τ_R is inserted and in this instance is equal to 0.0845169 s. The middle panel is identical to the top panel; however, it is plotted as a semi-log plot. Finally, the error in the least squares fit is plotted in the bottom panel.

3.4 Photon burst statistics: Autocorrelation analysis

3.4.1 Autocorrelation: theory

Autocorrelation analysis is an extremely sensitive method for detecting the presence of fluorescence bursts in single molecule experiments. This analysis method essentially measures the average of a fluctuating signal as opposed to the mean spectral intensity.[14, 16-20] The concept relies on analysis of local concentration fluctuations in a small volume, and is essentially a measure of the temporal behavior of a dilute system. The number of molecules contained within the focal volume at a given time is governed by the Poisson distribution (as previously discussed). Therefore, the root mean square fluctuation can be defined by N, the number of particles, as being,

$$\frac{\sqrt{\langle(\delta N)^2\rangle}}{\langle N\rangle} = \frac{\sqrt{\langle(N-\langle N\rangle)^2\rangle}}{\langle N\rangle} = \frac{1}{\sqrt{\langle N\rangle}} \qquad \text{(Equation 3.7)}$$

It is clearly seen that the relative fluctuation becomes smaller when the number of particles measured is increased. It is therefore important to minimize the number of molecules in the probe volume. This is essentially a compromise since if there are too few molecules in the solution there will be long dark periods were no single molecule bursts are observed.

If a constant excitation power is assumed the fluctuation of the fluorescence signal in a small volume element defined by a laser beam with a Gaussian intensity profile can simply be defined as deviations from the temporal average of the signal (*F(t)*). This also assumes that the fluorescence emitted in the focal volume is recorded one photon at a time.

$$F(t) = qQ\int_V I(r)C(r,t)dV \qquad \text{(Equation 3.8)}$$

Q stands for the fluorescence quantum yield, q is the optical detection quantum efficiency. C(r,t) is defined as the concentration of a specific molecule at time t and position r. The Gaussian intensity probe volume, I(r), is a combination of both the excitation and collection efficiency functions and is approximated by a Gaussian intensity distribution[21] as shown in ***Equation 3.9***.

$$I(r) = I_0 e^{\frac{-2(x^2+y^2)}{w_0^2}} e^{\frac{-2z^2}{z_0^2}} \qquad \text{(Equation 3.9)}$$

w_0 and z_0 are the radius and height at which the volume element has decreased by a factor $1/e^2$.

3.4.2 Autocorrelation: theoretical fit

If a constant excitation power is assumed the fluctuation of the fluorescence signal can be defined as deviations from the temporal average of the signal. This also assumes that the fluorescence emitted in the focal volume is recorded one photon at a time.

$$\langle F(t) \rangle = \frac{1}{T} \int_0^T F(t)\,dt$$
$$\delta F(t) = F(t) - \langle F(t) \rangle \qquad \text{(Equation 3.10)}$$

T is defined as the total measurement time and F(t) is the fluorescence signal at time t. Using the information from the above Equation along with the florescence intensity distribution of ***Equation 3.8,*** the normalized autocorrelation function can be described as follows.

$$G(\tau) = \frac{\langle \delta F(t) \cdot \delta F(t+\tau) \rangle}{\langle F(t) \rangle^2} \qquad \text{(Equation 3.11)}$$

The signal, F(t), in ***Equation 3.11*** is analyzed with itself and at a lag time τ. It should also be noted that the autocorrelation amplitude G(0) is simply the normalized variance of the fluctuating signal. In a flowing system the autocorrelation function depends on the average flow time through the probe volume τ_{flow}. A theoretical fit to the function can be described according to,

$$G(\tau) = 1 + \frac{1}{N} A \exp\left\{\left(\frac{\tau}{\tau_{flow}}\right)^2 A\right\}$$
$$A = \left(1 + \frac{\tau}{\tau_d}\right)^{-1}\left(1 + \left(\frac{\omega}{z}\right)^2 \frac{\tau}{\tau_d}\right) \qquad \text{(Equation 3.12)}$$

where τ_D is the characteristic diffusion time, N is the mean probe volume occupancy, ω defines the laser beam waist radius and 2z defines the probe depth. The diffusion time, τ_D, is a characteristic molecular residence time in the probe volume and inversely related to the translational diffusion coefficient for the molecule.

$$D = \frac{w^2}{4\tau_d} \qquad \text{(Equation 3.13)}$$

The flow velocity v can then be extracted from the characteristic flow time according to,

$$v = \frac{w}{\tau_{flow}} \qquad \text{(Equation 3.14)}$$

In a flowing system the autocorrelation function depends on the average flow time through the probe volume τ_{flow}. It should be noted that in the case that directed flow is negligible or defined to be zero, the autocorrelation function simplifies to

$$G(\tau) = 1 + \frac{1}{N}\left(1 + \frac{\tau}{\tau_d}\right)^{-1}\left(1 + \left(\frac{\omega}{z}\right)^2 \frac{\tau}{\tau_d}\right) \qquad \text{(Equation 3.15)}$$

3.4.3 Autocorrelation: examples

In typical fluorescence correlation spectroscopy experiments the autocorrelation curve is usually generated in real time using a high speed digital correlator.[20] Such correlators are extremely expensive. For example, correlators can typically generate data with sub microsecond resolution; however such short correlation times are truly only necessary if information on molecular kinetics is required. In all experiments shown in the following chapters the autocorrelation curve is used as a tool to distinguish between diffusion, linear flow velocities, and photon burst intensities. With this in mind, it is perfectly acceptable for

the minimum autocorrelation resolution to be equivalent to the dwell times of the photon burst scans. It is therefore possible to utilize post data acquisitions.

$$G(\tau) = \sum_{t=0}^{N-1} g(t)g(t+\tau) \qquad \text{(Equation 3.16)}$$

Here $g(t)$ is the total number of counts during the time interval $(t,t+\Delta t)$, $g(t+\tau)$ is the number of counts detected in an interval of Δt at a later time $t+\tau$, and N is the total number of time intervals in the dataset.

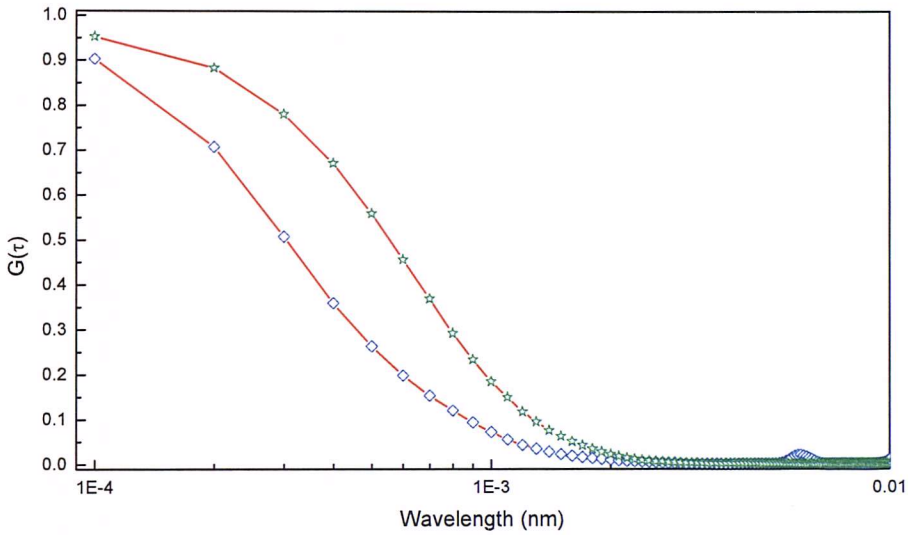


Figure 3.7 Autocorrelation analysis of photon burst scans of 1 μm fluorescent beads moving through 150 μm wide microchannels at flow rates of 500 nL min^{-1} (diamond) and 1000 nL min–1 (stars). Solid lines represent fits from Equation 3.15.

Figure 3.7 shows a typical autocorrelation curve for *E. coli* expressed with green fluorescent protein taken at flow velocities of 1μl/min (green stars) and 5 μl/min (blue diamond) within a 60 μm wide microfluidic channel. Least squares fits to Equation 3.12 are plotted using a solid red line. From these fits, information such as diffusion times, flow velocities, and probe volumes can be extracted and will be discussed in detail in the following chapters.

3.4.4 Calculation of autocorrelation curves

As with the previous analysis methods discussed, the autocorrelation curves were determined and analyzed using Matlab 6.5. In fact Matlab, is ideally suited for correlation analysis due to built in functions within the signal processing toolbox. It should be noted that there is no true autocorrelation function in Matlab, rather it is treated as a special case of the built in cross-

correlation function '*xcorr*'. *xcorr(x,y,lag)* returns the cross-correlation sequence of a length 2*N-1 vector, where x and y are vectors of length N. Hence, the autocorrelation function can be determined by cross-correlating the photon burst scan with itself. The complete function looks as follows: *xcorr(Counts,Counts,tau)*. *Counts* = x = y is the vector containing the burst scan data and tau is the correlation or lag time. As this graph will be symmetrical around a lag time of 0, only the right hand portion of the curve is needed to define the autocorrelation function.

The correlation curve produced with Matlab's built in function is not normalized and hence must be done so according to the following Equation:

$$G(\tau) = \frac{1}{T \bullet \bar{n}^2} xcorr(Counts, Counts, tau) \qquad \text{(Equation 3.17)}$$

T is defined as the total acquisition time and $\bar{n}^2$ is the root mean square of the vector *Counts*.

The least squares fitting routine used was more sophisticated than that used in determining the Poisson recurrence times, as in this case, six variables are required for the fit. They are as follows: T_d – diffusion time (s), T_f – flow through time (s), R/d – radius to depth ratio of the probe volume (no units), N – normalization parameter, anol – a factor relating to the effects of anomalous diffusion (no units), and B – a background correction factor. It was found that the quality of fit was highly dependant on the starting parameters. In the majority of cases a reasonable starting point was as follows:

T_d= 1.97e-005	T_f = 3.21e-004	R/d = 1
N = 3.72e-005	anol = 2	B = 10

Upper and lower boundary conditions were also required to ensure a good fit. In all cases they were as follows:

Upper boundary conditions

T_d= 1	T_f = 1	R/d = 2
N = 0.1	anol = 2.1	B = inf

Lower boundary conditions

T_d= 1e-10	T_f = 1e-10	R/d = 0.5
N = 1e-10	anol = 1.4	B = 0

The fitting algorithm used was based on the *'fmincon'* function available in the optimization toolbox for Matlab (version 6.5). *x = fmincon(G(τ),x0,A,b,lb,ub)* starts at the initial parameters x0 and finds a minimum x to the function described in $G(\tau)$ subject to the linear inequalities A*x <= b. x0 can be a scalar, vector, or matrix. lb and ub define lower and upper bounds on the design variables, x, so that the solution is always in the range lb <= x <= ub. The Levenberg-Marquardt algorithm is the default method used by *fmincon*. It has proved to be more robust than the Gauss-Newton method and iteratively more efficient than an unconstrained method. Although this method proved to be most successful at fitting the autocorrelation functions it is not without its drawbacks. For example, the time required for the fitting routine can be relatively long when compared to methods used by other commercial fitting packages such as those used in Origin 6.0 (Microcal).

The complete source code for the program is available in Appendix 2.1. The program itself can be split up into 5 distinct operations. 1) Importing the data. 2) Calculation of the autocorrelation function. 3) Least squares fit of the autocorrelation function. 4) Extraction of variables. 5) Plotting the results. An example of the output from a burst scan of *E. coli* cells travelling at a flow velocity of 1 µl/min from step 4 is shown below:

File Name: e:\temp\500nm-Cell\\Cell-Lys\1-014.Asc
Dwell Time: 1.000000e-004
Number of Data points: 325000

Initial Parameters
Bkg threshold Starting guess: 2.350277e-001
Addition to Bkg threshold: 2.000000e-001
Tolerance of fits: 1.000000e-008

Poisson Background Statistics
Background Threshold: 1.578743e+000
Number of autocorrelation points: 200
Autocorrelation fit starting at point: 1
Starting Parameter for autocorrelation fit Td: 1.970000e-005
Starting Parameter for autocorrelation fit Tf: 3.210000e-004
Starting Parameter for autocorrelation fit R/d: 1
Starting Parameter for autocorrelation fit N: 3.720000e-005
Starting Parameter for autocorrelation fit A: 2
Starting Parameter for autocorrelation fit B: 10

Autocorrelation Statistics
Diffusion time: 3.026466e-004
flow through time: 4.089597e-004
Probe Width / depth: 8.894875e-001

Normalization Constant: 2.521657e-007
Anomalous Diffusion component: 1.702034e+000
Bkg Shift: 4.507115e+003

The plot from step 5 for the same system described above in shown in ***Figure 3.8***. In the top portion of the Figure the autocorrelation curve is plotted ('o') along with a least squares fit to Equation 3.12 (red line). In the bottom half of the Figure, the percent error per data point between the experimental data and the least squares fit is shown.

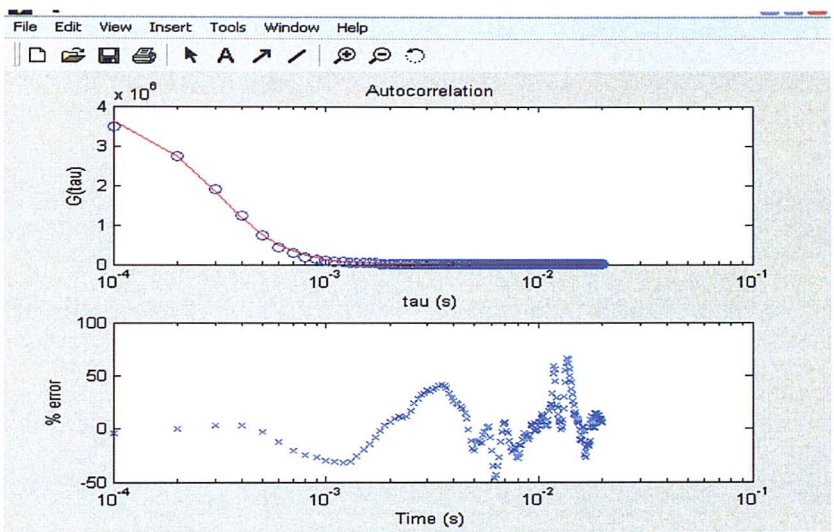


Figure 3.8 Graphical output of the Matlab program for the calculation and analysis of autocorrelation curves. A least squares fits to the theoretical function is shown with a solid red lines.

3.5 Photon burst histograms

Photon burst histograms are a useful means of discriminating between fluorescent molecules or particles. For example, molecules with different molecular weights will exhibit different burst characteristics as each molecule passes through the detection probe volume. In the following sections, three of the most useful types of histograms will be described. They are as follows: the burst height histogram (BHH), the burst area histogram (BAH), and finally the burst width histogram (BWH).[22, 23]

3.5.1 Burst height histogram

Burst height histograms (BHH) were obtained using a simple extension of the peak locating algorithm (PLA). The PLA returns a Boolean vector showing local maxima positions; hence, a unit value of 1 is assigned to a local maximum and a value of 0 is assigned to all other

regions. Wherever there is a 1 in the PLA vector the height can be extracted and inserted into a new 'BurstHeight' vector. From this vector the burst height histogram is determined and is binned between 0 and the maximum burst height over the entire burst scan. The data output of the program looks as follows:

File Name: e:\temp\500nm-Cell\\Cell-Lys\1-014.Asc
Dwell Time: 1.000000e-004
Number of Bins: 325000

Initial Parameters
Bkg threshold Starting guess: 2.350277e-001
Addition to Bkg threshold: 2.000000e-001
Tolerance of fits: 1.000000e-008

Peak Location Rectangle size: 15
Search for Peaks greater than: 7

Total number of peaks: 128
Bin Widths Selected surrounding Local Maxima: 100
Burst Width Bkg threshold value: 8.000000e-001

Burst Height Statistics
Mean Height: 8.784313e+001
Standard Deviation in Height: 9.467039e+001
Relative Standard Deviation in Height: 1.077721e+002

The important information extracted from such an analysis is the total number of peaks averaged, mean height, standard deviation, and the relative standard deviation. These values are determined over the total number of peaks defined above a pre-defined threshold.

3.5.2 Burst area histogram

The Burst area histogram (BAH) is the most computationally demanding of all three histograms described. Once a peak is found using the PLA, the peak area is determined by analyzing a specified number of bins either side of the peak maximum until the background threshold value is reached. Once this is done, the program searches for the next peak and continuously repeats until all peaks are accounted for. This is achieved by extracting the burst from the raw data and inserting it into a matrix $\omega(r)$ with each column associated to a single particle burst r, (where r is defined as a particle burst). Typically a given matrix has up to 4000 columns (particle bursts) and 500 rows (250 bins to the left and right of each burst maxima). The challenge in this approach is to remove all data points below a defined threshold to the left and right of a particle burst. This can be done by either vectorizing the matrix or by using a more computationally demanding *loop (for, if, etc...)*. Although under normal circumstances vectorization results in greatly decreased computation times, the

matrices can be as large as [4000 x 4000]. Hence the *'for loop'* approach results in quicker computation times. Times varied between 2 and 60 s depending on the total number of peaks within a burst scan. The complete source code is available in Appendix 2.1 and can be used with a 2 column ascii file. The first column containing the time and the second column containing the counts. The output of the program is similar to that of the BHH and an example is shown below for the analysis of a photon burst scan of *E. coli* cells expressed with GFP.

File Name: e:\temp\500nm-Cell\\Cell-Lys\1-014.Asc
Dwell Time: 1.000000e-004
Number of Bins: 325000

Initial Parameters
Bkg threshold Starting guess: 2.350277e-001
Addition to Bkg threshold: 2.000000e-001
Tolerance of fits: 1.000000e-008

Peak Location Rectangle size: 15
Search for Peaks greater than: 7

Total number of peaks: 128
Bin Widths Selected surrounding Local Maxima: 100
Burst Width Bkg threshold value: 8.000000e-001

Burst Area Statistics
Mean Area: 4.567578e+002
Standard Deviation in Area: 4.243782e+002
Relative Standard Deviation in Area: 9.291099e+001

3.5.3 Burst width histogram

Burst widths are calculated by determining the number of time bins a particle takes to travel through the probe volume. The complete set of burst times are then histogramed so that the histogram bin width is identical to that of the dwell time of the photon burst scan. A wide distribution in burst areas is directly related to the spatial intensity variation in a focused excitation beam as well due to a wide range of molecular trajectories as molecules diffuse through the probe volume. It will be shown in later chapters that this distribution can be controlled and is dependant on flow velocities of the analyte solution through the microfluidic channel as well as the channel width. As in the case of the BHH's and BAH's, the output of the program is as follows.

File Name: e:\temp\500nm-Cell\\Cell-Lys\1-014.Asc
Dwell Time: 1.000000e-004
Number of Bins: 325000

Initial Parameters

Bkg threshold Starting guess: 2.350277e-001
Addition to Bkg threshold: 2.000000e-001
Tolerance of fits: 1.000000e-008

Peak Location Rectangle size: 15
Search for Peaks greater than: 7

Total number of peaks: 128
Bin Widths Selected surrounding Local Maxima: 100
Burst Width Bkg threshold value: 8.000000e-001

Burst Width Statistics
Mean Width: 1.392188e-003
Standard Deviation in Width: 7.728268e-004
Relative Standard Deviation in Width: 5.551169e+001

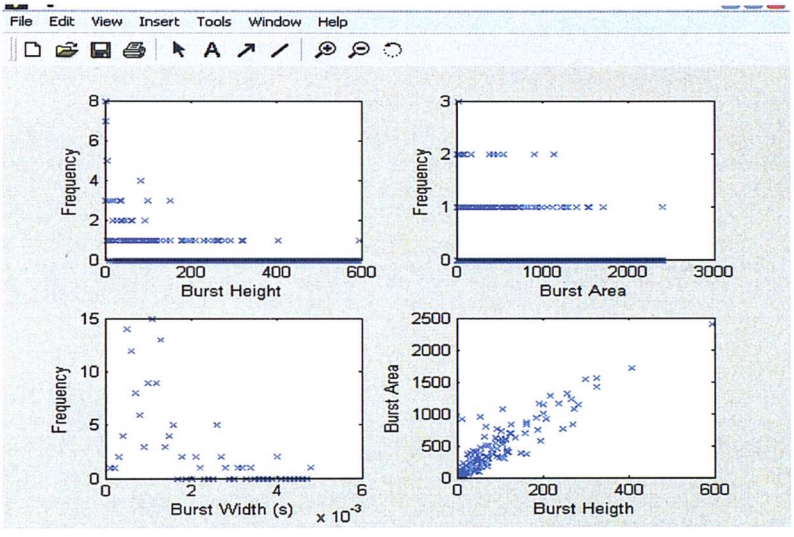


Figure 3.9 Burst width, area, and height histograms for a photon burst scan of single cells expressing green fluorescent protein. The histograms were calculated over 128 cell bursts.

The program also prints out a combined plot for the BHH, BAH, BWH. An example is shown in ***Figure 3.9*** for a photon burst scan with a total of 128 peaks. It should be noted that due to the low number of peaks, these histograms do not have a well defined distribution. This will be discussed in detail in Chapter 5. The top half of the Figure consists of the BHH (left) and the BAH (right). The bottom half consists of the BWH (left) as well as a plot of burst height versus the burst area.

3.6 Fluorescence lifetimes analysis

Fluorescence photons are typically emitted between 1 and 100 ns after absorption of a photon. For a discrete molecular population, the fluorescence lifetime is usually mono-exponential

and can be characterized by the summation of both radiative and non radiative decay processes. Lifetimes are highly dependant on the statistical nature of the emission process as well as the surrounding local environment. The key advantage of measuring single-molecule fluorescence lifetimes is in the ability to directly measure molecular lifetimes as opposed to measuring an ensemble averaged lifetime. Such measurements can provide information on functional dynamics, not typically possible using conventional bulk measurement techniques.[24, 25] For example, proteins fold into a unique three-dimensional conformation in solution, and it is this conformation which helps the proteins carry out their intended function. Indeed, many genetic diseases are the result of misfolding proteins, usually caused by a mutation in the DNA sequence which encodes the protein. Due to the complexity of protein structures, important aspects of protein folding are difficult to study using conventional bulk fluorescence measurements; hence, a single molecule approach is ideally suited, as ensemble averaging is avoided.[26, 27]

3.6.1 Fluorescence lifetimes: Theory

The objective of time resolved fluorescence measurements is to recover information relating to the time dependant radiative decay process. When a molecule is excited with a pulse of light, the excited state is generated instantaneously (< 1 fs), and the resulting time-dependant emission decay rate equation can be written according to ***Equation 3.18***.

$$-\frac{dn(t)}{dt} = (k_r + k_{nr})n(t) \qquad \text{(Equation 3.18)}$$

where n(t) is the number of excited molecules at time t following the excitation. k_r is the radiative rate constant and k_{nr} is the non radiative rate constant. ***Equation 3.18*** describes the deactivation processes that remove the excess energy gained in the absorption transition. When ***Equation 3.18*** is integrated (***Equation 3.19***), an expression describing the temporal behavior of the excited state concentration is obtained.

$$n(t) = n_0 e^{-\frac{t}{\tau_f}} + C \qquad \text{(Equation 3.19)}$$

C is an integration constant, $k_r + k_{nr}$ is equal to the reciprocal of the molecular fluorescence lifetime ($1/\tau_f$). At time zero, $n = n_0$, and hence the pre-exponential factor A in ***Equation 3.20*** equals n_0.

$$n(t) = Ae^{-\frac{t}{\tau_f}} \qquad \text{(Equation 3.20)}$$

The fluorescence lifetime describes the average duration of emission after the termination of the excitation source. Furthermore, it can be described in terms of the time dependant fluorescence intensity as is shown in ***Equation 3.21.***

$$I(t) = I_0 e^{-\frac{t}{\tau_f}} \qquad \text{(Equation 3.21)}$$

Here I_0 is the intensity at time t = 0 and τ_f is the fluorescence lifetime.

The fluorescence lifetime can be obtained by determining the time at which the decay intensity decreases by 1/e of its initial value from the slope of a semi log plot of I(t) versus t.

For a system containing n freely, non interacting species, the observed decay will simply be a sum of each of the individual emitting terms (***Equation 3.22***). This simplistic approach can be used in the interpretation of 'multi-exponential' decays if it is assumed that the recovered parameters posses *real, physical* origin.

$$I(t) = \sum_i A_i e^{-\frac{t}{(\tau_f)_i}} \qquad \text{(Equation 3.22)}$$

where A_i is the i^{th} pre-exponential factor and $\sum_i A_i$ is normalized to unity.

3.6.2 Approach for the fitting of fluorescence lifetimes

It is important to note that the measured decay curve is a convolution of both the instrument response function and the true fluorescence decay. The instrument response can be experimentally approximated by measuring the systems response to scattered excitation light or by using a dye with an extremely short lifetime (< 25 ps). Therefore the experimental data must be mathematically analyzed in order to extract the true fluorescence lifetimes. The most common approach is to use a least squares analysis (LSA) to extract the lifetimes from the convolved data. An LSA can be performed for such deconvolutions as the following conditions hold in a TCSPC experiment. 1) The uncertainty in the experiment is strictly governed by Poissonian counting statistics and hence the greater the number of photon counts

accumulated, the greater the precision. 2) The uncertainty in the measurement follows a Poissonian distribution; however, for large enough counts, it can be approximated to follow a Gaussian distribution.

In an LSA, the ideal description of a data set is one that minimizes the weighted sum of the squares of the deviation of the experimental data N(t) and the calculated decay $N_c(t)$. This can be accomplished by minimizing the following function:

$$\chi^2 = \sum_{k=1}^{n} \frac{1}{\sigma_k^2}[N(t_k) - N_c(t_k)]^2 \qquad \text{(Equation 3.23)}$$

Where n is the number of time bins or channels used in the decay and σ_k is the standard deviation at each data point k. χ^2 is the sum of the squared deviation between N(t) and $N_c(t)$. From Poissonian statistics the standard deviation is defined as the square root of the number of photons

$$\sigma_k^2 = \sqrt{N(t_k)} \qquad \text{(Equation 3.24)}$$

In a multi exponential model the values of A_i and τ_i are varied until the lowest possible χ^2 is achieved. In all cases a deconvolution method based on the Levenberg-Marquardt algorithm was used. This is the most popular and successful choice for the analysis of TCSPC data.[28] The procedure matched the convolved functions with that of N(t). It should be noted that χ^2 depends on the number of channels and hence a reduced chi squares (RCS, χ_R^2) was used and is defined by $\chi^2/(n-p)$. p is the number of fioating parameters and n is the number of data points. This approach is completely independent on the number of data points.

3.6.3 Fluorescence lifetime fitting program (J-Life)

A program written in Matlab was developed to calculate single molecule (and particle lifetimes). The source code can be found in Appendix 2.2. The graphical user interface (GUI) is shown in ***Figure 3.10.***

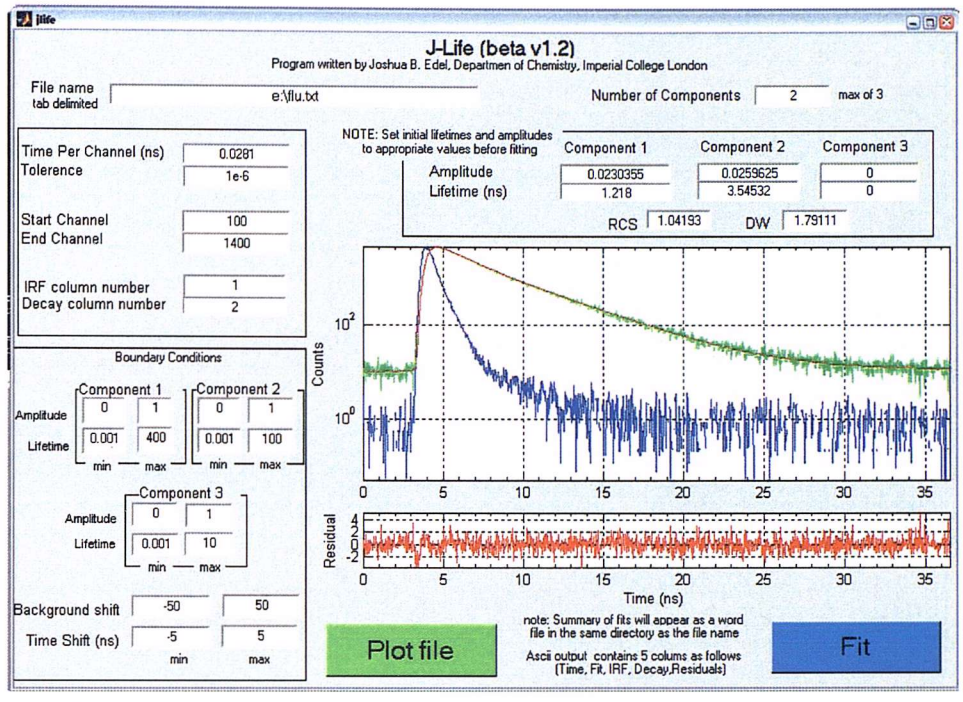


Figure 3.10 GUI of the TCSPC lifetime fitting program. The program shown can fit up to 3 components.

In this program, between 1 and 3 fluorescence lifetimes can be used to describe a decay. The GUI shown in ***Figure 3.10*** is for 2 components. At the top of the program the file location is entered. This should be an *ascii file* containing two or more columns, with at least one belonging to experimental fluorescence decay and another belonging to the instrument response. For each component an initial amplitude and lifetime guess should be entered. The tolerance can be adjusted to control the quality of the fit. Typically a termination tolerance of 1e-6 is sufficient for a reasonable fit. This value can be varied between 0.1 – 1e-12 depending on the quality of fit required. The fit can also be restricted to an interval defined by the start and end channels. "Plot file" can be used to plot the decays and determining which channels should be used in the fits. Once all the appropriate parameters are defined, "fit" should be pressed and the program will commence the fitting routine. A summary of the output is obtained in a text document and is shown below. In addition a graphical output is plotted within the GUI as well as a separate Excel file, an example of which is shown in ***Figure 3.11***.

File creation: 04/07/2003 12:05:3
Channels: 4096
Acqu. time: 240000
SYNC level: -26
IntegralCount: 437926
MaxCount: 10195
MaxTime: 6.662036e+000

Time Per Channel: 2.810986e-002

COMPONENT 1
Lifetime: 3.531763e+000 Amplitude: 2.597962e-002 yield: 7.667038e+001

COMPONENT 2
Lifetime: 1.212507e+000 Amplitude: 2.302609e-002 yield: 2.332962e+001

Average Lifetime: 2.990690e+000

STATS
Background Correction Intensity: 9.537568e+000
Instrument Response Correction Intensity: -2.049290e+000
Shift in Instrument Response: 1.058093e-002
Reduced Chi Sq: 1.037784e+000
Derb Wat: 1.789138e+000

Briefly, individual component lifetimes are given along with amplitudes, and yields. Statistics on the quality of the fit are summarized by showing the reduced chi squares value and the Durbin Watson (DW) parameter. This essentially provides a numerical test for correlations between residuals at adjacent points. A '*good fit*' has a DW greater than 1.5 and a RCS between 0.8 and 1.3. Prior to the summary of the fluorescence components, details on starting acquisition parameters are given (i.e. acquisition time, total counts, count rates etc...). An example of the graphical output is shown in ***Figure 3.11*** for CdSe crystalline quantum dots. In the top half of the plot the red curve is the LSA fit, the green is the instrument response function and the blue curve is the experimental decay. In the bottom half the residuals are plotted over the entire range of the decay.

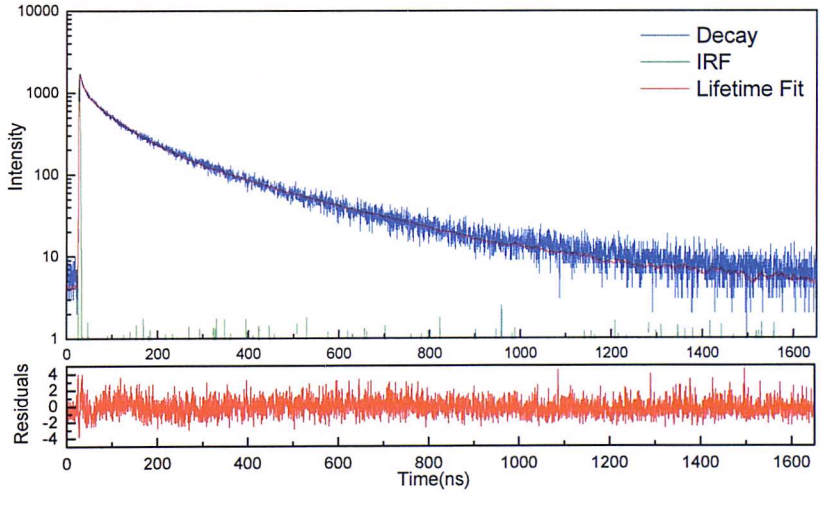


Figure 3.11 Fluorescence lifetime decay (blue) for CdSe Nanocrystalline quantum dots. The green curve is the instrument response function and the red curve is the least squares fit. The lower panel displays the residuals of the fit.

3.7 Summary

In this chapter a selection of analysis methods were developed for single molecule and particle detection in solution. Examination of these analysis methods along with fluorescence lifetime studies will be shown in the following chapters to be most useful in distinguishing between different molecules and particles in freely flowing systems with microfluidic channels.

The dominant analysis methods discussed were the photon burst recurrence time analysis, autocorrelation analysis, photon burst histogram analysis, and fluorescence lifetimes analysis. The autocorrelation and recurrence time analysis routines could be fit to theoretical functions and information such as diffusion coefficients, probe volumes, flow through times, recurrence times can be obtained. Photon burst histograms yield statistics pertaining to single or multiple burst widths, heights, and areas. TCSPC is used to extract single particle and cell fluorescence lifetimes using a least squares analysis deconvolution routine.

All routines were written in Matlab as it afforded maximum potential for customization in the analysis of the raw data.

3.6 References

(1) Michalet, X.; Weiss, S. *Comptes Rendus Physique* **2002**, *3*, 619-644.

(2) Papoulis, A. *Probability, Random Variables, and Stochastic Processes*, 3rd ed.; McGraw-Hill: New York, **1991**.

(3) Treussart, F.; Alleaume, R.; Le Floc'h, V.; Roch, J. F. *Comptes Rendus Physique* **2002**, *3*, 501-508.

(4) Dittrich, P. S.; Schwille, P. *Applied Physics B-Lasers and Optics* **2001**, *73*, 829-837.

(5) Chen, Y.; Müller, J. D.; Berland, K. M.; Gratton, E. *Methods - A Companion to Methods in Enzymology* **1999**, *19*, 234-252.

(6) Feller, W. *An Introduction to Probability Theory and its Applications*; Wiley: New York, **1968**.

(7) Li, H. T.; Ying, L. M.; Green, J. J.; Balasubramanian, S.; Klenerman, D. *Analytical Chemistry* **2003**, *75*, 1664-1670.

(8) Segers-Nolten, G. M. J.; Wyman, C.; Wijgers, N.; Vermeulen, W.; Lenferink, A. T. M.; Hoeijmakers, J. H. J.; Greve, J.; Otto, C. *Nucleic Acids Research* **2002**, *30*, 4720-4727.

(9) Medina, M. A.; Schwille, P. *Bioessays* **2002**, *24*, 758-764.

(10) Ferris, M. M.; Rowlen, K. L. *Review of Scientific Instruments* **2002**, *73*, 2404-2410.

(11) Schwille, P. *Cell Biochemistry and Biophysics* **2001**, *34*, 383-408.

(12) Ishii, Y.; Yanagida, T. *Single Molecules* **2000**, *1*, 5-16.

(13) Booer, A. K., *http://www.mathtools.net/* **1992**.

(14) Edel, J. B.; Hill, E. K.; de Mello, A. J. *Analyst* **2001**, *126*, 1953-1957.

(15) Osborne, M. A.; Balasubramanian, S.; Furey, W. S.; Klenerman, D. *Journal of Physical Chemistry B* **1998**, *102*, 3160 - 3167.

(16) Bacia, K.; Schwille, P. *Methods* **2003**, *29*, 74-85.

(17) Dittrich, P. S.; Schwille, P. *Analytical Chemistry* **2002**, *74*, 4472-4479.

(18) Zhong, Z. H.; Pramanik, A.; Ekberg, K.; Jansson, O. T.; Jornvall, H.; Wahren, J.; Rigler, R. *Diabetologia* **2001**, *44*, 1184-1188.

(19) Basché, T.; Kettner, R.; Tittel, J.; Kummer, S. *Exp. Tech. Phys.* **1995**, *41*, 197-204.

(20) Peck, K.; Stryer, L.; Glazer, A. N.; Mathies, R. A. *Proceedings of the National Academy of Sciences USA* **1989**, *86*, 4087 - 4091.

(21) Dickson, L. D. *Applied Optics* **1970**, *9*, 1854-1861.

(22) Herten, D. P.; Tinnefeld, P.; Sauer, M. *Applied Physics B-Lasers and Optics* **2000**, *71*, 765-771.

(23) Enderlein, J.; Robbins, D. L.; Ambrose, W. P.; Keller, R. A. *Journal of Physical Chemistry A* **1998**, *102*, 6089 - 6094.

(24) Kollner, M.; Wolfrum, J. *Chemical Physics Letters* **1992**, *200*, 199-204.

(25) Maus, M.; Cotlet, M.; Hofkens, J.; Gensch, T.; De Schryver, F. C.; Schaffer, J.; Seidel, C. A. M. *Analytical Chemistry* **2001**, *73*, 2078-2086.

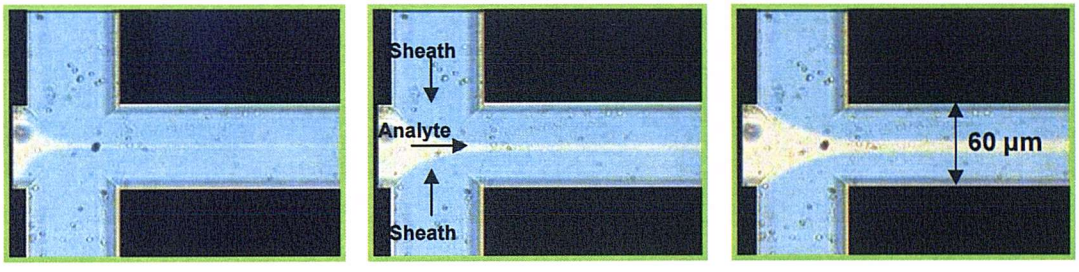
(26) Zhuang, X. W.; Rief, M. *Current Opinion in Structural Biology* **2003**, *13*, 88-97.

(27) Rhoades, E.; Gussakovsky, E.; Haran, G. *Proceedings of the National Academy of Sciences of the United States of America* **2003**, *100*, 3197-3202.

(28) Marquardt, D. W. *J. Soc. Ind. Appl. Math.* **1963**, *11*.

- 4 -

This chapter details a method for improving molecular detection efficiencies using hydrodynamic focussing within a microfluidic channel. In the first part of this chapter a theoretical analysis of the approach is presented and the dependence of particle size and analyte flow rates on molecular detection efficiency is investigated. In the second half of this chapter, experimental results confirming increases in molecular detection efficiency within microfluidic channels are presented.



Hydrodynamic focussing in microstructures

4.1 Introduction

Recently there have been reports of using confocal fluorescence spectroscopy to monitor flow velocities of solid particles within flowing streams.[1-3] Although particulate flow monitoring will be discussed in a later chapter a single example is as follows. Ferris et al. devised a confocal optical arrangement that was incorporated into the design of a relatively simple flow cytometer optimized for rapid enumeration of fluorescent nanometric particles. The measured particle detection efficiency was approximately 5 % which is equivalent to the detection efficiency reported in many single molecule studies.[2] This chapter addresses the need for improving molecular detection efficiencies (MDE) in single molecule confocal based experiments. The approach used to achieve improvements in MDE involves hydrodynamic focussing of an analyte stream within a microfluidic channel. This method allows focussing of an analyte stream down to the same order of magnitude as that of typical probe volume widths. A cartoon representation of the focussing method is shown in ***Figure 4.1.*** In an unfocussed sample stream the dimensions of the probe volume and sample volume are mismatched which directly results in poor molecular detection efficiencies as the majority of analyte molecules flowing through the microchannel remain undetected. Conversely, in a focussed stream the probe volume and sample volumes can approximately have the same dimensions. This leads to higher molecular detection efficiencies due to a reduced range of molecular trajectories through the channel, and therefore probe volume. A key benefit of a confocal based approach is the low detection volumes. This greatly reduces the amount of sample needed for analysis over conventional bulk detection methods. When a dilute solution (analyte) is present at a concentration of approximately 10^{-9} M there is on average less than one fluorescent molecule or particle resident in a 0.5 fl probe volume. Unfortunately, confocal-based detection probe volumes are typically on the order of 0.5 fl and hence molecular detection efficiencies can be extremely poor - the majority of molecules will not be detected.

Other approaches to improving molecular detection efficiencies in SMD experiments involve the enlargement of the focal region of the laser beam to create a detection volume in the low picoliter range.[4, 5] A primary disadvantage with increasing the detection volume is in the large background signal that arises when the probe volume is enlarged to this scale. This signal can often be larger than the fluorescence signal from the target molecule, and is directly related to the increase in the number of solvent/impurity molecules in the probe volume. The use of femtoliter probe volumes is important as it minimizes the background signals, which originate from Raleigh and Raman scattering by solvent molecules. For example, hydrodynamic focussing has been used in conventional capillaries to narrow the sample stream through the

use of a sheath flow (orthogonal to excitation).[6, 7] This ensures that the entire sample is delivered to the probe region. Under appropriate conditions, each molecule within the sample can be detected sequentially and with high efficiency. This approach is conventionally termed single-molecule flow cytometry (SMFC). In SMFC, individual molecules are motivated within the sample stream at the same rate, and experience the same radiation field during their passage through the detection volume. This allows the identification of molecular size on the basis of fluorescence burst characteristics. This approach has been used for DNA fragment sizing[4], proof-of-concept for DNA sequencing[8] and hybridization analysis.[9] However, as previously mentioned, the use of large probe volumes results in high background signals. Consequently, a number of methods to suppress background signals have been proposed and instigated. These include, pulsed laser excitation coupled with time-gated detection[10] (to discriminate between fluorescence and scattering signals) and photobleaching[11, 12] of the sheath flow upstream of the detection volume (to remove the luminescence background from impurity species). Although in many instances these approaches are successful, they add a considerable degree of experimental complexity.

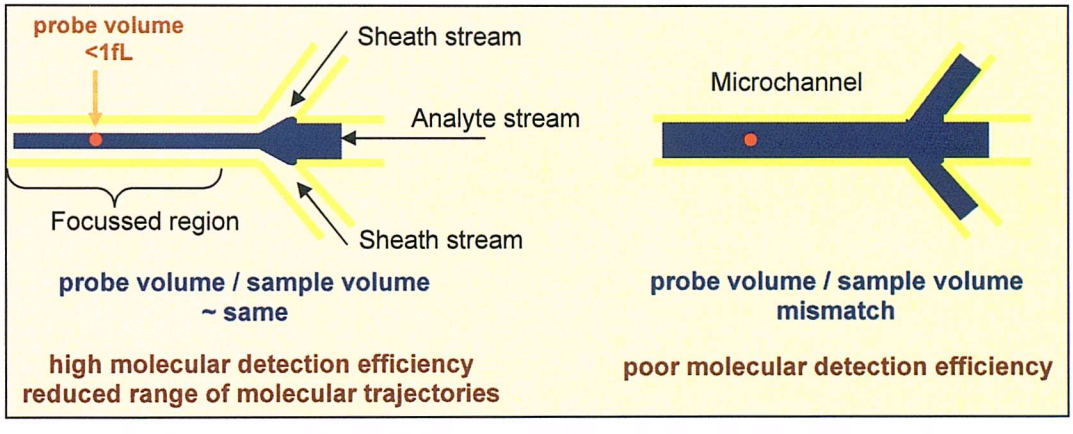


Figure 4.1 Cartoon representation of hydrodynamic focussing in microstructures. In a focussed flow the analyte stream width can have approximately the same dimensions as the probe volume.

Another approach to improve molecular detection efficiencies has been described by Foquet et al.[13] They fabricated fluidic channels with dimensions smaller than 1 μm and used the system to detect individual DNA molecules. The small dimensions facilitated efficient single molecule detection and minimized the probability of simultaneous events, i.e. only one molecule would pass the detection volume at a given time. Molecules were electrokinetically delivered at speeds as high as 5 mm/s within the nanochannels, corresponding to only a few milliseconds of analysis time per molecule. The system was used to characterize a mixture of nine DNA fragments. The amount of sample required for each analysis was ~10 000 molecules, or 76 fg. Although this approach proved to be highly promising, significant

drawbacks are associated with nanometre sized channels. The primary disadvantage is in the possibility of chip blockage when using such small dimensions. In this chapter it will be shown that molecular detection efficiencies can be improved simply by hydrodynamic focussing of an analyte stream within a physical microchannel. This approach subsequently results in minimizing the inherent effects associated with enlarging detection probe volumes as well as decreasing channel dimensions.

4.2 Experimental approach

4.2.1 Experimental materials

Fluorescent microbeads (yellow/green Fluospheres ®, Molecular Probes; Europe B.V.) having a mean diameter of 0.93 μm were used for the analyte flow in all experiments. Absorption and emission maxima were 505 nm and 515 nm respectively. The beads were sonicated for 10 minutes immediately before use to ensure good dispersion. A working solution of approximately $2.3x10^6$ beads/cm^3 was used (effective concentration of 1 μg/cm^3). This is equivalent to a 20,000 fold dilution of the stock solution. All dilutions were performed in TBE (tris-borate-EDTA) buffer. The TBE buffer was prepared at 0.1 x concentration (8.9 mM each of tris(methoxy)aminomethane and boric acid, 0.2 mM in ethylenediaminetretraacetic acid; prepared from a solid TBE mixture; Fluka chemical) in a minimum of 18 MΩ deionized water (water purification system, Elga Ltd., Bucks, U.K.). The sheath flow consisted of a concentrated Bromthymol blue solution and was used for alignment of the analyte flow within the microfluidic channel.

Three different focussing microfluidic devices were used and had channel widths ranging from 20 - 100 μm. The depth in all cases was 30 μm. Unless otherwise stated, all experimental results were obtained with the inlet and outlet channels having a width of 60 μm. Details of the fabrication procedure are described in Chapter 2. Two separate syringe pumps (Harvard Apparatus, Cambridge, MA, USA) were used to deliver sheath and analyte solutions at various flow rates from 1 ml gastight syringes into the capillary tubing. Typical flow rates ranged from 0.01 – 20 μL/min. Separate syringe pumps were found to be critical in ensuring a stable focussed flow through the microchannel. It was also found to be essential to use two separate syringes to drive the sheath flows; this was needed to obtain a constant pressure.

4.2.2 Hydrodynamic focussing in microstructures

Examples of hydrodynamic focussing within 60 μm wide microfluidic channels are shown in ***Figure 4.2*** and ***Figure 4.3***. In the former, the analyte flow rate is kept constant at 5 μl/min and the sheath flow rate is (blue indicator dye) systematically decreased from 11 μl/min (top left) down to 0.25 μl/min (bottom right). In ***Figure 4.3*** the analyte flow rate is kept constant at 2 μl/min and the sheath flow rate systematically decreased from 2 μl/min (top left) down to 0.25 μl/min (bottom right). The focussed analyte stream width typically remains constant down the length of the channel. This phenomenon will be discussed in detail in section 4.2.3. It will be shown that under specific flow conditions, the focussing stream is broadened by diffusion into the sheath flow.

In all cases, it was important for fluid flow within the microchannel to be laminar with a Reynolds number (Re) much less than 2000 so that the focussed stream would not suffer from turbulence effects[14, 15] and flow instabilities. Stability of the focussed streams proved to be good, and the analyte stream would remain focussed for several hours at a time without any observable spatial variation. In order to achieve long term stability, several factors must be observed. Firstly, the solvents used in the analyte and sheath streams must be well matched (in terms of viscosity and miscibility). For example, if sheath and analyte streams were made up of organic and aqueous solvents respectively, instability in the focussed stream would occur over long periods due to a mismatch in surface tensions. Secondly, identical flow velocities are needed for both sheath streams. If this does not occur, not only will the focussed stream be off centre but also an unstable flow would often result. Thirdly, the microfluidic device used must have a well defined cross section and have few surface related defects. Any defect will encourage unstable flow. It is for this reason that microfluidic channels were cleaned with concentrated chromosulphuric acid prior to use to ensure all contaminates are removed from the channel walls.

An example of varying the dimensions of the inlet channels is shown in ***Figure 4.4***. The sheath width is 60 μm and the analyte inlet width is 100 μm. Several qualitative observations can be made when comparing ***Figures 4.2 – 4.4***. Firstly, analyte focussing down to approximately 1/10 of the channel width is possible irrespective of the analyte flow rate. Secondly, the degree of analyte focussing is directly dependant on the channel size and cross-section. Thirdly, a larger sheath to analyte flow ratio is required in wider microfluidic channels to ensure high degrees of focussing. All three of these issues will be addressed in the following sections.

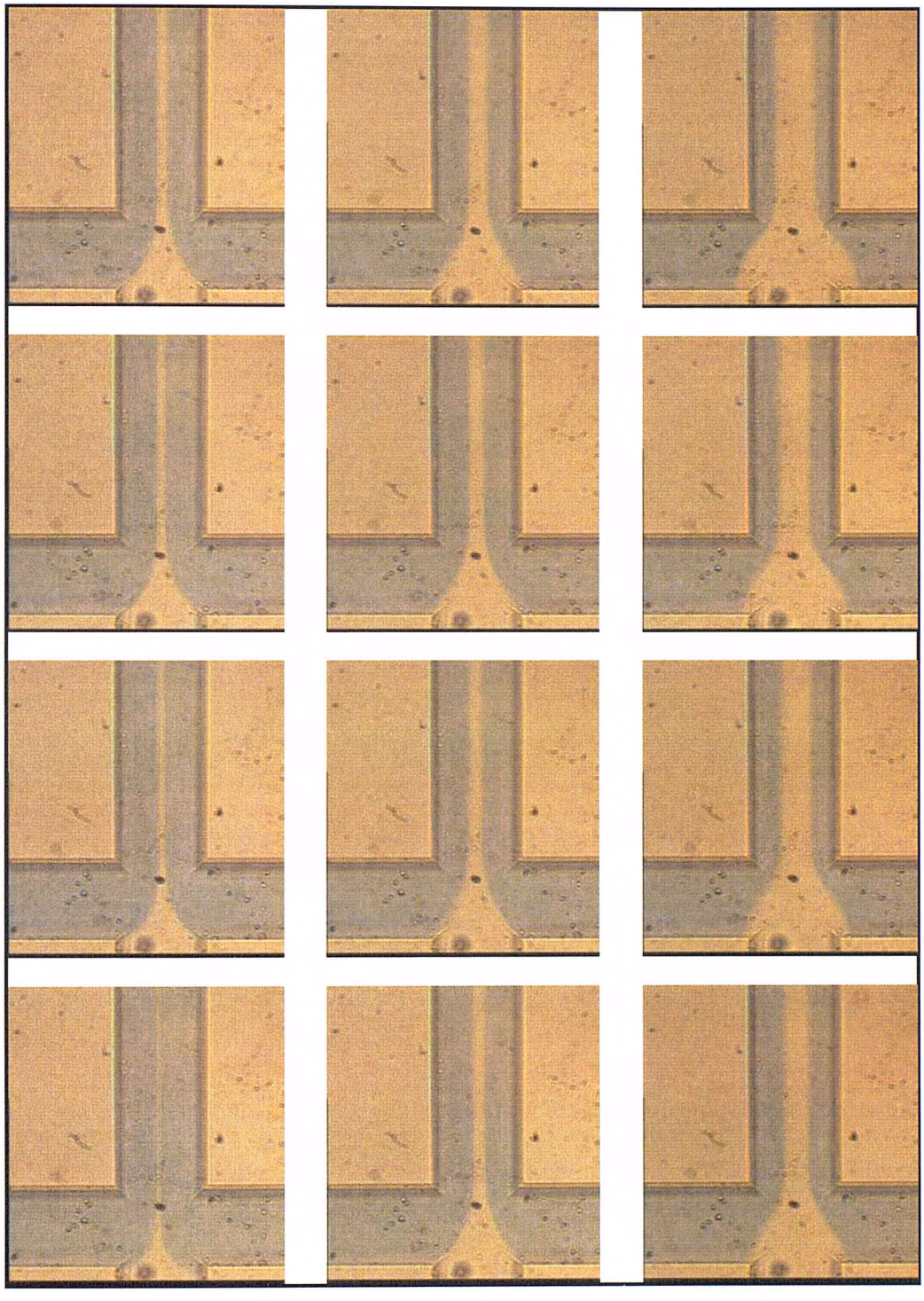


Figure 4.2 Hydrodynamic focussing in a 60 µm wide microfluidic channel. The sheath stream is represented by a blue dye. The analyte flow rate was 5 µl/min and the sheath flow rate was varied between 11 µl/min (top left) to 0.25 µl/min (bottom right).

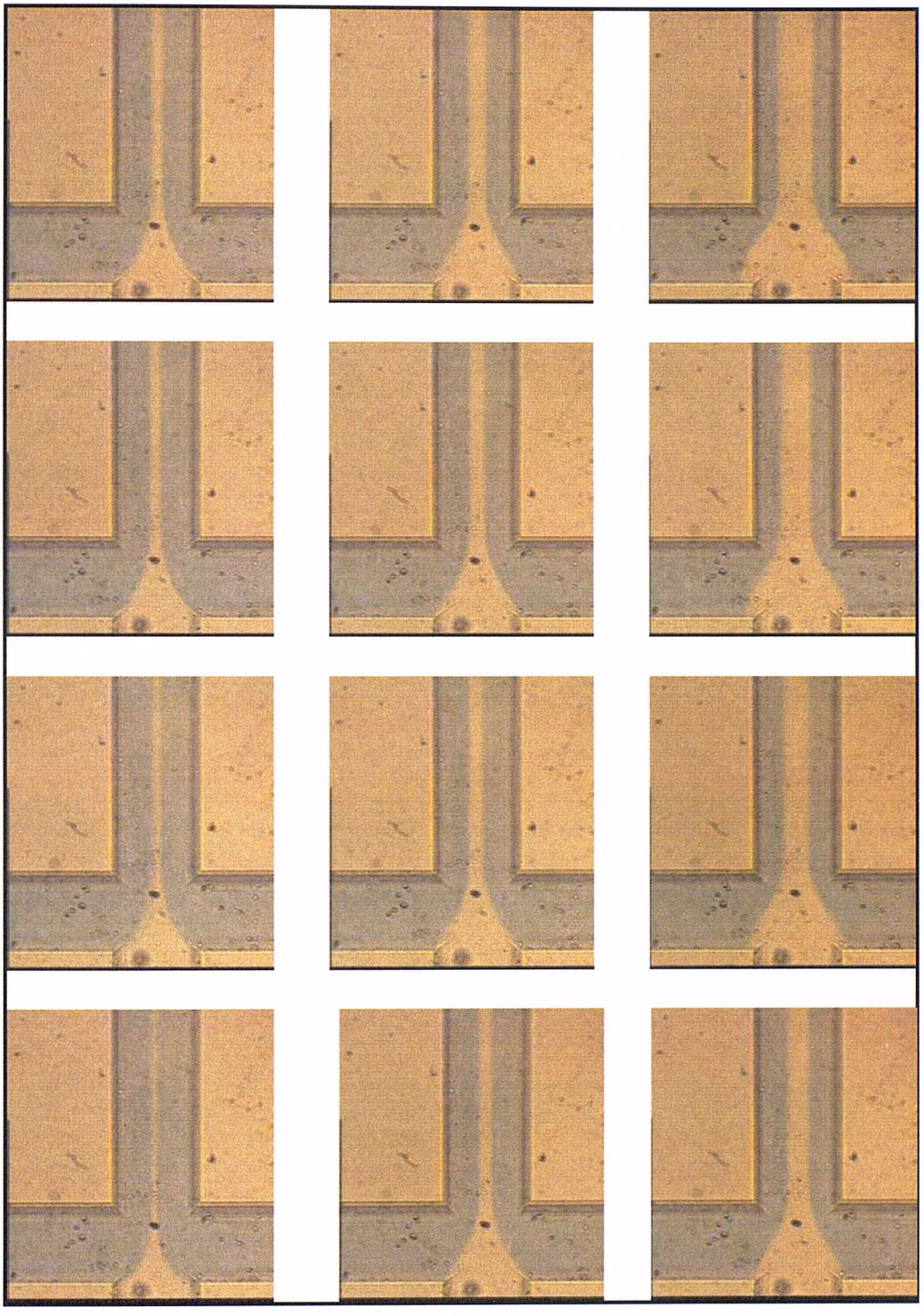


Figure 4.3 Hydrodynamic focussing in a 60 µm wide microfluidic channel. The sheath stream is represented by a blue dye. The analyte flow rate was 1 µl/min and the sheath flow rate was varied between 2 µl/min (top left) to 0.25 µl/min (bottom right).

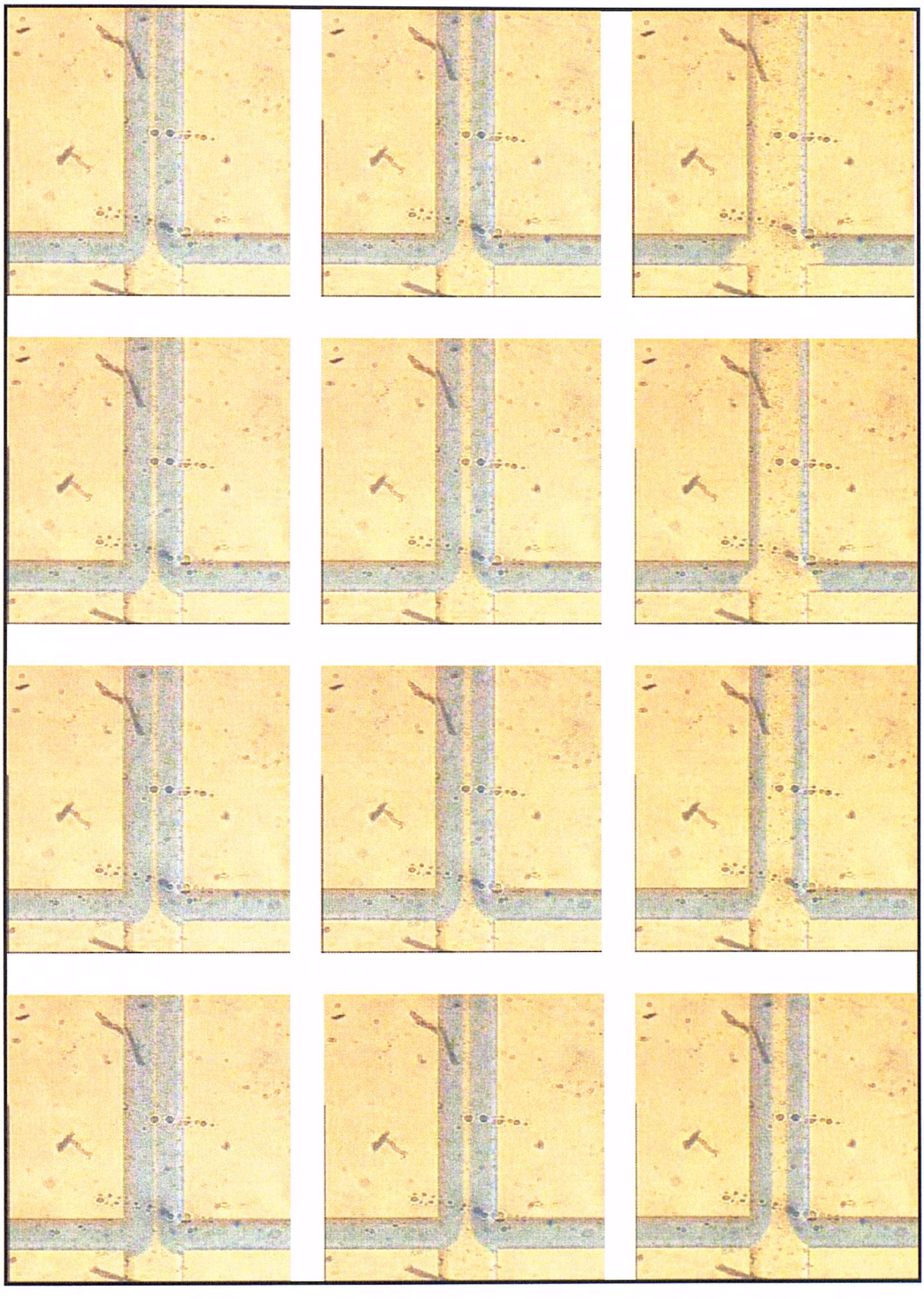


Figure 4.4 Hydrodynamic focussing in a 100 µm wide microfluidic channel. The sheath stream is represented by a blue dye. The analyte flow rate was 3 µl/min and the sheath flow rate was varied between 18 µl/min (top left) to 0.05 µl/min (bottom right).

4.2.3 Focussing width versus flow rate

Figure 4.5 shows focussing widths obtained for various analyte and sheath flow rate combinations in 60 and 100 μm channels. It is interesting to note that all analyte flow rate curves follow a similar trend as the sheath flow is increased. Minimum focussing was achieved using an analyte flow rate of 5 μl/min and a sheath flow of 10 μl/min in a 60 μm wide channel. In this instance, a focussing width of 3.8 μm was achieved. In all other cases, at analyte flow velocities of 1, 3, 7, and 9 μl/min the minimum focussing width was slightly higher, and varied between 5 – 10 μm depending on chip dimensions and sheath flow rates. With the microfluidic chip geometries used, the limiting width appears to be just below $1/10^{th}$ of the channel width.

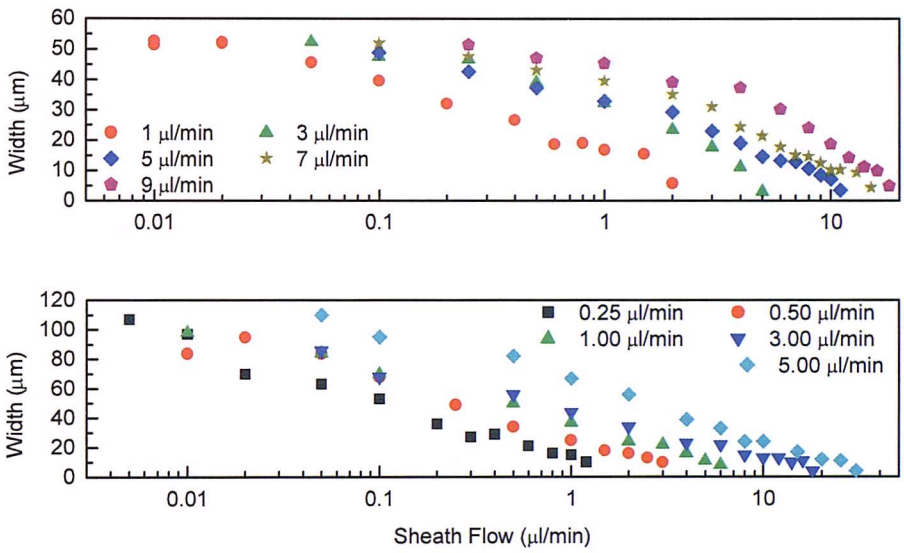


Figure 4.5 a) Focussing width relative to sheath flow rate for a 60 μm wide channel. The analyte flow rates are 1, 3, 5, 7, 9 μl/min. b) Focussing width relative to sheath flow rate for a 100 μm wide channel. The analyte flow rates are 0.25, 0.5, 1, 3, 5 μl/min

4.2.4 Focussing symmetry within the microchannels

Actual focussing widths were determined by importing the raw captured images (as shown in *Figure 4.4*) into Matlab and extracting 1-dimensional cross sections. This is possible as an image is composed of 3 channels (*Red, Green, Blue*) with each pixel in each channel represented by a value ranging from 1 – 255. The cross sections were extracted from the *red* channel and were averaged over 100 pixels 1 mm down stream in the detection channel. This produced a maximum difference between the intensities of the blue sheath flow and the

analyte flow. This approach is more accurate and quicker than simply measuring the focussed widths by visual inspection.

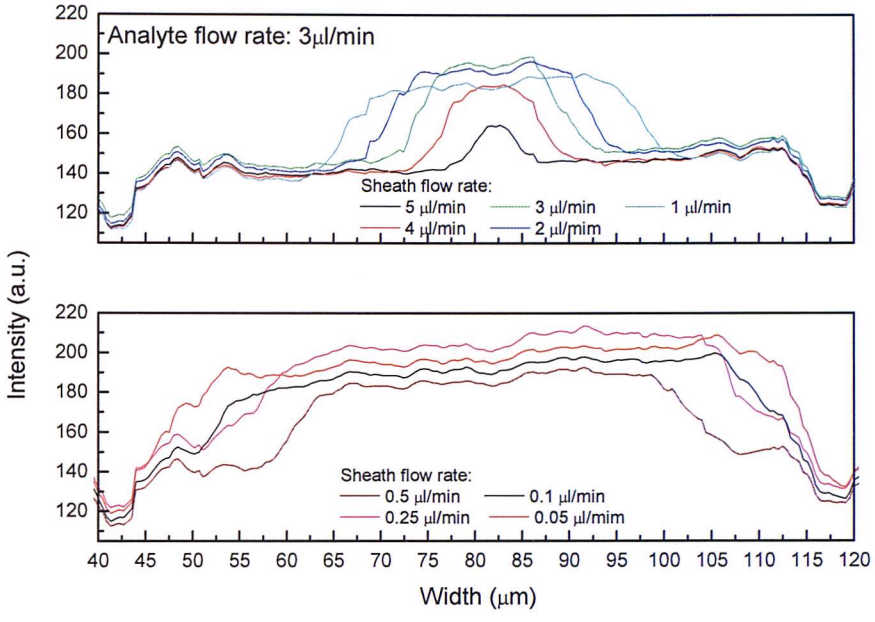


Figure 4.6 Focussing width profile within a 60 µm wide microfluidic channel. The analyte flow rate was 3 µl/min and the sheath flow was varied between 0.05 µl/min and 5 µl/min.

Examples of the cross sections are shown in ***Figure 4.6***. These plots are extremely useful for evaluating the symmetry of fluid flow within the channels as well as monitoring the quality of the focussing. In this case the analyte flow rate was 3 µl/min and the sheath flow rate varied from 0.05 µl/min – 5 µl/min. The x axis is defined as the width of the cross section. Using this approach, the sheath flow is easily distinguishable between that of the analyte flow. The stable base line at an intensity of 140 is due to the blue sheath and is easily distinguishable from analyte flow with peak maxima ranging from 160 - 200 counts. The focussing width was determined by the full width half maximum of these cross sections. From these plots it can be seen that the overall symmetry of the focussed stream remains constant and is always centered around the central portion of the microfluidic channel. As the sheath flow rate is decreased the focussed analyte stream gradually broadens about the central portion of the chip. The channel boundaries are defined by the minima in the cross sections (i.e. 42.5 µm and 117.5 µm respectively). The quality of the sheath symmetry is highly dependant on the conditions discussed in section 4.2.1.

4.2.5 Minimum focussing width

4.2.5.1 Theory

At first sight it is not entirely obvious that the focussed analyte width is independent of the applied pressure of the sheath stream (i.e. the volumetric flow rate). The focussing properties are in fact strictly dependant on the ratio, α, between the sheath and analyte flow rates[16] as shown in ***Equation 4.1***.

$$\alpha = \frac{F_s}{F_a} \qquad \text{(Equation 4.1)}$$

In this instance F_s is defined as the sheath flow rate and F_a is defined as the analyte flow rate. If α goes below a lower boundary condition α_{min}, the analyte flow rate will take preference and the analyte will go into the sheath channels. Hence no hydrodynamic focussing will occur. If α goes above an upper boundary condition α_{max}, the sheath flow rate will take preference and the sheath flow will go into the analyte channel. Again no focussing will occur. It is therefore essential that in order to achieve hydrodynamic focussing the following condition in ***Equation 4.2*** must be satisfied.

$$\alpha_{min} \leq \alpha \leq \alpha_{max} \qquad \text{(Equation 4.2)}$$

Here α_{max} and α_{min} are completely independent of overall flow velocities used, but are dependant on the overall dimensions and cross section of the microfluidic channel used.

Figure 4.7 illustrates a plot of α against the focussed width for a variety of sheath and analyte flow rates within a 60 μm channel. As expected α is independent of flow rate. From this plot, the boundary conditions of α were deduced to be α_{min} = 0.014 and α_{max}= 2.0. This implies a minimum focussing width of 3 μm is obtainable with the 60 μm microfluidic channel. These values are different to those reported by Knight et al. (α_{min} = 0.48 and α_{max}= 1.28)[16]; however, this was expected as the cross section of the microfluidic channels studied was significantly different (Knight et al. used 10 μm wide channels with a high aspect ratio). Conversely in the 20 μm and 100 μm wide channels, minimum focussing widths of 8 μm and 2 μm are theoretically obtainable.

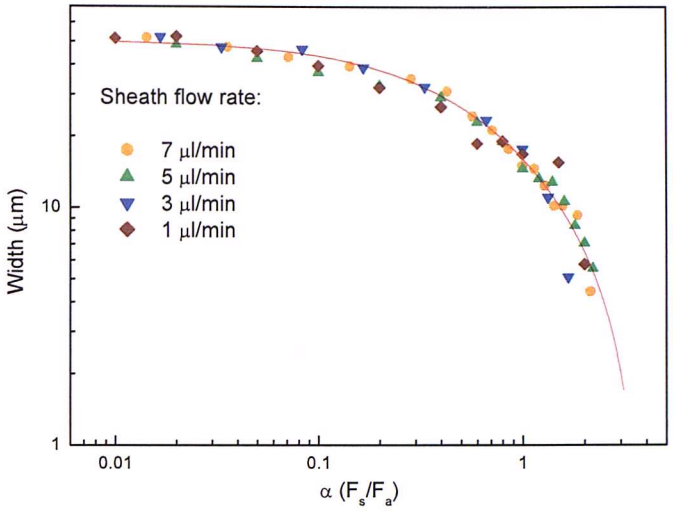


Figure 4.7 Variations of focussing width as a function of α for a variety of sheath and analyte flow rates within a 60 µm wide microfluidic channel. The red curve is a least squares fit governed by Equation 4.3.

4.2.5.2 Theoretical limits of the focussing width

The solid red line in ***Figure 4.7*** is a least-squares fit to a functional form described by Knight et al. [16] The ratio of the inlet current to the outlet current in the circuit is proportional to the ratio of the inlet fluid flux to the outlet flux in the mixer. Together with the assumption of a rectangular focussing cross section, this yields an expression for the focussing width (ω_f), i.e.,

$$\omega_f = \omega_c \beta \frac{1 + 2\sigma - 2\sigma\alpha}{1 + 2\sigma\gamma\alpha} \qquad \text{(Equation 4.3)}$$

ω_c is defined as the channel width, β is a system constant, σ and γ are constants calculated from the flow conditions in a rectangular channel.

An example of theoretical focussing widths versus α for a variety of channel dimensions using ***Equation 4.3*** is shown in ***Figure 4.8***. It is interesting to note that focussing widths below 10 nm are theoretically possible (green curve in ***Figure 4.8***) for a given set of channel dimensions. Although the potential for achieving such high focussing efficiencies is highly attractive for improving molecular detection efficiencies in SMD, diffusion of molecules out of the analyte stream will potentially result in an actual decrease in the overall detection efficiency. A series of simulations in the following sections will address this potential problem.

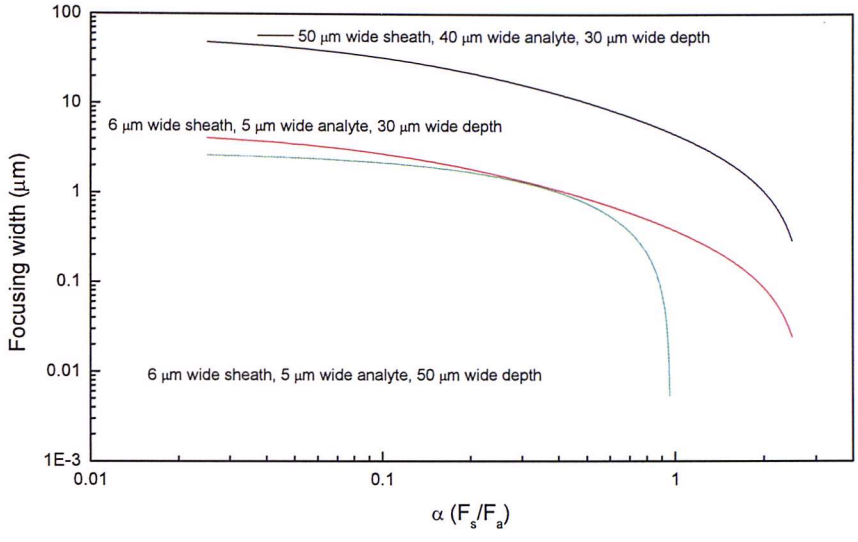


Figure 4.8 Simulation of focussing width versus α for a variety of channel dimensions.

4.3 Hydrodynamic focussing simulations

4.3.1 Analyte diffusion in focussed sample streams

4.3.1.1 Analyte diffusion

Understanding analyte flow characteristics within microchannels is highly critical in determining improvements in overall molecular detection efficiencies within a focussed sample stream. Calculating the residence time of a molecule within a focussed analyte stream becomes quite complex; this is due to the residence time of a molecule being dependant on its spatial location. The spatial location of molecules within the stream changes over time due to Brownian motion. Diffusion occurring orthogonal to the direction of flow (i.e. across the width dimension of the microfluidic channel) directly results in a decrease in the residence time of the molecules within the focussed analyte stream.

4.3.1.2 Diffusion within microchannels

Because Reynolds numbers in typical microfluidic channels are significantly below 2000, laminar flow is observed with no convective mixing of fluids. Consequently, the only means by which analyte molecules can move transverse to the direction of flow is by diffusion. The distance travelled by a molecule via diffusive motion is governed by the Einstein Equation.

This Equation simply states that the root mean square distance travelled (W_{rms}) by a molecule in a time interval, t is proportional to the diffusion coefficient (***Equation 4.4***).

$$W_{rms} = \sqrt{2Dt} \qquad \text{(Equation 4.4)}$$

where D is the molecular diffusion coefficient (cm^2/s). The diffusion coefficient (***Equation 4.5***) scales roughly with the inverse of the size of the molecule (the hydrodynamic radius) and also depends to some extent on the shape of the molecule and the surroundings. Therefore, small molecules have large diffusion coefficients and will move a larger average distance per unit time than large molecules having a smaller diffusion coefficient.

$$D = \frac{kT}{6\pi\upsilon r} \qquad \text{(Equation 4.5)}$$

T is the temperature in Kelvin, k is the Boltzman constant, r is the hydrodynamic radius (m) of the molecule and υ is the solvent viscosity (kg/m/s). In the following Monte-Carlo simulations, the molecular radius will be varied to investigate the percentage of molecules escaping from a focussed analyte stream prior to detection. As the detection probe volume is approximately 1 μm in radius, sheath and analyte flow conditions that ensures minimal diffusion across the sheath and analyte boundaries must be met.

4.3.1.3 Simulation overview

Several assumptions had to be made to simplify the workings of the simulations used. Firstly, the microfluidic channel was assumed to have a rectangular cross section. This assumption was needed to ensure that the linear velocity (v_y) of the analyte stream within the microfluidic channel could be defined by ***Equation 4.6.***

$$v_y = \frac{F}{wd} \qquad \text{(Equation 4.6)}$$

F is defined as the volumetric flow rate (m^3/s), w and d are the channel width and depth respectively (m). Secondly, it is assumed that negligible particle loss is observed prior to complete focussing. Finally, it is assumed that once the analyte stream is completely focussed, the flow rate is a summation of both the sheath and analyte flow velocities. Hence, the linear flow rate remains uniform down the length of the channel.

Although the source code for the simulation will be given in the Appendix 2.5, the principles behind the algorithm are as follows. The time to go down the complete length of the channel can be defined according to ***Equation 4.7.***

$$\tau = v_y l \qquad \text{(Equation 4.7)}$$

v_y is the linear velocity and l is defined to be a length relating to the length of the focussed channel. From this along with ***Equation 4.4*** one can obtain the maximum possible distance of diffusion perpendicular to the flow from the centre of the focussed stream , i.e.

$$W_{\max} = W_{rms} + \frac{f}{2} \qquad \text{(Equation 4.8)}$$

If W_{max} exceeds the channel width dimension then W_{max} is defined to be equal to the channel width. f is equivalent to the analyte focussing width. Finally the fraction of particles lost from the focussed analyte stream is defined as the ratio

$$\Gamma = \frac{W_{rms}}{W_{\max}} \qquad \text{(Equation(4.9)}$$

The simulation itself is performed by generating 200 series of randomly located particles using an incremental step size and allowing the particles to diffuse randomly in the y axis (governed by the Einstein Equation) within the confines of the microfluidic channel.

4.3.1.4 Simulation output

Figure 4.9 shows results from simulations performed within a 60 μm wide microfluidic channel. The initial focussed analyte stream width was 10 μm and the complete length of the focussing channel was 16 mm. The flow rate within the microfluidic channel was defined to be 1 μl/min. This correlated to a linear velocity of 9.26 mm/s. The particle size was varied between 1000 nm (comparable to cells such as *Escherichia coli*) down to 0.1 nm (approximate size of single molecule). Qualitatively, it can be seen that there is negligible diffusion outside of the analyte stream when particle sizes are 1000 nm and 100 nm. When the particle size is decreased down to 0.1 nm virtually complete diffusion occurs perpendicular to the linear flow direction and hence a good fraction of particles are lost from the analyte stream (70 %). Total particle loss will be investigated in section 4.3.3.

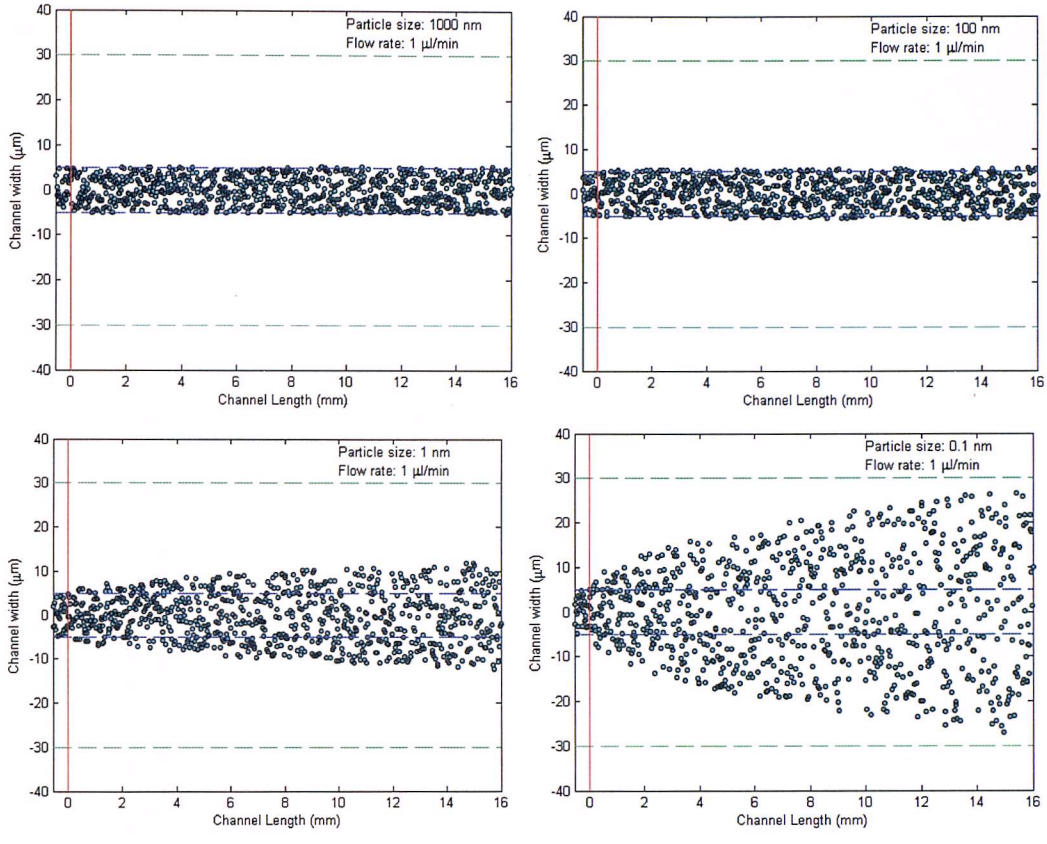


Figure 4.9 Simulation of particles diffusing from a hydrodynamically focussed analyte stream with a flow rate of 1 µl/min. The channel width and focussed stream are 60 µm and 10 µm respectively.

From *Figure 4.9* it is clear that if molecular detection efficiencies are to be improved by focussing an analyte stream, prior information pertaining to the size and dimensions of the particles or molecules is required. It is also important to appropriately choose the detection location within the channel so that particle losses due to diffusion will not be appreciable. Detection efficiencies can clearly be improved with larger particles (1000 nm and 100 nm). The detection optics can also be placed anywhere down the length of the channel when larger particles are used due to negligible particle losses. The next section will investigate how the flow rate affects the MDE.

4.3.2 Particle velocity dependence on diffusion from the analyte stream

4.3.2.1 Improving molecular detection efficiencies

The linear flow rate within the analyte stream has a direct effect on whether there will be significant loss of particles from the analyte stream. If the linear velocity is decreased overall losses can be expected to be significant. On the other hand if the linear velocity is increased,

diffusion of particles outside of the analyte stream can be greatly diminished as the overall time required for the particle to travel the length of the channel will be greatly decreased. In order to confirm this, simulations were performed which were identical to those in section 4.3.1.4 except that the flow rate was variable. The velocity was varied from 0.01 µl/min – 5 µl/min. Examples are shown for 1000 nm and 1 nm particles in ***Figure 4.10*** and ***Figure 4.11*** respectively. The channel dimensions were 60 µm wide and 16 mm long. As in section 4.3.1.4 there was negligible loss of 1000 nm particles from the focussed analyte stream at all flow rates. At an ultra-low flow rate of 0.01 µl/min (0.093 mm /s), it can be qualitatively seen that there is still a negligible fraction of particles that escape from the focussed analyte stream.

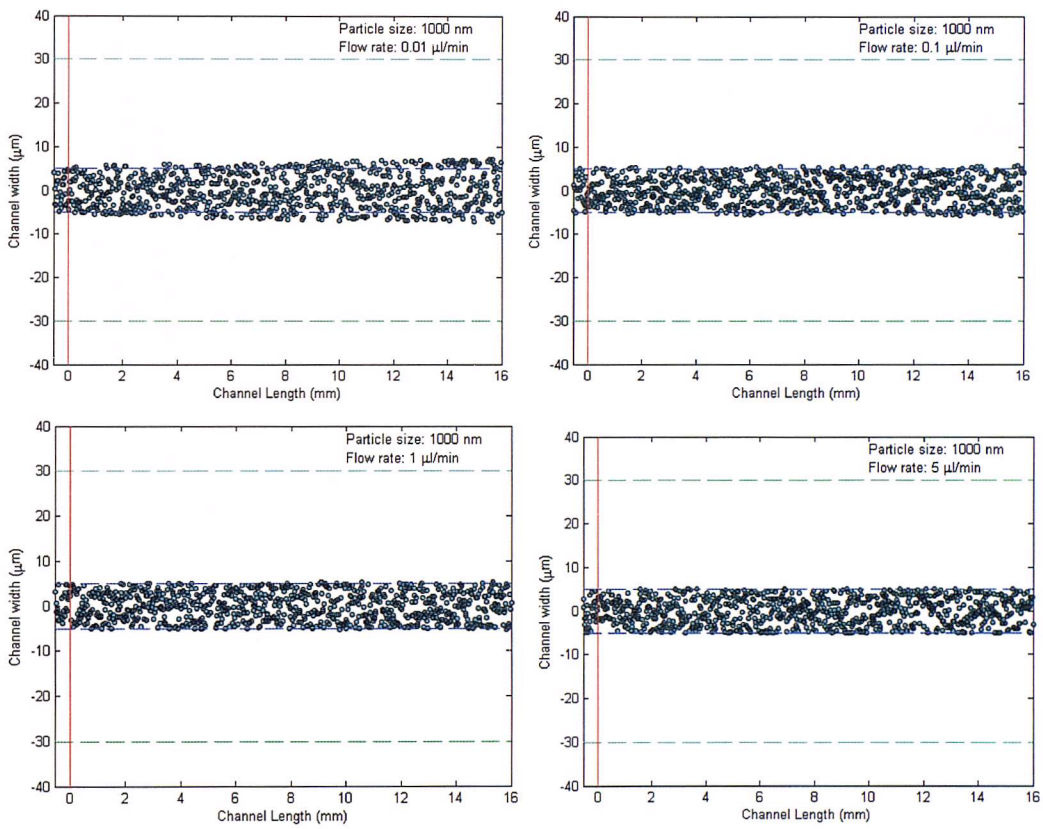


Figure 4.10 Simulation of 1000 nm particles diffusing from a hydrodynamically focussed analyte stream at flow rate ranging from 0.01 µl/min 5 µl/min. The channel width and focussed stream are 60 µm and 10 µm respectively.

As expected, ***Figure 4.11*** shows that smaller particles diffuse over much greater distances at lower flow rates. A flow rate of 0.01 µl/min essentially produces complete diffusion, or maximum possible particle loss from the focussed analyte stream. These conditions would result in absolutely no improvement in the MDE. If small particles or molecules are to be efficiently hydrodynamically focussed, high flow rates are required to ensure negligible

diffusion along the microfluidic channel. This can clearly be seen in ***Figure 4.11d*** where the flow rate was set to 5 µl/min. This volumetric flow rate correlated to a linear flow rate of 46.3 mm/s. This means that a particle requires 346 µs to travel the entire length of the microfluidic channel. Qualitatively it can also be seen that due to such a high linear velocity, less than 10 % of particles escape from the analyte stream. If the detection region can further be restricted to a point within the first 6 mm of the focussed analyte stream, losses are decreased even further and are virtually non existent. The detection efficiency can therefore be improved simply by increasing the linear flow rate. Therefore the sheath and analyte flow rates should be maximized while maintaining α_{max} below the critical ratio to maximize the MDE.

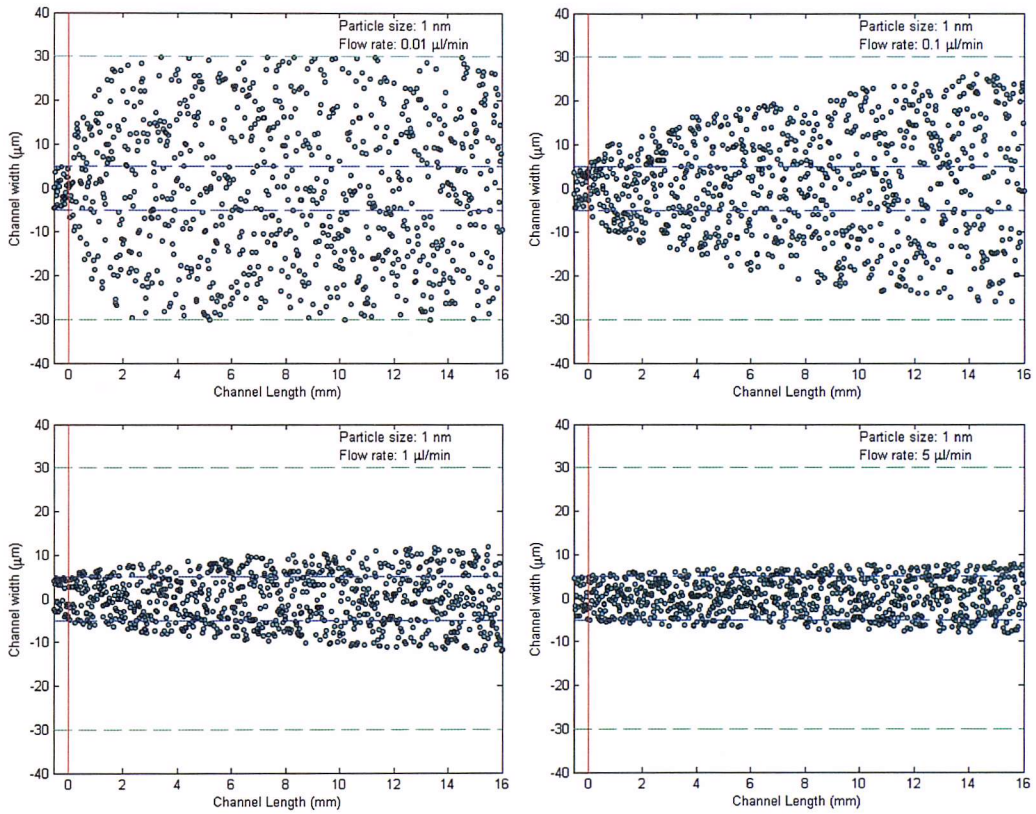


Figure 4.11 Simulation of 1 nm particles diffusing from a hydrodynamically focussed analyte stream at flow rates ranging from 0.01 µl/min 5 µl/min. The channel width and focussed stream are 60 µm and 10 µm respectively.

4.3.2.2 Rapid mixing

Although the strict purpose of the simulations undertaken was to design a method to improve the MDE, decreasing the MDE can potentially have several significant advantages for other applications such as rapid mixing of an analyte and sheath stream within a microfluidic

channel.[17-21] Mix times can be on the order of microseconds under appropriate conditions. For example Knight et al. determined that mix times below 10 μs are easily attained and reproducible. Knight et al. could not resolve $\alpha > 1.26$ due to optical limitations, yielding an effective dead time in this experiment of approximately 5 μs. This is to be compared to a typical dead time of 80 μs or more in turbulent mixers.

Unfortunately it is not possible with a 3 inlet, 1 outlet chip (used in current studies) to obtain both rapid mixing and improvements in MDEs with small molecules. A far more sophisticated chip would be required.

4.3.3 Quantitative determination of escaped particles from the analyte stream

The previous section dealt with a qualitative analysis of the simulations and how particle size and flow rate affects the distribution of particles within the microfluidic channel. In this section a more quantitative discussion will be presented on particle loss from focussed analyte streams under various flow rates and for various particle sizes. ***Figure 4.12a*** shows the percent of particles lost from the analyte stream as a function of the channel length. The focussing width remained constant at 10 μm within a 60 μm wide microfluidic channel. The particle radius in this case was 0.1 nm and the flow rate was varied between 0.01 μl/min – 5 μl/min. The horizontal dashed arrow defines the maximum possible percentage of particle loss (i.e. the point at which all particles are evenly distributed within the microfluidic channel). This can also be considered to be the point at which complete mixing occurs. At a length of 0.1 mm down the analyte stream 77 % of particles originating in the focussed stream escaped into the sheath stream at a flow rate of 0.01 μl/min. This compares to only 14 % at a flow rate of 5 μl/min. When the particle size is increased to 1000 nm (***Figure 4.12b***) less than 4 % of all particles diffuse out of the analyte stream for all the flow rates in question. No more than 30 % of all particles diffuse out of the analyte stream by the exit point in the microfluidic channel.

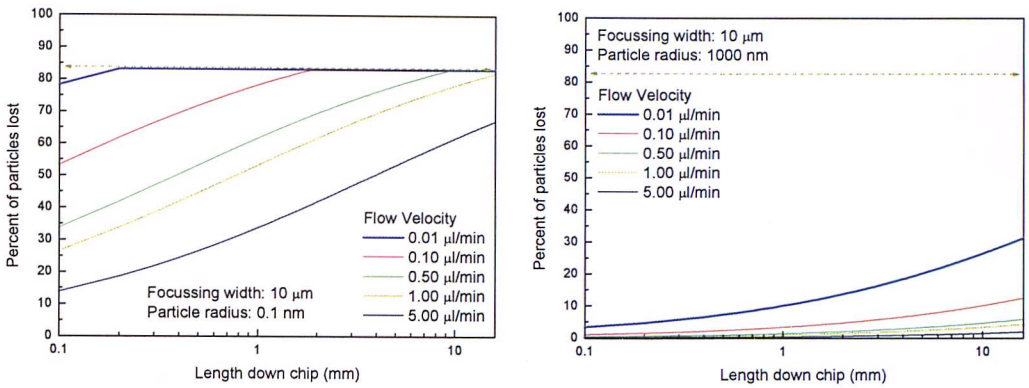


Figure 4.12 (left) Percent of particles lost from the analyte stream as a function of the channel length for a particle radius of 0.1 nm and focussing width of 10 µm. **(right)** Same as left with a particle radius of 1000 nm.

The fraction of particles lost from the focussed analyte stream is crucial in determining improvements in MDE. As the fraction of particles diffusing out of the analyte stream is most easily observed for smaller particles, ***Figure 4.13*** shows the fraction of lost particles when the particle radius is 10 nm and the flow rate is 1 µl/min. The fraction is defined as the percentage of particles lost divided by the percentage point at which all particles will be evenly distributed within the microfluidic channel. It should be noted that it is not experimentally possible to obtain focussing widths of 100 nm and 1000 nm within a 60 µm wide microfluidic channel. However, this is shown in ***Figure 4.13*** for the sake of monitoring the trend at ultra - low focussing widths. As expected, the fraction of particles lost from highly focussed streams is greatly increased as the focussing width is decreased. Under typical conditions for improving the MDE, less than 10 % of particles will diffuse out of the analyte stream for a particle size of 10 nm. If the particles sizes are increased to 100 nm – 1000 nm there are negligible loses due to diffusion out of the analyte stream.

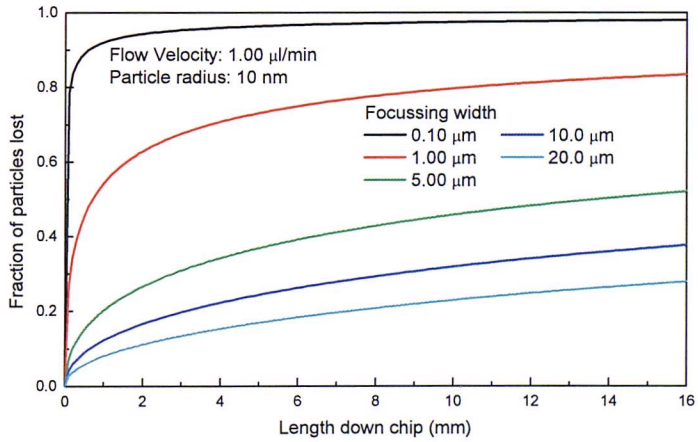


Figure 4.13 Fraction of particles lost for a particle radius of 10 nm at a flow rate of 1 µl/min at various analyte focussing widths.

The majority of work in this thesis involves the use of larger biological molecules and cells as well as fluorescent particles; therefore, improving MDEs can theoretically be achieved using this approach. If smaller molecules were investigated greater care and control over the hydrodynamic focussing experiment would be required to ensure improvements in MDE.

4.3.4 Monte Carlo simulation of a single particle focussing experiment.

The initial motivation behind writing a Monte-Carlo simulation for a single particle experiments within a hydrodynamically focussed microchannel was to qualitatively compare trends in statistics (e.g. autocorrelation function and Poisson distribution) between experimental and theoretical results. This section is simply meant to be an overview of the simulation performed and comparisons between experimental results will be discussed in section 4.4. The simulation itself can be broken down into 4 processes: First, the chip boundary conditions must be appropriately assigned. This can easily be performed by defining the initial x,y,z coordinates of the channel by a series of vectors xv,yv,zv. These three vectors contain information relating to the chip depth, width and length. In Matlab the '*ndgrid*' function can than be used to define a complete grid space over the initial vectors. If the step size in the vector is small enough the grid will in turn be a good approximation to a microfluidic channel. Second, the particle paths must be modelled and confined to within the chip boundary. Although the source code is available in Appendix 2.5, an abridged version containing the fundamental routine of the simulation for a particulate trajectory is shown below. It should be noted that the code does not include chip boundary conditions.

Generation of random numbers

*x = xi*randn(1,N) + v*dt;*	*xi is the time step*
*y = xi*randn(1,N);*	*v is the linear velocity*
*z = xi*randn(1,N);*	*randn returns a vector of N random number*

Intial trajectory position

x(1) =x';	*x' is a user defined starting position*
y(1)= y';	
z(1) = z';	

Calculation of the trajectory

x = cumsum(x);	*returns the cumulative sum*
y = cumsum(y);	
z = cumsum(z);	

Third, the random walk must be repeated several hundred to thousands of times to obtain sufficient single molecule trajectories for reliable statistics. Finally, the molecular trajectories and the grid defining the chip coordinates must be convolved with the excitation function, defined by the following Equation:

$$I = \frac{2P}{\pi w^2} e^{\frac{-2(x^2+y^2)}{w^2}}$$

$$w = w_0 \left(1 + \left(\frac{\lambda z}{\pi w_0^2}\right)^2\right)^{0.5} \qquad \text{(Equation 4.10)}$$

Here, w_0 denotes the $1/e^2$ beam waist radius, λ the laser excitation wavelength, and P is the total laser power (in photons per time unit). An example of the simulation output for the hydrodynamic focussing of an analyte stream containing 1000 nm particles is shown in ***Figure 4.14***. The focussing widths were 2 µm (top left) and 20 µm (bottom left) within a 60 µm wide channel. The laser excitation wavelength was 488 nm and the initial sheath and analyte flow rate was 1 µl/min.

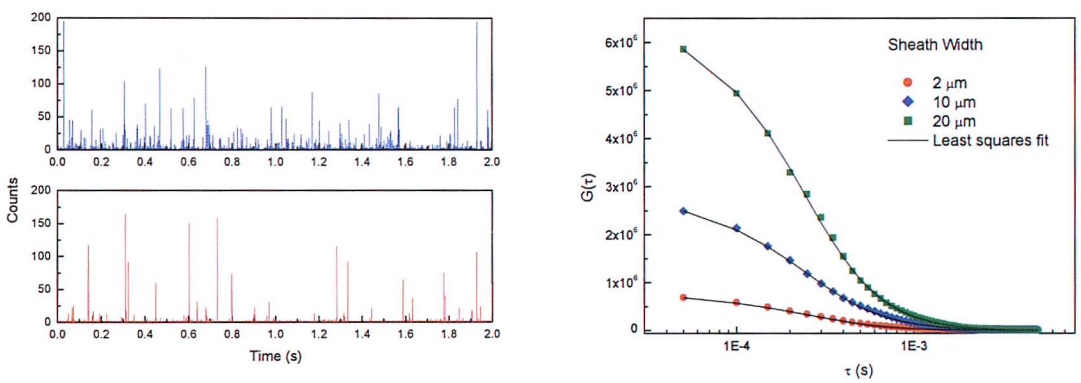


Figure 4.14 (Left) Simulation of two SMD experiments within hydrodynamically focussed microchannels for 1000 nm particles. The analyte flow rate was 1 µl/min. The sheath flow rate was (top left) 2 µl/min and (bottom left) 0.5 µl/min. The channel width was 60 µm. **(Right)** Simulated autocorrelation curves produced from the photon burst scans for 1000 nm fluorescent particles.

4.4 Experimental results

4.4.1 Sheath and analyte flow dependence on molecular detection efficiency

4.4.1.1 Single particle counting: Variation in sheath flow rate

Figure 4.15 shows single particle burst scans for 0.93 μm fluorescent microspheres in a hydrodynamically focussed channel with an analyte flow rate of 1000 nl/min. The main channel width was 60 μm wide. The sheath flow rates in *Figures 4.15 a-c* are 40 nl/min, 600 nl/min and 1500 nl/min respectively. These sheath velocities directly correlate to focussed analyte streams of 55 μm, 15 μm and 3 μm respectively. The dwell times for all experiments were set to 50 μs so that single particle bursts could be completely resolved as well as ensuring single particle occupancy within the confocal probe volume. If the sheath velocities were increased further, lower dwell times would be required for single bursts to be completely resolved. Although the acquisition system offered dwell times as low as 100 ns, using such low dwell times would result in a dramatic decrease in burst count rates. Qualitatively, several conclusions can be made. First, the number of single particle bursts detected increases as the sheath flow rate increases. The syringe pumps are operating under a constant pressure environment; therefore, regardless of sheath flow rate if the analyte flow rate remains constant, the same number of fluorescent particles are delivered into the microfluidic channel per unit time. Therefore an increase in observed bursts is directly related to the focussed analyte stream being reduced in width (the focussed width to probe volume ratio decreases as the sheath flow is increased). Second, as the sheath flow rate is increased, the individual bursts appear to be visually more uniform in width. This is primarily caused by the range of possible particle trajectories through the probe volume decreasing, and was observed due to the diffraction-limited focus of the laser beam (1 μm radius) being approximately 3 times smaller than the focussed width at higher sheath flow rates and 60 times smaller at lower sheath flow rates.

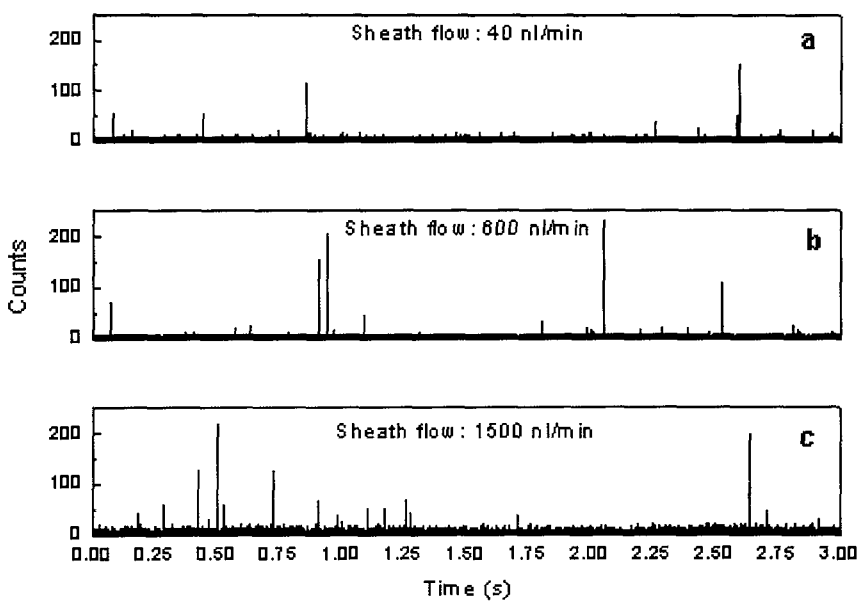


Figure 4.15 Single photon burst scans of 0.93 μm fluorescent particles in a focussed analyte stream at various sheath flow rates. The analyte flow rate is constant at 1000 nl/min.

Figure 4.16 shows the total number of particle bursts detected in a 16 second time interval as a function of sheath velocity. This is shown for analyte flow rates of 1 µl/min and 3 µl/min. In both cases the total number of peaks detected and hence the MDE improves by a factor of 10 at the highest sheath flow rates. The focussing width was negligible at the lowest sheath rates and it can therefore be assumed that the total number of peaks detected in these cases is comparable to an unfocussed system. A clear benefit of using a hydrodynamically focussed stream is in the lower sample consumption that is needed per unit time over a conventionally unfocussed approach. This is turn allows for lower sample consumptions, quicker measurement times, and general improvements in the signal relative to background. Improving the molecular detection efficiency is crucial when using sub-femtoliter probe volumes as the majority of molecules or particles surrounding the probe volume normally go undetected. At an analyte flow rate of 1 µl/min, there were approximately 1300 particles passing through the microfluidic channel within a 16 s interval. 127 of these particles could be detected at a sheath flow rate of 1500 µl/min. This results in 1 in 10 particles being detected within the probe volume. In an un-sheathed environment the total fraction of particles detected decreases to 1 %. Other techniques have been proposed to isolate analyte trajectories to improve molecular detection efficiencies in single molecule studies.[13] The dominant trend is to use channels with dimensions ranging from 0.5 – 1 µm. Although this approach ensures the majority of molecules will be detected, severe problems arise through channels blocking due to impurities and analyte crystallization. Hence, ultra-small channels are not viable for long term or high-throughput measurements. A stable focussed flow in microchannels can offer the same degree of improvement in molecular detection efficiencies without the added complexity of nanochannel fabrication and the potential for blocking.

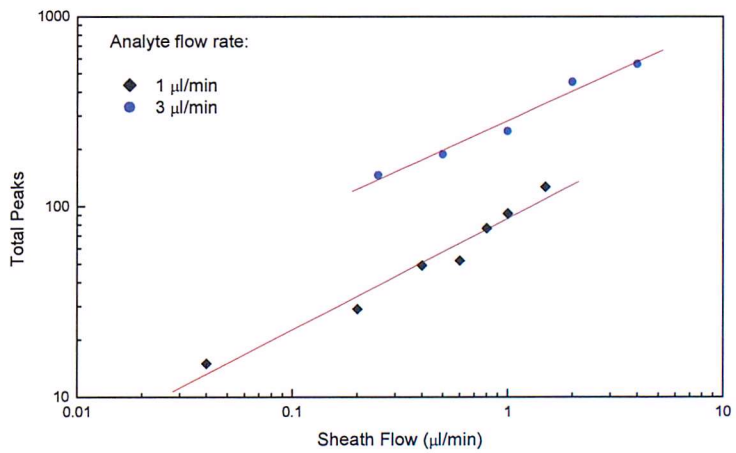


Figure 4.16 Total particles detected from single photon burst scans of 0.93 µm fluorescent particles in a focussed analyte stream at various sheath flow rates. The analyte flow rates were 1 µl/min and 3 µl/min respectively.

Changing the focussing channel width dimension to 20 μm and 100 μm respectively did not result in a significant change in the MDE. This is a result of the minimum focussing width being similar in all the chip designs used. By using an appropriate chip design it would theoretically be possible to focus the analyte stream down to 1 μm and hence one would expect to see a further increase in the MDE. It should be stressed at this point that decreasing the channel dimensions below 20 μm is not viable as the 0.93 μm particles would start aggregating along surface defects of the channel wall and eventually result in blocking of the chip. In order to maintain high detection efficiencies it is more important to optimize the chip design in order to guarantee appropriate α values for a specific system while keeping channel widths as large as possible.

4.4.1.2 Single particle counting: Variation in analyte flow rate

In the previous section, variation in the sheath flow was discussed with respect to a constant analyte flow rate. In the following section the reverse scenario will be discussed (i.e. constant sheath flow rate). Extracting information regarding the MDE from such a scenario is more complex as 2 parameters will be effected simultaneously. Firstly, the focussed analyte width and secondly, the number of particles entering the focussed analyte stream per unit time. In the previous section, the former parameter remained constant; hence a direct comparison between sheath flow rate and the MDE could be easily obtained. ***Figure 4.17*** shows an example of a photon burst scan obtained at a constant sheath flow rate of 1 μl/min and analyte flow rates of 1 and 3 μl/min respectively. At the higher analyte flow rates a total of 249 bursts were detected within a 16 s scan time. At the lower analyte flow rates a total of 92 bursts were detected within the same time frame. The difference in the total bursts is not directly related to a change in the MDE but rather due to a change in the overall throughput of the particles passing through the channel per unit time.

Increasing the analyte flow rates by a factor of 3 should also increase the total detected particles by a factor of 3 per unit time in an unfocussed analyte stream. Under focussing conditions the reverse occurs, if an analyte flow rate of 3 μl/min is used; fewer particles will be detected when compared to lower analyte flow rates. A decrease in the analyte flow rate should improve the overall detection efficiency as the analyte stream is more tightly focussed. Thus, a larger proportion of the molecular trajectories will pass through the detection probe volume. Increasing the analyte flow rate will result in a less tightly focussed stream and hence a larger degree of molecular trajectories will arise resulting in a poorer MDE.

There is clearly a heavy compromise between throughput and improvement in the MDE. Ideally improvement in both could be achieved; however, high speed acquisition electronics would be required along with highly fluorescent samples. This would not be a problem when looking at large fluorescent particles or fluorescently expressed cells. If smaller molecules with overall lower fluorescent intensities are to be studied, improvements in the MDEs will most likely have to take precedence over high throughput.

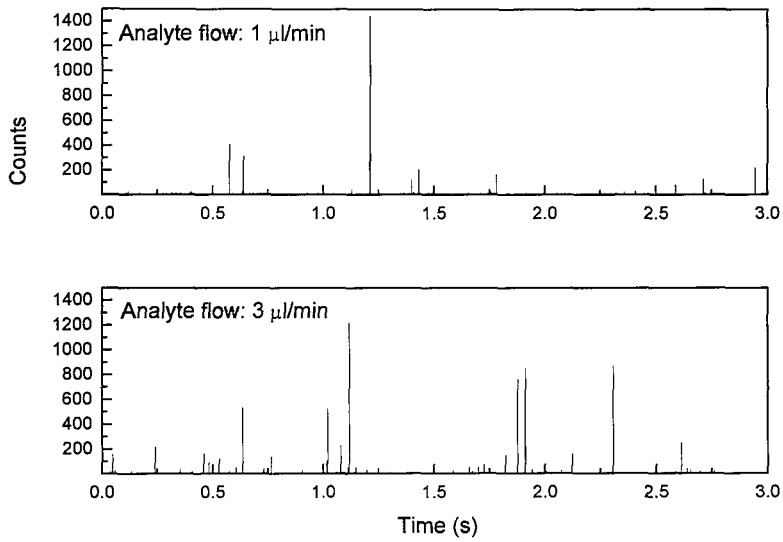


Figure 4.17 Single photon burst scans of 0.93 µm fluorescent particles in a focussed analyte stream taken at a sheath flow rate of 1 µl/min and an analyte flow rate of 1 and 3 µl/min within a 60 µm wide microfluidic channels.

4.4.1.3 Poisson recurrence time analysis

An ideal method to statistically monitor improvements in molecular detection efficiencies is by calculating recurrence times. This approach relies on the use of Poisson statistics as burst interval distributions are predicted to follow a Poissonian model, in which peak separation frequencies adopt an exponential form. The model simply states that longer intervals between photon bursts are less probable than shorter intervals at a given sheath flow rate. It is also expected that τ_R should be inversely proportional to concentration, sheath flow rate (at a constant analyte flow) or solvent viscosity in a range of systems. ***Figure 4.18a*** shows frequency $N(\Delta t)$ versus time plots for two analyte flow rates as a function of sheath flow rate. In both cases the recurrence times between events decreases by a factor of 10 in an unfocussed stream when compared to that of a highly focussed stream. An unfocussed stream is defined to be at α_{min} were essentially no focussing occurs. Within the 60 µm wide microchannel and an analyte flow rate of 1 µl/min, α_{min} occurred at approximately 20 nl/min. The results clearly support the data shown in ***Figure 4.16*** where a 10 fold improvement in the molecular detection efficiency is achievable.

In ***Figure 4.18b*** a simpler analysis is shown. In this case the total fluorescent bursts counted at a given flow rate and time interval are taken into account. From this, the average interburst time (AIT) can be deduced. ***Figure 4.18b*** shows plots of average interburst time versus sheath flow rate. The average interburst time is essentially the ratio of the complete scan time over the total number of peaks detected. It is analogous to calculating the recurrence time since information pertaining to event frequency is obtained. As with the recurrence times the AIT decreases by a factor of 10 between the highest and lowest sheath flows for both initial analyte flow rates of 1 μl/min and 3 μl/min respectively. Similar trends were observed for higher and lower analyte flow rates as well as when using different chip geometries. This is expected as it is the α parameter which governs the stability of the focussed flow: the burst frequency will be directly related to the degree of focussing and the combined linear velocity governed by α.

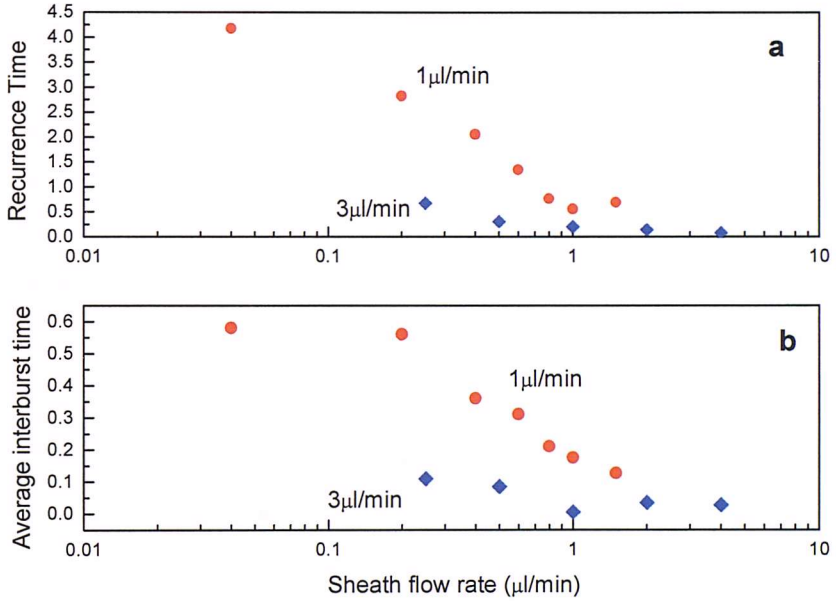


Figure 4.18 **(a)** Recurrence times from single photon burst scans of 0.93 μm fluorescent particles in a focussed analyte stream at various sheath flow rates. The anlyte flow rates were 1 μl/min and 3 μl/min respectively. **(b)** Average interburst time.

The recurrence times themselves decay approximately exponentially with respect to the sheath flow rate. At a sheath and analyte flow rate of 1.5 and 3 μl/min respectively, the photon burst recurrence time was 600 ms. The recurrence time could easily be decreased to maximize throughput through the microfluidic channel by increasing the particle concentration. This was not performed as the strict purpose of these experiments was to characterize MDEs and not maximize throughput. Diffusion of the particles from the analyte stream was virtually non existent as the particles had a radius of 0.93 μm and hence diffusion effects will be minimal.

4.4.1.4 Autocorrelation analysis

Autocorrelation analysis is a useful tool for characterizing and distinguishing between photon bursts. Although this will be discussed in detail in another chapter, autocorrelation curves in this section will be used to confirm stable sheath flow within the microchip as well as to compare the curves qualitatively with data obtained from SMD Monte-Carlo simulations. Several autocorrelation curves for single particle burst scans are shown in ***Figure 4.19a*** for analyte flow rates of 1 µl/min (top) and 3 µl/min respectively (bottom). Two observations can be made. First, when comparing both sets of curves the full width half maxima in the top set are much larger than in the bottom. This is directly a result of the total linear velocity (analyte + sheath) being much larger when the flow rate is increased. Secondly, as the sheath flow rate is increased the curve maximum decreases. This is directly due to a decrease in the photon burst width as well as a decrease in the burst area as the linear velocity is increased. Note that the autocorrelation curves are normalized for the total number of peaks. A simulated autocorrelation curve is shown in ***Figure 4.19b*** for a hydrodynamically focussed analyte stream (2 µm and 10 µm) within a 60 µm microchannel containing 1 µm fluorescent spheres. The details of how the simulation was performed are described in section 4.3.4. The linear flow rate down the length of the 60 µm wide channel was defined to be 18 mm/s and 23 mm/s which is comparable to the sheath and analyte flow rates in the top of ***Figure 4.19a***. The analyte focussed stream width is also comparable between the experimental and simulated data.

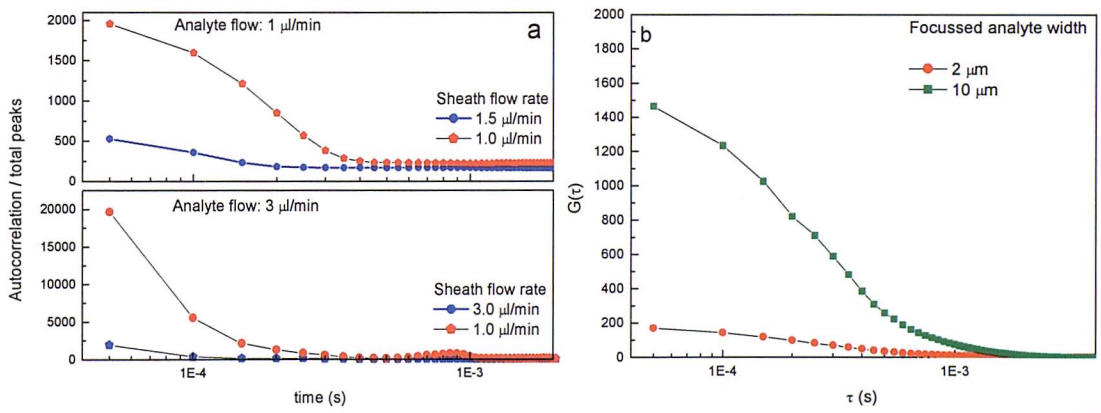


Figure 4.19 **(a)** Autocorrelation curves for single photon burst scans of 0.93 µm fluorescent particles in a focussed analyte stream at various sheath and analyte flow rates. **(b)** Simulated autocorrelation curve for a hydrodynamically focussed analyte stream with linear velocities of 18 and 23 mm/s within a 60 µm wide microfluidic channel.

Qualitatively, the experimental and theoretical data are quite similar. As focussing is increased by increasing the sheath flow rate the autocorrelation curve maxima in both

instances decrease by approximately the same order of magnitude. Unfortunately the simulations cannot be compared quantitatively with the experimental data as parameters such as the collection efficiency function (CEF) from the oil immersion objective, loses due to optics and detection, as well as quantum yields and absorption cross sections of the fluorophores must be taken into account. Such a simulation would be possible; however, calculating the CEF would be complex to perform and would not introduce additional valuable information.

4.4.2 Photon burst characteristics

4.4.2.1 Burst width analysis

One of the potential downsides of hydrodynamically focussing analyte flows is in the linear velocity of the focussed stream increasing. This means that the particles burst width will also decrease as the sheath flow is increased. This effect can be seen in ***Figure 4.20***. For example, at an analyte flow rate of 1 µl/min and a sheath flow rate of 40 nl/min, the average burst width was measured to be 670 µs. When a sheath flow rate of 1.5 µl/min is used the average burst width decreases further to 260 µs. At an analyte flow rate of 3 µl/min and a sheath flow rate of 250 nl/min, the average burst width was 249 µs. When a sheath flow rate of 4 µl/min was used the average burst width decreases to 109 µs. It is therefore crucial to have relatively low dwell times (between 10 µs – 50 µs) to obtain statistically reliable information regarding the burst distributions. The downside can be overcome by simply using a multichannel scalar capable of sub-millisecond dwell times.

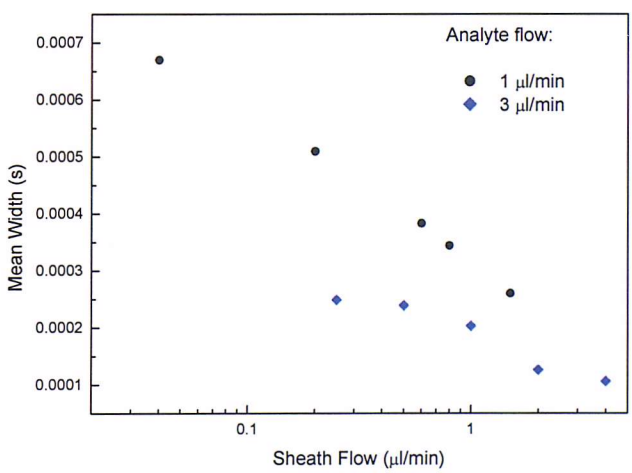


Figure 4.20 Mean particle burst width in a hydrodynamically focussed analyte stream. The analyte flow rate was 1 µl/min (black) and 3 µl/min (blue) respectively. The sheath flow rate was varied between 0.04 – 4 µl/min.

A clear benefit in minimizing the focussed analyte stream width is seen in ***Figure 4.21***. A histogram of burst width distributions is plotted for an analyte flow rate of 1 µl/min and sheath flow rates of 0.2 µl/min, 0.6 µl/min, and 1.5 µl/min. The average peak width in each case was 510 µs, 383 µs, and 260 µs respectively. As the sheath flow rate is increased the average burst width decreases, the overall distribution sharpens, and the full width half maximum in the distributions decrease. This can be better determined from the decrease in relative standard deviations in the burst widths. They are 48 %, 41%, and 35 % respectively. Another benefit of focussing can be seen in the width distribution maxima. At a sheath flow rate of 1.5 µl/min the distribution maximum occurs at 250 µs with a count rate of 27 counts. This is much higher than in ***Figure 4.21*** where a distribution maximum was recorded at 350 µs with only 6 counts.

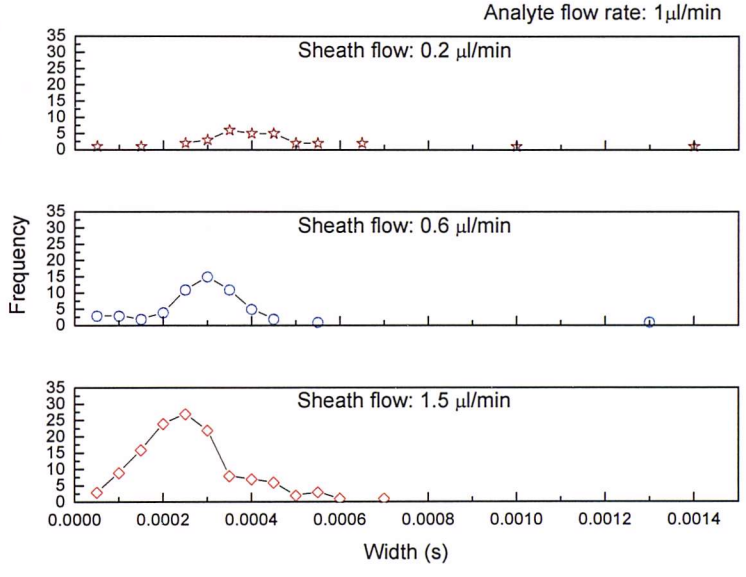


Figure 4.21 Burst width histogram for hydrodynamically focussed steams at a constant analyte flow rate of 1 µl/min. The sheath flow rates are 0.2, 0.6, 1.5 µl/min which correspond to focussed analyte stream widths of 32, 19, 12 µm respectively.

4.4.2.2 Burst height analysis

Perhaps an initially surprising effect was the increase in average burst height as the sheath flow rate was increased. This trend is shown in ***Figure 4.22*** for analyte flow rates of 1 µl/min and 3 µl/min respectively and sheath flow rates ranging from 0.04 – 4 µl/min. On average the burst height increased by approximately 50 % when comparing a focussed and unfocussed analyte stream. It is possible that in highly focussed streams a larger proportion of the fluorophores embedded in the 0.93 µm beads can be more efficiently collected and detected:

this would directly result in an increase in the overall mean height. This effect becomes more significant when the focussing width approaches the width of the detection probe volume radius.

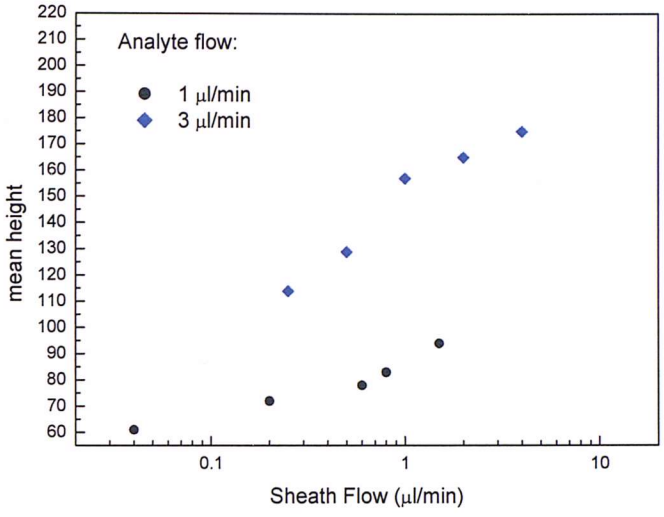


Figure 4.22 Mean burst height as a function of sheath flow rate. The analyte flow rates remained constant and were 1 µl/min (black) and 3 µl/min (blue).

4.5 Summary

In the first part of this chapter a detailed theoretical analysis was performed to monitor the possibility of particles or molecules diffusing out of the focussed stream and into the sheath flow. This was performed to determine if particles lost to diffusion will decrease the MDE within a hydrodynamically focussed channel. Large particles (greater than 100 nm) tend to diffuse slowly and hence few particles escaping from the analyte stream. Smaller particles and molecules will diffuse out of the analyte stream; however, the degree of diffusion was determined to be highly dependant on the initial sheath flow and analyte flow rates. The use of high flow rates (> 1 µl/min) results in negligible losses within a 16 mm long microfluidic channel.

In the second half of this chapter, experimental results were presented confirming the possibility of increasing MDEs within a microfluidic environment whilst maintaining sub femtoliter probe volumes. In the work presented, 0.93 µm fluorescent microspheres were used. An increase in the MDE of one order of magnitude was possible. This correlates to 1 in every 10 molecules being detected. This is much higher than typical reports in the literature for single particle and molecule spectroscopy using femtoliter probe volumes.

4.6 References

(1) Edel, J. B.; Hill, E. K.; de Mello, A. J. *Analyst* **2001**, *126*, 1953-1957.

(2) Ferris, M. M.; Rowlen, K. L. *Review of Scientific Instruments* **2002**, *73*, 2404-2410.

(3) Kunst, B. H.; Schots, A.; Visser, A. *Analytical Chemistry* **2002**, *74*, 5350-5357.

(4) van Orden, A.; Keller, R. A.; Ambrose, W. P. *Analytical Chemistry* **2000**, *72*, 37-41.

(5) Yan, X.; Grace, W. K.; Yoshida, T. M.; Habbersett, R. C.; Velappan, N.; Jett, J. H.; Keller, R. A.; Marrone, B. L. *Analytical Chemistry* **1999**, *71*, 5470-5480.

(6) Demas, J. N.; Wu, M.; Goodwin, P. M.; Affleck, R. L.; Keller, R. A. *Applied Spectroscopy* **1998**, *52*, 755-762.

(7) Nguyen, D. C.; Keller, R. A.; Jett, J. H.; Martin, J. C. *Analytical Chemistry* **1987**, *59*, 2158-2161.

(8) Goodwin, P. M.; Affleck, R. L.; Ambrose, W. P.; Demas, J. N.; Jett, J. H.; Martin, J. C.; Reha-Krantz, L. J.; Semin, D. J.; Schecker, J. A.; Wu, M.; Keller, R. A. *Exp. Tech. Phys.* **1995**, *41*, 279-294.

(9) Ramsey, J. M., *http://www.ornl.gov/sci/lsm/dnahyb.html*, **2003**.

(10) Soper, S. A.; Keller, R. A.; Shera, E. B.; Martin, J. C.; Jett, J. H. *Abstracts of Papers of the American Chemical Society* **1990**, *200*, 135 - ANYL.

(11) Affleck, R. L.; Ambrose, W. P.; Demas, J. N.; Goodwin, P. M.; Schecker, J. A.; Wu, J. M.; Keller, R. A. *Analytical Chemistry* **1996**, *68*, 2270-2276.

(12) Eggeling, C.; Widengren, J.; Rigler, R.; Seidel, C. A. M. *Analytical Chemistry* **1998**, *70*, 2651-2659.

(13) Foquet, M.; Korlach, J.; Zipfel, W.; Webb, W. W.; Craighead, H. G. *Analytical Chemistry* **2002**, *74*, 1415-1422.

(14) Papautsky, I.; Brazzle, J.; Ameel, T.; Frazier, A. B. *Sensors and Actuators A* **1999**, *73*, 101-108.

(15) Bessoth, F. G.; de Mello, A. J.; Manz, A. *Analytical Communications* **1999**, *36*, 213-215.

(16) Knight, J. B.; Vishwanath, A.; Brody, J. P.; Austin, R. H. *Physical Review Letters* **1998**, *80*, 3863-3866.

(17) Konermann, L.; Simmons, D. A. *Mass Spectrometry Reviews* **2003**, *22*, 1-26.

(18) Plenert, M. L.; Shear, J. B. *Proceedings of the National Academy of Sciences of the United States of America* **2003**, *100*, 3853-3857.

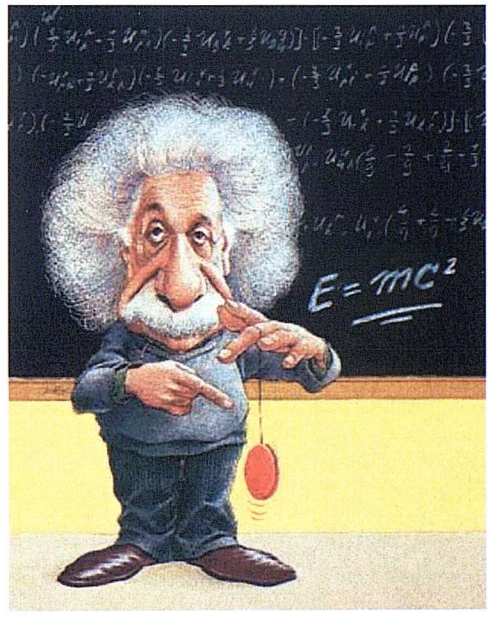
(19) Kunimatsu, H.; Inoue, Y.; Hirata, Y. *Kagaku Kogaku Ronbunshu* **2002**, *28*, 753-758.

(20) Pabit, S. A.; Hagen, S. J. *Biophysical Journal* **2002**, *83*, 2872-2878.

(21) Eaton, W. A.; Munoz, V.; Hagen, S. J.; Jas, G. S.; Lapidus, L. J.; Henry, E. R.; Hofrichter, J. *Annual Review of Biophysics and Biomolecular Structure* **2000**, *29*, 327-359.

- 5 -

Photon burst scan width and area histograms are used as a method to discriminate between different cell and particle populations within a microfluidic channel. Single particle and cell fluorescence lifetimes are also used to distinguish between different populations. Finally, a new statistical analysis method based on inter-photon burst arrival times is introduced and used to distinguish between different cell types under various flow velocity conditions.



Cells & particles: Population and distribution analysis

5.1 Introduction

The work described in this chapter aims at creating a simple analysis technique for sizing and discrimination of cells in freely flowing solutions. The approach utilizes standard confocal fluorescence microscopy incorporating femtoliter detection volumes. In order to assess the feasibility of this concept initial studies are performed using nanometer-sized fluorescent particles flowing though microchannels. This is subsequently followed by measurement and analysis of photon burst characteristics originating from single Escherichia coli cells expressed with different types of fluorescent proteins.

The motivation behind the current studies is to improve and simplify existing methods used for single cell sizing, counting and recognition. Conventional fluorescence activated cell sorters are highly efficient; however, they are mechanically complex, require heavy maintenance and most importantly are costly. The fluorescence-activated cell sorter (FACS) is the most common commercially available cell sorting technique available. To prepare a cell mixture for sorting in a FACS, cells in a suspension are reacted with a fluorescent dye such as fluorescein. Once labeled, the cells are forced to flow rapidly and single-file through the FACS. Up to 30,000 cells per second can be discriminated by a computer in modern FACS sorters. Replacing conventional approaches with microfluidic systems can result not only in higher throughput but also reduced costs and sample requirements. Inexpensive devices that rapidly sort live cells, particles, and even single molecules would greatly facilitate screening of combinatorial chemistry libraries or cell populations. Moreover, such devices would have wide applications in clinical medicine and basic biological and materials research.

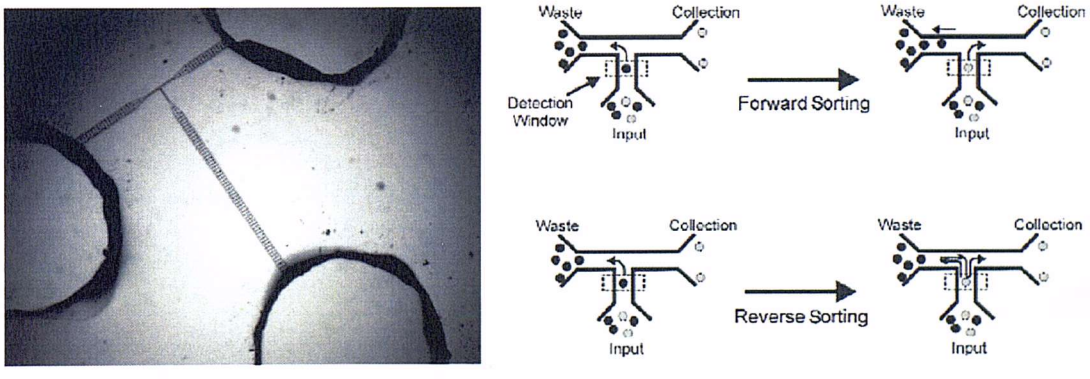


Figure 5.1 (Left) A microfluidic cell sorter fabricated by Fu et al.[1] The device shown has channels that are 100 μm wide at the wells, narrowing to 3 μm at the sorting junction. The channel depth is 4 μm, and the wells are 2 mm in diameter. (Right) A sketch of the algorithms that they used for the forward sorting and reverse sorting of cells is shown in the schematic of the T-shaped junction.

Recently there has been interest in integrating cell chemistry with microfluidics.[1-8] Several examples are as follows. Altendorf and colleagues used a microfluidic laminate-based structure incorporating hydrodynamic focusing and flow channels with dimensions less than 1 mm to analyze blood cell samples.[5] Optically transparent windows integral to the flow channels were used to intercept the sample streams with a tightly focused diode laser probe beam. The size and structure of the blood cells passing through the laser beam determined the intensity and directional distribution of the scattered light generated. Yager et al. demonstrated the ability to use single microfabricated silicon flow channels for the differential counting of granulocytes, lymphocytes, monocytes, red blood cells (RBCs), and platelets, in blood samples by means of laser light scattering. The microfabricated flow cytometer described used hydrodynamic focusing within the microstructure.[2] More recently Wheeler et al. developed a novel microfluidic device constructed from PDMS using multilayer soft lithography technology for the analysis of single cells. The microfluidic network enables the passive and gentle separation of a single cell from the bulk cell suspension.[9] In addition, Fu et al. have designed a disposal microfabricated fluorescence cell sorter (μFACS) for sorting various biological entities. An example of their microfluidic device as well as a schematic of the analysis approach is shown in ***Figure 5.1***. Their μFACS chips resulted in overall higher sensitivity, no cross contamination, and lower overall running costs over more conventional techniques. They were able to successfully separate a diversity of fluorescently emitting micron sized particles and also E. coli cells expressed with green fluorescent protein from non fluorescing-cells. Unfortunately this approach is limited to the separation of two different types of cells due to the configuration of their confocal spectrometer. The studies described herein, improve on the approach by utilizing the photon burst characteristics of single cells as a means of distinguishing between them.

5.2 Experimental

5.2.1 Materials

5.2.1.1 Fluorescent microspheres

Fluorescent microbeads (yellow/green Fluospheres ®, Molecular Probes; Europe B.V.) having a mean diameter of 0.93 μm, 0.5 μm, and 0.2 μm respectively were used for all experiments. Absorption and emission maxima for the beads were 505 nm and 515 nm

respectively. Excitation and emission spectra are shown in ***Figure 5.2***. Stock solutions were diluted by a factor which was dependant on the particle size and will be described in section 5.3.1.1. All dilutions were performed in TBE (tris-borate-EDTA) buffer. The TBE buffer was prepared at 0.1x concentration (8.9 mM each of tris(methoxy)aminomethane and boric acid, 0.2 mM in ethylenediaminetretraacetic acid; prepared from a solid TBE mixture; Fluka Chemicals) in 18 MΩ deionized water. Samples were sonicated for 10 minutes immediately before use to ensure that beads did not coagulate. Typical working solutions had a concentration of $2.3x10^7$ beads/cm^3 (effective concentration of 10 ng/L).

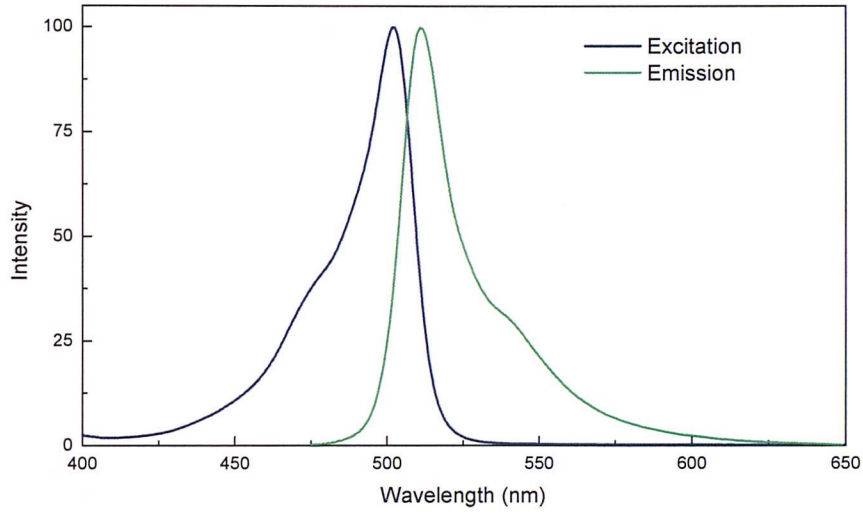


Figure 5.2 Normalized excitation (dark blue) and emission (green) spectra of 930 nm fluorescent microspheres. The absorption and emission maxima were 505 nm and 515 nm respectively and the spectra were acquired on a fluorescence/transmission spectrometer. λ_{ex} = 475 nm, λ_{em} = 550 nm.

5.2.1.2 Escherichia coli cells

Escherichia coli (E. coli) cells expressed with fluorescent proteins were synthesized by Pedro Lahoud in the Department of Biochemistry at Imperial College London according to the following procedure. E. Coli, strain BL21 Gold (DE3), containing the plasmid encoding fluorescent proteins (living colours™ range, Clontech, NJ) were grown to mid log phase in LB-media (1% Tryptone, 1% NaCl, 0.5% Bacto yeast extract) containing 100 μg/ml ampicillin at 37°C with shaking. Isopropyl b-D-1-thiogalactopyranoside (IPTG) was added to a final concentration of 1 mM and the temperature lowered to 30°C. Cells were allowed to express the protein for approximately 16 hours before harvesting by centrifugation at 3220 *g*, 10 minutes at 4°C. Cells were washed twice in 0.1 culture volumes re-suspension buffer (0.14 M NaCl, 1mM EDTA, 15% glycerol, 10 mM Na_2HPO_4/NaH_2PO_4 pH 7.2) before re-suspension to a final concentration of approximately 10^8 cells/ml. Cyano, green, and yellow

fluorescent protein were imbedded in all cells. The emission spectra of the expressed cells are shown in ***Figure 5.3***.

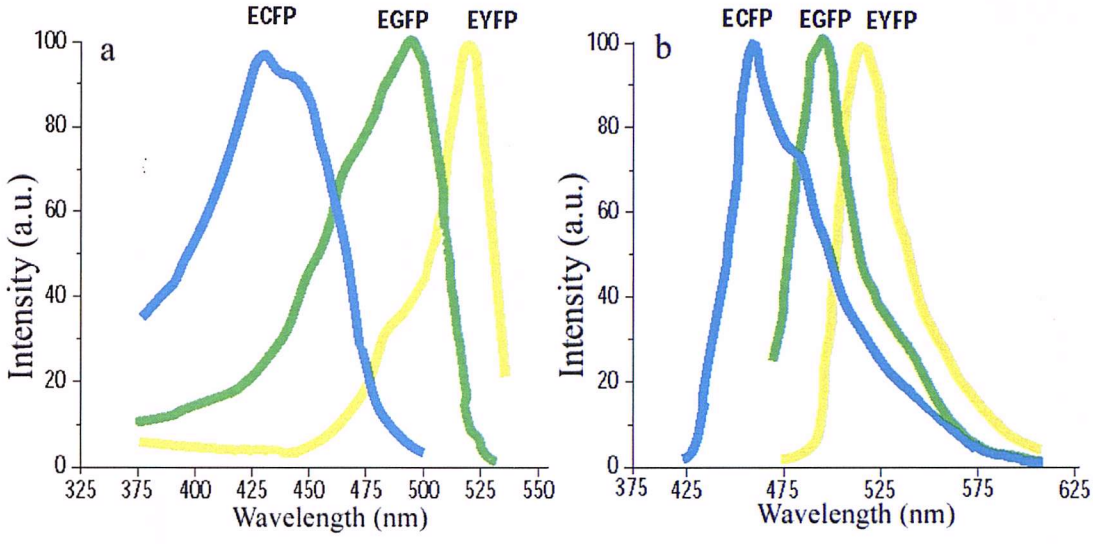


Figure 5.3 Excitation and emission spectra of cyano, green and yellow fluorescent protein. The emission maxima are 470, 504, and 525 nm for the cyano, green and yellow proteins respectively. Taken from Clontech (living colours range).[10]

Green fluorescent protein (GFP) of the jellyfish Aequorea victoria has become one of the most important fluorescent labels in biology.[11] It was originally discovered by Shimomura et al. as a companion protein to aequorin.[12] The fluorescing chromophore in GFP is 4-(p-hydroybenzylidene)-imidazolidin-5-one which is formed in a post-translational cyclization reaction from the three amino acids Serine65, tYrosine66, Glycine67. The structure of GFP and the chromophore can be seen in ***Figure 5.4***. GFP has become increasingly popular in biological experiments due to the fact that it is an auto-fluorescing protein[13-18] and does not need external species or labels to emit. It is for this reason that many different variants and mutants are synthesized from the wild-type, so that fluorescence emission can be tuned. Examples of these analogues include cyano fluorescent protein (CFP) which emits at higher energy and yellow fluorescent protein (YFP) which emits at lower energy with respect to GFP.

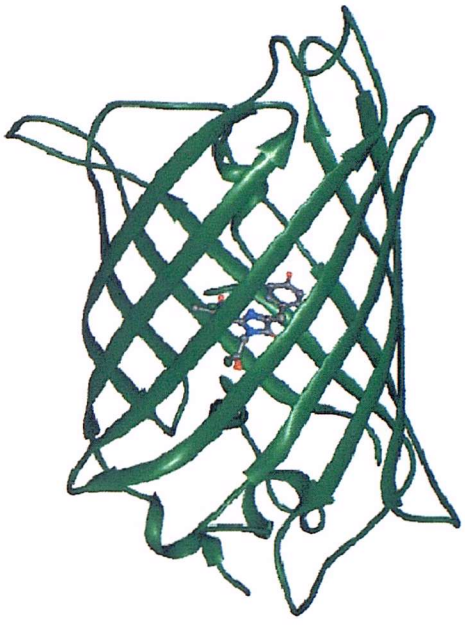


Figure 5.4 Three dimensional bucket structure of GFP showing the 11 β-strands forming a hollow cylinder through which is threaded a helix containing the chromophore. The drawing was obtained from the RCSB protein data bank.[19]

5.2.2 Microfluidics

A simple straight channel microchip design consisting of 1 input and 1 output was used for all experiments described in this chapter. The channel widths were either 150 μm or 60 μm wide, the channel length was 20 mm and the channel depth was 30 μm. Coverplates were bonded to etched substrates by heating in a high temperature oven to a maximum of 610 °C. The top plate was then optically polished down to a thickness of ~150 μm. Optical polishing of the coverplate was performed to reduce the substrate thickness below the working distance of the microscope objective (~150 μm). Access holes were then etched into the fluidic network via deep reactive ion etching using an 8M solution of sodium hydroxide and an applied voltage of 120V. It should be noted that the access holes in the chips used in this chapter are electrochemically drilled and not mechanically drilled as described in the experimental chapter. The drilling was performed electrochemically as the substrates were bonded and polished without access holes. An electrode diameter of 400 μm was used for drilling; hence access holes had a diameter of ~ 500 μm. These holes could easily be adjusted to any desired size simply by changing the electrode diameter.

5.2.3 Experimental approach

Fluorescent particles or cells were hydrodynamically delivered through the microfluidic channel network using a syringe pump at volumetric flow rates ranging from 0.1 – 10 μl/min.

The detection region was approximately 10 mm downstream of the inlet hole. Measurement of fluorescence lifetimes and all experiments involving GFP, CFP, and YFP were performed using a 438 nm pulsed diode laser with a repetition rate of 10 Mhz. The laser beam intensity was attenuated with a polarization filter as required to obtain an average count rate of 20, 000 cps. It was important for a constant excitation wavelength to be used for the analysis of different fluorescent proteins. This allows direct comparison of photon burst characteristics in subsequent analysis. The 438 laser line was chosen as both CFP and GFP have a reasonable absorption cross section at that wavelength. This laser line was also used to excite YFP as the onset of absorption occurs at approximately 430 nm (albeit with a much reduced absorption cross section).

The 488 nm argon ion line was used for the initial studies involving the characterization of the burst characteristics of the fluorescent particles (section 5.3).

5.3 Burst characterization

5.3.1 Photon burst height (PBH) analysis

5.3.1.1 PBH analysis for 200, 500, 930 nm fluorescent particles

Figure 5.5 shows burst scans for 930 nm, 500 nm, and 40 nm fluospheres at flow rates of 100, 1000, and 5000 nl/min respectively. The individual bursts vary significantly in height. This is primarily caused by the range of possible particle trajectories through the probe volume and due to the fact that the diffraction-limited focus of the laser beam is on the order of 100 times smaller than the channel width of the microfluidic device. In order to ensure single particle occupancy within the probe volume, the fluorescent particle had to be diluted from the stock solutions (2 % solids). A maximum particle concentration of 1.8×10^4 spheres/ml assures a maximum of 1 particle in the femtoliter probe volume at any instant. The initial particle concentration in a 2 % solution for 930 nm, 500 nm, 200 nm spheres are 2.7×10^{10}, 2.9×10^{11}, and 3.9×10^{12} particles/ml. With this in mind minimum dilutions of 2000 x, 16, 000 x, and 250 000 x had to be performed for the 930 nm, 500 nm, 200 nm particles to maintain single particle occupancy.

Several interesting points can be extracted from ***Figure 5.5***. Firstly, as the flow velocity decreases the photon burst frequency also decreases. Secondly, decreasing the particle size

does not result in a linear decrease in the photon burst height. Theoretically, average signal intensities of 100, 15, 0.8 (a.u.) would be expected for particle sizes of 930, 500, and 200 nm (***Table 5.1***), assuming photodegredation effects are constant or negligible. This can be attributed to the larger particles (930 nm) being approximately the same size, if not larger than the actual excitation probe volume. This results in a large proportion of all the fluorophores embedded within the microsphere not being excited. This effect would be expected to become less significant as the particle size is decreased or if the excitation probe volume is increased. This effect actually works as an advantage in the current experiments, since the photon burst characteristics of the particles are distinguishable based on the non-linearity of total fluorescence intensities.

Microsphere Diameter (μm)	*Fluorescein equivalents*	*Signal intensity (a.u.)*
0.930	1.3×10^7	100
0.50	2.0×10^6	15
0.20	1.1×10^5	0.8

Table 5.1 Fluorescein equivalents in fluorescent particles

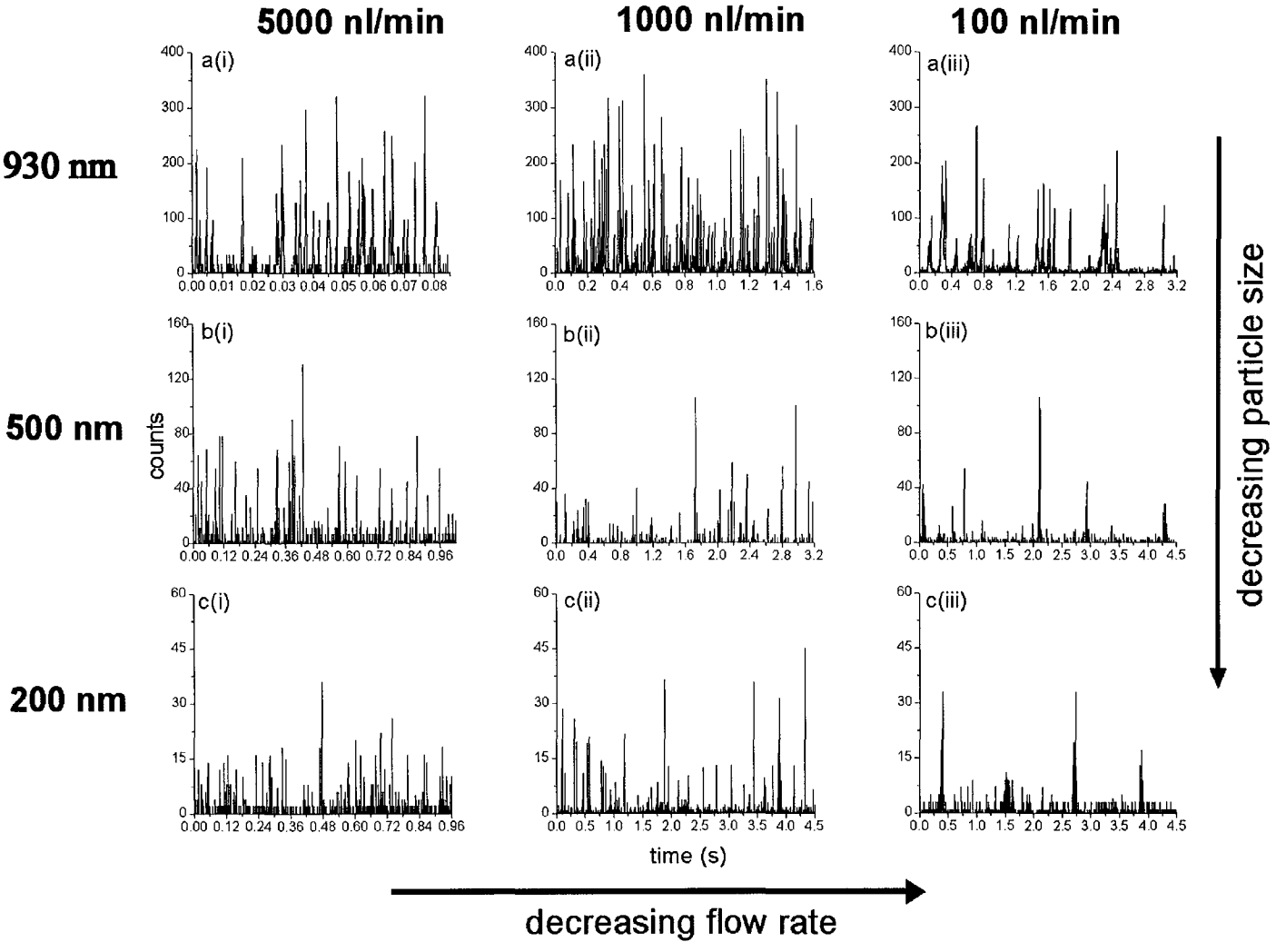


Figure 5.5 Representative single-particle fluorescence burst scans for 930 nm, 500 nm, and 200 nm Fluospheres at flow rates of 100, 1000, and 5000 nl/min respectively.

Figure 5.6 shows the peak height relative standard deviation at various flow rates for 0.93 μm, 0.5 μm, and 0.2 μm fluospheres in a microfluidic channel. At a flow rate of 5 μL/min a relative standard deviation of 30 % was obtained for the 0.93 μm spheres. This was determined from an accumulation of over 200 bursts. As the particle size decreases there is a general trend for the RSD to increase. The relative standard error in this case was 2.1 %. This value could be further decreased by increasing the number of bursts sampled. On average it took approximately 600 μs of recorded data to obtain 200 bursts at a flow rate of 5 μL/min. Calculations at higher flow rates were not performed as acquisition dwell times below 25 μs are necessary to obtain sufficient data points per burst.

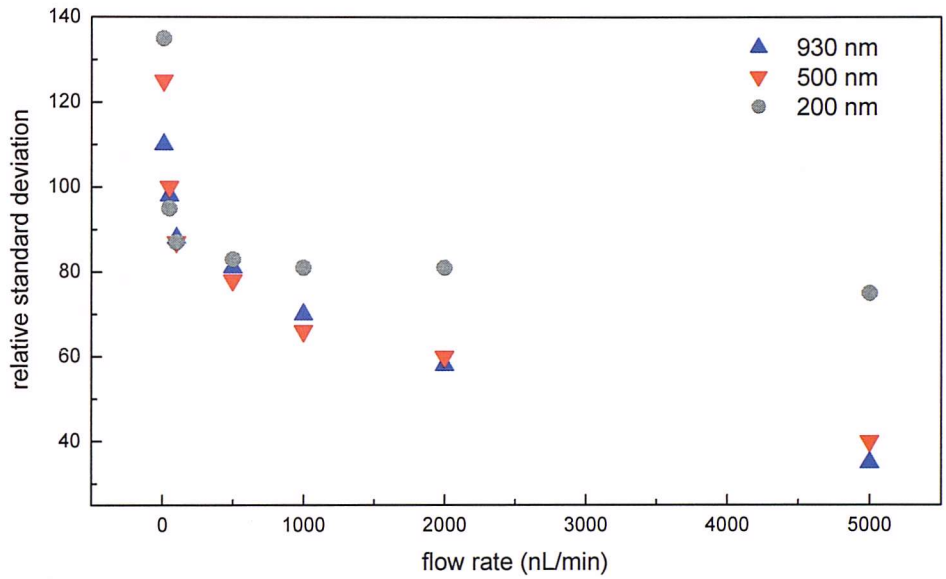


Figure 5.6 Peak height relative standard deviation with respect to flow velocity.

5.3.1.2 PBH analysis for E. coli expressed with GFP, CFP, YFP

The volume of an E. coli cell can be approximated by a cuboid with dimensions of 1 μm x 1 μm x 2 μm long. This results in an internal volume of 2 μm^3 or 2 x 10^{-15} l. The approximate amount of GFP protein in 1 ml of expressed cells was 15 μg assuming a yield of 15 mg/l. As a result the final concentration of GFP in solution is approximately 15 μg/ml. This directly results in the concentration of GFP within a cell being approximately 7500 μg/ml as E. coli occupies approximately 0.2 % of the solution. GFP is a protein consisting of 238 amino acids and has an approximate molecular weight of 27 or 30 kDa. From the above information it can be deduced that there are a maximum of 500 fluorescent proteins per single cell.

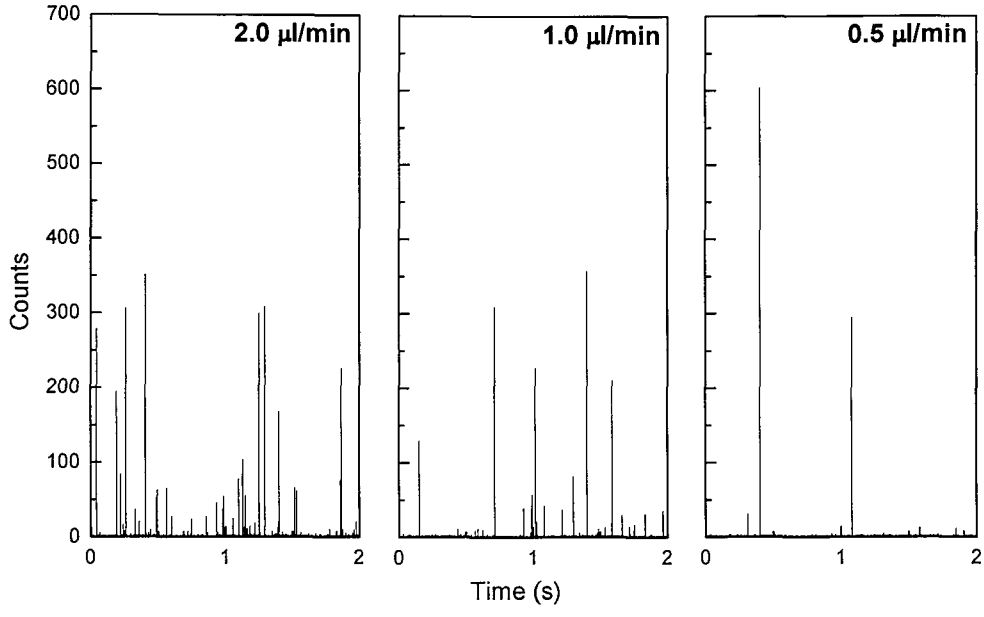


Figure 5.7 Single-cell fluorescence burst scans for E. coli expressed with GFP. The volumetric flow rates (left – right) are 2, 1, 0.5 µl/min respectively.

As with the fluospheres, it was essential that the probability of multiple cell occupancy within the detection probe is negligible. The cell concentration was determined to be approximately 10^8 cells/ml. Hence, a dilution factor of 200 was used for these studies. This ensured that there were 0.0005 cells per femtoliter. Examples of photon burst scans for E. coli expressed with GFP are shown in ***Figure 5.7***. The dwell time in all cases was set to 100 µs. The background threshold was set to 1.2 counts/bin and the average photon burst intensity for a flow rate of 2 µl/min was 192 counts. The relative standard deviation in burst height was 63 %. At this flow velocity 982 burst were counted within a 65 s period. Therefore, the burst frequency was 15.2 Hz. This can clearly be increased by at least a factor of 10, to a frequency of 152 Hz as the overall cell concentration was well below the single occupancy level. This can be achieved in two ways. First, the flow velocity could be increased appropriately. With this approach, the dwell time would have to be decreased to below 100 µs in order to resolve individual cell burst characteristics. Second, the cell concentration could be simply increased by a factor of 10.

Varying the protein type within the E. coli cells results in entirely different burst characteristics when compared to GFP (***Figure 5.8***). This is attributed to several factors which are as follows: Firstly, the absorption cross sections of each cell type are different at 438 nm. CFP and GFP have cross sections of ~6 x 10^3 $M^{-1}cm^{-1}$, ~5 x 10^3 $M^{-1}cm^{-1}$. YFP has an absorption cross section which is approximately 100 x lower. With this in mind, and assuming the cells are expressed with identical protein concentrations, the burst heights are expected to be different. A secondary effect on the burst height originates from varying fluorescence

quantum yields. The fluorescence quantum yields for CFP, GFP, and YFP are 0.4, 0.6, 0.7. For the acquisitions shown in ***Figure 5.8***, the average burst height for CFP was 127 counts with an RSD of 117 %. The dwell time in all plots was 100 μs and the flow rate was constant at 1 μl/min. For GFP expressed cells under identical conditions, an average burst contained 80 counts and the RSD was 112 %. In both cases these values were calculated from 500 bursts over a 65 s period. Burst statistics are significantly worse for YFP as a result of the low absorption cross section at 438 nm. A total of 200 bursts could be detected within a 65 s period at an identical cell concentration. The average burst height was 30 counts; however, the burst height deviation was reduced to an RSD of 85 %. This is most likely a result of bursts being hidden in the background noise and as such, could not be identified as bursts. The threshold in all 3 burst scans was 3 +/- 0.3 counts; hence the S/N in YFP was typically not larger than 10.

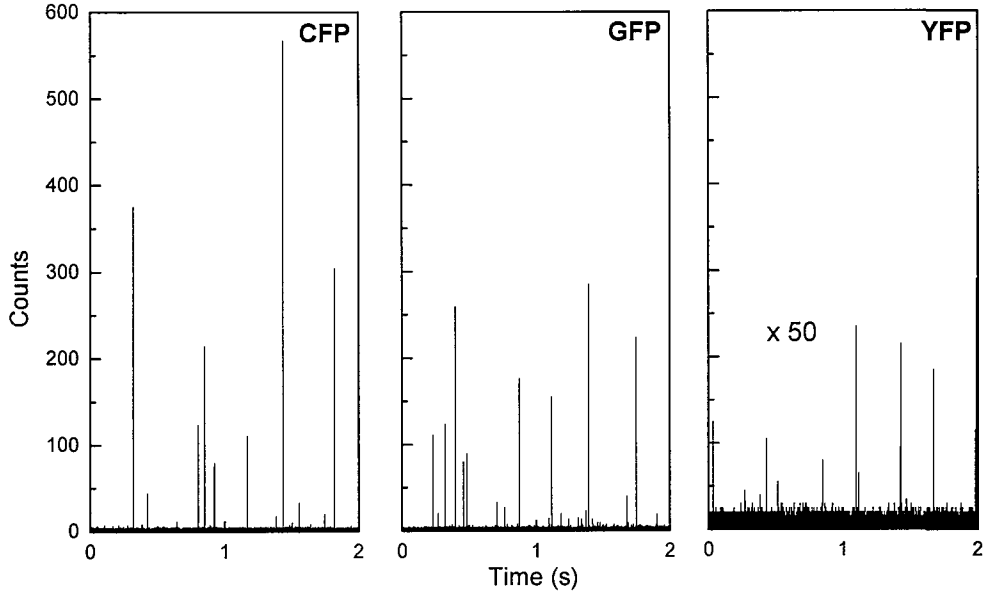


Figure 5.8 Representative single-cell fluorescence burst scans for E. coli expressed with CFP, GFP, and YFP (left – right). The volumetric flow rates in all the plots was 1.0 μl/min.

5.3.2 Photon burst width (PBW) analysis

5.3.2.1 PBW analysis for 200, 500, 930 nm fluorescent particles

Figure 5.9 shows histograms of burst width distributions of 930 nm, 500 nm, and 200 nm fluorescent particle solutions traveling at volumetric flow rates between 5 μL/min and 100 nL/min through a microfluidic channel. At high flow rates a relatively even distribution of particle widths is observed (e.g. ***Figure 5.9ai***), whereas at a much lower flow rate (e.g. ***Figure***

5.9aii) the particle width distribution becomes heavily skewed towards larger burst widths. These effects can be explained as follows: at lower flow rates, diffusion of the particles through the probe volume is the dominating factor in determining the trajectory through the probe volume hence the burst widths are expected to be predominately random. The random behavior of the particle burst widths is clearly seen in ***Figure 5.9aiii.***

For all experiments the probe volume width (defined by the diffraction limited beam waist diameter) was measured to be approximately 1 μm, hence the laser beam was a factor of ~100 times smaller than the microfluidic channel. At higher flow rates diffusion is negligible with respect to bulk flow motion and hence all particles travel through the probe volume with a predominantly constant trajectory. Thus a more even distribution of burst widths is expected. ***Figures 5.9b and 5.9c*** show similar trends for 500 nm and 200 nm fluospheres (with flow rates identical to those in ***Figure 5.9a***). As expected the overall burst heights are not only smaller, but the burst widths are also much smaller. It is interesting to note that the relative standard deviation is slightly larger when compared to the data obtained for 930 nm fluospheres. This can be attributed to a greater domination of diffusive motion for smaller particles at a higher flow rate.

Table 5.2 summarizes the average burst width (ms) for the 3 particle sizes given at 3 flow rates. It can be seen that the average burst width decreases as particle size increases. In addition the burst width (for a given particle size) is observed to decrease as volumetric flow rate is increased. At the two higher flow rates the mean burst width increases by a factor of 5 for all particles when going from a flow rate of 5 μl/min to 1 μl/min. The standard deviation in the photon burst width histograms at these flow rates was below 60 %. At lower flow rates the RSD typically increases to ~ 150 %. This trend can be most easily seen graphically in ***Figure 5.9c.***

	Flow rate:5 μl/min	***1 μl/min***	***100 nl/min***
930 nm	2.02 ms	10.5 ms	255 ms
500 nm	1.6 ms	16 ms	72 ms
200 nm	0.88 ms	5 ms	60 ms

Table 5.2 Summary of average burst width for 3 particle sizes at 3 flow rates

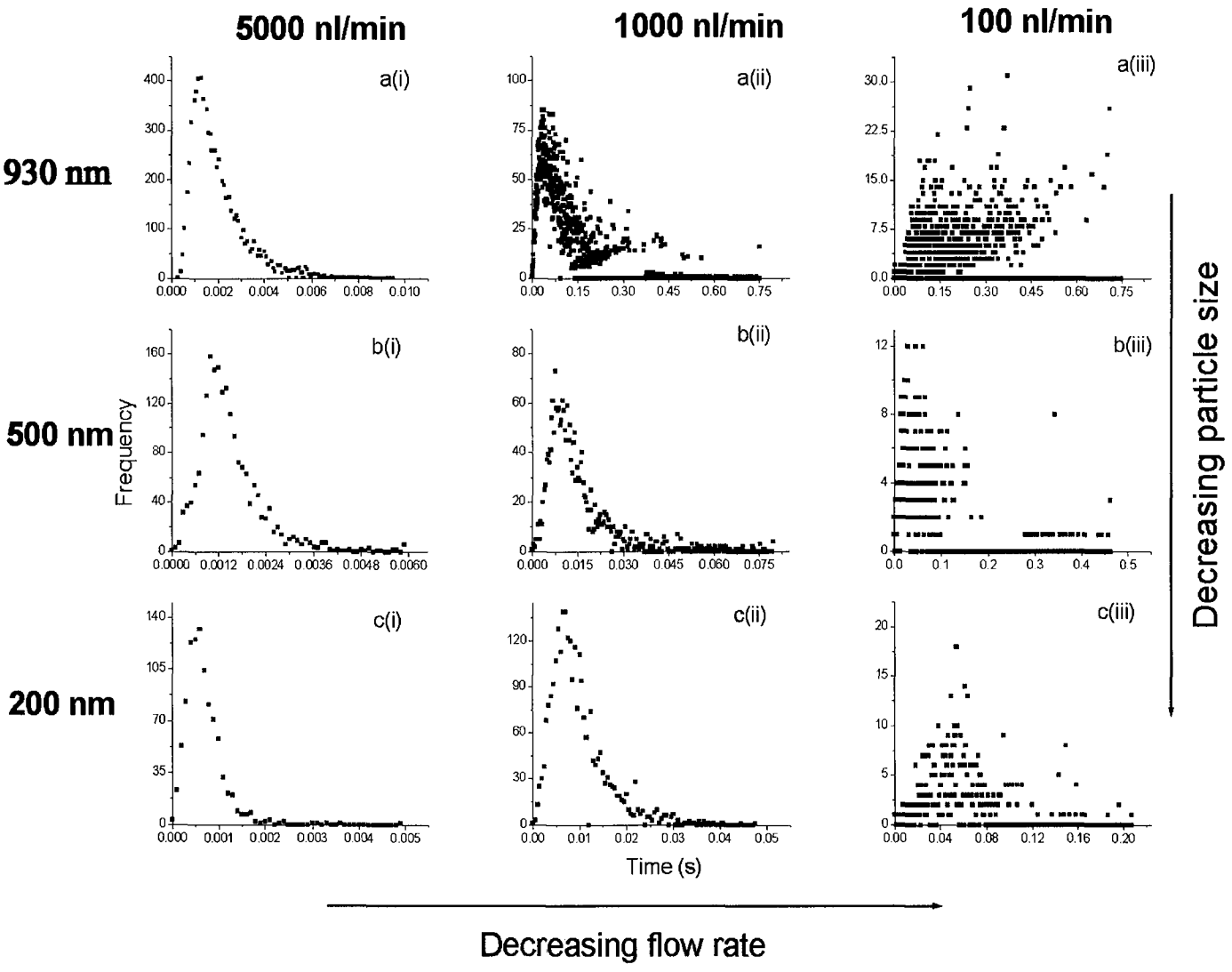


Figure 5.9 Histogram burst width distributions for 930 nm, 500 nm, and 200 nm Fluospheres at flow rates of 100, 1000, and 5000 nl/min respectively.

5.3.2.2 PBW analysis for E. coli expressed with GFP, CFP, YFP

Flow dependant burst width histograms of the E. coli cells exhibit similar trends to these of the fluorescent particles. As such this information will not be detailed. What is more important are the observed changes in burst width histogram between the various fluorescent proteins. Such histograms can be seen in ***Figure 5.10*** and are a result of an accumulation of 200 burst widths for each distribution. The flow velocity in all three cases was constant at 1 µl/min. The distributions were normalized in order to be able to offer a direct comparison between the different cells. The CFP and GFP histograms are similar due to the absorption cross sections and quantum yields being virtually identical. With this in mind the CFP and GFP photon bursts can still be distinguished strictly based on the burst widths. CFP had an average burst width of 922 µs and a RSD of 40 %. The GFP cells had a smaller average burst width of 793 µs. In this case the RSD was slightly lower at 33 %.

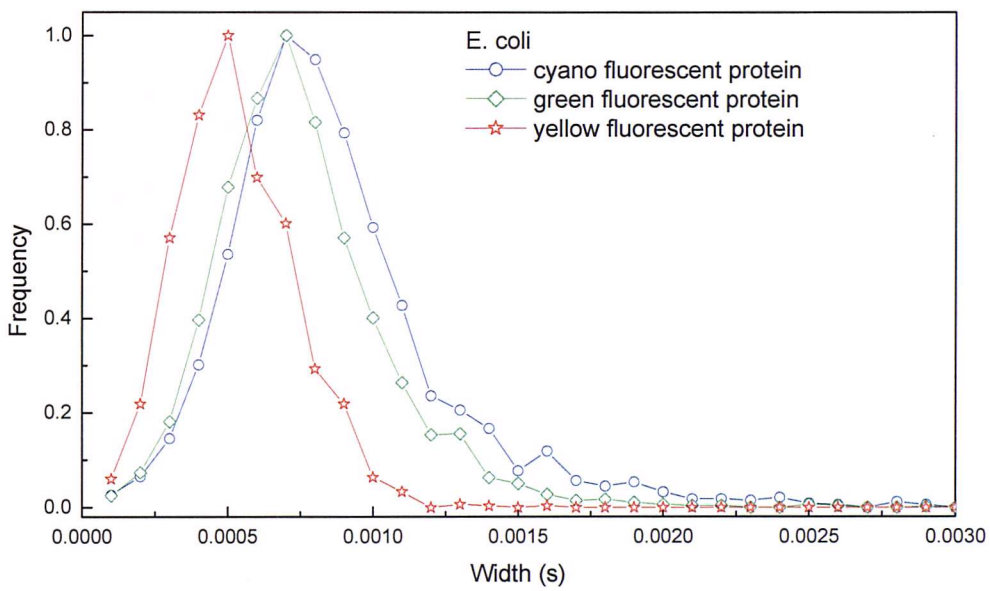


Figure 5.10 Histogram of burst width distributions for E.coli expressed with CFP, GFP, and YFP. The flow velocity was 1 µl/min for all measurements.

E.coli expressing YFP exhibit a drastically different mean burst width. The average width was 572 µs with a RSD of 31 %. The lower value is predominantly due to the lower absorption cross section at 438 nm. This in fact turns out to be a great advantage as single cells expressing YFP can be distinguished from single cells expressing GFP and CFP strictly on burst height and width characteristics. Algorithms such as those described in chapter 7 can be useful in assigning single cell types with minimum error. A clear benefit of this approach is that no separation or sorting methods are required to distinguish between cell populations. The majority of single molecule microfabricated cell sorters reported in the literature

demonstrate sorting with 2 different cell types. This is primarily due to experimental limitations. With the statistical approach described herein, there is no limitation to how many types of cells can be identified. The only requirement is for the fluorophores within the cells to generate different photon burst characteristics.

5.3.3 Photon burst area (PBA) analysis

5.3.3.1 PBA analysis for 200, 500, 930 nm fluorescent particles

Figure 5.11 shows histograms of burst area distributions of fluosphere solutions traveling at volumetric flow rates ranging between 5 μL/min and 100 nL/min. The defined peak distribution observed at high flow rates disappears quickly as the flow rate is decreased. This is observed since histograms are binned into 1 count intervals. Consequently, the distribution or standard deviation is expected to be larger than when compared to burst width data. Without binning data further, into count intervals greater 1, the particle burst area histograms on their own cannot be used to distinguish between particles of a given size and velocity.

Table 5.3 summarizes the average burst area (counts) for the 3 particle sizes at 3 flow rates. It can be seen that the average burst area decreases as particle size increases. In addition burst areas (for a given particle size) are observed to decrease as volumetric flow rate is increased. RSD's were significantly higher when compared to the average burst heights and widths.

	Flow rate:5 μl/min	***1 μl/min***	***100 nl/min***
930 nm	254	6000	16500
500 nm	181	506	2700
200 nm	79	317	2000

Table 5.3 Summary of average burst areas for 3 particle sizes at 3 flow rates

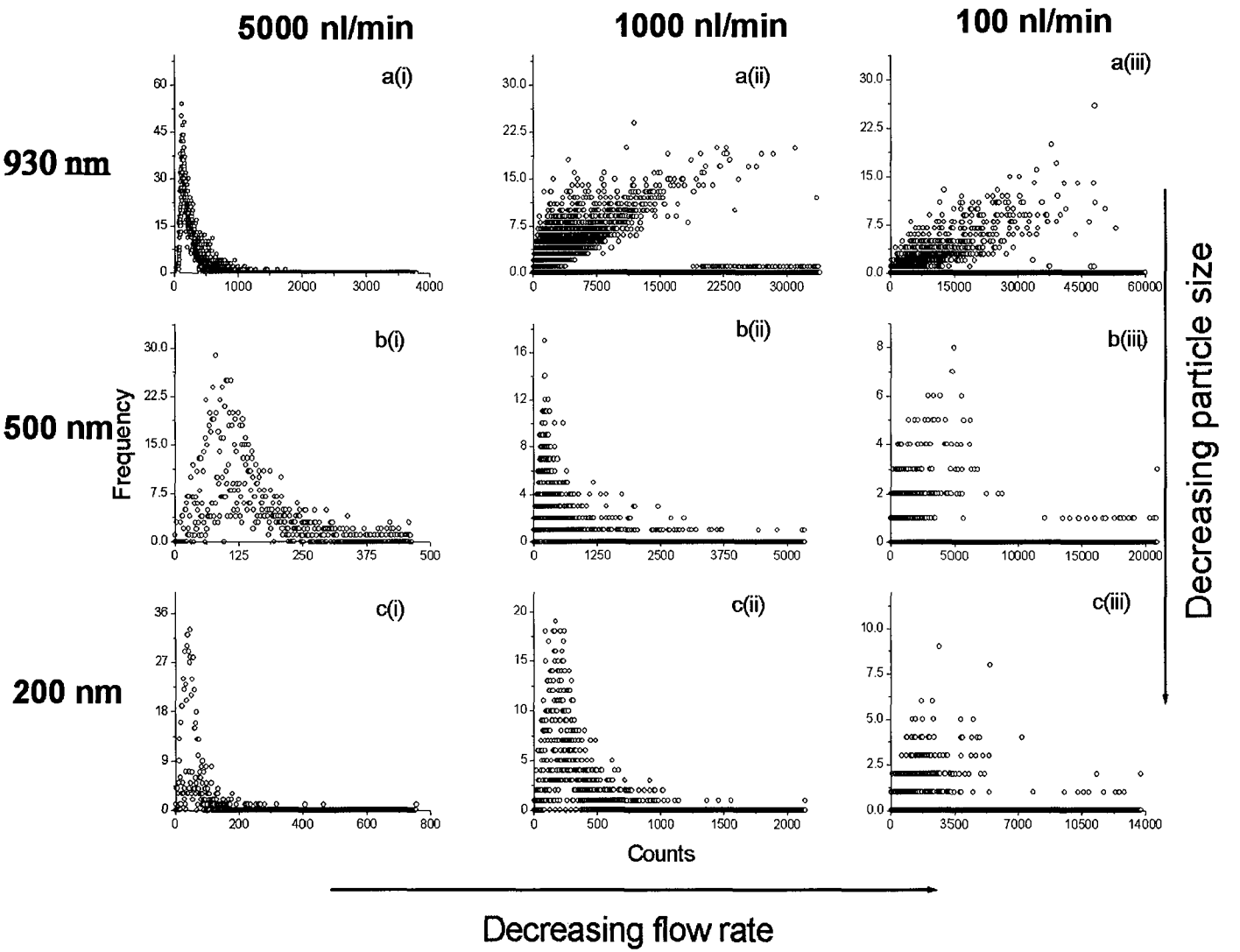


Figure 5.11 Histogram burst area distributions for 930 nm, 500 nm, and 200 nm Fluospheres at flow rates of 100, 1000, and 5000 nl/min respectively.

5.3.3.2 PBA analysis for E. coli expressed with GFP, CFP, YFP

Unlike the burst width and height distributions, the burst area histograms (as shown in section 5.3.3.1) did not have clearly defined distributions, even at a flow velocity of 5 µl/min. It was therefore decided that the burst area statistics of E. coli cells expressed with the 3 types of fluorescent protein would not be used in order to distinguish between cells.

5.4 Burst width deconvolution

In the previous section burst width distributions were used as a potential method for distinguishing between cells expressed with different fluorescent proteins. In this section burst width distributions are assessed as tools to statistically distinguish between different cell populations.

5.4.1 Deconvolution of E. coli mixtures

A burst width histogram for a mixture of 33 % of each of the E. coli cell populations is shown in ***Figure 5.12*** (blue diamonds). The flow velocity was held constant at 1 µl/min and the dwell time was 100 µs. A total of 500 photon bursts were used to generate the histogram. The relative contributions of the burst width distributions for individual components (i.e. the pure samples) were calculated through deconvolution analysis. The fitting routine used minimizes the function shown in ***Equation 5.1***.

$$\chi^2 = \sum_{k=1}^{n} \frac{1}{\sigma_k^2} \left[N(t_k) - N_{CFP}(t_k) - N_{GFP}(t_k) - N_{YFP}(t_k) \right]^2 \qquad \text{(Equation 5.1)}$$

Here n is the number of time bins used in the burst width histogram and σ_k is the standard deviation at each data point k. χ^2 is the chi squared. N(t) is the least squares fit, and $N_{CFP}(t)$, $N_{gFP}(t)$, $N_{YFP}(t)$ are the burst width histograms for the samples. A least squares fit produced yields of 35 %, 33 %, and 32 % respectively for CFP, GFP, and YFP. The initial parameters were randomly generated (and varied several times) in order to confirm that the yields produced were not generated by convergence in local minima in the χ^2 hypersurface. In all cases the yields did not vary by more than +/- 1 %.

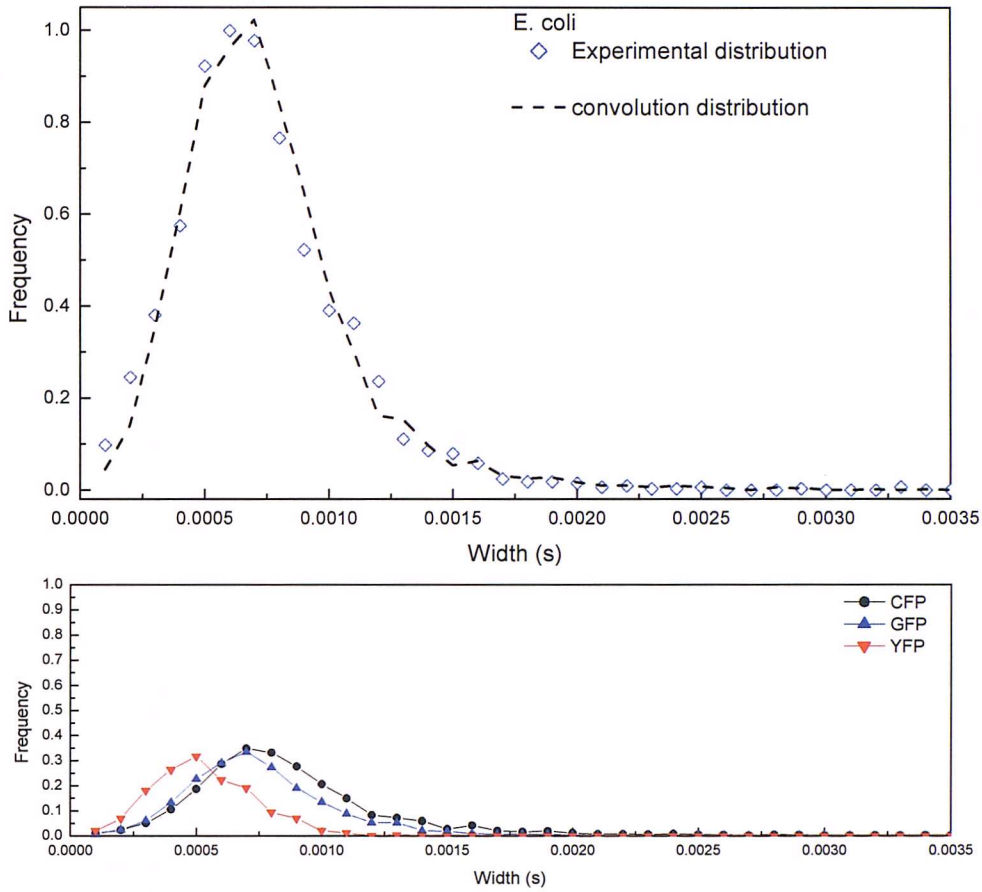


Figure 5.12 (Top) Burst width histogram for a mixture of 33 % of each of CFP, GFP, and YFP (blue diamonds). The deconvolved distribution is represented by a dashed line. (Bottom) Component distributions for CFP, GFP and YFP.

Decreasing the total number of particle bursts used in the analysis to 100 cells still generated correctly assigned distributions with an error of less than 10 %. When experimental distributions were generated using less than 100 cells, the errors associated with the yields were much higher. Nevertheless, this approach successfully extracts valuable information regarding cell populations and can be performed with as little as 100 cells. Lower cell counts can also be used; however, if there are greater than 3 types of cells within the sample, much larger errors will be associated with the measurement.

5.4.2 Deconvolution of Particle - E. coli mixture

The approach described above was also tested with a mixture of 90 %, 500 nm fluorescent particles and 10 % E. coli cells expressing GFP (***Figure 5.13***). The volumetric flow rate in this case was 3 µl/min and the dwell time was 100 µs. The combined cell and particle concentration was diluted to allow detection of 600 bursts within a 65 s interval. As in the

previous case, burst width distributions of the pure samples were extracted from the experimental data.

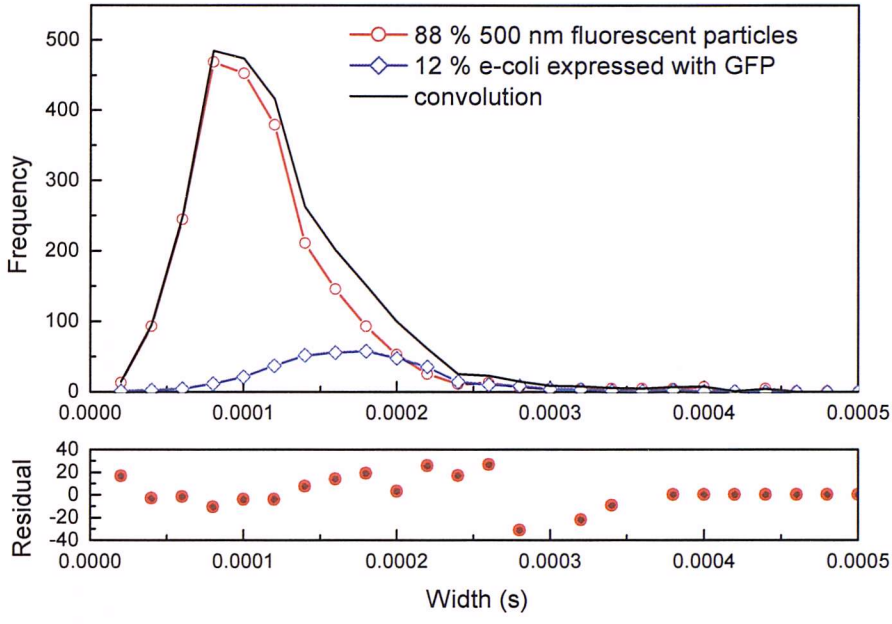


Figure 5.13 Deconvolved burst width histograms for a mixture of 10 % E. coli expressed with GFP (blue) and 90 % particles (red). The convolved distribution is represented by a black line. The residual is plotted in the bottom half.

The fitting routine is governed by the minimization of the function shown in ***Equation 5.2***.

$$\chi^2 = \sum_{k=1}^{n} \frac{1}{\sigma_k^2}\left[N(t_k) - N_{GFP}(t_k) - N_{PARTICLES}(t_k)\right]^2 \qquad \text{(Equation 5.2)}$$

In this case $N_{PARTICLES}(t_k)$ is the distribution for the pure particles, all other parameters are the same as in ***Equation 5.1***.

Analysis resulted in yields of 88 % and 12 % for the 500 nm particles and the E. coli cells expressing GFP respectively. An error below +/- 2 % was obtainable in the deconvolution process. As in section 5.4.1 the initial starting parameters were randomly defined and varied several times to confirm that the yields produced were in fact correct and not an artifact of the optimization routine. The residuals resulting from the deconvolution process are plotted in the bottom of ***Figure 5.13***.

5.5 Time correlated single photon counting

Fluorescent lifetimes have been used with great success to distinguish between fluorophores since fluorescence lifetimes are dependant on the fluorophore and its local environment.[20-25] This essentially makes lifetime analysis a sensitive tool for monitoring the environment or state of a molecular species. The majority of single molecule lifetime measurements in solution require statistical methods, most notably the maximum likelihood estimator, to distinguish between fluorophore lifetimes.[26] As the cells and particles used in this chapter typically contain more than 500 fluorophores, resorting to such sophisticated algorithms is not required. As such single cell and particle lifetimes can be determined using standard deconvolution procedures, as described in Chapter 3.

5.5.1 Fluorescent particle lifetimes

5.5.1.1 Bulk lifetime

To date, lifetimes of the fluorescent particles used in this work have not been reported. A bulk fluorescence decay originating from 500 nm particles at 100 x dilution from stock is shown in ***Figure 5.14***. Fitting to a bi-exponential decay model yielded a satisfactory fit with a reduced chi-square value of 1.25. The component fluorescence lifetimes were 4.65 and 2.36 ns with amplitudes of 79 and 21 % respectively. The laser repetition rate was set to 10 MHz and decays were collected at an emission wavelength of 515 nm.

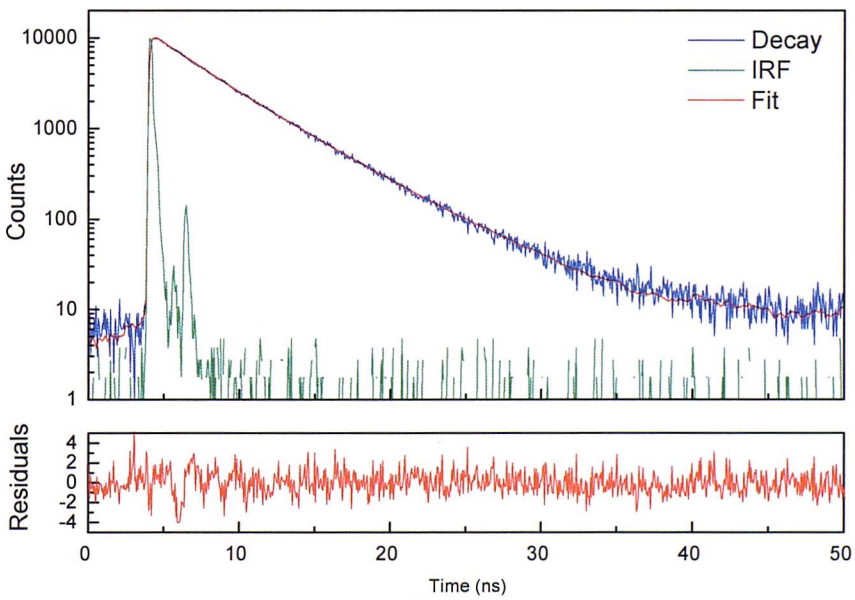


Figure 5.14 (Top) Fluorescence decay (blue) for 500 nm fluorescent particles in a 0.1 x TBE buffer solution. Decay fit (red) and IRF (green) are also shown. The lower panel displays the residuals of the fit.

5.5.1.2 Single particle lifetimes

Fluorescence decay curves originating from individual 500 nm fluorescent particles are shown in ***Figure 5.15*** along with a least squares fit. A volumetric flow rate of 1 µl/min and a dwell time of 100 µs was used. Under the experimental conditions, the particles remain within the detection probe volume for less than 1 ms. Hence, when compared to bulk fluorescence lifetimes a relatively small number of photons are registered for the whole decay. On average a single particle decay will be an accumulation of approximately 1000 photons (~ 100 counts at the channel of maximum intensity). The error associated with the measurement will therefore be higher than 10 %. In comparison, an accumulation of at least 100, 000 photons is typically performed when measuring lifetimes from bulk solution.

As a result of the poorer statistics associated with single particle lifetime measurements it is not typically possible to fit data to multiexponential models. It is only possible to extract the component with the maximum yield or the average fluorescence lifetime. The average fluorescence lifetime from a total of 130 fluorescent particles was 4.67 ns. The distribution of extracted lifetimes can be seen in ***Figure 5.16***. The standard deviation was 0.29 ns and the standard error was 0.03 ns. The lifetime of the 500 nm fluospheres was in good agreement with the longer and dominant component recovered from bulk analysis.

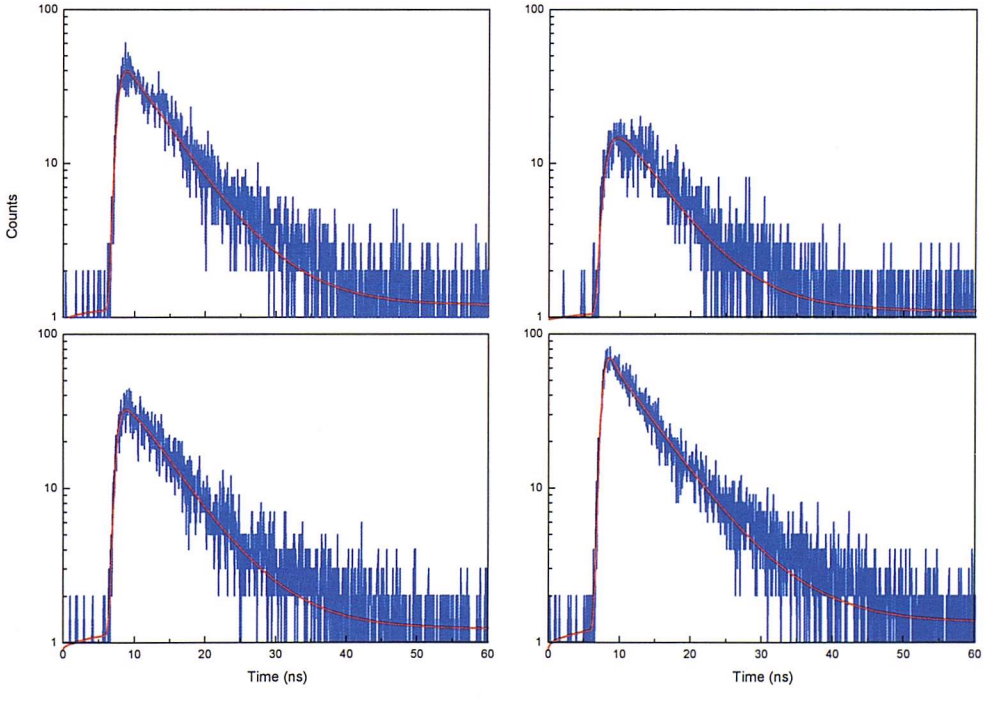


Figure 5.15 Fluorescence lifetime decays (blue) for 4 single 500 nm fluorescent particles along with a least squares decay fit (red).

The distribution of the single particle fluorescence lifetimes is relatively narrow and follows a Gaussian distribution. The majority of single particle lifetimes ranged between 4.5 ns and 5.4 ns. The reduced chi–squared values for the single particle decays ranged from 0.5 – 0.9.

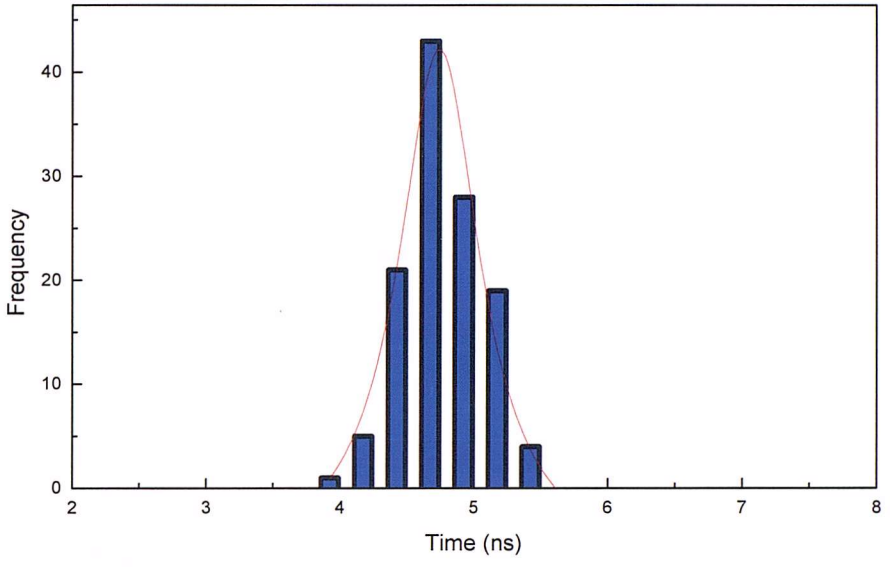


Figure 5.16 Lifetime histogram from an accumulation of 130 single fluorescent particle decays. A Gaussian fit is shown in red.

5.5.2 E. coli expressed with fluorescent proteins

5.5.2.1 Bulk lifetime

Measurement of the fluorescence decays originating from fluorescent proteins such as CFP, GFP, and YFP using TCSPC have previously shown that a simple mono-exponential decay function is not sufficient to describe the radiative deactivation of the excited states. This is a result of complex photophysics which involves proton transfer kinetics.[27] As such, the fluorescence lifetimes are highly dependant on the surrounding environment as well as the excitation wavelength. It is for this reason that the use of a 2 or 3 component exponential decay model is required. A summary of the component fluorescence lifetimes and amplitudes for CFP, GFP, and YFP (in solution) are shown in ***Table 5.4***. The excitation source was a 438 nm pulsed diode laser with emission being collected between 450 nm and 650 nm.

The average lifetimes for CFP, GFP, and YFP were 3.12 ns, 3.04 ns, and 3.53 ns respectively. For all 3 proteins, the component which produced the largest amplitude (> 37 %) had a lifetime on the order of 3.3 ns. Unfortunately it is not possible to compare these lifetimes data currently available in the literature as the tri-exponential decays for all 3 proteins are highly dependant on the excitation wavelength as well as the emission wavelength. The predominant

approach in the literature is to use a band pass filter or a monochromator to acquire emission over a 10 nm interval. Our experimental configuration is set up for single particle based measurements; therefore, a long pass filter is simply used to cut off the excitation source.

	tau 1 / ns	Amp 1 / %	tau 2 / ns	Amp 2 / %	tau 3 / ns	Amp 3 / %	<tau>	χ2	DW
CFP	3.94	37.80	1.61	34.37	0.22	27.83	3.12	1.12	1.54
GFP	3.21	61.09	1.45	11.11	1.05	27.80	3.04	1.03	1.66
YFP	8.42	2.41	3.23	71.81	0.42	25.78	3.53	1.31	1.41

Table 5.4 Summary of lifetimes and amplitudes for CFP, GFP, YFP

The lifetimes for E. coli cells expressed with fluorescent proteins, under the same conditions as described in the previous paragraph, produced drastically different lifetimes. In all 3 cases the longest components had lifetimes on the order of 8 - 10 ns and amplitudes varying from 1 – 5 %. The lifetimes obtained for E. coli expressing green fluorescent are similar to those reported by Jakobs et al. using a similar instrumental set-up.[28] A complete summary of the amplitudes along with the lifetimes is shown in ***Table 5.5***.

	tau 1 / ns	Amp 1 / %	tau 2 / ns	Amp 2 / %	tau 3 / ns	Amp 3 / %	<tau>	χ2	DW
CFP	7.91	1.41	3.01	58.08	0.96	40.51	2.28	1.13	1.49
GFP	9.44	0.67	2.53	85.92	0.24	13.41	2.69	1.26	1.41
YFP	7.73	4.49	2.70	57.28	0.38	38.23	3.39	1.44	1.20

Table 5.5 Summary of yields and amplitudes for E. coli expressing CFP, GFP, YFP

The average lifetimes for E. coli expressing CFP, GFP, and YFP were 2.28 ns, 2.69 ns, and 3.39 ns respectively. For all 3 proteins, the component which produced the largest amplitudes (> 57 %) had lifetimes ranging from 2.5– 3 ns. Although the bulk lifetimes are in themselves relatively complex in nature, the variation in average lifetime between the cell population is sufficiently large to allow cell-type identification. It should be emphasised that each cell contains a minimum of 500 protein molecules hence the lifetimes can be still considered to be an ensemble measurement.

5.5.2.2 Single cell lifetimes

Fluorescence lifetime histograms for single E. coli cells expressed with CFP and GFP are shown in ***Figure 5.17***. The flow velocity through the microfluidic channel was 100 μs and an accumulation of 75 single lifetimes were used in the histograms. The decays were analyzed using a mono-exponential decay function. The average lifetimes from the histograms were 2.83 ns and 2.52 ns for CFP and GFP respectively. The standard deviation in the single cell histograms for CPF and GFP were 0.2 ns and 0.4 ns respectively. Both average values agree well with the bulk average lifetimes. It is reassuring to note that with such similar fluorescence lifetimes between the 2 types of cells, it is still possible to discriminate between single cells passing through the probe volume. The measurement of single cell lifetimes along with respective burst heights and widths appears to be a powerful approach to discriminating, sorting, and counting different cell types. A fluorescence lifetime histogram for single E. coli cells expressed with YFP was not performed as the total number of bursts registered was not sufficient to obtain statistically reliable information pertaining to the distribution.

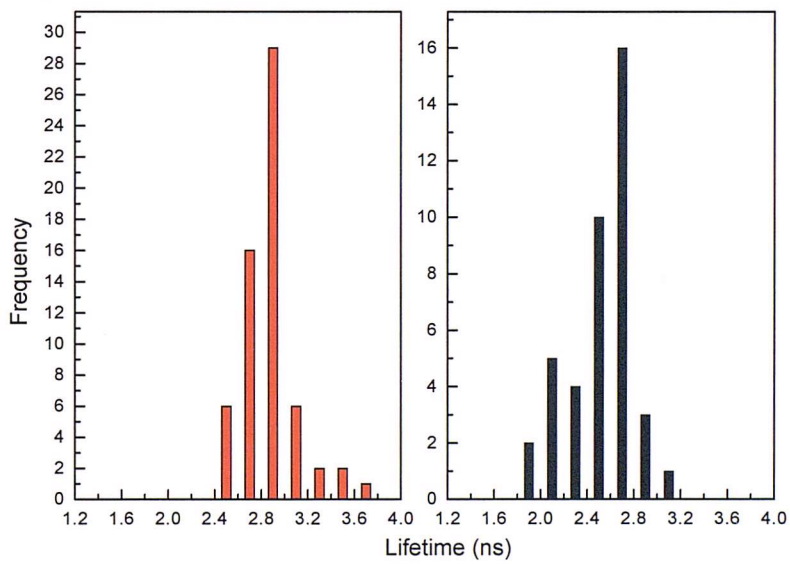


Figure 5.17 Lifetime histogram from an accumulation of ~75 single E. coli cells expressed with CFP (left) and GFP (Right).

It is interesting to note that when comparing the lifetime histograms of CFP or GFP with the fluorescent particles, there is negligible overlap amongst them. The proteins have lifetimes ranging from 2.4 – 3.8 ns, the particle lifetimes ranges from 3.8 -5.5. Clearly in solution with both cells expressed with fluorescent protein and cells expressed with BODIPY FL, all cells passing through the detection volume can be distinguished with 100 % certainty.

5.5.3 Inter-photon burst recurrence times

Until recently single molecule fluorescence experiments relied on binning photon burst scans into set intervals to allow observation of the number of fluorescence photons arriving in each time interval. Although this approach has proved to be valuable for single molecule fluorescence based experiments, more information can be obtained by registering and performing statistics on individual photon arrival times. A number of research groups have proposed a theoretical basis for the analysis of individual photon arrival times from single molecules.[29-32] In this section an analysis method based on inter-photon burst recurrence times is presented. With this approach photons from single particles can be used to distinguish between different molecular populations in a freely flowing solution within a microfluidic channel.

5.5.3.1 Experimental approach

In this section a description of the experimental approach is described (***Figure 5.18***). A picosecond laser pulse train with a repetition rate of 10 Mhz (100 ns) is used to excite analyte molecules within the detection probe volume (***Figure 5.18a***). Samples are delivered through the microchannel at various flow rates. Once the analyte is excited within the detection probe volume, molecular de-excitation can be achieved by either emission of a photon or via a non-radiative relaxation mechanisms. Hence, a single laser pulse will not necessarily result in a photon being emitted. This can be described in terms of a 2 state system, and defines an "on" state if a photon is registered and an "off" state if no photon is registered for a given laser pulse. When a photon is registered the TCSPC electronics designate its arrival time relative to the first excitation pulse. The acquisition card used has a time resolution of 100 ns. Therefore, a maximum of 1 photon can be registered from a single laser pulse. Each photon is assigned its arrival time, t_1, t_2,....., t_n as shown in ***Figure 5.18b***.

The time tagged photons are then binned into predefined intervals to extract the single particle or molecule photon burst scan as shown in step ***Figure 5.18c***. The interval or dwell time is typically set to approximately100 μs; however, the binning interval of the data is strictly dependant on the flow velocity of the solution. The algorithm for the conversion of the time tagged photons to a photon burst scan is available in appendix 2.3. From this scan the peaks are located and the background threshold calculated using the Poisson method described in Chapter 3 (***Figure 5.18d***). All photons not associated with a photon burst or photons which were below the threshold are discarded. The remaining time tagged photons are extracted into *"photon bar codes"* (***Figure 5.18e)*** and analysed calculating the difference between consecutive photon arrival times.

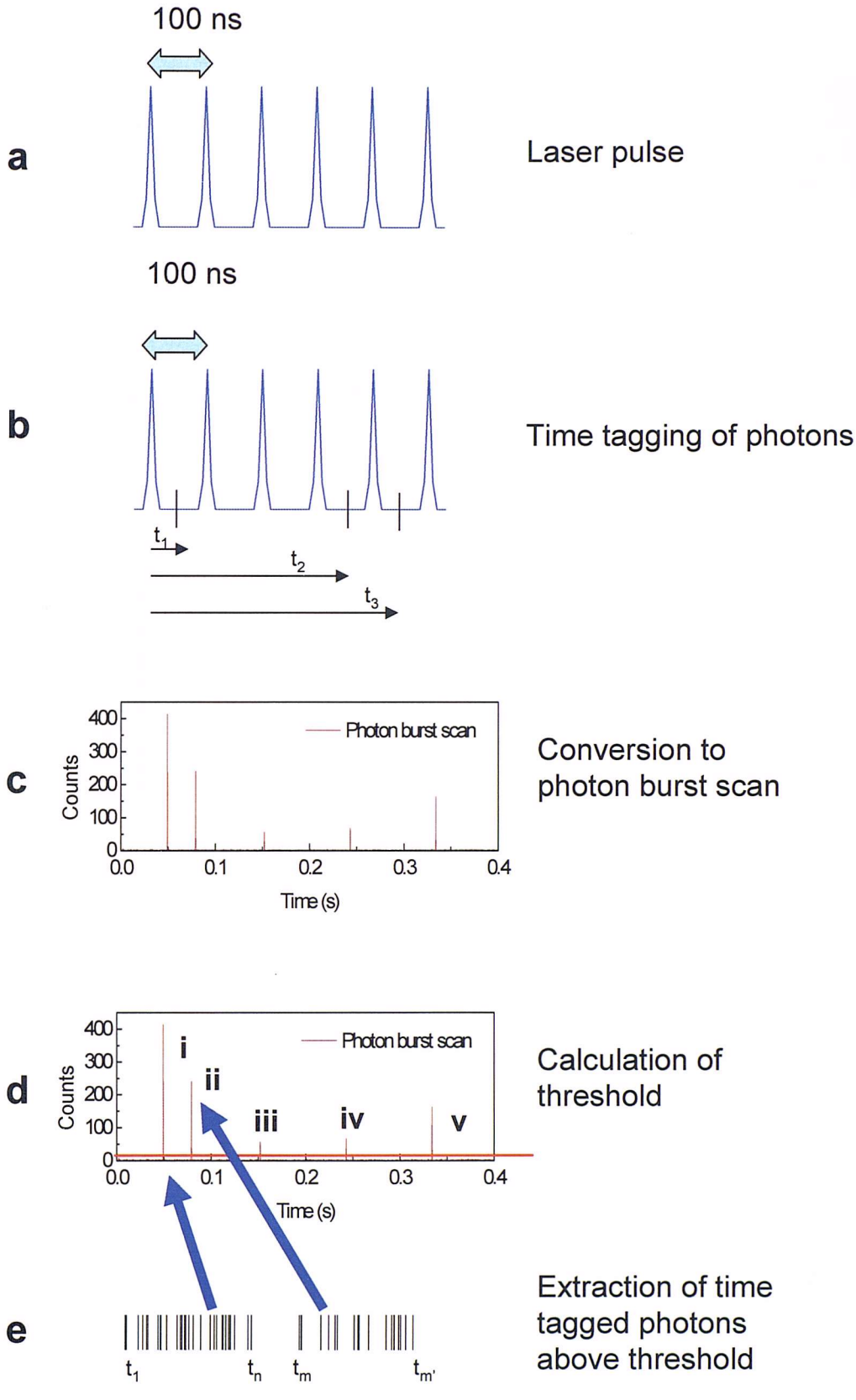


Figure 5.18 Schematic principle of the initial steps of an inter-photon burst recurrence time analysis.

It will be shown that the *photon bar codes* for E. coli cells expressing different fluorescent proteins and fluorescent particles are distinguishable based upon a recurrence time analysis. The recurrence times are calculated as follows: **P** is defined as a unit vector containing all times a photon burst is recorded (from ***Figure 5.18e***). From this vector Δt is determined by taking the difference between all consecutive points in this vector(i.e. $\mathbf{R_t}(i) = \mathbf{P}(i+1)-\mathbf{P}(i)$). The vector $\mathbf{R_t}$ contains the complete list of time differences between consecutive photons for a photon burst scan. This is then histogramed into bins with a resolution of 100 ns to obtain the inter-photon burst recurrence frequency.

5.5.3.2 Recurrence time analysis

Examples of the normalized inter-photon burst recurrence frequencies versus time for E. coli cells expressed with GFP is shown in ***Figure 5.19***. These curves were calculated from a photon burst scan with a minimum of 1000 cells. The flow velocity through the microfluidic channel was varied between 0.5 µl/min to 5 µl/min. Two unique contributions arise from the inter-photon burst frequency plots. The decay between 100 ns and 100 µs is a result of a contribution arising from the photon arrival times associated from individual molecules (i.e. equivalent to $t_n - t_{n-1}$ in ***Figure 5.18e***). This contribution has no dependence on the flow rate of the analyte. The second contribution between 10 ms – 1s is a result of photon arrival times between different molecules (equivalent to $t_m - t_n$ in ***Figure 5.18e***). This contribution is equivalent to a standard exponential Poisson recurrence time analysis as described in Chapter 3.

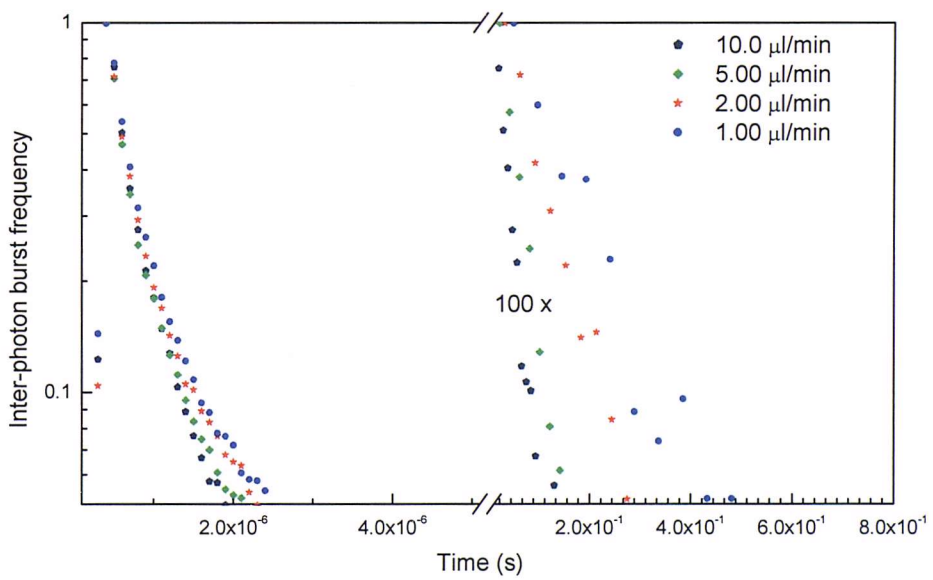


Figure 5.19 Normalized inter-photon burst frequency versus time for E. coli expressed with GFP. The 1st contribution (left) arises from photons associated with a burst, the 2nd from the inter – burst recurrence time.

The first contribution exhibits a negligible change when the flow velocity is changed; however in the second contribution, there is a clear shift in the exponential decays as the flow velocity is increased. This is a result of the inter-burst frequency being strictly dependant on the total number of molecular events recorded per unit time. As the flow velocity is increased the number of events is also increased ($t_m - t_n$ on average is much lower at higher flow velocities). This is clearly seen when the 2nd contribution is fitted to a single exponential decay (***Equation 3.5***). The recurrence times varies between 29 ms and 122 for flow velocities ranging from 1 – 10 µl/min.

In ***Figure 5.20*** the first contribution of the inter-photon burst frequency is shown for E. coli expressed with CFP, GFP, and YFP. The flow velocity through the microfluidic channel was set at 1 µl/min and in all 3 cases a minimum of 1000 bursts were accumulated to calculate the decay. The decays do not fit to a mono-exponential model such as in a typical single molecule Poisson recurrence time analysis. However, qualitatively there is a clear change in the decay profile for cells expressed with different proteins. This effect is a direct result of variation in absorption cross sections and fluorescence quantum yields as well as the excitation and emission efficiencies. A large difference in these parameters will result in drastically different inter-photon burst decays. This is clearly seen in ***Figure 5.20***. It is possible to discriminate with high certainty between CFP and YFP due to their drastically different absorption cross-sections at 438 nm. This simple analysis method is an ideal approach for discriminating between fluorophores imbedded within cells.

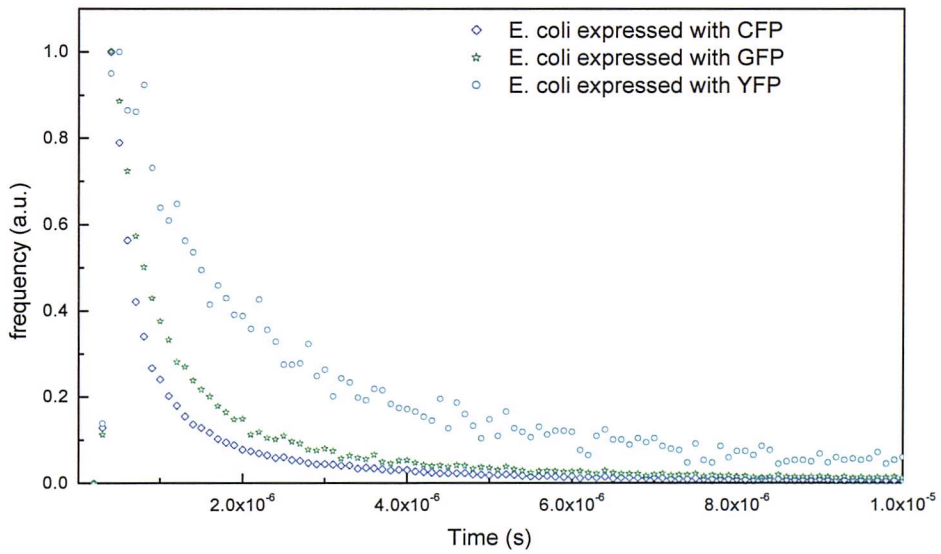


Figure 5.20 Normalized 1st contribution of the inter-photon burst frequency for E. coli expressed with CFP, GFP, and YFP.

5.6 Summary

In this chapter, analysis techniques were developed to discriminate between different cell and particle populations. The approaches described can be used in single cell sizing and counting applications with high precision.

The first method uses fluorescence lifetimes, as well as burst width histograms to characterize individual fluorescent particles or cells traveling through a femtolitre probe volume. The simplicity of the approach for obtaining well defined burst width distributions could be extremely valuable for single molecule cell sorting experiments. In the approach taken herein, we are able to use a sub femtoliter probe volume while controlling the shape of the BWH without making any changes to a basic confocal microscopic experiment. Strictly using photon burst characteristics, it was possible to discriminate between various analyte populations. The second approach described used single cell fluorescence lifetimes to discriminate between E. coli expressed with various fluorescent proteins as well as fluorescently labeled particles. It is seen that the larger the difference between the fluorescence lifetimes of the components, the greater the precision in the classifying of the cells or particles. Nevertheless, fluorophores with relatively small differences in lifetime could still be discriminated. The final analysis method, used single photon time tagging as well as inter-photon burst times to discriminate between cells expressed with different fluorescent proteins. All 3 methods described proved to be useful at discriminating between single cells or particles with high precision.

5.7 References

(1) Fu, A. Y.; Spence, C.; Scherer, A.; Arnold, F. H.; Quake, S. R. *Nature Biotechnology* **1999**, *17*, 1109-1111.

(2) Altendorf, E.; Zebert, D.; Holl, M.; Yager, P. In *Transducers 97 - 1997 International Conference on Solid-State Sensors and Actuators, Digest of Technical Papers, Vols 1 and 2*, 1997, pp 531-534.

(3) Monaghan, P. B.; Manz, A.; Nichols, W. W. In *Micro Total Analysis Systems 2000, Proceedings*, 2000, pp 111-114.

(4) Telleman, P.; Larsen, U. D.; Kutter, J. P.; Friis, P.; Wolff, A. In *Microfluidic Devices and Systems Iii*, 2000; Vol. 4177, pp 30-39.

(5) Altendorf, E.; Zebert, D.; Holl, M.; Vannelli, A.; Wu, C. C.; Schulte, T. In *Micro Total Analysis Systems '98*, 2000, pp 73-76.

(6) Fu, A. Y.; Chou, H. P.; Spence, C.; Arnold, F. H.; Quake, S. R. *Analytical Chemistry* **2002**, *74*, 2451-2457.

(7) Andersson, H.; van den Berg, A. *Sensors and Actuators B-Chemical* **2003**, *92*, 315-325.

(8) Wolff, A.; Perch-Nielsen, I. R.; Larsen, U. D.; Friis, P.; Goranovic, G.; Poulsen, C. R.; Kutter, J. P.; Telleman, P. *Lab on a Chip* **2003**, *3*, 22-27.

(9) Wheeler, A. R.; Throndset, W. R.; Whelan, R. J.; Leach, A. M.; Zare, R. N.; Liao, Y. H.; Farrell, K.; Manger, I. D.; Daridon, A. *Analytical Chemistry* **2003**, *75*, 3581-3586.

(10) Clontech *http://www.bdbiosciences.com/clontech/.*

(11) Tsien, R. Y. *Annual Review of Biochemistry* **1998**, *67*, 509-544.

(12) Shimomura, O.; Johnson, F. H.; Saiga, Y. *J. Cell. Comp. Physiol.* **1962**, *59*, 223-239.

(13) Mashanov, G. I.; Tacon, D.; Knight, A. E.; Peckham, M.; Molloy, J. E. *Methods* **2003**, *29*, 142-152.

(14) Chesnokov, Y. V.; Meister, A.; Manteuffel, R. *Plant Science* **2002**, *162*, 59-77.

(15) Lee, A. K.; Falkow, S. *Infection and Immunity* **1998**, *66*, 3964-3967.

(16) Walmsley, R. M.; Billinton, N.; Heyer, W. D. *Yeast* **1997**, *13*, 1535-1545.

(17) Park, J.; Kim, K. A.; Ryu, J.; Choi, E. Y.; Lee, K. S.; Choi, S. Y. *Journal of Microbiology and Biotechnology* **2000**, *10*, 797-804.

(18) Hirschmann, F.; Verhoeyen, E.; Wirth, D.; Bauwens, S.; Hauser, H.; Rudert, M. *Osteoarthritis and Cartilage* **2002**, *10*, 109-118.

(19) The protein data bank. *http://www.rcsb.org/pdb/.*

(20) Ha, T.; Chemle, D. S.; Enderle, T.; Weiss, S. *Bioimaging* **1997**, *5*, 99-104.

(21) Herten, D. P.; Tinnefeld, P.; Sauer, M. *Applied Physics B-Lasers and Optics* **2000**, *71*, 765-771.

(22) Li, T. F. *Pattern Recognition* **1996**, *29*, 337-339.

(23) Maus, M.; Cotlet, M.; Hofkens, J.; Gensch, T.; De Schryver, F. C.; Schaffer, J.; Seidel, C. A. M. *Analytical Chemistry* **2001**, *73*, 2078-2086.

(24) Sauer, M.; Arden-Jacob, J.; Drexhage, K. H.; Gobel, F.; Lieberwirth, U.; Muhlegger, K.; Muller, R.; Wolfrum, J.; Zander, C. *Bioimaging* **1998**, *6*, 14-24.

(25) Sauer, M.; Angerer, B.; Han, K. T.; Zander, C. *Physical Chemistry Chemical Physics* **1999**, *1*, 2471-2477.

(26) Enderlein, J.; Goodwin, P. M.; van Orden, A.; Ambrose, W. P.; Erdmann, R.; Keller, R. A. *Chemical Physics Letters* **1997**, *270*, 464-470.

(27) Suhling, K.; Davis, D. M.; Phillips, D. *Journal of Fluorescence* **2002**, *12*, 91-95.

(28) Jakobs, S.; Subramaniam, V.; Schonle, A.; Jovin, T. M.; Hell, S. W. *Febs Letters* **2000**, *479*, 131-135.

(29) Burzykowski, T.; Szubiakowski, J.; Ryden, T. *Chemical Physics* **2003**, *288*, 291-307.

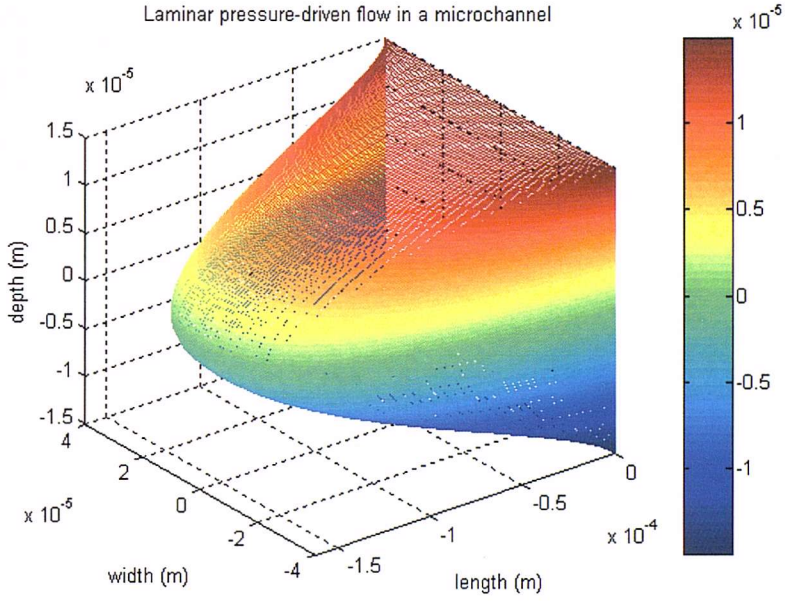
(30) Yang, H.; Xie, X. S. *Journal of Chemical Physics* **2002**, *117*, 10965-10979.

(31) Novikov, E.; Hofkens, J.; Cotlet, M.; Maus, M.; De Schryver, F. C.; Boens, N. *Spectrochimica Acta Part a-Molecular and Biomolecular Spectroscopy* **2001**, *57*, 2109-2133.

(32) Cook, R. J.; Kimble, H. J. *Physical Review Letters* **1985**, *54*, 1023-1026.

- 6 -

A non-invasive, optical technique for measuring particulate flow within microfluidic channels is developed. Confocal fluorescence detection is used to probe single fluorescently labelled microspheres passing through a focused laser beam at a variety of flow rates. Statistical methods (including autocorrelation and Poisson statistics) are subsequently used to analyze the resulting fluorescence bursts and generate velocity data for the flowing particles.



Determination of bulk particulate flow velocities in microchannels

6.1 Introduction

The study of solid particles within flowing streams is of great interest and importance in biological and industrial systems. Examples include the measurement of the effect of various interventions on regional blood flow[1], particulate flow in smokestacks and the study of fuel injection in combustion engines. Furthermore, particles have also been used to monitor bulk flow in micro structures[2] as well as simulating the inhalation of airborne particles.[3]

Key requirements when measuring particulate velocities include the need for a sensitive, non-invasive detection protocol as well as the ability to continuously monitor a given system. This is important, since invasive methods, which place a probe in the flow, cause disruption and induce an error in the velocity measurement. Fluorescence methods are inherently sensitive, non-invasive and selective, and therefore are well-suited for use in velocimetry measurements. A common technique for such measurements is particle velocimetry. This approach relies on the fundamentals of the Doppler shift. The Doppler shift describes an apparent change of the wavelength of a wave, due to the difference in velocity between the source of the wave and the observer. In laser Doppler techniques light incident on a moving object is scattered and frequency shifted according to standard physical models. Unfortunately, laser Doppler techniques involve the use of complicated and expensive instrumentation, and require that the laser beam, optics, and detector be precisely aligned. Particle Image Velocimetry (PIV) is another well-established technique used in both macroscopic and microscopic flow systems to measure fluid velocity fields.

PIV techniques work by calculating the displacement of many small "tracer" particles injected into a fluid. The particles are assumed to follow the fluid motion as well as not significantly changing the fluid properties such as density, volume and viscosity. Conventionally, a pulsed laser is used to illuminate and fix the motion of the particles while a CCD camera images the particles. After a defined time-delay a second image of the particles is recorded. A correlation algorithm is applied to the pair of images to yield the mean displacement of the particles between the two exposures. Division of the displacement by the time-delay returns the velocity field of the fluid. PIV has been used to investigate a wide variety of fluid flow fields in systems including micro-channels and micro-nozzles.[4] Recently, Manz and co-workers have used Shah Convolution Fourier Transform Detection (SCOFT) for velocity measurements of fluorescent microspheres within microfluidic channels.[5] Their approach used a novel convolution-detection method to convert multiple-point detection, time-domain electropherograms to frequency-domain plots. An example of this is shown in ***Figure 6.1*** where the Fourier transform was calculated when 1 μm fluorescent microspheres were

introduced into the detection area by applying a field strength of 161 V/cm. The time-domain signal was implemented using 50 – 40 μm wide slits above the detection probe volume. The subsequent Fourier transform yielded the magnitude plot in the frequency domain, as shown in ***Figure 6.1***. A fundamental peak at 7.1 Hz with a S/N of 16 was observed. This translates to a velocity of (7.1 Hz x 70 μm) 497 μm/s.

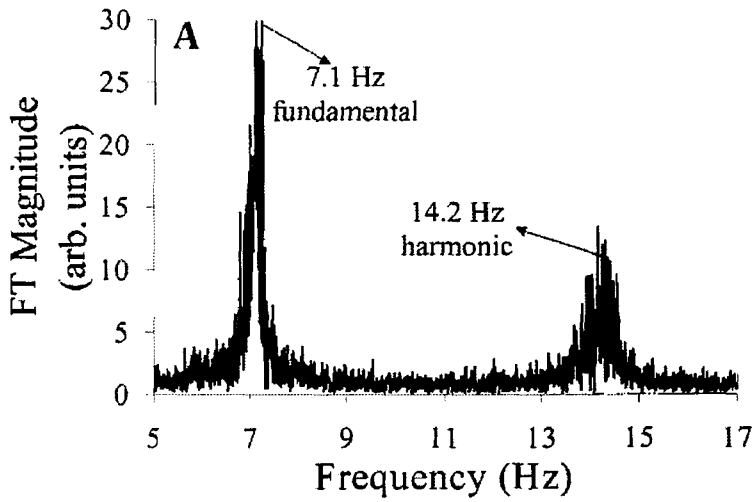


Figure 6.1 FT signals collected when the fluorescent microspheres were introduced into the detection area. Conditions: 0.1 X TBE buffer, pH 8.4; electric field strength 161 V/cm. Reprinted from Manz et al.[5]

The studies in this chapter present an approach for measuring particulate flow using a non-invasive, single point detection method. More common methods are invasive and require the use of multiple point detection systems. A glass-PDMS microfluidic device is used, as it is insensitive to the small probe volumes associated with confocal detection and minimizes the degree of sample consumed. Specifically, a confocal fluorescence detection approach is used to probe single microspheres passing through a focused laser beam at a variety flow rates. Simple statistical methods are subsequently used to investigate the resulting fluorescence bursts and generate velocity data for hydrodynamically flowing particles. The mean burst frequency was shown to be directly proportional to flow speed. Furthermore the Poisson recurrence time and the autocorrelation width are similarly shown to be inversely proportional to flow speed. Using the above methods, from a single acquisition, we show that particulate flow velocities can be determined.

6.2 Experimental

6.2.1 Materials

Fluorescent microbeads having a mean diameter of 0.93 μm were used for all experiments. Absorption and emission maxima of the microbeads were 505 nm and 515 nm respectively. The beads were sonicated for 10 minutes immediately before use to ensure good dispersion. A working solution of approximately $2.3x10^7$ beads/cm^3 was used (effective concentration of 10 μg/cm^3). All dilutions were performed in TBE buffer.

6.2.2 Microfluidic devices

Initial trial experiments were performed using a microchannel made from square bore fused silica capillary (Composite Metals, UK). Initial alignment experiments were performed using this approach while the microfluidic devices were being fabricated. A square capillary was chosen in order to minimize aberrational effects due to the curvature of the walls in standard circular bore capillaries. The channels were 50 μm wide and 50 μm deep with a wall thickness of 135 μm. Windows, 2 mm wide, were burned into the protective polyimide coating and a 5 cm capillary section was secured onto a glass microscope slide using epoxy glue. The capillary was interfaced with a syringe pump with the use of PTFE tubing (152 μm i.d., Composite Metals, UK).

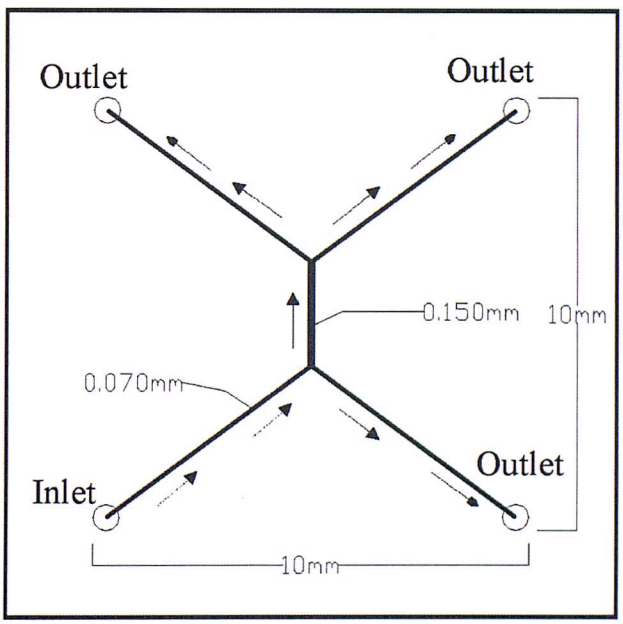


Figure 6.2 Schematic of "Double-Y" PDMS microchip. The detection volume was positioned at a point midway along the wide (150 μm) channel.

Further experiments were performed using a Poly(dimethylsiolxane) (PDMS) microfluidic device. This is the only instance in the thesis where a glass microfluidic device was not used. This was due to initial development of microfluidic devices focussing on rapid prototyping using elastomeric materials. The resulting PDMS microstructured channels are 150 μm wide and approximately 50 μm deep. A simple 'double-Y' channel pattern (***Figure 6.2***) was designed to allow flexibility in the number of inlets and outlets. However, in all studies described in this chapter, one inlet and three outlets were used.

The structured substrates are approximately 1 cm^2 and 5 mm thick. The PDMS substrate was covered with a 18 x 18 mm glass cover slip (grade 0; BDH Merck, Poole, Dorset, UK) having a thickness of less than 130 μm (the maximum working distance of the microscope objective is 150 μm). A reversible seal is formed between the glass and PDMS. This allows for facile cleaning of the microchip when needed. Cleaning of the PDMS surface was typically performed by sonicating the substrate in ethanol followed by rinsing in deionised water. Hole reservoirs were bored in the PDMS and 3 cm long pieces of 75 i.d. / 150 o.d. capillary (Polymicro Technologies, Phoenix, AZ, USA) were inserted into the reservoir holes. The capillaries were secured in each port with Loctite Prism 406 cyanoacrylate adhesive (RS Components, Corby, UK).

The PDMS devices proved to be difficult to handle due to the elasticity of the PDMS. This could potentially cause deformation in the microfabricated channels arising from the pressure applied by the oil immersion objective. This limitation was overcome by improving the rigidity of the device by adding extra curing agent in the PDMS fabrication process as well as by mounting the device on a glass substrate.

6.2.3 Chip and sample integration

The microchip is placed on a translation stage and appropriately aligned under the microscope objective. A syringe pump (Harvard Apparatus, Cambridge, MA, USA) is used to deliver solutions at various flow rates from either a 500 μL or 50 μL gastight syringe (Hamilton) into the capillary tubing. Typical flow rates ranged from 0.05 – 8 μL/min. As this was one of the initial experiments performed during this thesaural work, the confocal spectrometer was simpler in structure than the optimized system described in Chapter 2. Although the fundamental principles are the same, the initial system built was designed strictly to run single molecule or particle fluorescence photon burst scans[6] (***Figure 6.3***), and as such is sufficient

for the experiments described within this chapter. The optimized system was capable of single molecule TCSPC, Raman spectroscopy as well as time dependant emission spectroscopy.

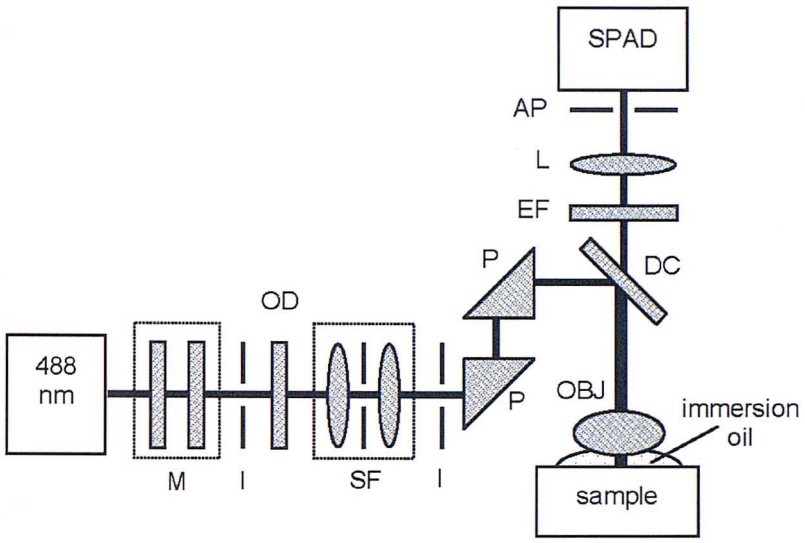


Figure 6.3 Component-based confocal detection optics. (M, mirror; I, adjustable iris; OD, neutral density filter; SF, spatial filter; P, right-angled prism; OBJ, 100x microscope objective; DC, dichroic beamsplitter; EF, emission filter; L, lens; AP, confocal aperture; SPAD, detector).

6.3 Results

6.3.1 Photon burst scans: Burst frequency

Figure 6.4 shows examples of fluorescent bursts scans from 0.93 μm fluospheres at volumetric flow rates of 50 nL/min and 1000 nL/min respectively. Average signal intensities, using a dwell time of 1 ms, were typically on the order of 300 counts. A signal to noise ratio as high as 200 is typically observed for any given flow rate. An average background signal intensity of ~4 counts per bin for flow rates ranging from 50 – 8000 nL/min remained constant throughout each acquisition. The background threshold was therefore set to 10 counts per bin for all experiments as was predicted by a Poissonian analysis. Variation of the laser power (7 μW ± 3 μW) induced no significant change in the signal to noise ratio. In each case the particle density remained constant; therefore, with increased flow velocity it is easy to see that the detection of single particle events becomes more frequent. At higher flow velocities it is possible for the average photon burst height to decrease. This is due to the

beads typically being resident in the probe volume for shorter time periods. It was therefore important to select a low enough dwell time so that complete particle bursts can be registered.

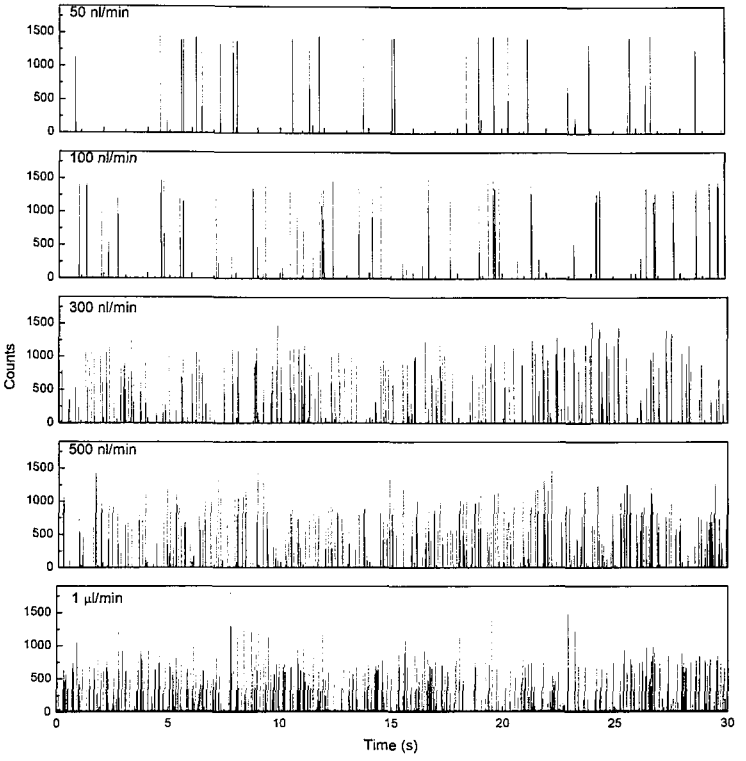


Figure 6.4 Representative single particle photon burst scans at a variety of flow rates for 0.93 µm fluospheres in TBE buffer.

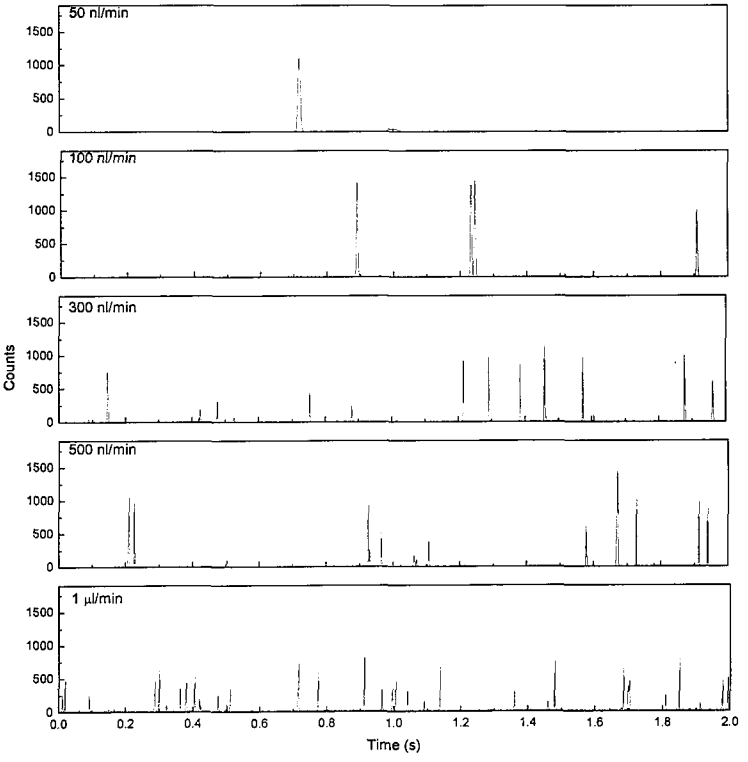


Figure 6.5 Expanded portions of the single particle photon burst scans as a function of volumetric flow rate.

Expanded portions of the burst scans are shown in ***Figure 6.5*** and clearly illustrate the low-level background signal as well as the variation in burst frequency and burst width. Analysis of the dwell time versus burst width yields information relating to the time spent by individual fluospheres in the probe volume. For example at a flow rate of 1000 nL/min, between dwell times of 10 μs – 800 μs, a least squares fit produces a nearly horizontal line. It is at these dwell times in which single particle bursts are observed. At longer dwell times, a burst is a result of an accumulation of at least 2 particles traversing the probe volume and therefore the burst width is increased. This can be more clearly seen in ***Figure 6.6***. At higher dwell times each burst originates from the passing of more than one particle through the probe volume. From the horizontal line the burst width was then averaged to be 1.38 ms. It should be noted that much higher signal to noise ratios are obtained when compared to single molecule detection. This is due to the fact that each particle contains approximately 1.0×10^7 fluorescein equivalents.

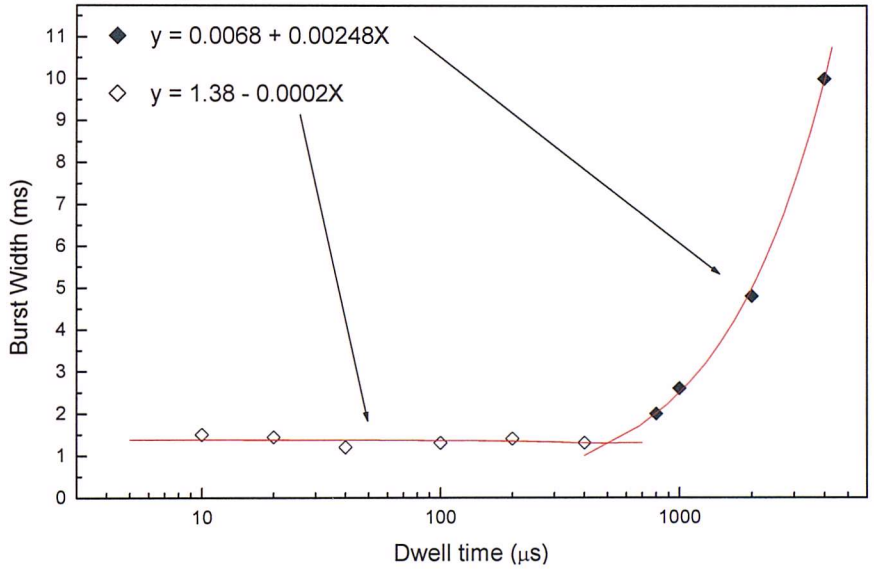


Figure 6.6 Average photon burst width for 0.93 μm fluorescent particles travelling at a flow rate of 1 μl/min in TBE buffer.

6.3.2 Autocorrelation dependence on flow velocity

Figure 6.7 shows normalized autocorrelation curves with respect to the curve maxima for different bulk volumetric flow velocities. As expected, at higher flow rates, the FWHM is smaller than when compared to lower flow velocities. A reduced FWHM is directly associated with a reduced residence time in the probe volume. This trend is consistent with the experimental data as the flow velocity increases.

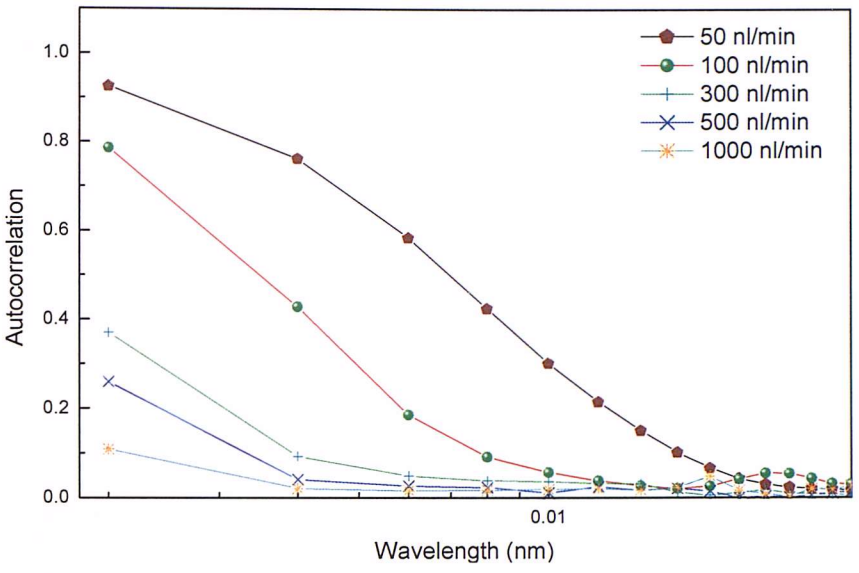


Figure 6.7 Experimental autocorrelation curves for 0.93 μm fluorescent beads flowing through a microfluidic channel. The dwell time was 2 ms.

As previously mentioned there are clear variations in the width of the autocorrelation curve as a function of volumetric flow rate. Primarily, the width of a curve narrows with increasing particle velocity. The reduced curve width is related to the reduced residence time of a particle in the probe volume. ***Figure 6.8*** plots the inverse of the FWHM value against flow rate for a series of autocorrelation functions. As the particle residence time is inversely proportional to the volumetric flow rate, the FWHM is also proportional to the residence time.[7]

The linear relationship observed in ***Figure 6.8*** demonstrates the application of confocal fluorescence detection as a non-invasive method for flow velocity determination within microfluidic channels. A least squares fit produces an R^2 value equal to 0.998 and thus appears to be a good method for extracting flow velocities. It should be noted that calibration of particulate motion was done in terms of volumetric flow rate and not in terms of linear flow velocities. This is due to several reasons which are as follows. Actual particulate velocities are dependent on channel dimensions within a given fluidic network. Since these vary within the structure presented (and indeed will normally vary in any microfluidic circuit) volumetric flow rates provide the most suitable measure of particulate motion. Furthermore, calculation of a simple mean linear flow velocity would be misleading, since parabolic flow profiles are generated by hydrodynamic pumping methods.[8]

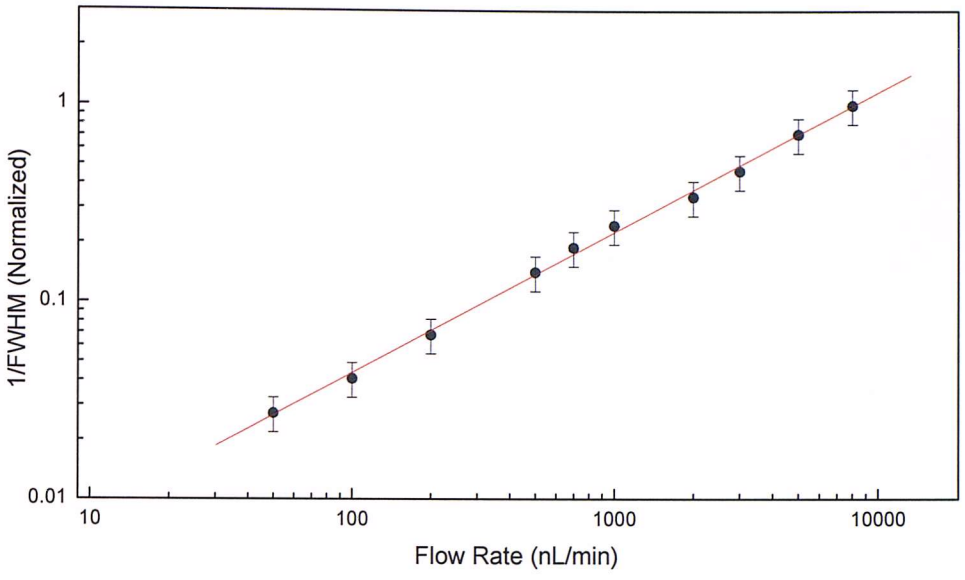


Figure 6.8 1/FWHM value of the autocorrelation curve as a function of flow rate (gradient 0.75).

6.3.3 Recurrence time dependence on flow velocity

Figure 6.9 shows the frequency N(Δt) versus time plots for a variety of flow rates. These data were calculated using the protocol described in Chapter 3 for Poisson recurrence times. The reciprocal gradient of a least square fit of these lines produces the recurrence time, τ_r. These distributions were calculated with a minimum of 1000 photon bursts; such a quantity was required to obtain improved theoretical fits to Poisson recurrence times.

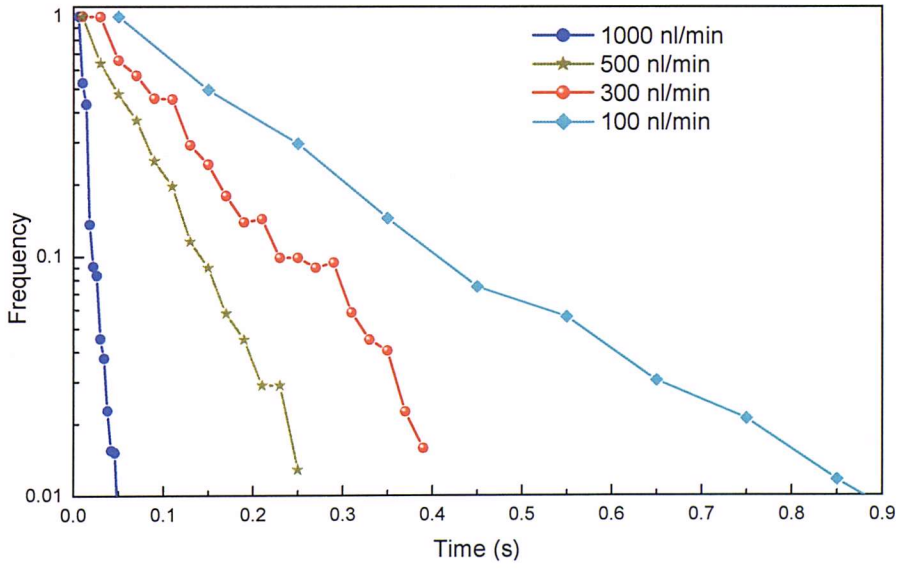


Figure 6.9 Inter burst separation distributions determined for a variety of flow rates for 0.93 μm fluorescent particles.

Typical burst recurrence times should be inversely proportional to flow rate. Therefore, a linear relationship will exist between the burst recurrence rate and the flow rate for a given sample concentration and cross-sectional area of the micro-channel. ***Figures 6.10*** and ***6.11*** show plots of frequency versus flow rate and the reciprocal of the recurrence time versus flow rate respectively (each point is the average of 64000 bins of data). In both cases a linear relationship is observed when data are plotted on a log-log scale. The R^2 values, for a least squares linear fit, in both cases are above 0.98. It is interesting to note that in neither case do the extrapolated values at a flow rate of 0 nL/min yield a frequency of 0 counts or a $1/\tau_R = 0$. This is due to natural diffusive behaviour of the fluospheres through the excitation cavity of the probe volume. Data points below 50 nL/min were not obtained due to restrictions on the attainable flow rates with the pumping source. At flow rates above 2000 nL/min, although not obvious from a log-log plot, there is a slight gradual trend for the burst frequencies to deviate from the regression line. This is due to the fact that a proportion of bursts are not fully resolved on the timescale of the measurement. Increasing the chip capillary cross-section would minimize this effect, although the burst detection frequency would be reduced.

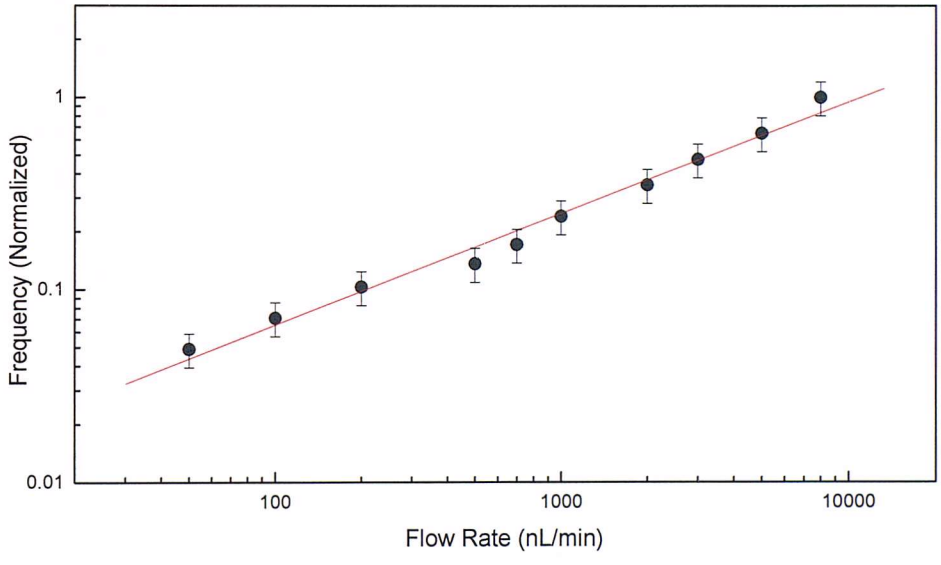


Figure 6.10 Variation in the normalized burst frequency as a function of flow rate for 0.93 μm fluorescent particles (gradient 0.72). The detection region within the PDMS chip was positioned at a point midway along the 150 μm wide channel.

The mean burst frequency is shown to be directly proportional to particle velocity, and both the Poisson recurrence time and the autocorrelation FWHM are inversely proportional to flow speed. This is consistent with observations made in a previous study.[8] The recurrence time and frequency plots in ***Figures 6.10*** and ***6.11*** have reduced R^2 values of 0.982 and 0.985 respectively. A possible explanation for the reduced precision relative to the autocorrelation

curves arises from the fact that in order to obtain frequency and recurrence times the background signal must be manually removed from the raw data resulting in a slightly larger error. Conversely, the FWHM is calculated by simply operating on the raw data to generate the autocorrelation curve. However, measurement of both recurrence times and burst frequencies provide alternative and facile methods of flow velocity determination within microfluidic channels.

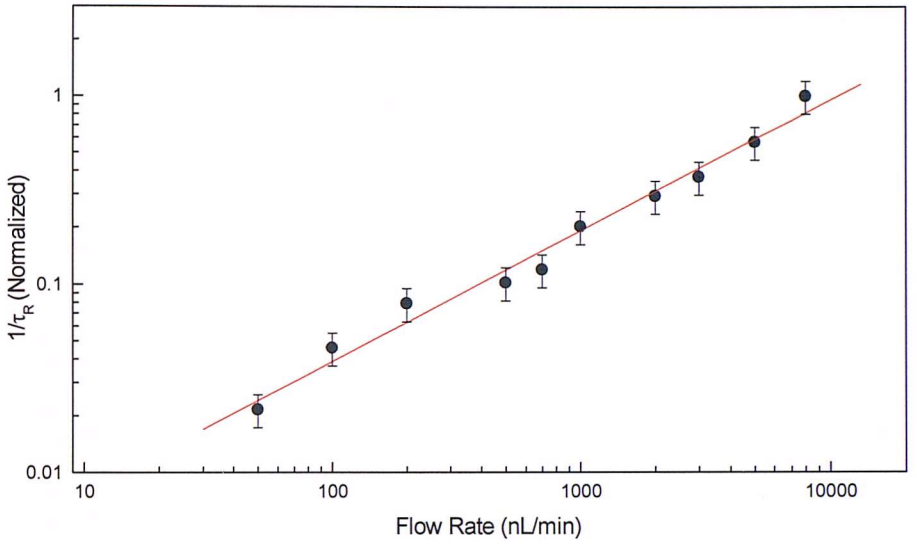


Figure 6.11 Variation in the normalized recurrence time as a function of flow rate for 0.93 μm fluorescent particles (gradient 0.78). The detection region within the PDMS chip was positioned at a point midway along the 150 μm wide channel.

6.4 Summary

The linear relationships observed in **Figures 6.8, 6.10, and 6.11** offer an indirect and non-invasive method for flow speed determination. The mean burst frequency was shown to be directly proportional to flow speed. The Poisson recurrence time as well as the autocorrelation width was similarly shown to be inversely proportional to flow speed. From a single 10 s acquisition, particulate flow velocities can be determined from recurrence, frequency, and autocorrelation data. The component-based confocal fluorescence detection system used is simple, inexpensive and capable of single point fluorescence detection of particles in flowing streams in a microfluidic device. The small probe volumes associated with confocal fluorescence were shown to be insensitive to sample downsizing and high sensitivity detection was achieved in a microfluidic device.

A single particle confocal spectroscopy approach to the determination of particle flow velocities is appealing as it requires only a single detection point in order to determine the particulate flow velocity. Although the component based system built is relatively complex, it can be stripped down to its bare necessities for particulate flow analysis which would in turn make the detection system simple, inexpensive and applicable to a diversity of planar chip systems.

The studies reported within this chapter relate strictly to the measurement of micron size particulate flow velocities, however, a parallel approach can be used in order to determine molecular flow velocities. A natural progression from the experiments described in this chapter would involve assessing the relevance of flow velocities of biologically important macromolecules confined within microfluidic channels. Differently sized macromolecules are expected to have different burst characteristics as a result of diffusion (perpendicular to the direction of flow) within the microfluidic channel. Flow velocity measurements of this kind may prove useful in applications such as high throughput screening and cellular assays.

6.5 References

(1) Conhaim, R. L.; Rodenkirch, L. A. *American Journal of Physiology-Heart and Circulatory Physiology* **1996**, *40*, H996-H1003.

(2) Barker, S. L. R.; Ross, D.; Tarlov, M. J.; Gaitan, M.; Locascio, L. E. *Analytical Chemistry* **2000**, *72*, 5925-5929.

(3) Robertson, H. T.; Glenny, R. W.; Stanford, D.; McInnes, L. M.; Luchtel, D. L.; Covert, D. *Journal of Applied Physiology* **1997**, *82*, 943-953.

(4) Santiago, J. G.; Wereley, S. T.; Meinhart, C. D.; Beebe, D. J.; Adrian, R. J. *Experiments in Fluids* **1998**, *25*, 316-319.

(5) Kwok, Y. C.; Jeffery, N. T.; Manz, A. *Analytical Chemistry* **2001**, 73, 1748-1753.

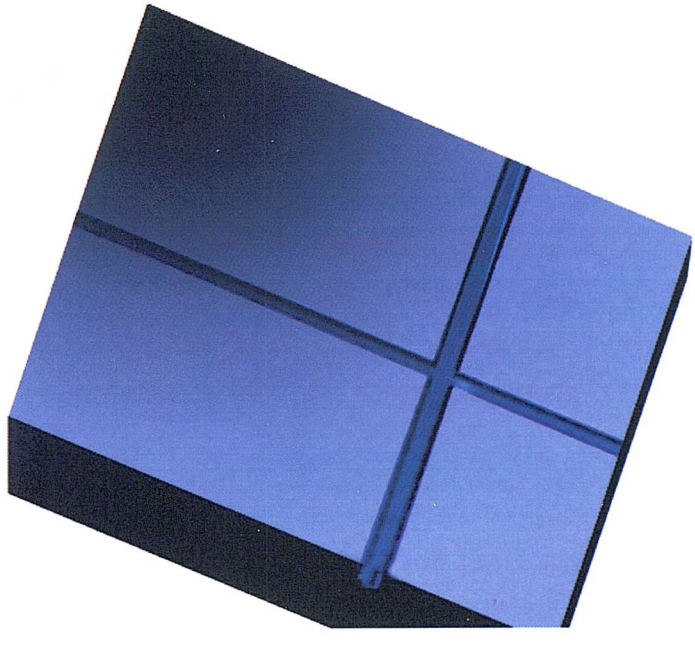
(6) Hill, E. K.; de Mello, A. J. *Analyst* **2000**, 125, 1033-1036.

(7) Hill, E. K. Unpublished results **2000**.

(8) Gosch, M.; Blom, H.; Holm, J.; Heino, T.; Rigler, R. *Analytical Chemistry* **2000**, 72, 3260-3265.

- 7 -

A simple statistical method is described that can distinguish between particles traveling at different flow rates through a confocal probe volume within a microfluidic channel. The method is based on the use of a maximum likelihood estimator statistical algorithm. From the results described in this chapter, this approach appears to be capable of distinguishing between individual fluorescence particle bursts traveling at different flow velocities.



Determination of single particle flow velocities in microchannels

7.1 Introduction

In the studies presented in Chapter 7, a statistical approach using the maximum likelihood estimator (MLE) is used to calculate the flow velocities of single particles moving through a confocal detection volume based on the analysis of characteristics of individual fluorescence photon bursts. A cartoon representation of the ideas behind this method is shown in ***Figure 7.1***. The use of microfluidic devices in such experiments afford significant reductions in the active volume needed for analysis. In confocal spectroscopy experiments, probe volumes are typically in the sub-femtolitre regime and hence total sample consumption for a single experiment within a microfluidic channel can be as low as several picolitres. These small volumes are crucial as many 'real-world' samples are only available in limited quantities.

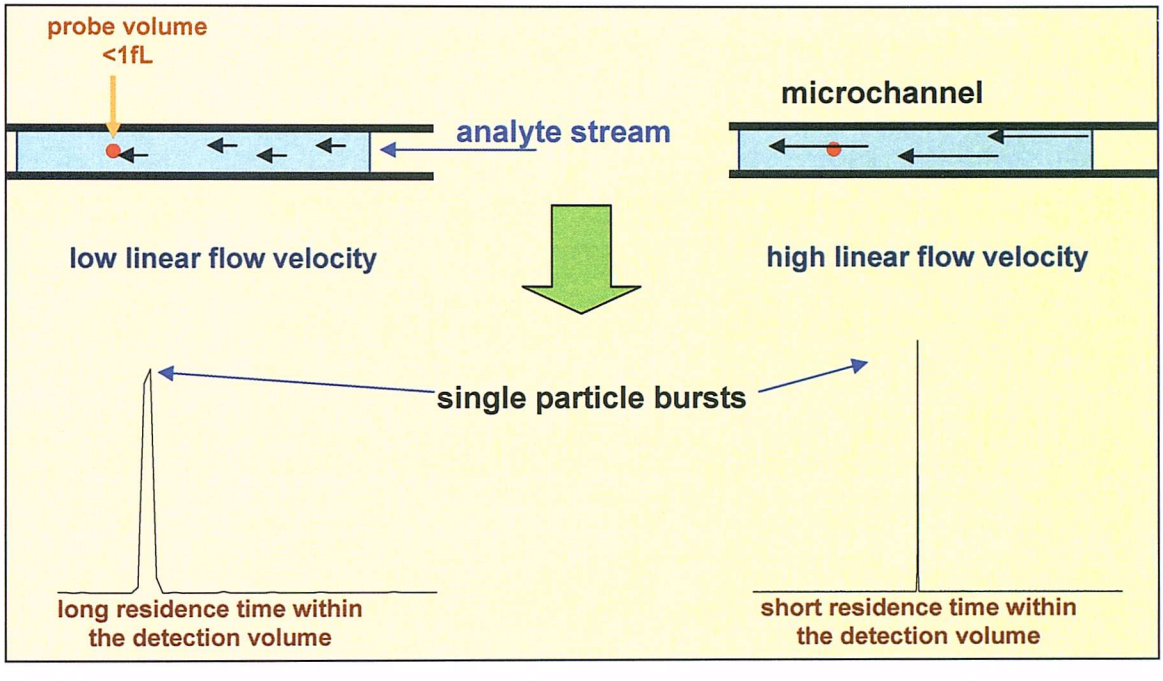


Figure 7.1 Cartoon representation of flow velocity dependence on single particle photon burst characteristics

Solving flow velocities of single molecules or particles within fluidic streams can be considered mathematically as a 'classification' problem. A common approach to solving such a problem involves the creation of a decision rule, which separates classes based on a present observation and minimizes the probability of misclassification. For example, a single molecule fluorescence lifetime can be statistically compared to the lifetime describing the bulk solution. If both values are comparable and within acceptable errors, the single molecule can be classified to be the same as those molecules in the bulk solution. An approach such as this can only be used if sufficient background information is available. For example, in the case of determining the flow velocities of single particles, the probability function for a given

particle burst at a given flow velocity must either be explicitly known or must be derived from past observations. The probability function in this case would be characteristic of a single particle's burst width, area, and height for a specific flow velocity. A number of techniques have been proposed to statistically classify parameters (such as fluorescence lifetimes and molecular concentrations) of a system.[1] One approach is to use a maximum likelihood estimator (MLE). An MLE is a useful mathematical tool or *'Equation'* which is used in order to compare the likelihood of two or more systems either being the same or different. A direct MLE approach requires a solution to maximize the likelihood function of the unknown prior probabilities of classes in a mixture (e.g. a solution obtained with low precision from an experimental system can only be compared to another system in which all parameters of the solution are available at high precision). This is generally considered to be a complicated multi-parameter optimization problem. In order to solve for particle flow velocities in this manner a database is needed containing prior information on the characteristics of the particles being studied with respect to flow velocity.

An interesting application of the MLE is in the determination of fluorescence lifetimes in single molecule time correlated single photon counting (SM-TCSPC) experiments.[2-5] In a typical SM–TCSPC experiment, less than 200 total photon counts are registered (over the entire decay). This contrasts with conventional TCSPC measurements, where between 10^5 and 10^7 counts are typically collected over an entire decay and results in difficulties in recovering molecular fluorescence lifetimes and pre-exponential factors. The MLE method has been used to great advantage in statistically comparing single molecule fluorescence lifetimes (obtained to low precision) with respect to the bulk lifetime (obtained to high precision). Kollner et al. first used an MLE approach to determine the minimum number of photons required for the recovery of fluorescence lifetimes from TCSPC data.[6] The same authors also reported the use of the MLE for fluorescence lifetime pattern recognition in ultra sensitive molecule identification.[7] An example of this work is shown in ***Figure 7.2*** for the calculation of fluorescence lifetimes. The MLE analysis was performed on single molecule bursts which contained more than 30 collected photons. The resulting distribution of measured fluorescence lifetimes is relatively broad in the case of BodipydUTP. This was thought to be caused by a change in the fluorescence lifetimes due to adsorption of the molecules on the surface walls.

More recently Maus et al. compared the MLE approach with a nonlinear least-squares method for the analysis of single molecule fluorescence lifetimes.[2] The MLE proved to be more reliable for low photon count rates, with nonlinear least-squares methods generally underestimating lifetime values by approximately 5%. Although the information extracted

from single particle bursts, using confocal spectroscopy, is less well defined (for example, individual particles travel with a different trajectories through the detection volume) when compared to a fluorescence decay time measurement, particle burst characteristics are highly dependent on flow velocities through the detection volume. With this in mind, an MLE approach should provide for a useful method to statistically determine system parameters (such as flow velocities) of single particles in microchannel environments.

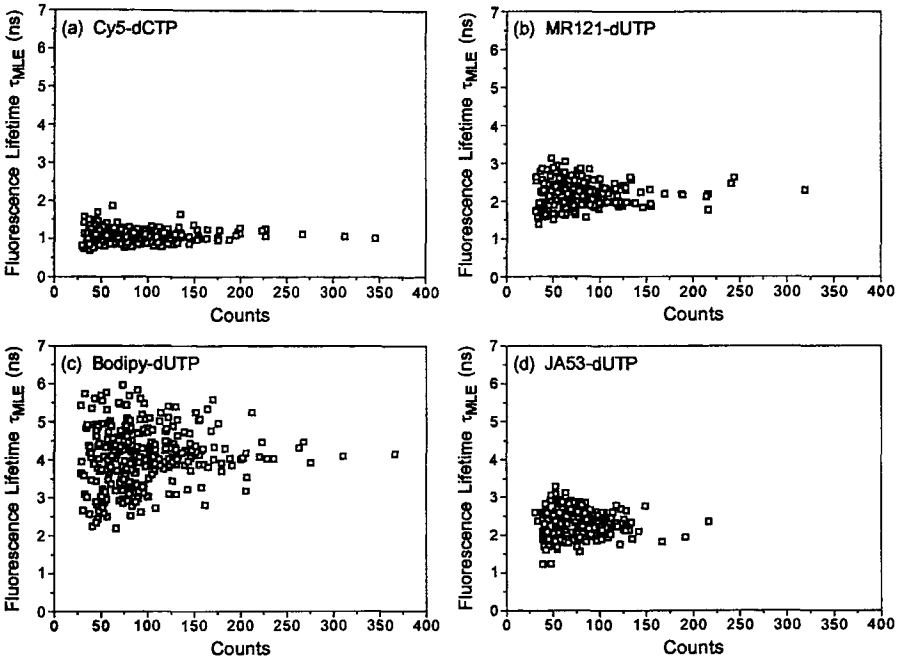


Figure 7.2 Fluorescence lifetimes obtained by the MLE for single (a) Cy5-dCTP, (b) MR121-dUTP, (c) Bodipy-dUTP and (d) JA53-dUTP molecules in water against number of detected photons per burst. Taken from Sauer et al.[4]

7.2 Experimental

7.2.1 Materials

Fluorescent microbeads (yellow/green Fluospheres ®, Molecular Probes; Europe B.V.) having a mean diameter of 0.93 μm were used for all experiments. All dilutions were performed in tris-borate-EDTA buffer (TBE). The TBE buffer was prepared at 0.1x concentration (8.9 mM each of tris(methoxy)aminomethane and boric acid, 0.2 mM in ethylenediaminetretraacetic acid; prepared from a solid TBE mixture; Fluka Chemicals) in 18 MΩ deionized water. The beads were sonicated for 10 minutes immediately before use to prevent agglomeration. Typical working solutions had a concentration of 2.3×10^7 beads/cm^3 (effective concentration of 10 ng/L). ***Figure 7.3a*** shows examples of fluorescence burst scans

originating from 0.93 μm Fluospheres at volumetric flow rates of 2000 and 300 nL/min respectively. Average signal intensities, using a dwell time of 300 μs, were typically of the order of 300 counts for both flow rates. It can be seen in all scans that burst heights vary significantly in magnitude. This is primarily caused by the range of possible particle trajectories through the probe volume and is observed due to the diffraction limited focus of the laser beam being approximately 100 times smaller than the channel width of the microfluidic device. Mean burst widths are 10.3 ms and 3.5 ms for flow rates of 300 nL/min and 2000 nL/min respectively. The relative standard deviation (RSD) in burst width for both flow rates was approximately 60 % (calculated from a minimum of 2000 particle bursts). The mean burst areas were 2040 and 650 counts for respective flow rates of 300 nL/min and 2000 nL/min. In this case RSD values were 119 % and 110 % respectively. ***Figure 7.3b*** shows expanded portions of the fluorescence burst scans. Qualitatively, it can be observed that there is a large change in the photon burst characteristics of individual particles as they traverse the detection probe volume when the flow velocity is changed. It is this characteristic which allows the use of a statistical method distinguish between flow velocities of individual particles.

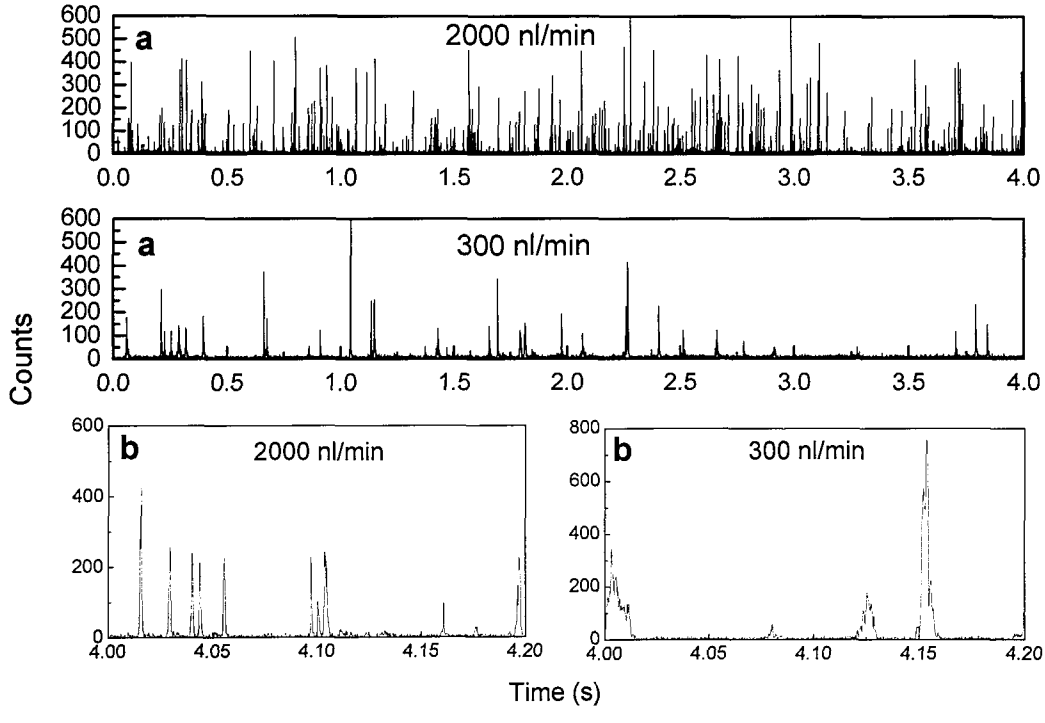


Figure 7.3 (a) Fluorescence burst scans originating from 0.93 μm Fluospheres flowing through a microchannel at volumetric flow rates of 2000 nL/min and 300 nL/min. (b) Expanded portions of (a).

7.2.2 Microfluidic devices

Microfluidic devices were manufactured in-house and comprised a thermally bonded structured glass-glass device containing a microchannel network. The microchannel had a width of 100 μm and the depth was 30 μm. The channel length was 16 mm. Fluidic access holes with a diameter of 400 μm were drilled prior to bonding. Fused silica capillaries (150 μm id and 350 μm od) were glued in the access hole reservoirs using Araldite 2014 (RS Components, UK).

7.2.3 Experimental protocol

The completed microchip was placed on a translation stage and appropriately aligned under the microscope objective. A precision syringe pump (PHD 2000, Harvard Apparatus, Cambridge, MA, USA) was used to deliver solutions at flow rates ranging from 10 nL/min – 5000 nL/min using a 1 ml gastight syringe (SGE Europe Ltd, UK). Excitation of fluorescent particles was performed with the 488 nm line of a tunable argon ion laser. Excitation of the sample occurred 10 mm down stream from the inlet hole of the microfluidic channel.

7.3 Theory

7.3.1 Particle burst identification and isolation

Although the details of the identification routine were explained in Chapter 3, it is perhaps important to repeat the fundamental details in this chapter as it composes the basis for the statistical method described. The peak-locating algorithm is based on a Toeplitz matrix that determines local peak maxima down a column vector. Briefly, the program searches for a given peak maximum above a specific threshold value which can be defined as three standard deviations from the mean background count rate, i.e. $n_{threshold} = \mu + 3\sqrt{\mu}$. Adoption of a threshold that lies 3 standard deviations above the mean yields confidence limits greater than 99%. Once a peak is found, the peak area is determined by analyzing a specified number of bins either side of the peak maximum until the background threshold value is reached. Once this is done, the program searches for the next peak and continuously repeats until all peaks are accounted for. Once each particle burst was located, the burst was extracted from the raw data and inserted into a matrix with each column associated to a single particle burst, ω(r) (where r is defined as a given particle burst). Typically a given matrix has up to 4000 columns (particle bursts) and 500 rows (250 bins to the left and right of each burst maxima).

7.3.2 Maximum likelihood estimator

7.3.2.1 Peak probability distribution function

Particles or molecules travelling at specific flow rates through a confocal volume would be expected to have well-defined burst widths, heights, and areas. Hence, bursts travelling with different velocities should be distinguishable based on such parameters. As photon counts are accumulated in channels or bins, classification routines can be used to discriminate between particles travelling at different flow rates. This is due to particle burst characteristics over a range of bins being directly dependant on the flow velocity. The approach used herein utilises a maximum likelihood estimator (γ_j) as shown in ***Equation 7.1***,

$$\gamma_j = \sum_{1}^{k} n_i \log\left(\frac{n_i}{Np_i(j)}\right) \qquad \text{(Equation 7.1)}$$

where n_i is the number of counts in channel i. k is the number of channels (or bins) for each particle burst $\omega(r)$ and $p_i(j)$ is the probability that a group of photons will fall in channel i if the particles have a velocity j. N is a parameter related to the signal strength, or the total number of counts, for a given particle burst.

$$N = \sum_{t=-\delta}^{\delta} n_i(t) \qquad \text{(Equation 7.2)}$$

If a particle burst is defined to have a maximum at time $t = 0$, then a given particle burst is summed over the time interval $[-\delta,\ldots.t=0,\ldots.\delta]$. Hence $k = 2\delta$. A given particle is expected to be of the type j if γ_j produces a minimum for a given probability function $p_i(j)$. i.e. j can have a value between $j1$ and $j\psi$. Therefore, $p_i(j1)\ldots.. p_i(j\psi)$ defines the peak probability distribution (PPD) of particles travelling with flow rates $j1\ldots.j\psi$.

$$\xi_j = \min\left[\gamma_{j1},\ldots,\gamma_{j\psi}\right] \qquad \text{(Equation 7.3)}$$

In ***Equation 7.3*** the minimum value, ξ_j, then defines a particle to have a flow rate j. This procedure essentially produces an approach similar to that of a least squares test on each particle burst with respect to the peak probability distribution of a given flow rate.

The peak probability distribution function, $p_i(j)$, for a particle travelling at flow rate j in all cases was defined according to ***Equation 7.4:***

$$p_i(j) = \frac{\sum_{m=1}^{r} \omega_j(m,t)}{\sum_{t=-\delta}^{\delta} \sum_{m=1}^{r} \omega_j(m,t)} \qquad \text{(Equation 7.4)}$$

Where $\omega_j(m,t)$ is the function defining a single particle burst and m is equal to the total number of bursts summed at a given flow rate j. Once again a particle burst is defined to have a maximum at time $t = 0$, and therefore the denominator is the summation of the total counts over the time interval $[-\delta,\ldots.t = 0,\ldots.\delta]$.

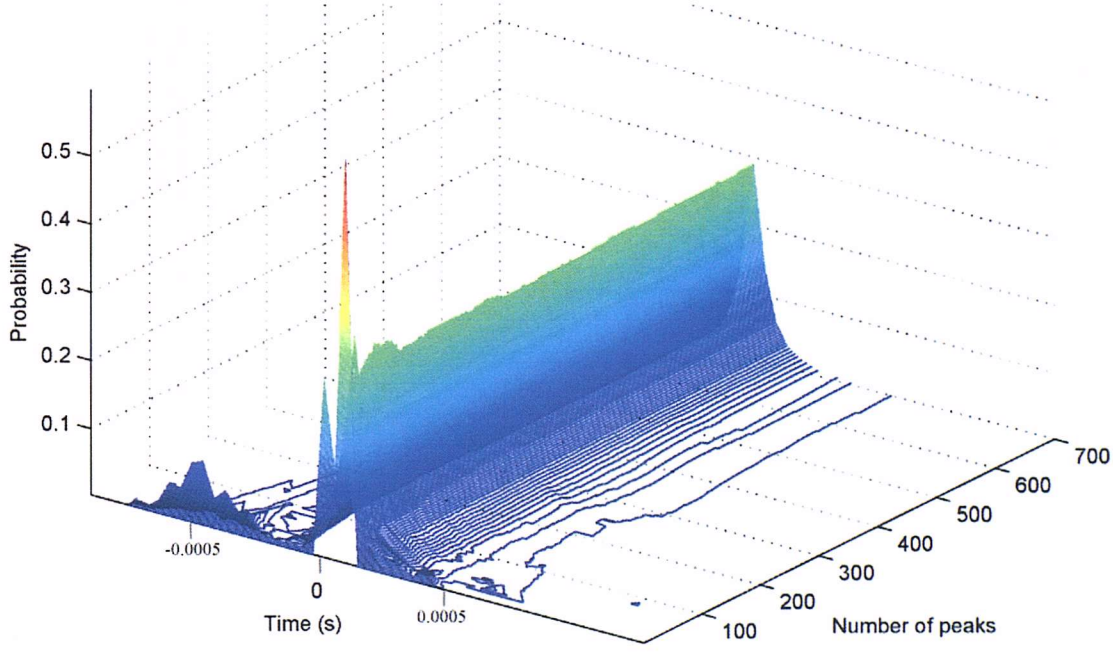


Figure 7.4a Variation of the peak probability distribution function for 0.93 µm fluorescent particles travelling at a flow rate of 2000 nL/min as a function of the number of bursts analysed.

Figure 7.4a shows the change in the probability function versus the number of peaks summed. These data were obtained for single particles travelling with a velocity of 2000 nL/min through a 100 µm wide microfluidic channel. It should be noted that summing 200 peaks or greater yields a stable probability function for single particle bursts and hence will result in a reliable PPD function. This effect can be better seen in ***Figure 7.4b*** where the probability distribution is calculated over 500, 700, and 900 peaks. There is essentially no change

between the 3 distributions. In fact, above 200 peaks, there is virtually no change between the PPD's which converges to a well defined distribution. It is this well defined distribution which is required to compare single particle flow velocities. Below this value, the probability distribution shows a large degree of fluctuation. This can be clearly seen in the 1st 50 peaks of ***Figure 7.4a***. This is generally expected as single particles can exhibit a variety of trajectories within the confocal probe volume. For all experiments described herein a summation of 700 single particle burst was performed at a given velocity j to define the probability distribution functions $p_i(j)$.

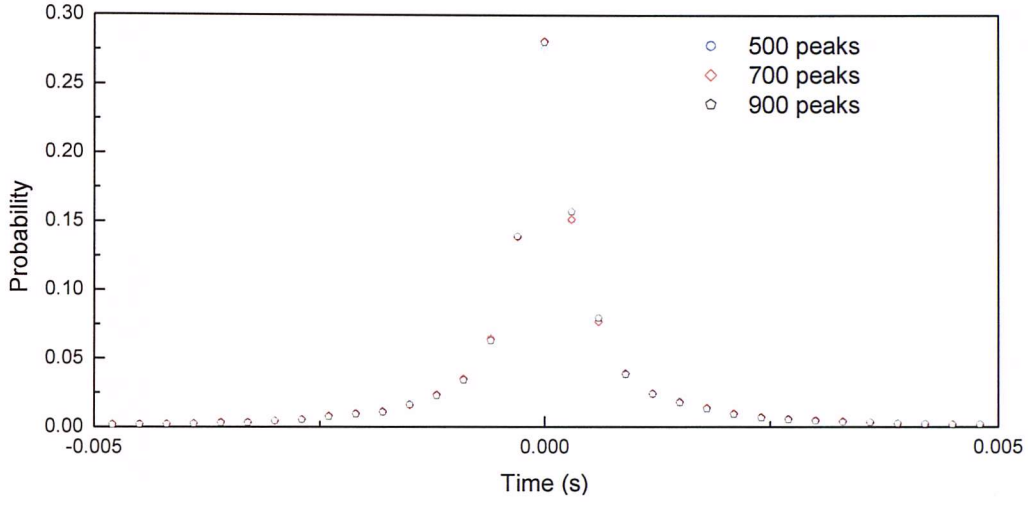


Figure 7.4b Variation of the peak probability distribution function for 0.93 μm fluorescent particles travelling at a flow rate of 2000 nL/min as a function of the number of bursts analysed.

7.3.2.2 Autocorrelation distribution function

The autocorrelation probability distribution (APD) function was calculated in an analogous manner to that of the PPD function. In this case, autocorrelation curves were used to calculate probability distributions as opposed to using more direct particle burst distributions. The APD was used to asses the difference in errors when assigning particulate velocities when compared to a PPD approach. An autocorrelation curve of a single particle burst is directly dependant on the particle's flow velocity, burst width, area and height; and therefore, presents the possibility of discriminating between velocities with just as high, if not higher, precision as a PPD approach. In a typical autocorrelation analysis the entire photon burst scan is used. However, in this approach, the autocorrelation curves are strictly determined from single particle bursts by applying the autocorrelation function to every column within the matrix $\omega(r)$. Hence, the APD incorporates a summation of individual particle burst autocorrelation curves. In this case, the modified maximum likelihood estimator (χ_j) is shown in ***Equation 7.5***,

$$\chi_j = \sum_1^k n_i \log\left(\frac{n_i}{N^a p_i(j)}\right) \qquad \text{(Equation 7.5)}$$

where n_i is the number of counts in channel i, k is the number of channels for a particles' autocorrelation curve $a(t)$ *and* N is a parameter related to the signal strength, or the total number of counts, for a given autocorrelation curve.

If a particles' autocorrelation curve is defined to have a maximum at time $t = 0$, then the curve is summed over the time interval $[t,.\delta]$. A given particle is expected to be of the type j if χ_j produces a minimum for a given probability function ${}^a p_i(j)$. i.e. j can have a value between $j1$ and $j\psi$. Therefore, ${}^a p_i(j1)\ldots..\ {}^a p_i(j\psi)$ defines the APD of particles travelling with flow rates $j1\ldots.j\psi$.

$${}^a\xi_j = \min\left[\chi_{j1},\ldots,\chi_{j\psi}\right] \qquad \text{(Equation 7.6)}$$

In ***Equation 7.6*** the minimum value, ${}^a\xi_j$, then defines a particle to have a flow rate j.

The APD function, $p_i(j)$, for a particle travelling at flow rate j in all cases was defined according to ***Equation 7.7***:

$${}^{a}\mathrm{p_i(j)} = \frac{\sum_{m=1}^{r} a_j(m,t)}{\sum_{t=0}^{\delta}\sum_{m=1}^{r} a_j(m,t)} \qquad \text{(Equation 7.7)}$$

Where $a_j(m,t)$ is the function defining a single particle autocorrelation curve. m is equal to the total number of bursts summed at a given flow rate j.

Figure 7.5 shows the change in the APD function versus the number of peaks summed. These data were obtained for single particles travelling with a velocity of 2000 nL/min. All other conditions were identical to those described for the PPD function. The distributions themselves are comparable to that of the PPD in the sense that summing 200 peaks or greater yields a stable probability function. There is virtually no change between the APD's after this point. Below this value, the probability distribution shows a large degree of fluctuation. Again, this can be clearly seen in the first 50 peaks of ***Figure 7.5***. Although an APD can be defined with as little as 100 particle bursts, to ensure the distribution has converged, a minimum of 700 particle bursts were used in determination of the APD's.

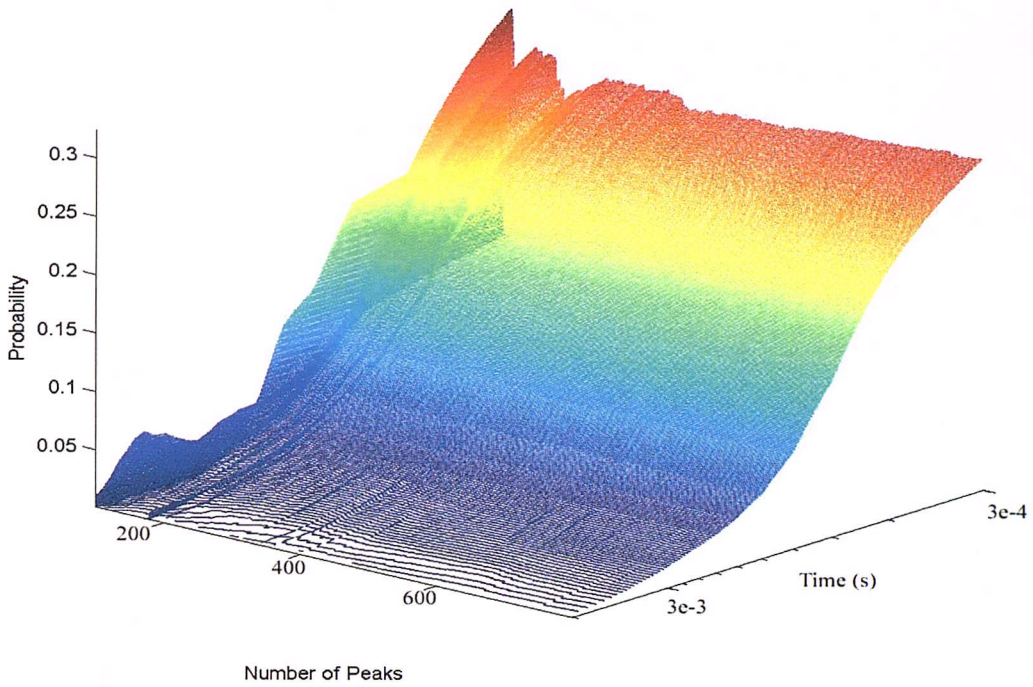


Figure 7.5 Variation of the autocorrelation probability distribution function for 0.93 μm fluorescent particles travelling at a flow rate of 2000 nL/min as a function of the number of bursts analysed.

7.4 Results

7.4.1 Probability distributions

7.4.1.1 Peak probability distribution

Figures 7.6a and 7.6b shows the peak probability distribution functions for particulate bursts at flow rates ranging from 100 nL/min – 2000 nL/min. Using this approach, it can be seen that as flow rate increases, the PPD full width half maximum narrows. It is interesting to note that the probability maximum of each function progressively decreases in magnitude as the flow rate is decreased. For example, the PPD maximum is 0.28 for a flow rate of 2000 nL/min whereas at a flow rate of 100 nL/min the PPD maximum is 0.03. This indicates that at lower flow rates there is a greater probability of a single particle burst occurring over a longer time frame than at higher volumetric flow rates. This is expected, as at higher flow rates particles spend on average less time within the confocal probe volume. For example, at a flow rate of 2000 nL/min it would be unlikely to find a photon burst duration of greater than 10 ms as the

calculated probability of this occurring would be less than 0.1 %. This is confirmed from experimental data (i.e. the average burst width is equal to 3.5 ms with an RSD of 60 %). If in fact there is prior knowledge of the particle and its environment, an exact flow rate can be statistically assigned from the fluorescence burst of a single particle.

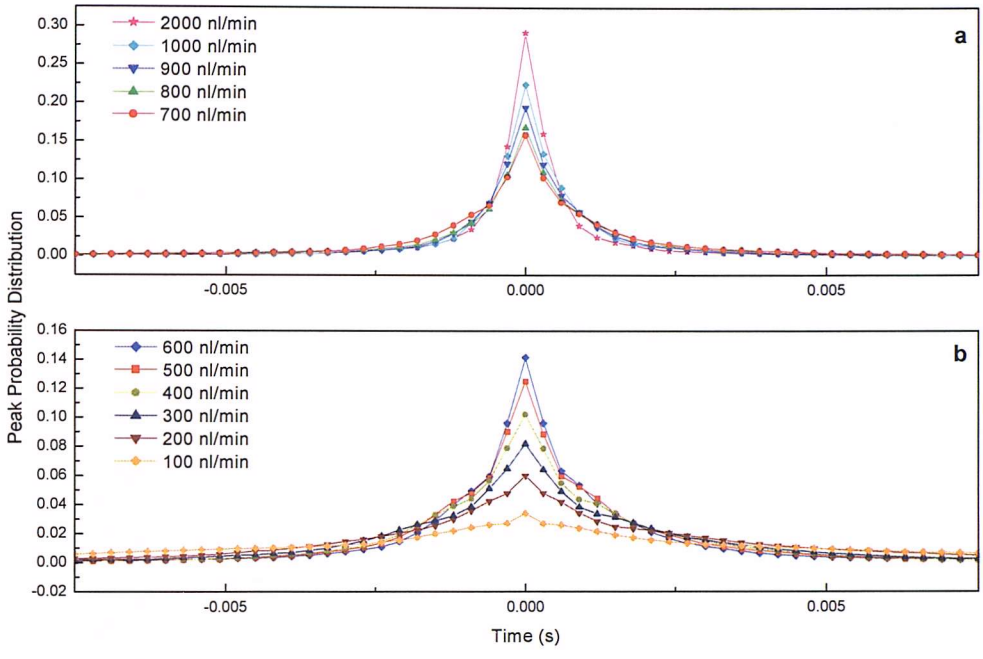


Figure 7.6 Peak probability distribution functions for 0.93 μm fluorescent particles travelling at flow rates between (a) 700 – 2000 nL/min and (b) 100 – 600 nl/min.

7.4.1.2 Autocorrelation probability distribution

Figure 7.7 shows the APD for single particle bursts with flow velocities ranging from 100 nL/min – 2000 nL/min. Photon burst scans were acquired with a dwell time of 300 μs; therefore the minimum autocorrelation time is also 300 μs. 200 data points were used per autocorrelation curve. Only the first 100 points are shown in ***Figure 7.7*** as the primary variation in the APD occurs at early times.

As with the previous approach (PPD), a difference is observed when comparing the APD at different flow velocities. As the flow rate increases, the APD full width half maximum (FWHM) decreases. The FWHM is defined by the time at which the autocorrelation curve is at half the maximum height. This can be directly attributed to the particulate burst width decreasing as the flow velocity is increased. Not only do the curve maxima decrease in magnitude as the flow velocity is increased, but the FWHM also increase as the velocity is decreased. For example, the APD maximum is 0.28 for a flow rate of 2000 nL/min whereas at a flow rate of 100 nL/min the APD maximum is 0.03. Not surprisingly, these maxima are

identical to the maxima in the PPD. This is attributed to the first point in the autocorrelation curves simply being the square of all data points for a given particle burst. This indicates that as the FWHM is increased there is a greater probability of a single particle burst occurring over a longer time. The autocorrelation curves, in a sense, can be considered to be a weighted distribution when compared to particle bursts and were calculated according to ***Equation 7.8***. Such a distribution is useful as it can potentially be used to classify single particle bursts with greater certainty than the simpler PPD. This is attributed to the fact that autocorrelation curves can typically discriminate more efficiently between particles travelling at different velocities than simply observing burst characteristics (area, width).

$$a(\tau) = \sum_{m=1}^{r} \sum_{t=0}^{N-1} g(t)g(t+\tau) \qquad \text{(Equation 7.8)}$$

Here $g(t)$ is the total number of counts during the time interval $(t,t+\Delta t)$, $g(t+\tau)$ is the number of counts detected in an interval of Δt at a later time $t+\tau$, N is the total number of time intervals in a single particle burst and r is defined as the total number of particle bursts.

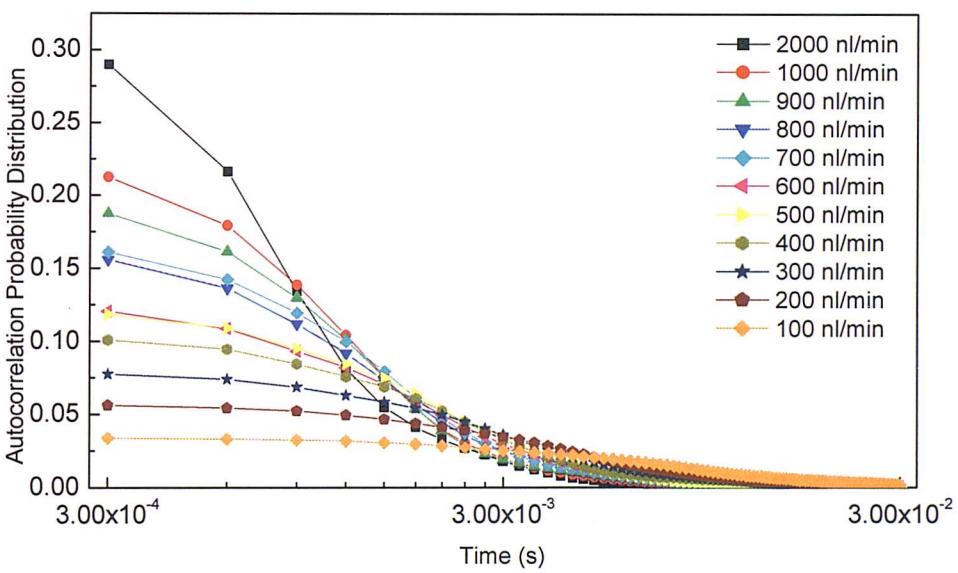


Figure 7.7 Autocorrelation probability distribution functions for 0.93 µm fluorescent particles travelling at flow rates between 100 – 2000 nL/min.

7.4.1.3 Theoretical approximation of the PPD

In the previous sections it was shown that purely experimental data could be used to calculate the PPD and APD according to ***Equations 7.4*** and ***7.7*** respectively. This approach would in fact be useful if and only if a sample with multiple flow velocities could be compared to a known standard. Another possibility would be to create the probability functions strictly from

theory. An example of a PPD obtained with a Monte Carlo method is shown in ***Figure 7.8***. The simulation itself was identical to that described in ***section 4.3.4*** without inclusion of hydrodynamic focussing. The simulated photon burst scans for particles flowing within a 100 μm wide microfluidic channel were then processed using standard analysis routines (i.e. BWH, BAH, BHH etc...). The flow velocity was defined to be 1000 nl/min and diffusion was considered to be negligible perpendicular to the direction of flow. For example, the diffusion time perpendicular to the flow direction for 1000 nm particles at a flow velocity of 1000 nl/min will not deviate by more than 1 – 2 % across the probe volume. An example of a case where diffusion of the particles through the probe volume is dominant (flow velocity of 200 nl/min) is shown in the bottom of ***Figure 7.8***. In this case, there is a clear mismatch between the PPD and the simulated curve which arises due to the effects of diffusion becoming more dominant. The simulated distribution was normalized to that of the experimental data to visualize the degree of mismatch. The clear mismatch in the curves arises due to diffusion not being taken into account in the simulated PPD. In all cases, the dwell time was defined to be 300 μs (the same as experimental data) and the resolution (or time constant) of the simulation was defined so that there would be a minimum of 5 points per particle burst.

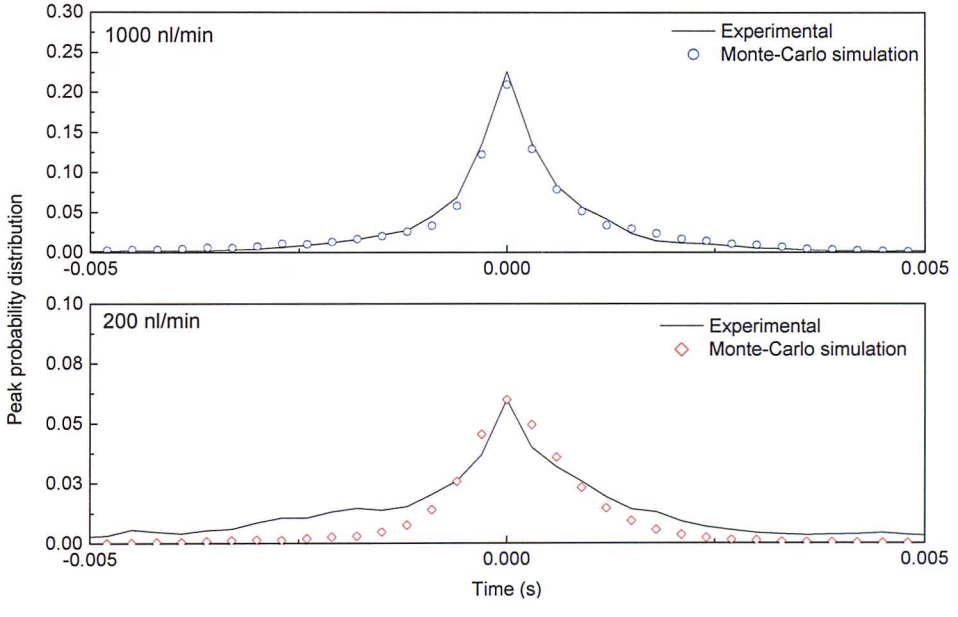


Figure 7.8 Experimental and simulated peak probability distribution functions for 0.93 μm fluorescent particles travelling at flow rate of 1000 nl/min (top) and 200 nl/min (bottom).

The Monte Carlo simulations themselves were in good agreement with the experimental data at higher flow velocities when diffusion becomes negligible. The slight divergence when comparing the experimental and theoretical data is attributed to the collection efficiency function of the detector as well as the microscope objective not being entirely accounted for. A more sophisticated simulation should result in an even better fit. With this in mind, the PPD

does not necessarily have to be determined with experimental data as a simulated PPD can prove to be just as efficient. This method would be extremely valuable if flow standards are not available.

7.4.2 Distinguishing between single particles travelling at 2 distinct flow rates

7.4.2.1 Using the peak probability distribution

If a system is assumed to consist of two particle populations travelling at distinct flow velocities (for example in an electrophoretic separation), a single particle may be statistically tested to be of a given velocity by inserting the particle's photon burst distribution (n_i in ***Equation 7.1***) into two separate MLE Equations. The PPD function in each equation is chosen to coincide with one of the two velocities in question. The two MLE equations can then be subtracted from one another ($\varepsilon = \gamma_a - \gamma_b$; $a=j1$, $b=j2$). If ε is less than 0 then the particle in question is more likely to resemble that of a system of particles travelling with a flow rate of velocity *a*. If on the other hand ε is greater than 0, the particle in question would have a higher probability of having a flow rate *b*. The greater the value of $|\varepsilon|$, the higher the probability a particle will be assigned a correct flow rate. If a particle in question is travelling at velocity *a* and has a burst distribution identical to that of the PPD, then γ_a would equal 0 and hence the particle can be identified with 100 % certainty to be travelling at a flow rate *a*.

Figures 7.9 a and 7.9 b show ε value histograms where γ_a is assigned using a PPD flow rate of 2000 nL/min and γ_b has assigned PPD flow rates ranging from 100 nL/min – 1000 nL/min. In all cases the trial data, n_i, inserted into γ_a and γ_b had particulate flow velocities of 2000 nL/min. The histograms were binned into values of 50 and were generated using a minimum of 700 particle bursts. An ideal situation would be for all particle bursts to resemble that of a PPD at a flow rate of 2000 nL/min and hence the ε values would be expected to be highly negative. For comparison, ***Figures 7.9 c and 7.9 d*** show ε value histograms where γ_a is assigned using a PPD flow rate of 500 nL/min and γ_b has assigned PPD flow rates ranging from 100 nL/min – 2000 nL/min. In all cases the trial data, n_i, inserted into γ_a and γ_b had particulate flow velocities of 500 nL/min.

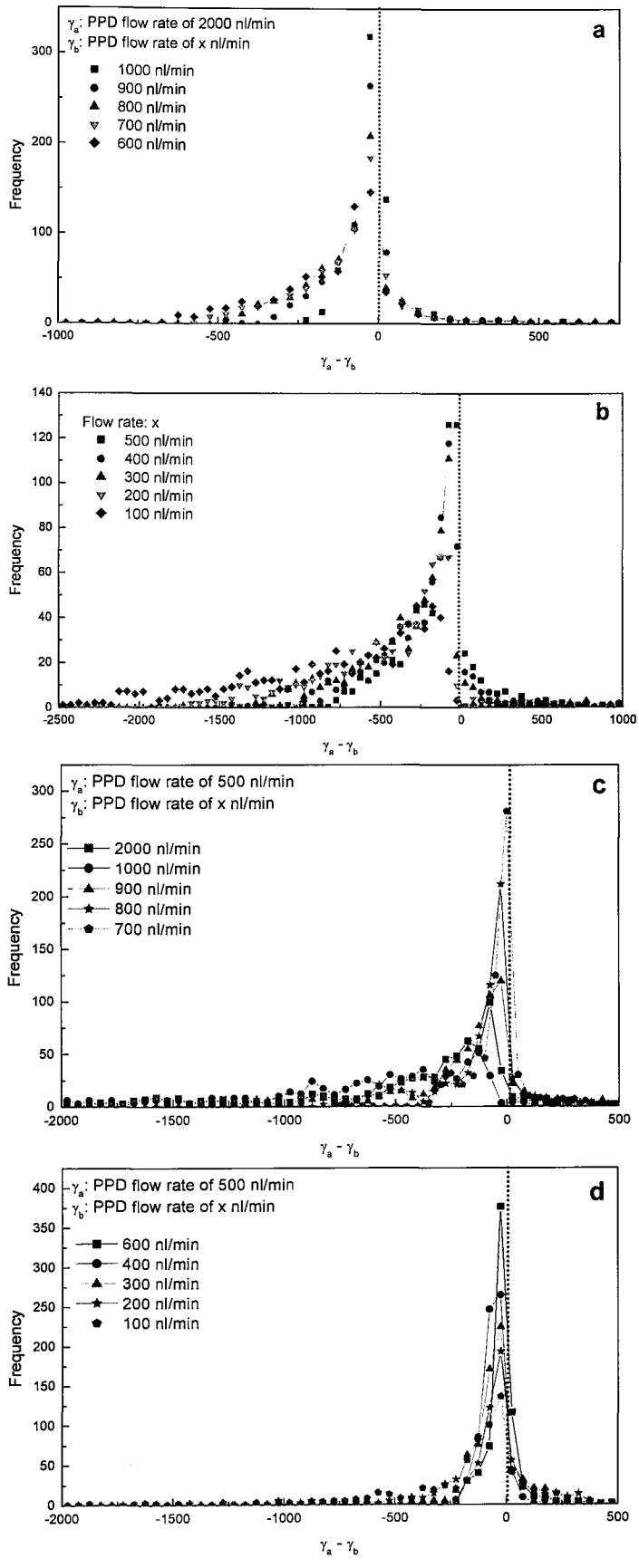


Figure 7.9 ε values for an actual particulate flow rate of 2000 nL/min. γ_a PPD had flow rates of 2000 nL/min (a –b), and 500 nl/min (c-d). The γ_b PPD has flow rates ranging from 100 – 2000 nL/min.

Several interesting observations can be made from ***Figure 7.9***. Firstly, for all γ_b, the majority of ε values were less than or equal to 0, hence the majority of the particles were assigned a correct flow rate of 2000 nL/min and 500 nl/min respectively. Secondly, as the γ_b PPD flow rate approached that of γ_a, ε is shifted towards more positive values. This occurs since particles travelling at flow rates in the vicinity of 2000 nL/min and 500 nl/min would have greater similarity in individual fluorescence burst character when compared to a system with particles travelling at a larger flow rate difference (e.g. 2000 nL/min and 100 nL/min). Thirdly, as the γ_b PPD flow rates approached values much lower than that used in γ_a, it was less likely for ε to be assigned a positive value and hence it was less likely for a particle burst to be assigned an incorrect velocity. As can be seen in ***Figure 7.9a and 7.9b***, ε also approached much lower negative values as the PPD flow rates of γ_b were decreased. For example, When the γ_b PPD was assigned a flow rate of 100 nL/min, a frequency of 10 particle bursts was obtained at ε = -1300. At a γ_b PPD flow rate of 1000 nL/min 0 particle bursts were recorded at ε = -1300.

7.4.2.2 Errors in assignment of flow velocities using the PPD

The degree of error associated with assigning single particles a specific velocity in the manner described above can be seen in ***Figure 7.10***. The percentage of ε greater and less than zero is plotted for the same system as described in ***Figure 7.9***. For a 20x difference in flow rates (2000 nL/min and 100 nL/min), there is virtually a 0 % error rate. Almost all particle bursts are correctly assigned a flow rate of 2000 nL/min. When a flow rate difference of 4x is used, 88 % of the particles travelling through the confocal probe volume are assigned a correct flow velocity of 2000 nL/min. Finally, when the PPD flow rates have a factor of two difference, 78% of all particle bursts still appear to have a particle burst characteristic resembling that to a PPD taken at a flow rate of 2000 nL/min.

It should be noted that the error in assignment will decrease if the width and depth dimensions of the microfluidic channel are decreased. This would be a result of a limitation in particle trajectories through the confocal probe volume; hence, each particle burst would be more similar in character. This would result in the average burst areas having a lower RSD (Chapter 3). This can easily be achieved by the use of hydrodynamic focussing within a wide microfluidic device or by the direct fabrication of a chip with smaller dimensions (Chapter 4). Clearly, if a specific quantity of particles is known to have the same velocity, ε can be averaged. This would result in a lower number of particles assigned incorrect velocities. A primary advantage of using the statistical approach developed is that a single particle can be assigned a single velocity with little uncertainty.

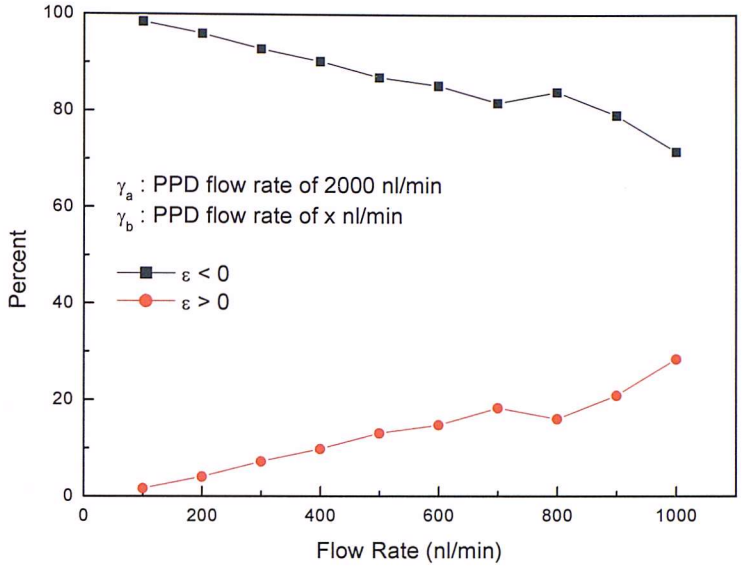


Figure 7.10 The percent error in assigning correct and incorrect flow velocities to single particles in a system with particles travelling at two distinct flow rates as a function of the PPD flow rate in γ_b. In all cases the γ_a PPD flow rate was defined to be 2000 nL/min.

7.4.2.3 Errors in assignment of flow velocities using the APD

The degree of error associated with assigning single particles a specific velocity using the APD function can be seen in the top panel of ***Figure 7.11***. Qualitatively, the trends are identical to the data shown in ***Figure 7.10***. The photon burst scans were acquired under identical conditions. The only difference was in the analysis method being used; the APD was used instead of the PPD. For a 20x difference in flow rates (2000 nL/min and 100 nL/min), there is virtually a 0 % error rate. Almost all particle bursts are correctly assigned a flow rate of 2000 nL/min. When a flow rate difference of 4x is used, an improvement in assignment occurred with 93 % of the particles travelling through the confocal probe volume being assigned a correct flow velocity of 2000 nL/min.

The bottom plot in ***Figure 7.11*** shows the difference in errors associated with assigning velocities using the APD and the PPD. At all flow velocities, higher precision was obtained with the APD function. For example, when a flow rate difference of 4x is used, 93 % of the particles are assigned a correct flow velocity whereas only 88 % of the particles are assigned correct velocities using the PPD. Although, the PPD produces larger errors, it is perhaps still beneficial to use this method if the analysis were to be conducted in real-time as the analyte travels within the probe volume. The APD requires post-data processing and as such, the autocorrelation algorithm used would result in a significant lag time.

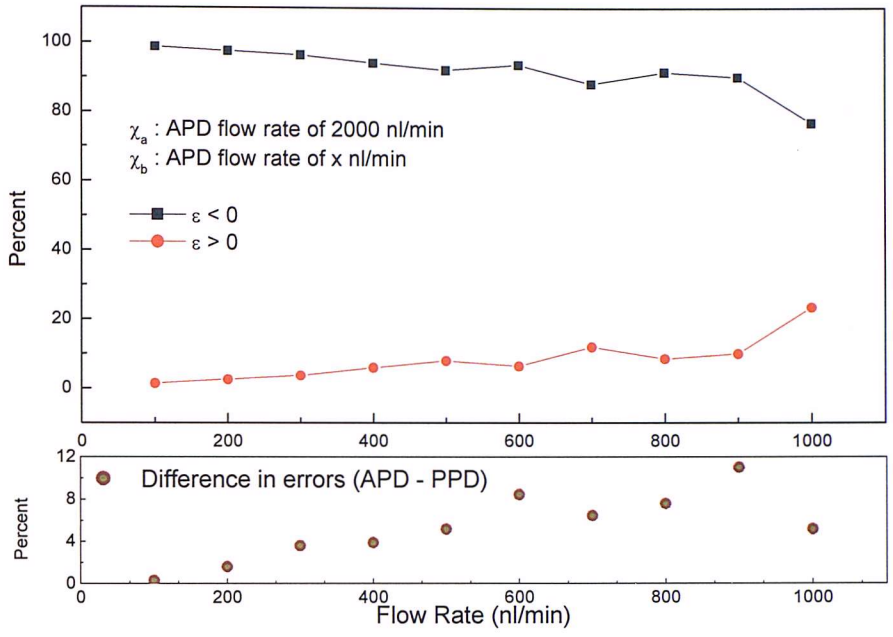


Figure 7.11 (Top) The percent error in assigning correct and incorrect flow velocities to single particles in a system with particles travelling at two distinct flow rates as a function of the APD flow rate in χ_b. In all cases the χ_a APD flow rate was defined to be 2000 nL/min. (Bottom) Difference between assigning velocities using the APD and PPD.

7.4.3 Distinguishing between single particles travelling at multiple flow rates

7.4.3.1 Using the peak probability distribution

The following paragraphs discuss a statistical approach that can distinguish between single particles travelling at different flow rates. Single particle bursts can easily be tested for a specific flow rate simply by comparing the MLE values using various PPD functions. As in ***Equation 7.3***, the minimum of these values (ξ_j) correlate a single particle flow rate to a theoretical value. ***Figure 7.12a*** plots the MLE values of 20 peaks using PPD flow rates ranging from 100 – 2000 nL/min. In this case the experimental particle burst data used in conjunction with these functions had a flow rate of 2000 nL/min. ξ_j in 90 % of the cases resulted from using a PPD flow rate of 2000 nL/min hence particle burst were correctly identified 9 times out of 10. Importantly, it should be noted that recovered MLE values increase as the trial PPD flow rate is decreased.

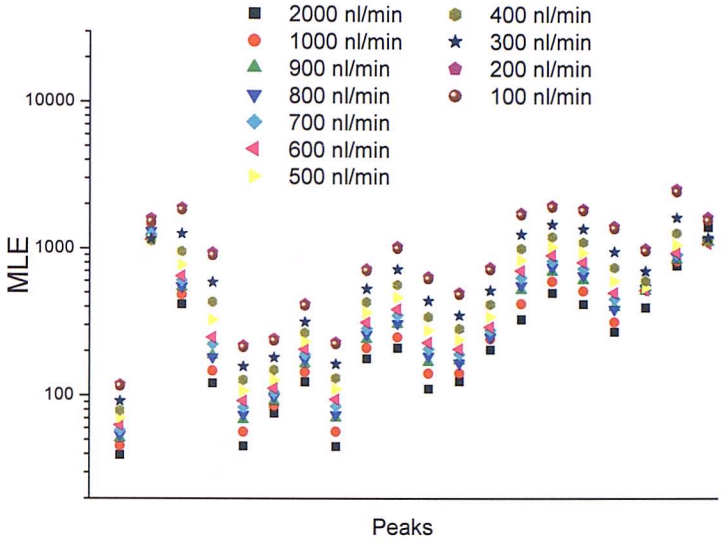


Figure 7.12 (a) MLE values calculated with PPD flow rates of 100 – 2000 nL/min for single particles travelling at a flow rate of 2000 nL/min.

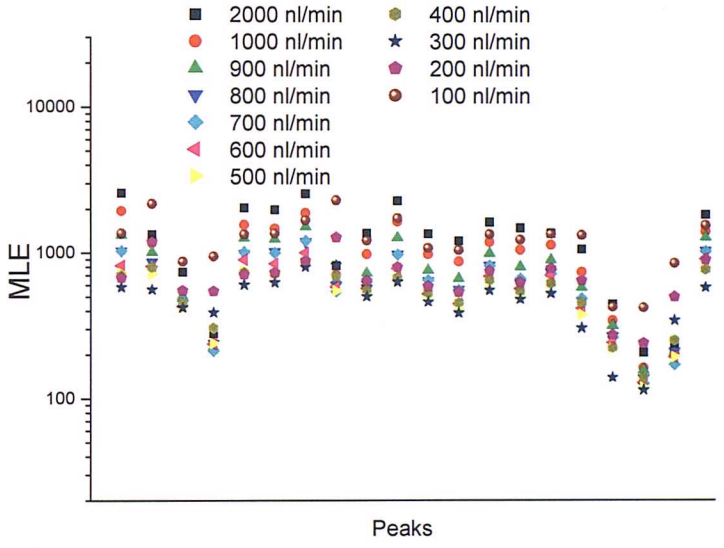


Figure 7.12 (b) MLE values calculated with PPD flow rates of 100 – 2000 nL/min for single particles travelling at a flow rate of 300 nL/min.

Figure 7.12b shows a similar plot to that in 7.10a, however in this case experimental data with a flow rate of 300 nL/min were used. As in the previous case, the majority of particles are correctly assigned to correct flow velocities. It should be noted that in the case of incorrectly assigned flow velocities, values within 0.5x - 2x of the actual velocity were assigned. For example, in a system with particles travelling at a flow rate of 300 nL/min all particle bursts would be assigned volumetric flow rates ranging from 200 nL/min - 400 nL/min using the MLE approach. In the majority of cases the highest MLE values for a given particle resulted from the use of a PPD flow rate of 2000 nL/min or 100 nL/min (the two extreme velocities surrounding the experimental flow rate of 300 nL/min). For a system where particles detected

in a confocal probe volume are travelling with relatively different velocities, the approach described above may prove to be highly beneficial in distinguishing between them.

7.4.3.2 Using the autocorrelation distribution

The APD can also be efficiently used to test whether a single particle has a specific velocity. An example of this is shown in ***Figure 7.13***. In this case the particles were travelling at a flow velocity of 2000 nl/min and the trial APD's had velocities ranging from 100 nl/min – 2000 nl/min. A clear trend shows that that χ_b continuously decreases as the trial APD flow velocity is increased. For all peaks, no velocities were incorrectly assigned. Varying the flow velocity conditions resulted in at least 90 % of all particles being assigned correct flow velocities and is comparable with the data obtained from PPD function analysis. The majority of incorrectly assigned particle flow velocities would occur at trial flow rates in the vicinity of the actual flow velocity due to the resemblance in the burst and autocorrelation characteristics.

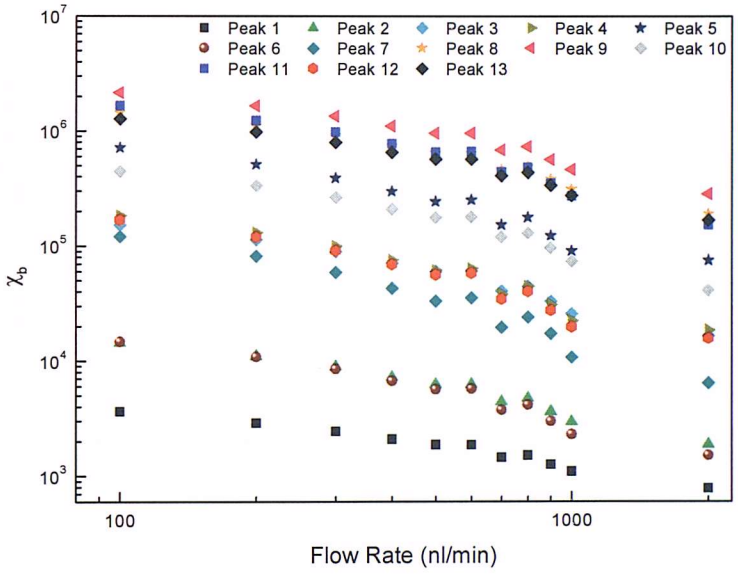


Figure 7.13 χ_b values calculated with APD flow rates of 100 – 2000 nL/min for single particles travelling at a flow rate of 2000 nL/min.

It must be emphasized that the likelihood of incorrectly assigning a particle burst should decrease as the overall flow velocities of both the APD and the particle velocities are increased within a microfluidic channel. This is a result of the linear velocity increasing within the channel and hence the burst widths and areas will be more clearly defined. This was demonstrated in chapter 5 – increasing the linear velocity results in more uniform burst width distributions. If analysis of the particle bursts does not need to be performed in real time, a combination of both the APD and PPD approaches results in an extremely powerful method for determining particulate velocities based strictly on a single particle burst.

7.5 Summary

A simple statistical method was developed to distinguish between particles traveling at different flow rates through a confocal probe volume within a microfluidic channel. The method is based on the use of the MLE (and was used in fluorescence particle burst pattern recognition). From the results described herein a similar approach appears to be completely compatible in distinguishing between individual fluorescence burst characteristics of particles traveling at different flow rates. Although fluorescent particles were used in this feasibility study, a similar approach could be used to distinguish between molecular flow velocities. In fact, this statistical method would be useful for any system where different flow characteristics are observed from different molecules or particles.

It should be realized that this approach for determining flow velocities is valuable if prior information on the PPD or APD is available (i.e. particle size, flow velocity). For example, if a database of PPD or APD functions is available for a large quantity of flow rates, the experimental data can be statistically compared and each particle or molecule studied can be assigned an appropriate flow rate. A Monte Carlo simulation can also be performed to extract theoretical PPD's at specific flow velocities. This is useful if standards are not available for a given system. The larger the difference in particle velocities the greater the certainty a single particle will be assigned a correct flow rate.

7.6 References

(1) Li, T. F. *Pattern Recognition* **1996**, *29*, 337-339.

(2) Maus, M.; Cotlet, M.; Hofkens, J.; Gensch, T.; De Schryver, F. C.; Schaffer, J.; Seidel, C. A. M. *Analytical Chemistry* **2001**, *73*, 2078-2086.

(3) Herten, D. P.; Tinnefeld, P.; Sauer, M. *Applied Physics B-Lasers and Optics* **2000**, *71*, 765-771.

(4) Sauer, M.; Angerer, B.; Han, K. T.; Zander, C. *Physical Chemistry Chemical Physics* **1999**, *1*, 2471-2477.

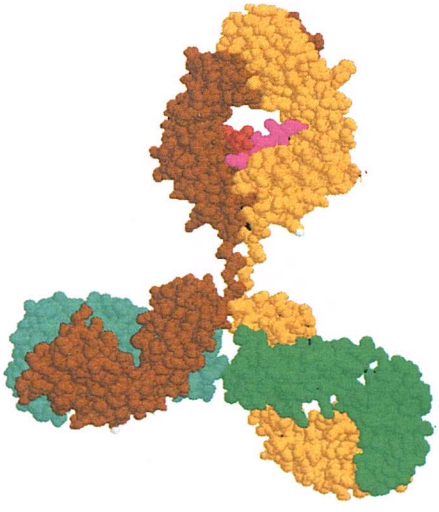
(5) Sauer, M.; Arden-Jacob, J.; Drexhage, K. H.; Gobel, F.; Lieberwirth, U.; Muhlegger, K.; Muller, R.; Wolfrum, J.; Zander, C. *Bioimaging* **1998**, *6*, 14-24.

(6) Kollner, M.; Wolfrum, J. *Chemical Physics Letters* **1992**, *200*, 199-204.

(7) Kollner, M.; Fischer, A.; ArdenJacob, J.; Drexhage, K. H.; Muller, R.; Seeger, S.; Wolfrum, J. *Chemical Physics Letters* **1996**, *250*, 355-360.

- 8 -

This chapter describes an approach to distinguish between protein labeled fluorescent particles in flowing solutions using single particle confocal spectroscopy. Analysis of autocorrelation curves, burst width histograms, and a burst area-height histograms are shown to be highly sensitive methods in distinguishing between proteins of different molecular weights. The basic techniques are then applied to the analysis of immunoglobulin G and anti human immunoglobulin G on human sperm heads.



Identification of single protein molecules in solution

8.1 Introduction

Immunoassays represent one of the most valuable protein identification methods used in bioanalytical sciences.[1-3] An immunoassay is essentially a test that utilizes antibodies to identify and quantify proteins or other biological molecules. Often the antibody is linked to a marker such as a fluorescent molecule, a radioactive molecule, or an enzyme. One of the most widely used methods to quantify antigen-antibody reactions is the enzyme-linked immunosorbent assay (ELISA).[4-6] For example Kwak and co-workers developed a new system designed for cell surface display of recombinant proteins on Escherichia coli. Fluorescence-activated cell-sorting analysis along with ELISA was used to confirm the successful expression of HIV-I on the surface of Escherichia coli.[7] ELISA was initially developed to detect serum antibodies, however they prove to be useful in many fields. For example, recently they have been used in environmental studies for the direct analysis of the quantization cross reacting of herbicides in environmental samples.[8] ELISA has become a fundamental tool for drug discovery, and clinical trials in the pharmaceutical industry because of the ability to assess large quantities of samples.

Although ELISA is currently the industry standard, the trend toward miniaturization and higher sample throughput has resulted in a preference for assays that are easily automated. With this in mind, several microfluidic-based systems have been proposed for use in assays and diagnostic tests. In most cases, proteins within microchannels are characterized using electrophoretic type separations.[9-12] For example, a microscale capillary electrophoresis device has been used to separate the products of a homogeneous reaction using monoclonal mouse immunoglobulin G (IgG).[10] A detection limit of 135 μg/ml was achieved for a mouse antibovine serum albumin-IgG assay. A bead based assay for use within microfluidic channels has recently been described by Buranda et al.[13] Their method involves real - time detection of soluble molecules binding to receptor-bearing microspheres. The assay can detect sub-femtomole quantities of antibody with a high signal-to-noise ratio over a dynamic range spanning nearly 4 orders of magnitude in analyte concentration. The primary benefit in using micron sized particles is the high immunosorptive area that is available for conjugation of the protein to the particle. Furthermore, since beads are exposed to the entire sample, collection takes place from the entire volume. This allows for rapid binding of the proteins to the microbeads.

Single microbead based assays can clearly improve detection limits even further. Although it is not immediately obvious, it will be shown in the following sections that only a handful of labeled particles and a sampling time below 1 s are required to distinguish between 2 types of

proteins in a free flowing solution. The approach used involves characterizing photon bursts of single fluorescent particles labeled with the proteins under investigation (in this case IgG and Human serum albumin) in a free flowing solution. The general aim is to be able to distinguish between different particles with high precision in a freely flowing solution within a microfluidic channel. This would allow for ultra rapid acquisition and analysis times and could potentially result in an extremely powerful approach to performing immunoassays. Using such an approach can directly improve measurement precision as well as decreasing overall sample consumption.[14-16]

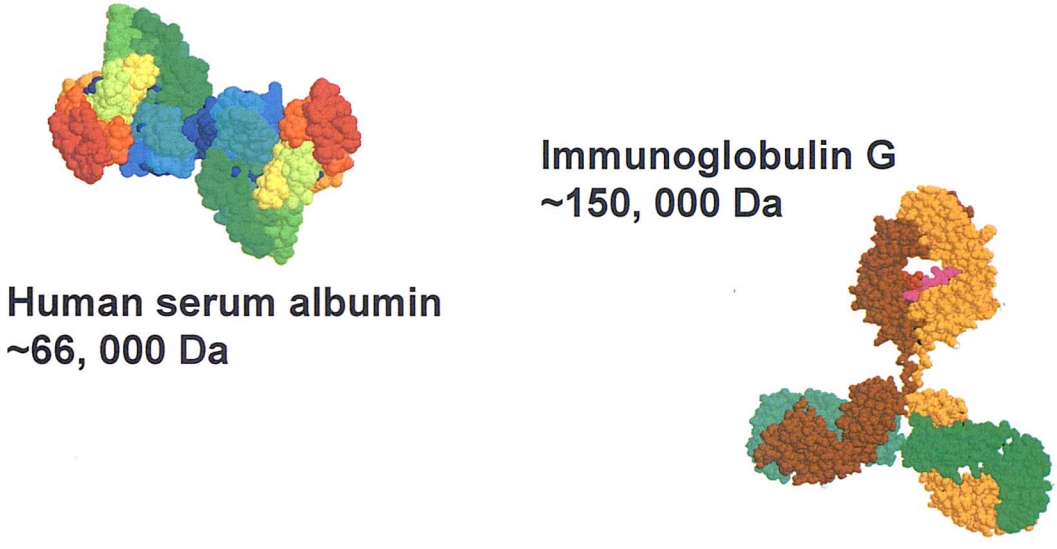


Figure 8.1 Model of the HSA and IgG molecules from x-ray diffraction studies.

IgG and HSA were chosen as model compounds for the current studies due to a large difference in their molecular weights. Hence, these molecules are useful in characterizing the detection system. IgG has molecular weight of 150, 000 Da and HSA has a molecular weight of 66, 000 Da. When a foreign substance such as a virus, bacterium, or foreign protein invades the human body, the body defends itself by invoking an immune response (IR). The substance eliciting an IR is called an antigen and the specific immunoglobulin that binds to the substance is called an antibody. IgG is an example of such an immunoglobulin and is the most abundant of the circulating antibodies. Representation of the structures of IgG and HSA are shown in ***Figure 8.1***. HSA contributes to many transport and regulatory processes in the body. It has multifunctional binding properties which range from various metals, calcium and copper, to fatty acids, hormones and therapeutic drugs. Distribution, free concentration, and metabolism of various pharmaceuticals can be significantly altered as a function of the magnitude of binding with HSA.[17]

In the first part of this chapter a method is developed to distinguish between IgG and HSA labeled fluorescent particles using single particle confocal spectroscopy. Statistical methods such as autocorrelation analysis, burst width histogram analysis, and a burst area-height analysis will be shown to be highly successful in distinguishing between proteins of different molecular weights. In the second part of the chapter, a "real life" application is presented which can potentially be used to distinguish between IgG and anti human IgG on human sperm heads. This approach will not only guarantee improvements in detection sensitivity, but also improve analytical throughput when compared to conventional approaches.

8.2 Experimental

8.2.1 Materials

Carboxylate modified fluorescent microbeads having a mean diameters of 200, 500, and 930 nm were used for all experiments. The beads were sonicated for 10 minutes immediately before use to ensure good dispersion. Covalent coupling of proteins was performed using a water soluble carbodiimide (EDAC, Molecular Probes) to activate the surface carboxyl groups of the microspheres. Human serum albumin (HSA) and immunoglobulin G (IgG) were purchased from Sigma chemicals.

8.2.1.1 Labeling of fluorescent spheres with protein

The covalent coupling of the fluorescent spheres to protein was performed according to the following generic procedure:

1) 1 litre of 50 mM phosphate buffer was prepared and adjusted to pH 7.4 with 0.1 M NaOH.

2) 1 litre of 50 mM 2-(N-Morpholino)-ethanesulfonic acid (MES) was prepared and adjusted to a pH 6.0.

3) IgG was purchased at a concentration of 50 mg/ml. Hence, a 20 x dilution was performed in MES buffer to obtain an IgG concentration of 2.5 mg/ml.

4) 100 µl of a 1% aqueous suspension of carboxylate modified microspheres was then added to the diluted IgG solution. This mixture was incubated at room temperature for approximately 15 min.

5) In order to activate the microspheres, 400 µg EDAC was then added to the solution and mixed by vortexing. At this point agglomeration of the particles is observed. The pH was therefore adjusted to 6.5 and the mixture was sonicated for 5 min. This caused the particles to redisperse.

6) If the pH was not adjusted before sonication, it was adjusted after with 0.1 M NaOH. The reaction mixture was allowed to incubate on an orbital shaker for 12 hr at room temperature. The vials were covered in aluminium foil to ensure a negligible amount of photodegredation of the fluorescent particles occurred prior to use.

7) 1.9 mg of glycine (Gly) was added to the vials to give a final concentration of 100 mM to quench the labeling reaction. The mixture was allowed to incubate for 30 min on an orbital shaker.

8) The final mixture of labeled particles was diluted in a phosphate buffer solution so that the final particle concentration would be $2.3x10^7$ beads/cm^3. For 930 nm particles, the mixture was further diluted by 300 x.

It was not necessary to separate the labeled protein microspheres from unreacted protein as significant dilutions ensure single particle occupancy within the probe volume at any instant. As such the presence of free protein did not affect the experiments. Prior to use, the diluted solutions were sonicated for a minimum of 10 minutes. The fluorescent beads cannot be stored below 0 °C hence the complete solutions were stored for a maximum of 3 days at 5 °C.

The HSA labeled particles were prepared in the manner described above with the following exception. HSA was purchased as a solid; therefore, 4 mg was dissolved in 2 ml of the MES buffer to obtain a working protein concentration of 2 mg/ml.

8.2.1.2 Characterization of IgG and HSA labeled particles

To confirm the binding of protein to the carboxylate modified particles, capillary electrophoresis (CE) was performed on the 500 nm labeled particles. A 200 x dilution from the stock particle concentration was used for all runs. All experiments were performed on a

P/ACE 2050 capillary electrophoresis system (Beckman Coulter, UK) equipped with an argon ion laser that provides an excitation wavelength of 488 nm. A notch filter (488nm) was employed at the detection window to filter the laser beam from emitted fluorescence. Separations were carried out in an uncoated fused-silica capillary with an internal diameter of 50 μm and an effective total length of 20 cm (27 cm). A constant voltage of 15 kV (556 V/cm, current, 140-150 μA) was used for separation and the positive electrode was on the sampling side. Sample injection occurred by pressure for 5s. The temperature of the capillary was kept at 25 °C. Before CE separations, new capillary columns were conditioned by rinsing with 0.1 M NaOH for 30 min and with water for 10 min, followed by running buffer for 5 min. The capillary was rinsed with running buffer for 2 min between separations. In order to prevent capillary blockage, the buffer was filtered using 0.2 μm filters (Fisher Scientific, UK). It was not possible to filter the particle solution as particle sizes were greater than the filtering pore size. In order to ensure blocking did not occur, a sufficiently dilute analyte solution was used. Prior to use the samples were sonicated for 5 min in ice cold water. The sonication in cold water ensures that protein labeled particles do not disintegrate due to the potential heating of water during sonication.

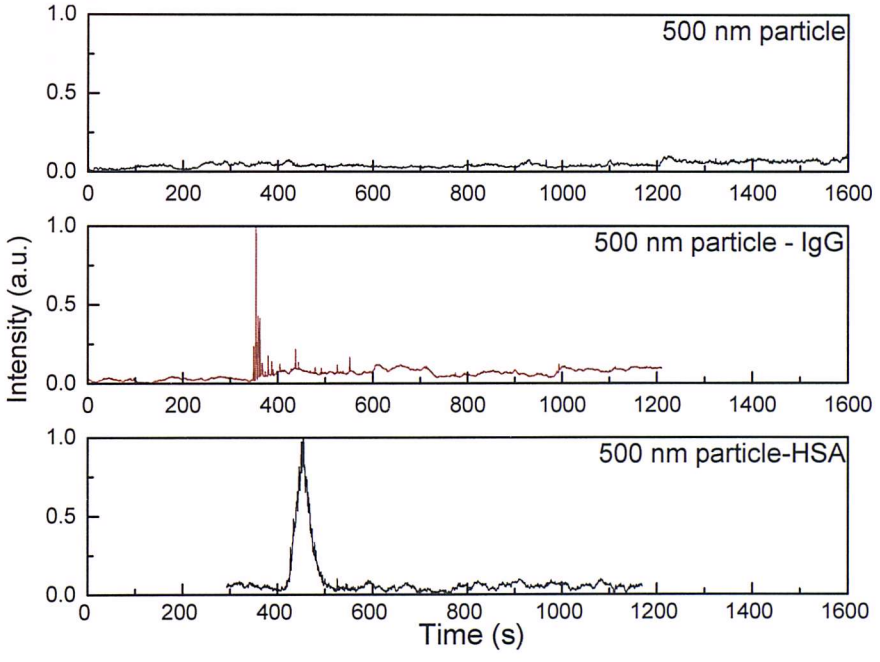


Figure 8.2 Electropherograms obtained by applying a separation voltage of 15 kV for 500 nm fluorescent particles (top), labeled with IgG (middle) and HSA (bottom) in a 50 mM phosphate buffer (pH 7.4).

Electropherograms of 500 nm particles and 500 nm particles labeled with HSA and IgG are shown in ***Figure 8.2***. Unfortunately a peak is not observed when analysing the unlabeled microspheres over a 30 minute period. Several scans were also run over time periods of 5

hours; however, a peak was never observed. This is most likely due to the highly negative charge character of each carboxylate modified particle at a pH of 7.4. Labeling of the particles with HSA and IgG will result in a significantly lower negative charge at a pH 7.4. Peaks from both HSA and IgG modified particles occurred 5 min after injection. This confirms that the particles were successfully labeled. The degree of labeling will be discussed in a later section of this chapter.

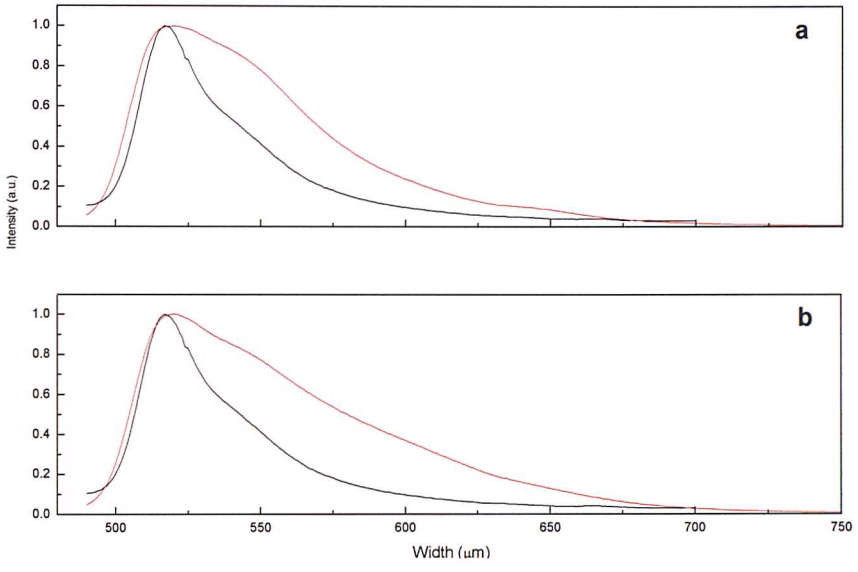


Figure 8.3 Emission spectra of (a) 500 nm carboxylate modified particles (black) and IgG labeled particles (red) (b) 500 nm carboxylate modified particles (black) and HSA labeled particles (red). An excitation wavelength of 460 nm was used for all measurements.

Electrophoresis is perhaps the best way to confirm whether or not labeling was in fact successful. Another, more indirect, approach is to simply look at photoluminescence characteristics. Fluorescently labeled particles typically exhibit changes in their emissive properties that arise from the interaction between fluorophore and protein.[18] An example of this is shown in ***Figure 8.3***. In both cases it can be seen that broadening of emission spectra occurs on binding. This does not directly confirm that the carboxylate modified particles have been successfully labeled but rather confirms that a photophysical change arises due to the interaction between the protein molecules and the free particles. It should be noted that the free particles and particle conjugates could be monitored and discriminated in real time using time-tagged TCSPC since fluorescence lifetimes of the labeled and unlabeled particles would almost certainly be different. Unfortunately, due to a lack of time these measurements were not performed.

8.2.2 Microfluidic channel design

All experiments were performed within microchannels of the following dimensions: width 60 μm, depth 30 μm and length 16 mm. Fused silica capillaries (150 μm id and 350 μm od) were used to interface the inlet reservoir with a syringe pump. The top plate of the microfluidic device in this case was polished down to a thickness of 90 μm. Although this made the device fragile, and susceptible to failure, this allowed for easier alignment between the center of the microchannel and the collection objective and focused laser beam. Proteins can potentially adsorb to glass surfaces and as a result block the microchannels. However, since the flow velocity of the analyte solution was above 500 nl/min and the particle density in solution was extremely low (to ensure single particle occupancy within the detection probe volume), protein adsorption was not a major concern. Nevertheless channels were pretreated with 33 % chromosulfuric acid to remove any potential contaminants within the channels. This was followed by purging the channel with 18 MΩ deionized water and followed by 0.1 M NaOH for a minimum of 15 minutes. Finally channels were rinsed again with deionized water and were then ready for use.

8.2.3 Sample delivery and microchannel alignment

The completed microchip was placed on a translation stage and appropriately aligned under the microscope objective. A precision syringe pump was used to deliver solutions at flow rates ranging from 500 nL/min – 2000 nL/min using a 1 ml gastight syringe. The 488 nm line from the argon ion laser was used as an excitation source for all measurements. Excitation of sample was performed 2 mm down stream from the inlet hole of the microfluidic channel. All protein labeled particle samples were kept at 5 °C until needed for the experiments. The measurements themselves were performed at room temperature. Prior to flowing the sample through the microchannel it was important to sonicate the analyte solution for a minimum of 5 minutes to minimize the potential for particle agglomeration. This procedure is crucial as agglomerates will result not only in much higher signal intensities but also in increased burst widths and decreased recurrence times. This would clearly have a direct consequence on the utility of the analysis methods being used.

8.3 Studies of particles labeled with IgG and HSA

8.3.1 Photon burst scan statistics of IgG and HSA labeled particles

Examples of photon burst scans for 500 nm particles labeled with IgG and HSA are shown in ***Figure 8.4***. The volumetric flow rate of the analyte solution through the microfluidic channel was 500 nl/min and the dwell time in all cases was 100 μs. Qualitatively there appears to be little difference in the photon burst frequencies between unlabeled versus labeled particles. This confirms that protein molecules only bind to one fluorescent bead. If a molecule was bound to more than one bead, signal intensities would be expected to be at least a factor of two greater and photon burst frequencies would decrease for a given sample concentration. The mean burst height for unlabeled particles was 71 counts with an RSD of 164 %. This was calculated over 1050 particle bursts. Photon bursts from IgG and HSA labeled 500 nm particles had mean heights of 91 counts and 85 counts respectively. The RSD in both cases was approximately 185 %. The values were generated using a minimum of 1000 particle bursts. A large excess of protein was added in the labeling process therefore it can be assumed that the majority of particles are fully labeled. This can be confirmed by measuring little change in the RSD when comparing labeled and unlabeled particles.

The 15 % increase in the labeled particle mean burst heights is attributed to the change in the hydrodynamic radius of the unlabeled and labeled particles. It will be shown in a later section that diffusion perpendicular to the direction of flow will have a direct consequence on the burst width distributions. There are approximately 10^6 carboxylate binding sites per 500 nm fluorescent particle. Hence, the radius of the labeled particles will incur an increase relative to the unlabeled particles. This means that burst characteristics are directly dependant on the difference in diffusion coefficients between labeled and unlabeled particles. The linear flow velocity within a 60 μm wide and 30 μm deep microchannel at a volumetric flow rate of 500 nl/min is 4.63 mm/s. Assuming the probe volume to be 2 μm in diameter, it can take up to 460 μs for a particle to traverse the probe volume. If it is also assumed that the hydrodynamic radius of the particle increases by 10 nm due to the binding of IgG or HSA, the diffusion time perpendicular to the flow direction will increase by approximately 5 – 10 %.

Figure 8.4d shows an example of a photon burst scan originating from a 50/50 mixture of IgG and HSA labeled particles. The mean burst height and RSD of the mixture was comparable to the burst scans of IgG and HSA labeled particles and as such simple burst height statistics cannot be used to distinguish between IgG and HSA labeled particles in a free flowing solution. Decreasing the flow rate could potentially be used to distinguish between photon burst heights as diffusion will play a more dominant role when compared to linear flow rate. This approach is somewhat problematic as the analytical throughput will be greatly decreased and hence detection and analysis times would be greatly increased.

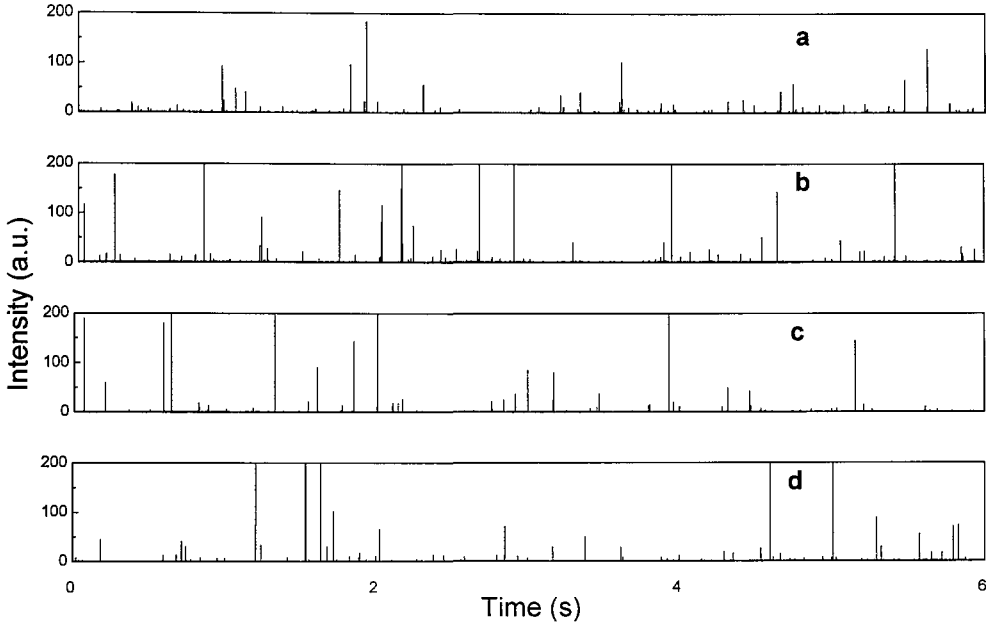


Figure 8.4 Photon burst scans for 500 nm particles (a), HSA labeled particles (b), IgG labeled particles (c) and 50/50 IgG-HSA labeled particles (d). A flow rate and dwell time of 500 nl/min and 100 μs was used for all scans.

8.3.2 Burst width histogram analysis for IgG and HSA labeled particles

8.3.2.1 Flow rate dependence on BWH for IgG and HSA labeled particles

Burst width histograms for 500 nm labeled and unlabeled particles are shown in ***Figure 8.5***. The histograms were generated for volumetric flow rates of 500 nl/min and 1000 nl/min. In all cases a minimum of 500 particle bursts were used in the calculation of the distributions. Clear statistical differences are observed between the labeled and unlabeled particles. For example, unlabeled particles have mean burst widths of 283 μs and 488 μs for flow velocities of 1000 nl/min and 500 nl/min respectively. It is interesting to note that the mean values are in good agreement with the theoretically obtained values for the particle residence times within the probe volume (e.g. 460 μs for 500 nl/min). This not only confirms the assumptions made in calculating the linear velocity but also confirms the detection probe volume did in fact have a radius on the order of 1 μm.

The mean burst width for IgG labeled particles was 537 μs and 1016 μs for flow rates of 1000 nl/min and 500 nl/min. This is an increase of 64 % and 68 % when compared to the unlabeled particles. This is most likely caused by diffusion perpendicular to the direction of flow. Not surprisingly, the percentage difference increases as the flow velocity decreases. Diffusion

perpendicular to the direction of flow is increased at lower flow rates; hence differences between labeled and unlabeled BWH's will not be as significant. It was not experimentally viable to decrease the flow velocity below 500 nl/min as collecting sufficient particle bursts would result in the collection of massive acquisition files (1-2 Gbyte). There is an obvious compromise if such flow based experiments are performed for immunoassays. Decreasing the flow velocity results in improved resolution and hence improved statistics. On the other hand, increasing the flow velocity results in decreasing the resolution and increasing the throughput; this can also improve the overall statistics. The choice of flow velocity will therefore be highly critical on the protein size.

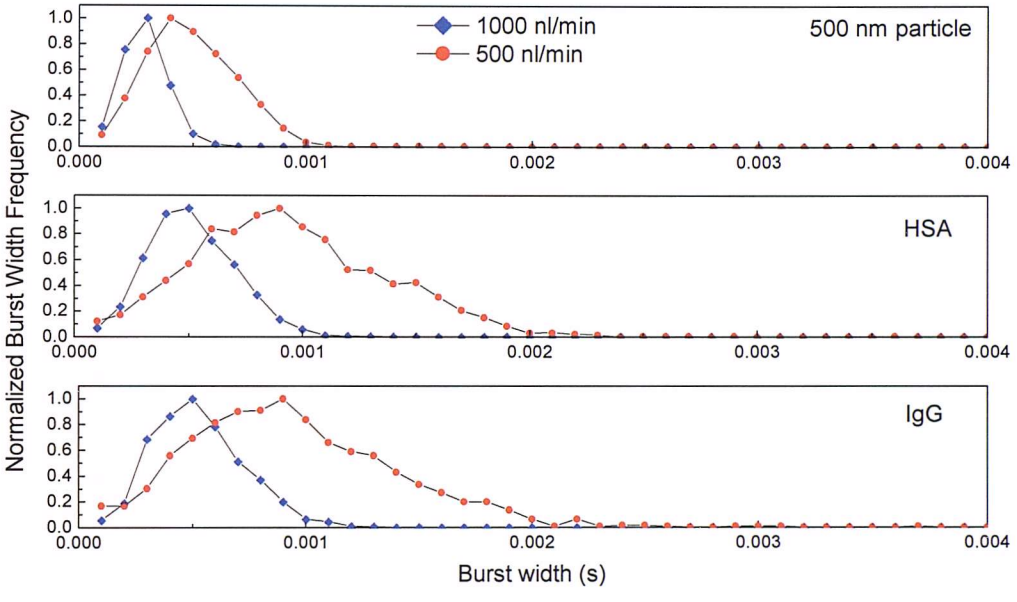


Figure 8.5 Burst width histograms for 500 nm particles (top), HSA labeled particles (middle), IgG labeled particles (bottom).

Changes in the mean burst width were also apparent when comparing HSA labeled particles to the IgG labeled particles. The mean burst width for HSA labeled fluospheres was 513 μs and 954 μs for flow velocities of 1000 nl/min and 500 nl/min respectively. The decrease can be directly attributed to the decrease in the hydrodynamic radius of the HSA modified spheres. HSA has a molecular weight of ~66,000 Da which is approximately a factor of two less than that of IgG (150,000 Da). The RSD in the histograms was below 35 % for all particles. As the RSD's were comparable for unlabeled and labeled particle burst widths, the labeling of the proteins could therefore be assumed to occur uniformly over the entire solution. If the degree of labeling was drastically different between particles, the RSD would be expected to greatly increase.

8.3.2.2 Particle size dependence on BWH for IgG and HSA labeled particles

Examples of burst width histograms for HSA labeled particles with a mean diameter of 200 nm, 500 nm, and 930 nm are shown in ***Figure 8.6***. The flow rate in all experiments was set to 1000 nl/min. Increasing the particle size from 500 nm to 930 nm resulted in a decrease in resolution between the labeled and unlabeled particles. The mean burst widths for 930 nm labeled and unlabeled particles were virtually identical and not statistically distinguishable. According to the certificate of analysis for carboxylate modified microspheres, the number of binding sites for 930 nm beads and 500 nm beads are virtually identical. The lack of change within the histogram is a result of a negligible difference in the hydrodynamic radius of the labeled and unlabeled particles. Higher percentage changes in the hydrodynamic radius result in greater differences in the BWH's. As the binding sites are almost identical for 500 nm and 930 nm particles, the smaller particles are more efficient at distinguishing between presence of protein due to the higher percentage increase in the radius.

It was expected that by decreasing the particle size to 200 nm significant changes in the BWH would be observed as the particle diameter is more closely matched to the hydrodynamic radius of the IgG and HSA proteins. The mean burst width for labeled and unlabeled particles was 367 μs and 544 μs respectively. There is only a 60 % change between both labeled and unlabeled particles and the change is almost identical to the studies performed on 500 nm particles. According to the certificate of analysis the number of binding sites per particle is a factor of 20 lower than the larger 500 nm particles. The smaller than expected change in the BWH's is possibly a consequence of the fewer binding sites resulting in a negligible change in the hydrodynamic radius when comparing labeled and unlabeled 200 nm particles.

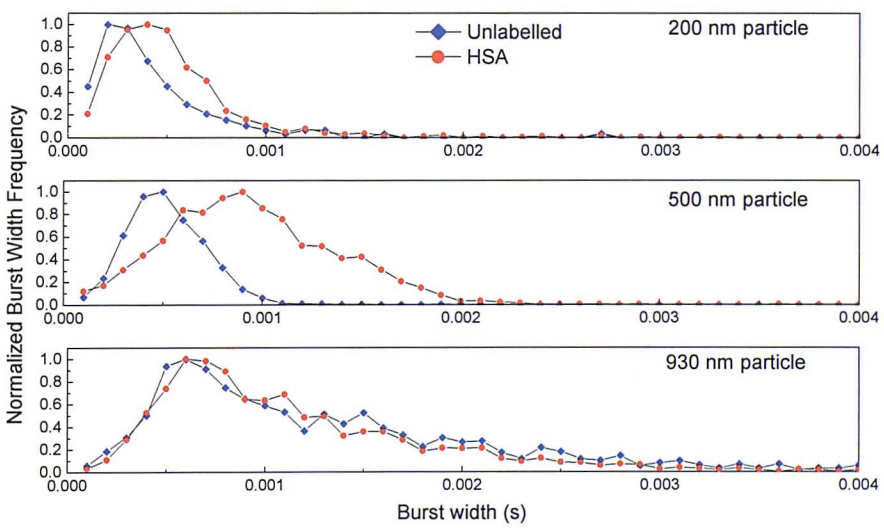


Figure 8.6 Comparison between labeled and unlabeled particle burst width histograms for 200 nm particles (top), 500nm particles (middle), 930 nm particles (bottom).

It should be noted that the histogram in the top of ***Figure 8.6*** does not start at zero. This is caused by the dwell time not being low enough to resolve particle burst widths which were less than 100 μs. It would perhaps be more appropriate to decrease the dwell time to 10 or 50 μs. However, by doing so, a direct comparison between particle sizes would not be possible.

8.3.3 Burst height versus area analysis for IgG and HSA labeled particles

The burst height statistics for labeled particles did not produce information that could be used to distinguish between different types of particles. Burst area statistics in the same sense as the burst height would also require large data samples to directly compare unlabeled and labeled particles. A more useful approach is to look at the characteristics of the burst height versus burst area. This should be directly proportional to the burst width if the burst width distribution has a reasonably low RSD. This can be achieved by utilizing flow rates greater than 500 nl/min within the 60 μm wide microfluidic channel. Examples of such plots are shown in ***Figure 8.7*** for 500 nm particles labeled with HSA and IgG. Plots for unlabeled particles and a mixture of HSA and IgG labeled particles are also shown. The volumetric flow rate in all experiments was 1000 nl/min.

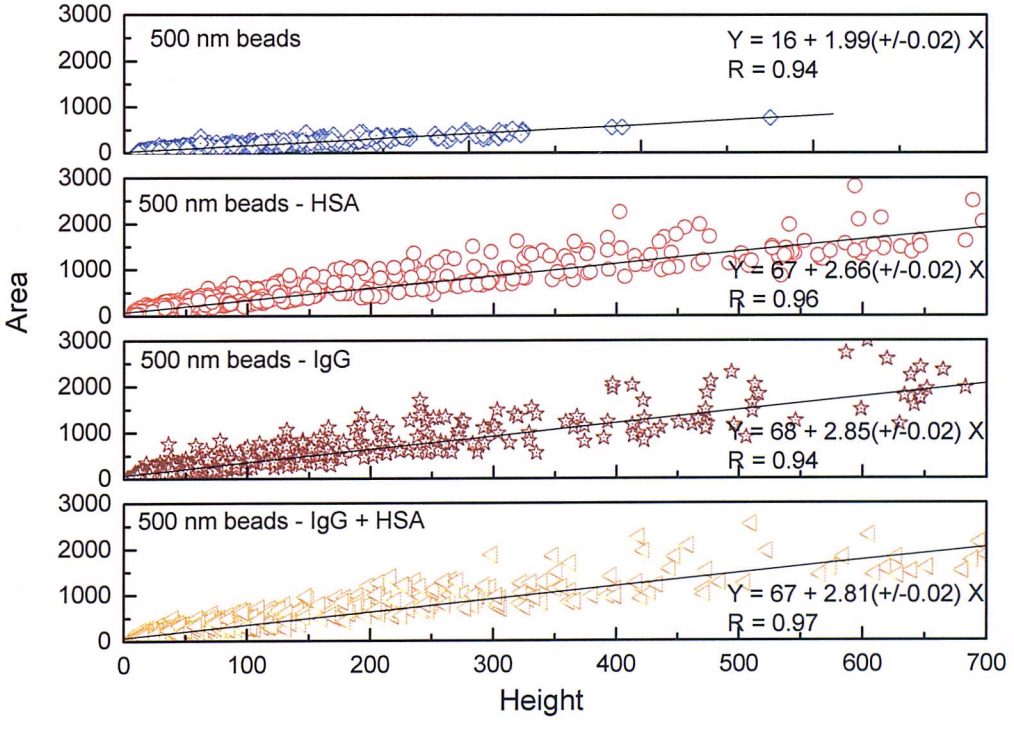


Figure 8.7 Comparison of burst height versus area plot for unlabeled 500 nm particles and for IgG and HSA labeled 500 nm particles.

A linear relationship was observed for a plot of area versus height and a least squares fit yielded a slope of 1.99 for the unlabeled particles. HSA and IgG labeled particles produced slopes of 2.66 and 2.85 respectively. All least squares fits produced a residual of at least 0.94; hence, the error in the slope was calculated to be not more than +/-0.02 within a 68 % confidence interval. The trend in the slope is identical to the trend in the mean burst widths, i.e. as the hydrodynamic radius increases, so does the slope and the mean burst width.

A 50-50 mixture of HSA and IgG labeled fluospheres yielded a slope of 2.81 which is statistically distinguishable to the slopes originating from analysis of IgG and HSA labeled particles. Initial results demonstrate that this approach can be useful in performing immunoassays in free flowing solutions. In ***Figure 8.7*** a minimum of 1000 particle burst were used to determine the slopes; however, this number could be decreased by a factor of 10 whilst still maintaining statistically different values between different particle populations. The slope trends were not just limited to the 500 nm particles; a summary for other particle sizes is shown in ***Table 8.1***. In all cases the volumetric flow rate was 500 nl/min and a minimum of 1000 particles were used to determine the slopes. For all particle sizes an increase in the hydrodynamic radius resulted in an increase in the slope and all data were consistent with the trends in the mean burst widths.

	938 nm	***500 nm***	***200 nm***
Unlabeled particle	4.19	1.99	2.26
HSA labeled particles	4.48	2.66	3.4
IgG labeled particles	4.67	2.85	4.74

Table 8.1 Slopes of burst area versus height plot for a flow rate of 500 nl/min

The experimental procedures described in this chapter along with the analysis of burst width histograms can potentially be used as an extremely sensitive method for immunoassays in a free flowing solution. It must be emphasized that a statistical analysis method that can distinguish between proteins in a free flowing solution without performing separations is extremely valuable as the overall experimental procedure and analysis times are significantly simplified.

8.3.4 Autocorrelation analysis for IgG and HSA labeled particles

Autocorrelation analysis also proved to be a useful tool in characterizing the unlabeled and labeled particles. Such an analysis is useful in this instance as it gives valuable information pertaining to particle residence times as well as intensities within the detection probe volume. It also gives qualitative information regarding changes in burst widths and areas when comparing several spectra. Examples of autocorrelation curves for 500 nm particles moving at flow rates of 0.5 µl/min and 1 µl/min are shown in ***Figure 8.8***. The curves were normalized over the number of peaks so that a direct comparison could be made between curve maxima as well as FWHM values. At both flow velocities, trends were identical, i.e. unlabeled particles produced the weakest signal. This was followed by HSA labeled particles and IgG labeled particles. Identical trends, relating to the change in hydrodynamic radius, were observed in the burst width histograms as well as in the height versus area plots. As expected FWHM values were higher at lower flow rates and hence could be used to distinguish between different labeled proteins with higher precision.

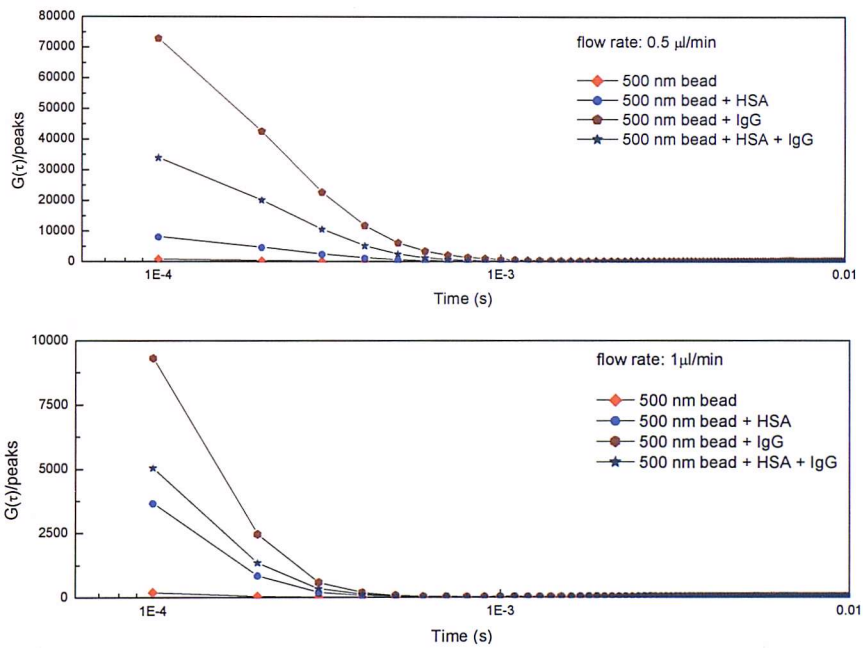


Figure 8.8 Autocorrelation curves for labeled and unlabeled fluorescent particles at flow rates of 1 and 0.5 µl/min.

At a volumetric flow rate of 500 nl/min, a 50/50 mixture of HSA labeled and IgG labeled particles produced a curve maximum (35,000) between that of both the pure IgG and HSA labeled particles. IgG labeled particles had a maximum of 74,000 while HSA labeled particles had a maximum of 9000. For comparison, the autocorrelation curve maximum for unlabeled particles was 900. It should be emphasized that the curve maximum is strictly dependant on the resolution or dwell time of the photon burst scan and as such occurred in all curves at a

100 μs (the dwell time was set to 100 μs). From a linear least square fit to the autocorrelation curves diffusion times were calculated to be 180 μs for unlabeled particles. They were 220 μs and 235 μs for the HSA and IgG labeled particles respectively. This is in good agreement with the curve maxima; as the diffusion time increases so do the curve maxima. In all cases the least squares fit also produced a detection probe volume width to depth ratio of approximately 1. When the volumetric flow rate was increased to 1000 nl/min the 50/50 mixture of HSA and IgG labeled particles did not produce a curve maximum directly between the curves for the pure IgG and HSA labeled particles. This was caused by particle diffusion playing a less dominant role at higher velocities and as such burst characteristics cannot be so easily distinguished.

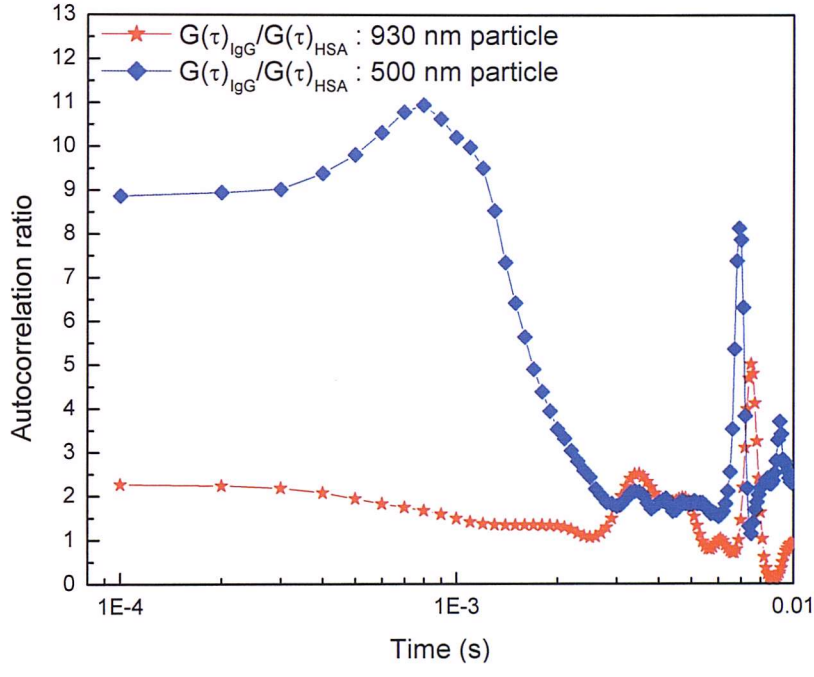


Figure 8.9 Ratio of autocorrelation curves between IgG and HSA labeled particles. The curves were measured for particle sizes of 500 nm (blue) and (930 nm) red. The volumetric flow rate was 500 nl/min.

Increasing the particle size to 930 nm results in a much smaller difference in autocorrelation curves between IgG and HSA labeled particles. However, unlike the burst width histograms it is still possible to distinguish between both IgG and HSA labeled particles. This is perhaps easiest to see by plotting the ratio of the autocorrelations curves between IgG and HSA labeled particles. This is shown in ***Figure 8.9*** for 500 nm as well as 930 nm particles. The volumetric flow rate in both cases was 500 nl/min and the dwell time was 100 μs. From 100 μs – 1 ms the ratio between the autocorrelation curves was approximately 2 for the 938 nm particles. Over the same time period the 500 nm particles produced a ratio of approximately 9.5. The lower overall ratio of the 930 nm particles was a direct result of a smaller difference

in the burst width characteristics of the HSA and IgG labeled particles. The decrease in the autocorrelation ratio between both curves ($\tau > 300$ μs) is due to background levels in the autocorrelation curves being reached and hence negligible changes would be expected within this time period.

8.4 Studies of particles labeled with IgG and anti IgG conjugates

8.4.1 Motivation behind distinguishing between IgG and anti IgG labeled particles

In the previous section of this chapter a detection and analysis method was demonstrated for performing immunoassays in a free flowing solution. In this section a direct and ultra-sensitive detection method is proposed for distinguishing between IgG and anti IgG in human sperm. Antibodies directed against sperm surface antigens tend to exert fertility-reducing effects. For example, if a sperm head is coated with greater than 80 % antibodies, it is likely that infertility will occur.[19] When antisperm antibodies are present, they bind to the surface of the sperm. Such sperm-bound antibodies may impair sperm movement, impair interaction of sperm and egg, as well as impair in the identification of the sperm for destruction by the immune system.

Conventional anti IgG sperm analysis methods require the use of a spermMAR test.[19] This is typically a laborious task and involves the following procedure. IgG is added and mixed with a latex bead/semen mixture. The antiserum binds to IgG on the surface of the beads and, if present, IgG on the surface of the sperm. This results in bead-bead and bead-sperm complexes that are typically observed and quantified through visual inspection with a microscope. As the sperm 'swim' through the bead sample, beads bind on the sperm if antibodies are present. Thus, sperm with IgG on the surface will have beads coating the sperm. Beads will also form agglomerates with each other. The optical microscope counting detection method not only results in poor detection efficiencies but also time consuming. With the confocal based approach utilized, it is possible to automate the entire detection process as well as increasing sensitivity, sampling time, and overall throughput.

8.4.2 Labeling of anti IgG onto IgG-particles

The IgG labeling procedure of the fluorescent particles was identical to that described in Section 8.2.1.1. Anti-human IgG (Fab specific) was purchased from Sigma Chemicals. The antiserum is developed in goat using a purified IgG Fab fragment as the immunogen. The antiserum was obtained by immunospecific purification which removed all goat serum proteins which do not specifically bind to the Fab fragment of human IgG. The antibody was diluted in a 0.02 M phosphate buffer at pH 7.4 containing 15 mM sodium azide as a preservative. This antibody reacts with all immunoglobulin and as such is an effective reagent in immunoassay procedures. The anti – IgG labeled particles were generated by mixing a mole equivalent of the antibody with the IgG bound to the labeled particles.

8.4.3 Results

8.4.3.1 Burst width histogram analysis for IgG and anti IgG labeled particles

Examples of photon burst scans for IgG and anti-IgG labeled particles are shown in ***Figure 8.10***. Burst width histograms for IgG labeled particles and Anti-IgG labeled particles are shown in ***Figure 8.11***. The particle size was 500 nm and the volumetric flow rate through the microfluidic channel was 500 nl/min. It should be emphasized that the following experiments were conducted using different conditions to previous experiments described hence the BWH for IgG labeled particles will not be similar. This is caused by a difference in alignment in the microfluidic channel as well as a difference in the laser power used. Increasing or decreasing the laser power will directly result in different photon burst characteristics as a result of non-linear photophysical effects. This is not considered to be a problem as long as experiments are performed using an identical optical set-up.

It is encouraging to see a shift of 400 μs in the histogram maxima between the IgG labeled particles and the anti-IgG labeled particles. The BWH on its own can therefore be used to quantify the difference between IgG and anti-IgG using single particle optical methods. IgG labeled particles had a mean burst width of 1.89 ms while anit-IgG labeled particles had a mean burst width of 2.14 ms. Both were determined using a minimum of 500 particle bursts. The RSD in both cases was below 40 % confirming a good uniformity in the overall burst widths. With such a clear difference in the BWH, deconvolution procedures as well as calibration plots make this technique useful in quantifying the proportion of IgG and anti – IgG on sperm heads or even in other biologically important systems.

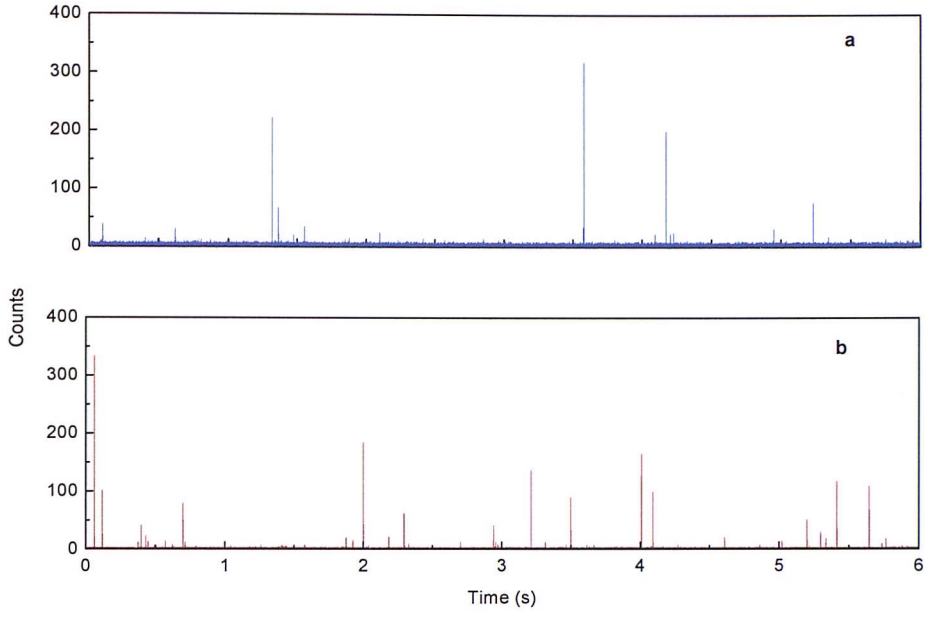


Figure 8.10 Photon burst scans for 500 nm particles (a) labeled with IgG and (b) anti –IgG. The flow rate was 500 nl/min.

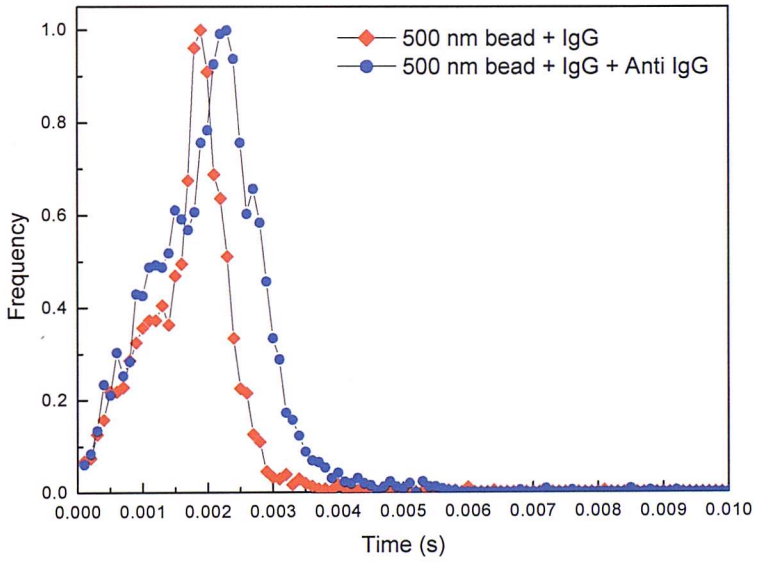


Figure 8.11 Burst width histograms for 500 nm particles labeled with IgG (diamond), anti –IgG (circle).

8.4.3.2 Autocorrelation curve analysis for IgG and anti IgG labeled particles

An autocorrelation analysis also proved to be a useful tool in distinguishing between IgG and anti-IgG. An example for 500 nm particles at a flow rate of 0.5 µl/min is shown in ***Figure 8.12***. The curves were normalized over the number of peaks so that a direct comparison could be made between curve maxima. The hydrodynamic radius of the IgG and anti-IgG labeled particles resulted in highly different autocorrelation curves.

IgG labeled particles produced a curve maximum of 3250. Anti - IgG labeled particles on the other hand, produced a curve maxima of 3750. This difference is a result of perpendicular diffusion from the direction of flow. The much larger anti IgG labeled particles resulted in longer diffusion times through the probe volume. From a linear least squares fit to the autocorrelation curves (***Equation 3.12***) diffusion times were calculated to be 600 μs for the IgG labeled particles. The anti – IgG labeled particles had a diffusion time of approximately 1000 μs. This is in good agreement with the curve maxima, i.e. as the diffusion time increases so do the curve maxima. In all cases the least squares fit also produced a detection probe width to depth ratio of approximately 1. As with the BWH, the degree of IgG and anti IgG in a mixture can be quantified by a direct comparison of the autocorrelation curves for the pure IgG and anti –IgG labeled particles.

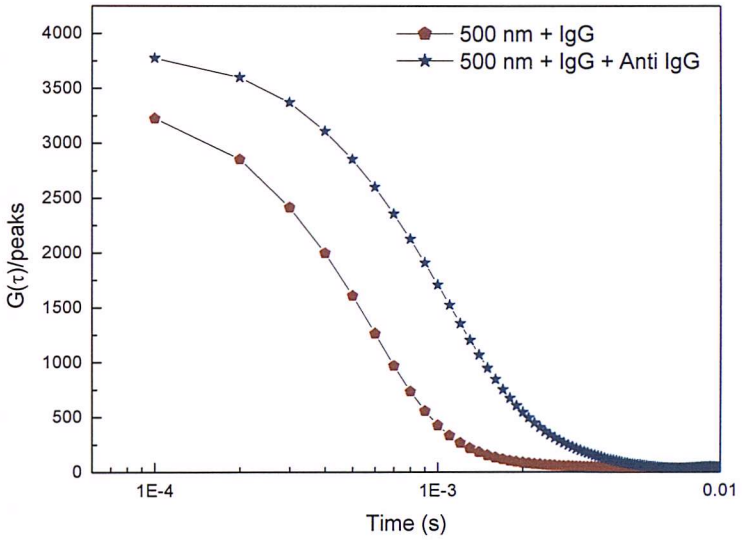


Figure 8.12 Autocorrelation curves for IgG labeled and anti-IgG labeled fluorescent particles at flow rates of 0.5 μl/min.

8.4.3.3 Height versus area distribution analysis for IgG and anti IgG labeled particles

A linear relationship was observed in the slope for a plot of burst height versus burst area, and a least squares fit yielded a slope of 6.66 for the IgG labeled particles. Anti human IgG labeled particles produced a slope of 12.6. From the least squares fit the error in the slope was calculated to be within +/-0.11. The burst height and area statistics for labeled particles, on their own, did not produce information that can be used to distinguish between different types of particles. On the other hand, plots of burst height versus burst area proved to be a valuable method in distinguishing between the different proteins. Using this method along with the BWH and autocorrelation curve analysis proved to be useful in distinguishing between IgG and anti human IgG in a freely flowing solution.

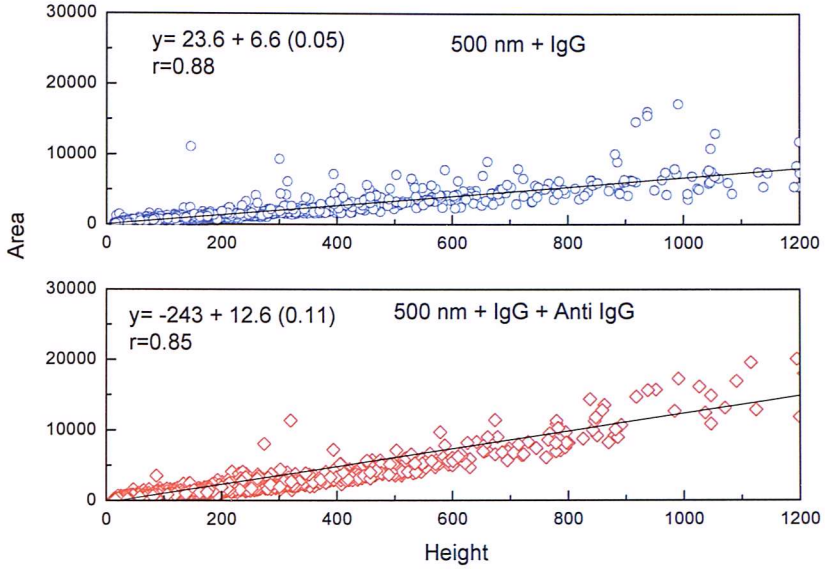


Figure 8.13 Area-height plots for IgG labeled and anti-IgG labeled fluorescent particles at flow rates of 0.5 µl/min.

8.5 Summary

This chapter has demonstrated the potential for using single particle confocal spectroscopy to detect proteins in a free flowing solution. The major advantage of this approach is in the ability to improve on throughput as well as detection limits when compared to more conventional techniques. The power of single particle detection to perform immunoassays in a freely flowing solution should not be underestimated. Conventional methods require more complicated procedures such as chromatographic or electrophoretic separation. This was clearly shown not to be required as long as an appropriate statistical analysis method is available. Acquisition and analysis times are on the order of seconds, which makes this approach at least a factor of 100 quicker than gel-electrophoresis. Methods such as autocorrelation analysis, burst width histogram analysis, and a burst area-height analysis were shown to be highly sensitive methods in distinguishing between proteins of different molecular weights. Differences in statistics between the labeled particles arose due to changes in hydrodynamic radius.

A "real life" application based on the analysis methods of the first part of the chapter was used to distinguish between IgG and anti human IgG on human sperm heads. Conventional detection methods involve human visualization of beads labeled with the proteins using an optical microscope. This is an extremely time consuming task and sensitivity is very poor. Fully automated procedure can be designed based on the single particle detection experiments described to distinguish and quantify the percentage of immunoglobulin on sperm heads. This approach will not only guarantee an improvement in detection sensitivity, but throughput can

be as high as 10,000 detected particles per second. This is achievable by increasing the volumetric flow rate. In all experiments shown a minimum of 300 particles were used per measurements (potentially a 30 ms acquisition time). However, this can be either decreased or increased depending on the precision required.

8.6 References

(1) Brodsky, A. S.; Johnston, A. P.; Trau, M.; Silver, P. A. *Current Opinion in Molecular Therapeutics* **2003**, *5*, 235-240.

(2) Thomas, J. H.; Ronkainen-Matsuno, N. J.; Farrell, S.; Halsall, H. B.; Heineman, W. R. *Microchemical Journal* **2003**, *74*, 267-276.

(3) Serke, S.; van Lessen, A.; Huhn, D. *Cytometry* **1998**, *33*, 179-187.

(4) Nguyen, X. D.; Eichler, H.; Dugrillon, A.; Piechaczek, C.; Braun, M.; Kluter, H. *Journal of Immunological Methods* **2003**, *275*, 57-68.

(5) Marchand, J.; Bord, A.; Penarier, G.; Laure, F.; Carayon, P.; Casellas, P. *Cytometry* **1999**, *35*, 227-234.

(6) Selvaganapathy, P. R.; Carlen, E. T.; Mastrangelo, C. H. *Proceedings of the IEEE* **2003**, *91*, 954-975.

(7) Kwak, Y. D.; Yoo, S. K.; Kim, E. J. *Clinical and Diagnostic Laboratory Immunology* **1999**, *6*, 499-503.

(8) Jones, G.; Wortberg, M.; Kreissig, S. B.; Hammock, B. D.; Rocke, D. M. *Analytica Chimica Acta* **1995**, *313*, 197-207.

(9) Colyer, C. L.; Tang, T.; Chiem, N.; Harrison, D. J. *Electrophoresis* **1997**, *18*, 1733-1741.

(10) Chiem, N.; Harrison, D. J. *Analytical Chemistry* **1997**, *69*, 373-378.

(11) Koutny, L. B.; Schmalzing, D.; Taylor, T. A.; Fuchs, M. *Analytical Chemistry* **1996**, *68*, 18-22.

(12) Chen, F. T. A.; Pentoney, S. L. *Journal of Chromatography A* **1994**, *680*, 425-430.

(13) Buranda, T.; Huang, J. M.; Perez-Luna, V. H.; Schreyer, B.; Sklar, L. A.; Lopez, G. P. *Analytical Chemistry* **2002**, *74*, 1149-+.

(14) Haupts, U.; Rudiger, M.; Ashman, S.; Turconi, S.; Bingham, R.; Wharton, C.; Hutchinson, J.; Carey, C.; Moore, K. J.; Pope, A. J. *Journal of Biomolecular Screening* **2003**, *8*, 19-33.

(15) Kraemer, B.; Neukammer, J.; Macdonald, R.; Roos, M.; Kroczek, R. *Cytometry* **2002**, 133-134.

(16) Michalet, X.; Weiss, S. *Comptes Rendus Physique* **2002**, *3*, 619-644.

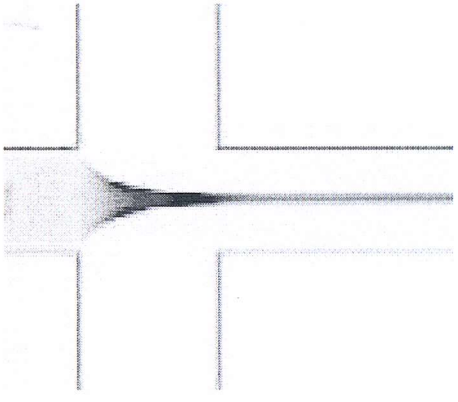
(17) http://techtran.msfc.nasa.gov/Patents/(36).html, 2003.

(18) *Private communication: Molecular Probes* **2003**.

(19) *ESHRE Monographs* **2002**, 18-20.

- 9 -

This chapter a summarizes the outcomes of the work presented in this thesis, suggestions for further system developments and an outlook on the future progression of SMD techniques



Overview

9.1 Project Aims

The development of techniques allowing the detection of single particles and molecules in solution has progressed significantly over the past decade. Since the first successful optical observation of single fluorescent molecules in 1976 a wide range of modifications of the basic idea have been reported. Consequently, measurement chemistry and biology have entered a new era where individual molecules can be detected, identified, counted, sorted, and in some cases, their physical and chemical properties measured.

The studies described in this thesis have detailed the development of single molecule and particle fluorescence detection with a particular focus on application in microfluidic systems. The primary motivation behind this work was twofold. An initial aim focussed on improving the operational flexibility of single molecule spectroscopic measurements, by creating an optical system capable of realising time-integrated, time-resolved and spectral information. Once achieved the system and associated data analysis techniques were used in combination with chip-based microfluidic systems to create new methods for the analysis of particles, cells and proteins in flowing solutions. In essence, the combination of SMD and microfluidics provides for a new-generation of analytical devices, where both the manipulation of small-volume samples and the detection of individual molecules can be performed with high-efficiency (in terms of analytical performance and sample throughput) and on ultra-short timescales.

9.2 Summary of achievements

A component based optical spectrometer was designed and developed to allow for single molecule and particle detection within microfluidic channels. The confocal system consists of a number key components: Optical excitation is achieved using either a multi line argon ion laser (operating between 457.9 and 514.5 nm) or a picosecond diode laser (operating at 404 or 440 nm); definition of sub-femtolitre excitation volumes is achieved using high-efficiency, adjustable confocal optics mounted on an optical bench; high-efficiency detection of emitted photons is realized through the use of a passively quenched, single-photon avalanche diode photodetector; and the use of a monochomator and TCSPC electronics allow both spectral and time-resolved fluorescence data to be measured.

Microfluidic devices were fabricated from either glass or PDMS using standard bulk micromachining techniques (including contact photolithography, wet-etching, thermal bonding and soft lithography). To ensure efficient optical interrogation of sample within

microchannel environments, microchip coverplates were optically polished down to a thickness of approximately 100 microns (which is less than the working distance of typical objective optics used for SMD measurements). Such microfluidic devices provided for efficient manipulation of sub-nanolitre volumes of sample and subseuqantly provided for reduced sample consumption, short analysis times and high sample throughput.

Once constructed the confocal spectrometer was used to define a number of new analytical techniques for the analysis of single molecules and particles in solution

(a)

A non-invasive, optical technique for measuring particulate flow within microfluidic channels was developed. Confocal fluorescence detection is used to probe single fluorescently labeled microspheres (0.93 mm diameter) passing through a focused laser beam at a variety of flow rates (50 $nLmin^{-1}$ - 8 $\mu L\ min^{-1}$). Simple statistical methods were used to investigate the resulting fluorescence bursts and generate velocity data for the flowing particles. Fluid manipulation was achieved by hydrodynamically pumping fluid through microchannels structured in a polydimethylsiloxane (PDMS) substrate. The mean fluorescence burst frequency is shown to be directly proportional to flow speed. Furthermore, the Poisson recurrence time and width of recovered autocorrelation curves is demonstrated to be inversely proportional to flow speed. The component-based confocal fluorescence detection system is simple and can be applied to a diversity of planar chip systems. In addition, velocity measurement only involves interrogation of the fluidic system at a single point along the flow stream, as opposed to more normal multiple-point measurements.

(b)

A non-invasive, optical technique for sizing single particles or molecules in free solution was demonstrated. Confocal fluorescence detection is used to probe single fluorescently labeled microspheres (200-920 nm diameter) passing through a focused laser beam at a variety of flow rates (100-1000 nL/min). Simple statistical methods are subsequently used to investigate the resulting fluorescence bursts and generate single-particle burst width and burst area distributions. Analysis of these distributions demonstrates that the average burst width and burst area decrease as particle size increases. In addition, both burst width and burst area (for a given particle size) are observed to decrease as volumetric flow rate is increased. The dependence of such distributions on particle size is proposed as a potential route to sizing single particles and molecules in microfluidic systems. Although, molecular detection efficiencies (in terms of the fraction of all molecules detected) are inferior to those achieved in single-molecule flow cytometry methods, the approach can be used to size species flowing

through a femtoliter detection volume, without the need to use sheath flows, expanded probe volumes or complex background suppression techniques.

(c)

A novel approach to improving molecular detection efficiencies when performing SMD in femtolitre probe volumes was demonstrated through use of hydrodynamic focusing of analyte streams within microchannels. Using this technique a minimum hydrodynamic focusing width of 1-μm was achieved within a 10-μm wide microfluidic channel. Since the probe volume radius in typical confocal experiments is of the same order as the focussed stream width a large proportion of all molecules travelling within the microfluidic device can be detected, resulting in improved collection and detection efficiencies. A theoretical Monte Carlo random walk simulation was also used to model hydrodynamic focusing effects within microchannels. Theoretical predictions compare well with experimental results.

(d)

A particle identification method based on the maximum likelihood estimator is used to discriminate between single particle flow velocities using confocal spectroscopy. Particles or molecules travelling at specific flow rates through a confocal volume are expected to have a definable burst widths, heights, and areas. Hence, single particles travelling with different velocities should be distinguishable based on such parameters. With this approach it is shown that for particles travelling with a flow rate difference of 20x, there is virtually a 0% error rate in assigning a particle to a given flow velocity, based on the analysis of a single fluorescence burst. When a flow rate difference of 4x is used, 90% of the particles travelling through the confocal probe volume are still assigned a correct flow velocity. Use of this method technique allows a statistically meaningful flow velocity to be assigned from the analysis of a single photon burst from a single particle.

(e)

The combination of time correlated single photon counting and single molecule spectroscopy is shown to be an effective tool for identifying and counting individual cells within flowing streams. It was possible to discriminate between single E. coli cells expressed with GFP and CFP based on *single cell* fluorescence lifetimes. These measurements along with burst height and width histograms appear to define a powerful approach to discriminating and counting different cell types in a free flowing solution. A novel technique was also developed using time tagged photon arrival times to discriminate between different types of fluorescent protein.

(f)

A technique based on the analysis of protein molecules (HSA and IgG) bound to nanometer sized particles in flowing streams was used to define a novel approach to ultra-fast immunoassay measurements. The major advantage of this approach is in the ability to improve on throughput as well as detection limits when compared to more conventional techniques. Methods such as autocorrelation analysis, burst width histogram analysis, and burst area-height analysis were shown to be highly sensitive methods in distinguishing between proteins of different molecular weights. Acquisition and analysis times are on the order of seconds, which makes this approach at least a factor of 100 quicker than gel-electrophoresis.

(g) See Appendix 1

Nanocrystalline semiconductors (or quantum dots) are of considerable scientific and commercial interest owing to their tunable optical and electronic properties, and potential uses in a wide range of electronic devices and biological applications. A confocal spectroscopic technique was shown to be highly useful in monitoring the synthesis of CdSe quantum dots within microfluidic reaction systems. Using this method, time dependent information such as fluorescence emission spectra and fluorescence lifetimes could be monitored in real time. This resulted in the ability to directly monitor and control the synthesis and the characteristics of the synthesized quantum dots in real time.

9.3 System improvements

The confocal spectrometer as designed is state-of-the art and ia able to perform single molecule detection, time correlated single photon counting, time-tagged photon counting, time-resolved emission spectroscopy, and Raman spectroscopy. Although this is a highly sensitive and flexible instrument, there are two potential system developments that should improve instrument performance when interfaced with microfluidic systems.

First, the short working distance of the microscope objective imposes a cumbersome constraint on sample formats. All top plates of the microfluidic devices in this thesis had to be optically polished to a thickness below 150 μm; the working distance of the microscope objective. This is generally a time consuming task and can take as much as 24 hr. Consequently, it would be of value to assess the possibility of using a 100 x water immersion objective. Although, the numerical aperture would be lower, the overall focal length would be longer. This would result in direct compatibility of the detection system with most microfluidic devices.

Secondly, it would be desirable to integrate an enhanced imaging CCD to the confocal spectrometer. This would allow real time visualization of the microfluidic channel and be especially useful during chip alignment and monitoring for chip failures (e.g. plugging and contamination). In addition, this modification would allow one to monitor single molecules or particles within well defined locations in a microfluidic channel. Thus providing more detailed information on fluid flow velocities and particle dynamics.

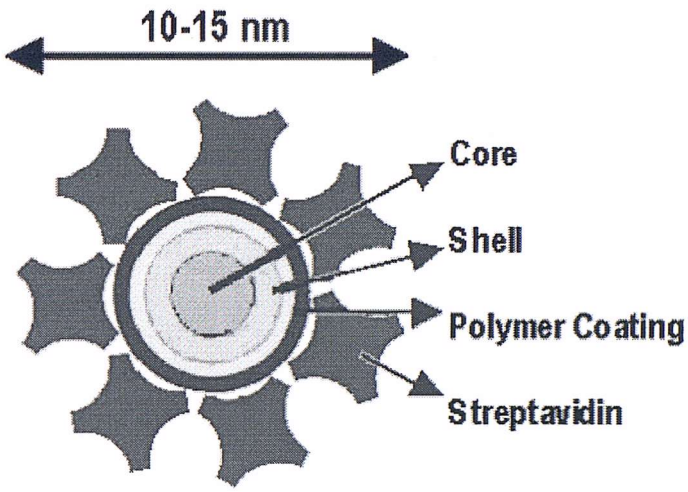
9.4 Outlook

The development of detection methods that interface with and utilise microfluidic devices merits further attention. As previously mentioned microfluidic systems offer several major advantages when processing analytical samples. These include improved analytical efficiencies, reduced analysis times, smaller sample volumes, and reduced reagent waste. It is for this reason that the integration of confocal spectroscopy with microfluidics is highly desirable. Microchannel devices are highly compatible with confocal microscopy as the channel dimensions are of the same order as typical excitation and probe volumes. Furthermore, due to the ongoing progress of micromachining technologies, it may be possible than within the next 10 years a complete confocal spectrometer will be available on a single chip no larger than a postage stamp!

The technical difficulties associated with achieving single molecule detection capability imply that the technique will not become a routine analysis method in clinical labs in the near future. However, single particle detection holds great promise as signal to noise ratios tend to be much larger than in a pure SMD experiment. This would allow for ultra-sensitive immunoassays to be performed without the drawback of low signals and long analysis times. More generally, SMD methods may prove to be highly important as a diagnostic tool in systems where an abundance of similar molecules masks the presence of discrete molecular anomalies that are markers in the early stages of disease or cancer.

What is clear is that the future of *"single molecule detection"* will be interesting and varied.

Appendix 1



Real time monitoring of quantum dot synthesis within microchannels

Although the work in this appendix is not directly related to the fundamental theme of my thesaural studies, it is perhaps important to include this work as it demonstrates a novel application of confocal microscopy – monitoring the formation of quantum dot nanoparticles in continuous real time. In the last decade semiconductor quantum dots (QD) have become a subject of intense research. QDs are in the transition regime between molecules and bulk solids. Due to quantum confinement effects QDs show unique physical and chemical properties such as size-dependent band gap shifts and size dependent photoluminescence. Consequently, there is considerable interest in synthesis routes that yield nanoparticles of well-defined sizes. One of the primary challenges associated with the synthesis of QDs is the ability to control the growth of the clusters.

In order to synthesize monodisperse QDs, efficient heat transfer across the reaction chamber is needed. Rapid mixing of reagents is also needed to ensure a homogeneous reaction environment. This is difficult to achieve in a conventional reaction chamber; however, microfluidics can be easily used to control these factors. Herein we show that by using a continuous flow microreactor, we are able to synthesise and control the size and monodispersity of certain nanoparticles as well as monitor the reaction in continuous real time using confocal spectroscopy.

Listed below are two publications as well as two proceedings included in appendix 1.

1) Edel, J. B., Fortt, R., de Mello, A.J. "Microfluidic Routes to the Controlled Production of Nanoparticles." *Chemical Communications* (10): 1136-1137, 2002.

2) Edel, J.B., de Mello, A.J., de Mello., J.C., "Controlled Quantum Dot Synthesis Within Microfluidic Circuits," *Proceedings of the 6th International Conference on Micro Total Analysis Systems* pp. 772-774, 2002.

3) Edel, J.B., Krishnadasan, S., cao-Romero, J. T., Vilar R., de Mello J.C., de Mello A.J., "Controlled Synthesis of Compound Semiconductor Nanoparticles Using Microfluidic Reactors." *Transducers 2003* (4B1.1): 1730-1733.

4) Edel, J.B., Krishnadasan, S., de Mello J.C., de Mello A.J., "Continuous real-time monitoring of quantum dot synthesis within microfluidic reactors," *Proceedings of the 7th International Conference on Micro Total Analysis Systems*, 2003.

COMMUNICATION

ChemComm www.rsc.org/chemcomm

Microfluidic routes to the controlled production of nanoparticles†

Joshua B. Edel, Robin Fortt, John C. deMello* and Andrew J. deMello*

Department of Chemistry, Imperial College of Science, Technology and Medicine, Exhibition Road, South Kensington, London, UK SW7 2AY. E-mail: a.demello@ic.ac.uk

Received (in Cambridge, UK) 26th March 2002, Accepted 15th April 2002
First published as an Advance Article on the web 23rd April 2002

A microfluidic procedure for the controlled production of cadmium sulfide nanoparticles is described

Nanocrystalline semiconductors are of considerable scientific and commercial interest owing to their tuneable optical and electronic properties, and potential applications in a wide range of electronic devices.[1] Physical characteristics of nanocrystallites are determined primarily by spatial confinement effects with properties such as the optical band gap often differing considerably from the bulk semiconductor. As these properties are ultimately determined by the physical size and shape of the crystallites, there is considerable interest in processing routes that yield nanoparticles of well-defined size.[2]

To date, techniques for producing highly monodisperse nanoparticles have been relatively complex and of a *post-hoc* nature[3–5] (A good review article by Trindade *et al* describes various approaches to synthesis of nanocrystalline semiconductors[6]). They are commonly produced in two stages: a poly-disperse sample is first obtained using standard synthetic routes, and nanoparticles of a given particle size are then isolated by means of repeated recrystallisations. This approach, whilst appropriate for small-scale production of nanoparticles, may not be ideally suited to large-scale production owing to the low product yield and the time consuming nature of the recrystallisation process.[3] At the time of writing there have been few—if any—*direct* (single-stage) approaches to the fabrication of monodisperse nanocrystallites. Fischer and Giersig[7] have previously used a fast flow (~1 ml min^{-1}) mixing chamber in conjunction with a chromatographic column to produce ultrasmall CdS nanoparticles. In this paper, we take an established synthetic procedure for cadmium sulfide nanoparticles and demonstrate how adaptation to a continuous flow microfluidic format leads to an immediate reduction in polydispersity. The procedure may offer an effective approach to synthesising nanoparticles *directly* and without recourse to subsequent recrystallisations.

Following Lakowicz *et al.*, nanoparticles of cadmium sulfide were obtained by mixing aqueous solutions of cadmium nitrate and sodium sulfide.[8] In conventional approaches to nanoparticle synthesis, the reactions are carried out in static macroscopic reaction vessels. Any variations in physical conditions across the reaction chamber (*e.g.* concentration or temperature gradients) are liable to influence the nature of the chemical product and in particular are likely to affect the size of the crystallites. In order to improve polydispersity, it is therefore necessary to eliminate local variations in reaction conditions, which is not trivial in a bulk reactor. Miniaturisation on the other hand affords a direct means of eliminating these local variations as the entire reaction volume can be held at a constant (uniform) temperature with near-absolute chemical homogeneity pertaining throughout.[9]

For bulk production of chemicals, the miniature reaction vessel must be used in a continuous flow format with the product being continuously extracted and the reactants continuously replenished. In order to preserve chemical homogeneity, it is essential that the entrant reagents should mix rapidly (faster than the time-scale of the reaction). Owing to the absence of turbulence in microengineered structures efficient mixing is a non-trivial process.[10] Mixing in microstructures is mediated almost exclusively by molecular diffusion and can be relatively slow. This leads to departures from chemical homogeneity and in the present context increases the polydispersity of the nanoparticles produced. To overcome this problem, a fast micromixer must be used (see ESI†). Specifically, we use the continuous flow micromixer developed by Bessoth *et al.*, which has been described in detail elsewhere.[11] In short, two inlet flows (containing either sodium sulfide or cadmium nitrate) are split into a series of separate multichannel streams (16 partial flows) before bringing them into final contact; as the diffusion time is proportional to the diffusion distance, splitting each reagent stream into n substreams of similar width decreases mixing times by a factor n^2. After mixing, the channels are sequentially combined in a reverse network until all partial flows are united in one outlet channel. The entire mixing volume for the micromixer is less than 600 nl.

An additional cause of polydispersity is coalescence of the newly formed nanoparticles to form larger crystallites. This may be discouraged to some extent by stabilising the nanoparticles with another semiconductor or chemical species.[12] However it is nevertheless important to extract the nanoparticles from the reaction volume as quickly as possible. It is therefore to be expected that varying the flow rate of the reagents through the micromixer will have a considerable influence on the size distribution of the nanoparticles.

To summarise the overall experimental procedure: CdS nanoparticles were obtained by directly mixing 4×10^{-4} M aqueous solutions of $Cd(NO_3)_2{\cdot}4H_2O$ and Na_2S. To aid stabilisation of the resulting nanoparticles, an equal quantity of sodium polyphosphate was added to the cadmium nitrate solution prior to mixing. A syringe pump was used to deliver the reagents into the microfluidic channel network at various flow rates (10–300 μL min^{-1}). The outlet flow from the mixer chip was coupled to a quartz flow cell (10 mm path length) and absorption spectra were obtained using a Perkin-Elmer, Lambda 15 UV–Vis spectrometer.

The inset of Fig. 1 shows an absorption spectrum for CdS nanoparticles obtained by mixing bulk (750 μL) solutions of Na_2S and $Cd(NO_3)_2{\cdot}4H_2O$. The shallow profile of the absorbance—which shows a gradual increase from 2.4 to 3.6 eV rather than a sharp onset at a specific energy—indicates that a broad range of crystallite sizes are present in the sample. A simplistic application of Brus' Equation would suggest that the nanoparticles range in size from roughly 12 nm (≡2.4 eV) to roughly 3.2 nm (≡3.6 eV); however we stress the highly approximate nature of this calculation. (In passing we note that, as with all the data reported here, no attempt was made to optimise the synthesis procedure. Reaction concentrations of 4×10^{-4} M were taken directly from the literature,[8] and it is likely that systematic variation of reaction conditions might yield nanoparticles of lower polydispersity.)

Fig. 1 shows, for a variety of flow rates, absorption spectra of fluid streams exiting the micromixer chip after mixing of the

† Electronic supplementary information ESI available: image of the central portion of the micromixer chip. See http://www.rsc.org/suppdata/cc/b2/b202998g/

DOI: 10.1039/b202998g

This journal is © The Royal Society of Chemistry 2002

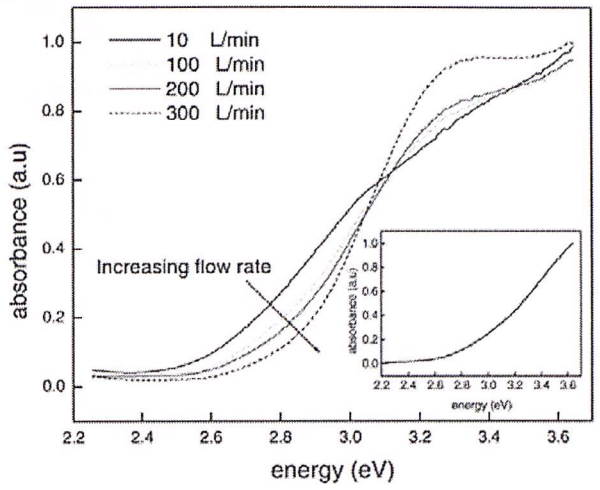


Fig. 1 Absorption spectra of fluid streams exiting the micromixer chip subsequent to mixing of cadmium nitrate and sodium sulfide solutions as a function of volumetric flow rate. Inset: absorption spectrum of nanoparticles produced by mixing bulk solutions.

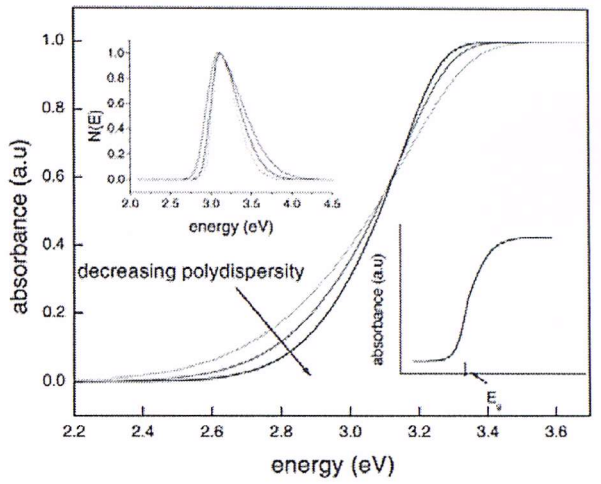


Fig. 2 Theoretical absorption spectra for samples of nanoparticles obtained by convolving an arbitrary single-particle absorption spectrum (inset right) with three crystallite distributions of similar shape but different second moments (inset left). E_g is defined as the energy at which the absorbance = ½.

cadmium nitrate and sodium sulfide solutions; the reagent concentrations were 4×10^{-4} M in all cases. Two important features are evident: first, the slopes of all absorption profiles in Fig. 1 are steeper than in the inset; and, secondly, there is a progressive steepening of the absorption profile as the volumetric flow rate is increased from 10 to 300 μL min^{-1}. The first observation indicates that the process of miniaturising the reaction volume is sufficient to lower the polydispersity of the crystallites. The second observation illustrates that increasing volumetric flow rates leads to further improvements in crystallite monodispersity. Both observations are consistent with the discussion above: miniaturisation improves homogeneity across the reaction volume; and increasing the flow rate lessens the likelihood of nanoparticle coalescence.

An interesting feature of the data presented in Fig. 1 is the existence of an approximate isosbestic point at 3.12 eV. This (and the variation in absorption profiles) may again be rationalized in terms of the polydispersity of the nanoparticles. If $N(E)$ represents the relative occurrence of particles with bandgap E and $A(E,E_G)$ represents the absorption spectrum of monodisperse particles of bandgap E_G, the average absorption spectrum of the population $<A(E)>$ may be approximated as $<A(E)> = A(E,E_G) \otimes N(E)$ where $\otimes$ denotes a convolution. (Here we have assumed that the absorption spectra of the variously sized nanoparticles are essentially identical in form, differing only in the location of the band edge.) In principle, if $A(E,E_G)$ is known, the underlying size distribution $N(E)$ may be inferred using deconvolution. In practice though this is seldom possible owing to noise in the input data and hence we make no attempt to extract size distributions here. We note however that the various absorption spectra will yield an isosbestic point only in special circumstances: underlying population distributions must be of similar form—with the same modal energy gap and skewness—but different variances. This is illustrated in Fig. 2 where we have taken an arbitrary non-symmetric absorption profile and performed convolutions with a series of skewed distributions with different second moments but identical first, third and fourth moments. The spectra are all seen to pass through a common point with the steepest absorption profile corresponding to the narrowest size distribution. The exact location of the isosbestic point is close to the modal energy gap of the particle distribution. Importantly, an isosbestic point is not obtained if the distributions have different third moments (skewness).

Relating this observation to the experimental data, it is apparent that varying the flow rate provides a means of improving monodispersity (reducing the second moment of the size distribution) without affecting the modal energy gap or altering the symmetry of the size distribution.

In conclusion, it can be seen that the use of microfluidic synthesis procedures offers distinct advantages over bulk scale fabrication procedures. The small size of the microreactor ensures that thermal and chemical homogeneity pertain throughout the entire reaction volume, leading to well controlled reaction conditions. Moreover, performing the reaction in a continuous flow format discourages coalescence of the newly formed nanoparticles. It should be noted that no effort has been made to optimise the microreactor in the current application. It is expected that refinements will lead to further improvements in resultant size distributions.

J. E. acknowledges the receipt of an Overseas Research Studentship from the UK Government. R. F. is grateful to SmithKlineBeecham for an EPSRC CASE studentship.

Notes and references

1 A. Alivisatos, *Science*, 1996, **271**, 933–937.
2 M. A. Hines and P. J. Guyot-Sionnest, *Phys. Chem.*, 1996, **100**, 468–471.
3 C. B. Murray, D. J. Norris and M. G. Bawendi, *J. Am. Chem. Soc*, 1993, **115**, 8706–8715.
4 D. V. Talapin, A. L. Rogach, A. Konowski, M. Haase and H. Weller, *Nano Lett.*, 2001, **4**, 207–211.
5 L. H. Qu, Z. A. Peng and X. G. Peng, *Nano Lett.*, 2001, **6**, 333–337.
6 T. Trindade, P. O'Brien and N. L. Pickett, *Chem. Mater.*, 2001, **13**, 3843–3858.
7 C. H. Fischer and M. Giersig, *Langmuir*, 1992, **8**, 1475–1478.
8 J. R. Lakowicz, I. Gryczynski and C. Murphy, *J. Phys. Chem. B*, 1999, **103**, 7613–7620.
9 M. U. Kopp, A. J. de Mello and A. Manz, *Science*, 1998, **280**, 1046–1048.
10 S. C. Jakeway, A. J. de Mello and E. L. Russell, *Fresenius J. Anal. Chem.*, 2000, **366**, 525–539.
11 F. G. Bessoth, A. J. deMello and A. Manz, *Anal. Commun.*, 1999, **36**, 213–215.
12 H. Weller, *Angew. Chem., Int. Ed. Engl.*, 1993, **32**, 41–53.

CONTROLLED QUANTUM DOT SYNTHESIS WITHIN MICROFLUIDIC CIRCUITS

Joshua B. Edel, Robin Fortt, John C. de Mello and Andrew J. de Mello
Department of Chemistry, Imperial College of Science, Technology and Medicine, Exhibition Road, South Kensington, London SW7 2AY.
joshua.edel@ic.ac.uk, a.demello@ic.ac.uk

Abstract

Nanocrystalline semiconductors are of considerable scientific and commercial interest owing to their tuneable optical and electronic properties, and potential applications in a wide range of electronic devices. We show that the use of microfluidic synthesis procedures offers distinct advantages over bulk scale fabrication procedures for the production of nanoparticles. The small size of the microreactor ensures that thermal and chemical homogeneity pertain throughout the entire reaction volume, leading to well controlled reaction conditions.

Keywords: semiconductor, nanoparticle, microreactor, quantum dots

1. Introduction

In the last decade semiconductor quantum dots (QD) have become the subject of one of the most rapidly growing branches of chemistry and physics. QD's or nanoparticles (NPs) are in the transition regime between molecules and the bulk material. Due to quantum confinement effects NPs show unique physical and chemical properties such as size-dependent band gap shifts and size dependent photoluminescence. Currently there is considerable interest in synthesizing nanoparticles of well-defined sizes [1]. One of the primary challenges associated with the synthesis of NP's is the ability to limit the size of growing clusters and to prevent them from interacting with each other. To date, techniques for producing highly monodisperse nanoparticles have been relatively complex and involve multiple processing steps. Herein we show that by using a continuous flow microreactor [2], operating within Low Reynold's number regimes, we are able to synthesise and control the size and monodispersity of certain nanoparticles.

2. Experimental

To generate CdS nanoparticles stock solutions of $Cd(NO_3)_2 \cdot 4H_2O$ and Na_2S were prepared at concentrations of $4x10^{-4}$ M and hydrodynamically delivered into a microfluidic channel network at various flow rates (1-600 μL/min). The outlet flow from a microfluidic reactor chip was coupled to a quartz flow cell and absorption spectra were taken. The microfluidic chip used is a two-layer device made up of a glass/silicon/glass sandwich and has an internal volume of 600 nL. Two inlet flows are split into a series of separate multichannel streams (16 partial flows). This is achieved

by repeated splitting of the channels in such a way that an array of symmetrical elements results. Wafer-through nozzles connecting the two fluidic layers allow the two liquid streams to converge and mix. Channels are then sequentially combined in a reverse network until all partial flows are united in one broad outlet channel.

3. Results and discussion

Absorption spectra of CdS colloids obtained at flow rates ranging from 0.025 – 0.30 ml/min are shown in **Figure 1**. The maximum gradient of absorption profiles increases as a function of volumetric flow rate, indicating a reduction the dispersity of the produced NPs [3].

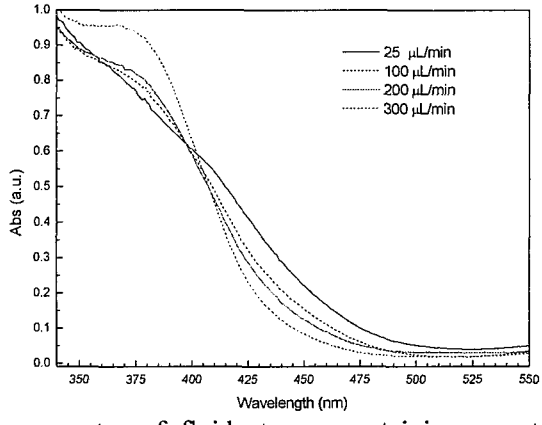


Figure 1. Absorption spectra of fluid stream containing quantum dots exiting the micromixer chip

Figure 2 shows absorption spectra of CdS using various initial cadmium concentrations at two different flow rates. Two key observations can be made. First, as the cadmium concentration is decreased absorption spectra shift to higher energies. Second, at higher flow rates the polydispersity of the produced NP populations is reduced.

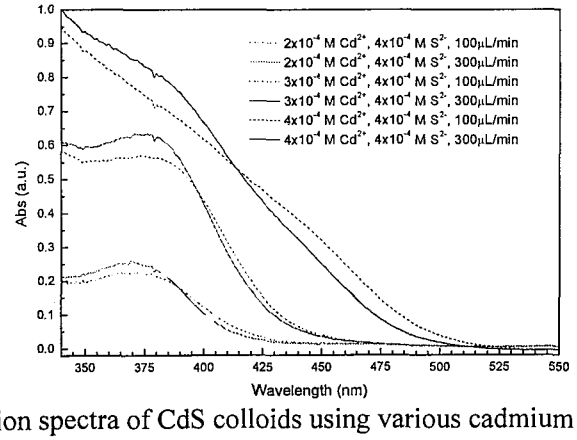


Figure 2 Absorption spectra of CdS colloids using various cadmium ion concentrations

An interesting feature of the data presented in Figure 1 is the existence of an approximate isosbestic point at 3.12 eV. This may be rationalized theoretically to be directly related to the polydispersity of the solution [3]. Let $N(E)$ be defined as the relative occurrence of particles with bandgap E, and $A(E,E_G)$ being defined as an absorption spectrum of a given set of monodisperse nanopartiles with a given bandgap E_G. The average absorption spectrum of the population $\langle A(E) \rangle$ may then be approximated by $\langle A(E) \rangle = A(E,E_G) \otimes N(E)$ ($\otimes$ denotes a convolution). It should be noted that various absorption spectra will yield an isosbestic point only in special circumstances: *underlying population distributions must be of similar form – with the same modal energy gap & skewness – but different variances.*

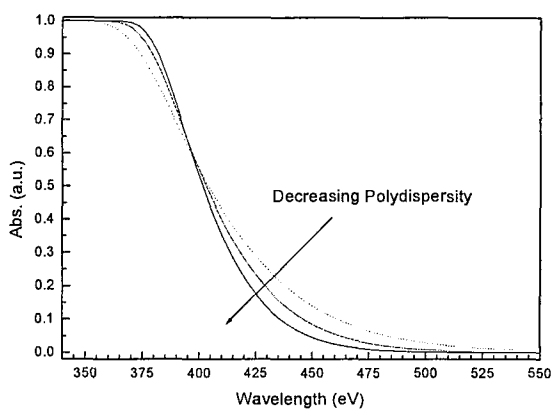


Figure3. Theoretical absorption spectra for samples of nanoparticles obtained by convolving an arbitrary single-particle absorption spectrum with three crystallite distributions of similar shape.

5. Conclusions

By adjusting experimental parameters such as concentration and flow rate both monodispersity and particle size of synthesised nanoparticles can be controlled.

Acknowledgements

J.B.E. acknowledges the receipt of an Overseas Research Studentship from the UK Government. R. F. is grateful to SmithKlineBeecham for an EPSRC CASE studentship.

References

1.M.A Hines, and P.J. Guyot-Sionnest,*J. Phys. Chem.*, 1996,**100**: 468 - 471.

2.F.G. Bessoth, A.J. de Mello, and A. Manz,*Anal. Commun.*,1999,**36**, 213 - 215.

3.J.B. Edel, R. Fortt, J.C. de Mello, A.J. de Mello,*Chem. Commun.*,2002,**10**, 1136-1137.

CONTROLLED SYNTHESIS OF COMPOUND SEMICONDUCTOR NANOPARTICLES USING MICROFLUIDIC REACTORS

Joshua B. Edel, Siva Krishnadasan, Jorge Torvilla cao-Romero, Ramon Vilar-Compte, John C. deMello & Andrew J. deMello*

Department of Chemistry, Imperial College London, Exhibition Road, South Kensington, London, SW7 2AZ, United Kingdom

Tel.: +44(0)207 594 5820, Fax: +44(0)207 594 5833, e-mail: a.demello@imperial.ac.uk

ABSTRACT

We describe the use of continuous-flow, microfluidic reactors for the controllable synthesis of compound semiconductor nanoparticles. Specifically, CdS nanoparticles are synthesised by rapid mixing of Na_2S and $Cd(NO_3)_2.4H_2O$ flow streams within a silicon/glass micromixer based on the principle of flow lamination. Room temperature syntheses at a variety of volumetric flow rates yield CdS nanoparticles of variable polydispersity. Analysis of absorption spectra of the CdS nanoparticles suggests that varying volumetric flow rates of reagent streams provides a simple and direct method of controlling population dispersity. Simple, single layer glass microstructures are also used to synthesise CdSe nanoparticles in continuous flow at temperatures between 180 and 240°C.

INTRODUCTION

Nanocrystalline semiconductors, with all three dimensions in the low nanometre range, are of significant scientific and commercial interest owing to their tuneable optical and electronic properties, and potential applications in a wide range of electronic and sensing devices [1]. The physical characteristics of such nanoparticles or quantum dots are determined primarily by spatial confinement effects with properties such as the optical band gap often differing considerably from the bulk semiconductor. Furthermore, because a large proportion of the constituent atoms are at or near the surface (rather than in a bulk environment), chemical properties, such as melting point are also variable. As these properties are ultimately determined by the physical size and three-dimensional shape of the crystallites, there is considerable interest in synthetic routes that yield nanoparticles of well-defined size and shape in high yield. To date, 'bottom-up' techniques for producing highly monodisperse nanoparticles have been far from robust and relatively complex in nature [2]. Synthetic routes follow a number of broad strategies. For example, nanoparticles may be formed by constrained growth within nanocavities such as zeolites and vesicles, or via biosynthetic reactions. More commonly, thermodynamic strategies, involving the strict control of reaction conditions (such as temperature, reagent concentrations and rate of mixing) are used to create particle populations of defined dispersity. For example, the injection of an organometallic precursor into a coordinating solvent at high temperature, followed by growth at lower temperatures yields a high degree of sample monodispersity when compared to other synthetic methods. Nevertheless, many applications require deviations about the mean particle diameter lower than one percent. This is beyond the tolerance of most standard syntheses which rarely yield size distributions better than 5%. To improve sample monodispersity even further, post-reaction treatments have proved effective. In these, a 'polydisperse' sample is first generated using traditional synthetic methods. Subsequently, nanoparticles of a given particle size are isolated by means of size-selective recrystallisation or precipitation. This approach, whilst attractive for small-scale production of nanoparticles, is not ideally suited to large-scale production due to low product yields and time consuming processing [2].

In recent years, there has been growing interest in microengineered structures for the synthesis of chemicals and biochemicals [3].These microfluidic reactors (consisting of microchannel networks whose cross-sectional dimensions are most easily measured in microns) exhibit significant advantages over ordinary bulk scale reactors. These include low unit cost, reduced sample consumption,

0-7803-7731-1/03/$17.00 ©2003 IEEE

faster reaction times and higher product yields and conversions. More importantly, miniaturisation ensures rapid mass- and heat-transfer thus providing high levels of control over reaction conditions [4]. These latter features of microfluidic reactors are exploited herein to synthesize monodisperse nanoparticles in a controllable fashion.

EXPERIMENTAL

Silicon/Glass Micromixer Fabrication

The microfluidic reactor we used for the synthesis of CdS nanoparticles operates according to the principle of distributive mixing, i.e. two inlet flows are split into a series of multichannel streams which, when combined within the silicon manifold, provide a large diffusional surface area for rapid mixing. This process is described schematically in Figure 1.

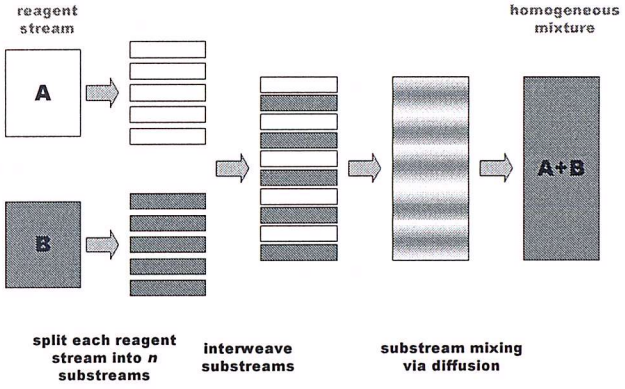


Figure 1: Principle of distributive mixing via flow lamination.

The mixer structure is made up of a glass–silicon–glass sandwich, has an internal volume of ~600 nL and externally measures 10x5x2 mm. Fabrication and design methods are discussed in detail elsewhere [5].

Glass Microfluidic Reactor Fabrication

A single-layer, glass microfluidic reactor was fabricated in-house and used for the synthesis of CdSe nanoparticles Channels were created using standard photolithographic procedures followed by wet chemical etching and bonding techniques. Briefly, a positive photoresist (S 1818, Shipley Corporation) was spin-coated onto the surface of a glass substrate (SLW, Hoya Corporation), and the channel design transferred to the substrate using a direct write laser lithography system (DWL2.0, Heidelberg Instruments). After soft-baking (95°C for 1 min) and exposure, the exposed regions of the photoresist were removed using a developer (Microposit 351, Shipley) and the remaining photoresist hard-baked (95°C for 5 min). Channels were then etched into the substrate using a buffered oxide etching solution (HF/NH_4F) at ambient temperature. Once complete, the etched substrate was sonicated sequentially in acetone, H_2SO_4/H_2O_2 and ultra pure water at ambient temperature, and dried with N_2 gas. Finally, a cover plate was thermally bonded to the substrate by heating the assembly at 550°C for 1 h, 580°C for 5 h and 555°C for 1 h. The complete device was then allowed to cool for 8 hours. Holes drilled in the top plate allow access to the fluidic network below. The reaction microchannel was 210 μm wide and 100 μm deep (the isotropic etching procedure results in a rounded channel profile, with a channel bed width of 10 μm).

Synthesis of CdS nanoparticles

CdS nanoparticles were obtained by directly mixing aqueous solutions of Na_2S ($2x10^{-4}$-$4x10^{-4}$M) and $Cd(NO_3)_2$ ($2x10^{-4}$-$4x10^{-4}$M) [6]. To aid stabilization of the resulting nanoparticles, an equal quantity of sodium polyphosphate was added to the $Cd(NO_3)_2$ nitrate solution prior to mixing. A syringe pump (PHD 2000, Harvard Instruments) was used to deliver reagents into the microfluidic channel network at various flow rates (10–300 μL/min). The outlet flow from the micromixer was coupled to a quartz flow cell (10 mm path length) and absorption spectra were obtained using a Perkin Elmer, Lambda 15 UV–Vis spectrometer.

Synthesis of CdSe nanoparticles

Selenium powder (9.5mg) was dissolved in trioctylphosphine (TOP, 2ml) under dry nitrogen with vigorous stirring. $Cd(AcO)_2$ (6.5mg) and trioctylphosphine-oxide (TOPO) (300mg) were then added to the solution. A syringe pump (PHD 200, Harvard Instruments) was then used to deliver the precursor solution into the microfluidic channel at a variety of flow rates (10–300 μL/min). Nucleation and nanoparticle growth is initiated by heating the entire chip substrate to between 180 and 240°C. Reaction products were monitored on-line using confocal fluorescence spectroscopy. Details of the experimental set-up are described in detail elsewhere.

RESULTS & DISCUSSION

Figure 2 shows representative absorption spectra of CdS nanoparticles synthesised using the microfluidic reactor (at volumetric flow rates between 10 and 300 μL/min) and by mixing bulk

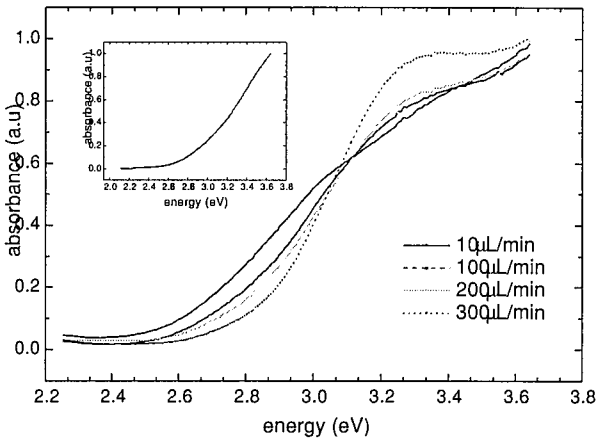


Figure 2: Absorption spectra of fluid streams exiting the micromixer chip subsequent to mixing of cadmium nitrate and sodium sulfide solutions. Inset: absorption spectrum of nanoparticles produced by mixing bulk solutions.

solutions of Na_2S and $Cd(NO_3)_2{\cdot}4H_2O$ [6]. It can be seen that the slopes of all absorption profiles for chip-based syntheses are greater than that observed for the bulk synthesis. Furthermore, the absorption front steepens as the volumetric flow rate is increased from 10 to 300 μL/min. The first observation indicates that the process of downsizing the reaction volume is adequate to lower the polydispersity of the produced nanoparticles. The second observation illustrates that an increasing volumetric flow rates leads to further improvements in particle monodispersity. Both observations demonstrate that system miniaturisation improves chemical homogeneity throughout the reaction volume. In the nucleation phase, nucleation and growth occur concurrently meaning that the earlier the nuclei form, the larger they ultimately grow. To obtain monodisperse nanoparticles, it is therefore important to ensure that nucleation occurs on a time-scale short compared with the characteristic growth time. An increased flow rate allows nucleation to occur rapidly and also lessens the likelihood of nanoparticle coalescence.

The data presented in Figure 2 also illustrate the existence of an approximate isosbestic point at 3.12 eV. The occurrence of this and the trend in absorption spectra with flow rate can be understood by consideration of sample polydispersity. If N(E) describes the relative occurrence of particles with bandgap E and $A(E,E_G)$ represents the absorption spectrum of monodisperse particles of bandgap E_G, the average absorption spectrum of the population may be approximated as $\langle A(E)\rangle = A(E,E_G)\otimes N(E)$. Figure 3 illustrates such an analysis where an

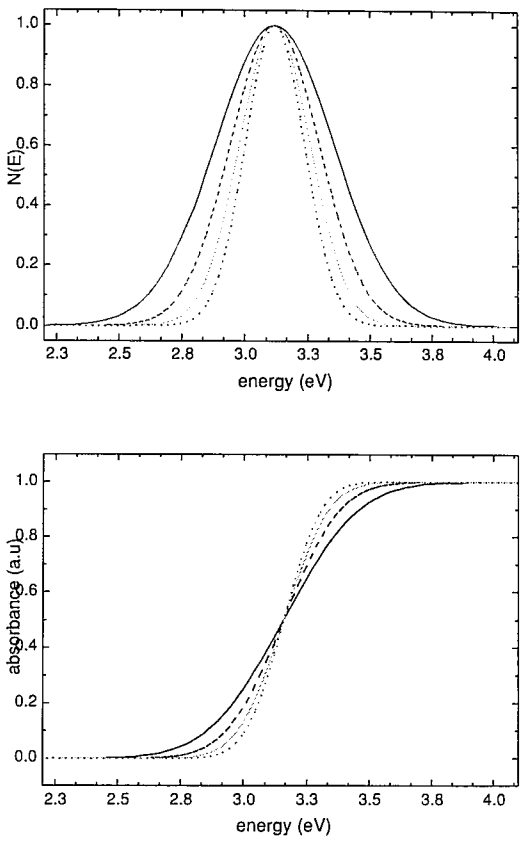


Figure 3: (a) Theoretical Gaussian population distributions for four nanoparticle populations, (b) resulting theoretical absorption spectra obtained by convolving an arbitrary single-particle absorption spectrum with each of the population distributions in (a).

arbitrary non-symmetric absorption profile (representing a monodisperse sample population) is convoluted with a series of symmetrical distributions of varying standard deviation. The resulting absorption spectra are seen to pass through a common (isosbestic) point with the steepest absorption profile corresponding to the narrowest size distribution. The exact location of the isosbestic point is close to the modal energy gap of the particle distribution. It should be noted that similar effects are observed when using asymmetric distributions, but an isosbestic point is not generated if the distributions have different third moments (skewness) [6]. This observation strongly suggests that varying the input reagent flow rate provides a means of improving monodispersity (reducing the second moment of the size distribution) without affecting the modal energy gap or altering the symmetry of the size distribution.

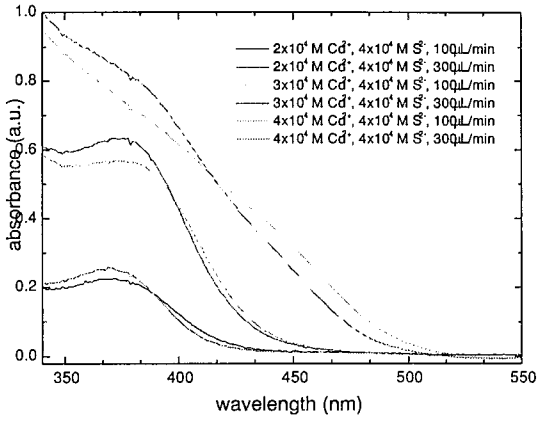


Figure 4: Absorption spectra of fluid streams exiting the micromixer chip as a function of both volumetric flow rate and Cd^{2+} concentration.

Figure 4 illustrates the variation of absorption spectra as a function of volumetric flow rate and Cd^{2+} concentration. In addition, to a steepeening of the absorption front as flow rate is increased, absorption spectra shift to lower energies as the Cd^{2+} concentration is increased. This trend indicates that as Cd^{2+} concentration is increased the average size of synthesized CdS nanoparticles also increases. Consequently, both the average size and monodispersity of the product may be controlled by simple variation of system parameters.

Measurement of photoluminescence (PL) spectra provides a direct method of sizing nanoparticles, since both peak wavelength and the full width at half maximum (fwhm) intensity increase with particle size and sample

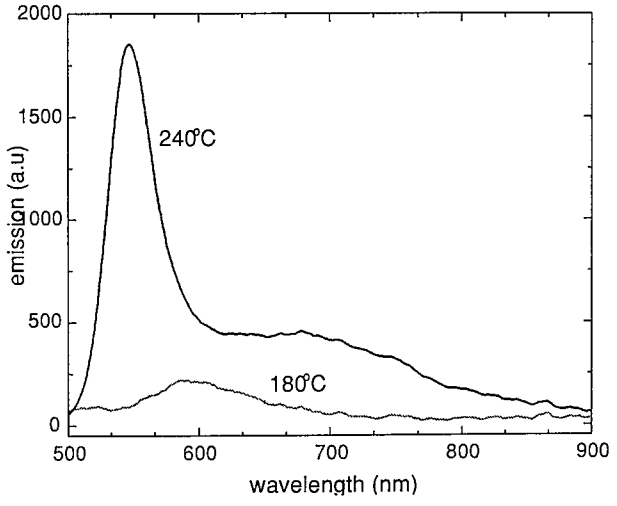


Figure 5: PL emission spectra of CdSe nanoparticles synthesised at 180 and 240°C. λ_{ex} = 458nm, residence time 50s.

polydispersity. Representative PL measurements (not shown) of CdS nanoparticles formed at high volumetric flow rates yield fwhm values of ~0.37eV. This compares well with reported post-hoc synthetic methods [7], indicating high sample monodispersity and a low concentration of surface defects.

Representative PL spectra of CdSe nanoparticles synthesised on a glass microfluidic reactor are shown in Figure 5. Initial results demonstrate formation of nanoparticles at temperatures above 180°C. As reaction temperature is increased a sharp emission at around 545 nm grows in. This is the band gap emission due to recombination of electron-hole pairs, and indicates a reasonably homogeneous size distribution of CdSe nanoparticles. The broad emission band at longer wavelengths is the subject of further investigation, but may be a consequence of radiative charge recombination at surface traps.

CONCLUSIONS

We have used simple microfluidic reactors to efficiently synthesize CdS and CdSe nanoparticles in continuous flow. Variation of system parameters, including temperature, flow rate and reagent concentration provide a high degree of control over both particle size and sample monodispersity. Current studies are focused on more precise control of reaction conditions and the functional integration of post-processing operations, such as particle stabilization and capping.

REFERENCES

[1] A.P. Alivisatos, "Semiconductor Clusters, Nanocrystals and Quantum Dots," *Science*, 271, 933-937 (1996).

[2] C.B. Murray, C.R. Kagan, M.G. Bawendi, "Synthesis and characterization of monodisperse nanocrystals and close-packed nanocrystal assemblies," *Ann. Rev. Mat. Sci.*, 30, 545-610 (2000) and references therein.

[3] K.F. Jensen, "Microreaction Engineering – is smaller better?," *Chem. Eng. Sci.*, 56, 293-303 (2001).

[4] J.B. Edel, R. Fortt, J.C. deMello & A.J. deMello, "Microfluidic routes to the controlled production of nanoparticles," *Chem. Commun.*, 1136-1137 (2002).

[5] F.G. Bessoth, A.J. deMello, A. Manz, "Microstructure for efficient continuous flow mixing," *Anal. Commun.*, 36, 213-215 (1999).

[6] J.R. Lakowicz, I. Grycynski, Z. Grycynski, C.J. Murphy, "Luminescence Spectral Properties of CdS Nanoparticles," *J. Phys. Chem. B*, 103, 7613-7620 (1999).

[7] L. Qi, H. Cölfen, M. Antonietti, "Synthesis and characterisation of CdS nanoparticles stabilised by double-hydrophilic block copolymers," *Nano Lett.*, 1, 61-65 (2001).

Continuous real-time monitoring of quantum dot synthesis within microfluidic reactors

Joshua B. Edel, Siva Krishnadasan, Jorge Tovilla cao-Romero, Ramon Vilar, John C. de Mello and Andrew J. DeMello

Department of Chemistry, Imperial College London, Exhibition Road, South Kensington, London SW7 2AZ, UK. joshua.edel@imperial.ac.uk

Abstract

Currently, one of the primary challenges associated with the synthesis of quantum dots or nanoparticles in bulk reaction chambers is the ability to control the nucleation and growth of clusters. Consequently, the ability to monitor particle formation in real time is highly desirable. Herein we demonstrate a strategy based on continuous-flow microfluidic reactors to monitor CdSe nanoparticle formation in real time.

Keywords: Confocal spectroscopy, Quantum dots, Microfluidic reactors, real-time monitoring

1. Introduction

Semiconductor quantum dots (QD) are currently a subject of intense research. QDs describe materials with dimensions in transition regime between molecules and bulk solids. Due to quantum confinement effects QDs show unique physical and chemical properties such as size-dependent band gap shifts and size dependent photoluminescence. Consequently, there is considerable interest in synthesis routes that yield nanoparticles of well-defined sizes [1]. Currently, one of the primary challenges associated with the synthesis of QDs in bulk reaction chambers is the ability to control the growth of the clusters. Consequantly, the ability to monitor the formation of particles in real time is highly desirable. Herein we demonstrate a strategy based on continuous-flow microfluidic reactors and confocal spectroscopy to synthesize and monitor CdSe nanoparticle formation in real time.

The ability to monitor the formation of particles in real time is highly desirable. Herein we demonstrate a strategy based on continuous-flow microfluidic reactors and confocal spectroscopy to synthesize and monitor CdSe nanoparticle formation in real time. Current real time microfluidic monitoring techniques are typically based on using flow cells coupled to a micromixer. Although this approach is viable, dead volumes are generally much greater than when monitoring a reaction directly within the walls of a microfluidic reaction chamber. An example of this was demonstrated by Edel et al. CdS nanoparticles

synthesized by hydrodynamically delivering the reactants into a microfluidic channel network at various flow rates (1-600 μL/min) [2].

2. Experimental

CdSe particles were synthesized as follows. Selenium powder (9.5mg) was dissolved in trioctylphosphine (TOP, 2ml) under dry nitrogen with vigorous stirring. $Cd(AcO)_2$ (6.5mg) and trioctylphosphine-oxide (TOPO) (300mg) were then added to the solution. A syringe pump (PHD 2000, Harvard Instruments) was then used to deliver the precursor solution into the microfluidic channel at a variety of flow rates (0.1 10 μL/min). Nucleation and nanoparticle growth is initiated by heating the entire chip substrate to between 180 and 290 °C. Residence times within the microfluidic chip ranged from 10 – 200 s. Reaction products were monitored on-line using a home built confocal fluorescence spectrometer (CFS).

A schematic of the spectrometer is shown in **Figure 1**. Precise details of the experimental system are described elsewhere [3]. A picosecond pulsed diode laser (at 438 nm) was used for all fluorescence lifetime measurements. Since fluorescence decaytimes were greater than 200 ns a laser repetition rate of 600 kHz was used. Fluorescence emission spectra were obtained using the 458 nm line from a multi-line CW air-cooled argon ion laser.

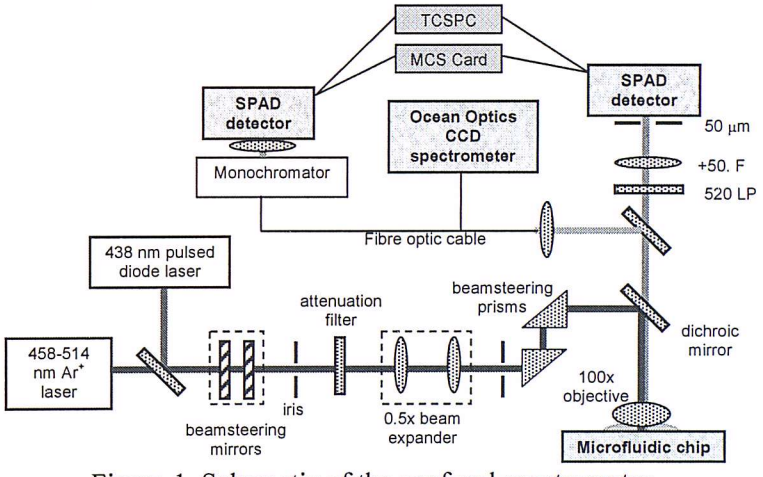


Figure 1. Schematic of the confocal spectrometer

3. Results and discussion

Figure 2 shows photoluminescence (PL) spectra of CdSe nanoparticles synthesized and monitored in real-time at a temperature of 290 °C. It is interesting to note that as the reactant flow rate is decreased spectra gradually shift to higher energies. This is a result of reactants spending increased times within the microfluidic system (yielding longer nucleation times) and forming larger nanoparticles. PL spectra provide a direct method of sizing nanoparticles as peak maxima are governed by the average particle size and the full width half maximum of the emission is directly related to the polydispersity of the particle population. **Figure 3** shows a fluorescence decay of a CdSe particles synthesized at 290 °C and at a flow rate of 2 μl/min. Analysis of the decay profile yielded a tri-exponential decay law with component lifetimes of 274 ns, 72.9 ns, and 7.55 ns.

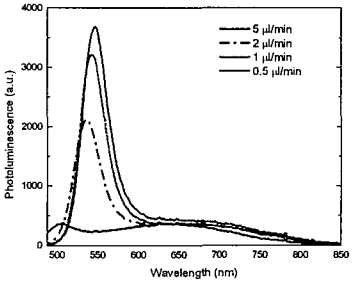


Figure 2. Photoluminescence spectra of CdSe nanoparticles synthesized at 290 °C and at flow rates ranging from 0.5 – 2 μl/min.

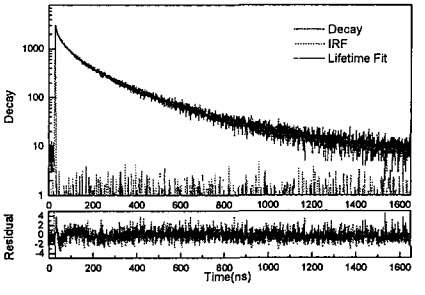


Figure 3. Fluorescence lifetime decay of CdSe nanoparticles synthesized at 290 °C and a flow rate of 2 μl/min within a microfluidic channel.

QDs tend to be highly photostable and fluorescence decay lifetimes range from nanoseconds to microseconds and hence, these particles would appear to be ideal for single molecule spectroscopy due to its improved spectral properties over typical organic dyes such as R-Phycoerythrin or rhodamine 6G. QD's such as CdSe also tend to have a much narrower full width half maximum (FWHM) and much more symmetrical emission spectra when compared to their organic counterparts. The benefits can be clearly seen in the single CdSe solution state burst spectra shown in **Figure 4**. This was obtained using the same confocal spectrometer described above. The overall signal to noise is much higher as well as the burst widths are more uniform than when compared to single molecule spectra of organic dyes such as rhodamine.

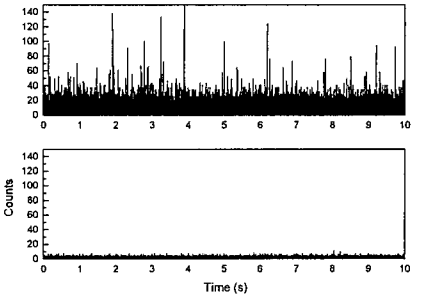


Figure 4. Single molecule detection of CdSe within a microfluidic channel

4. Conclusions

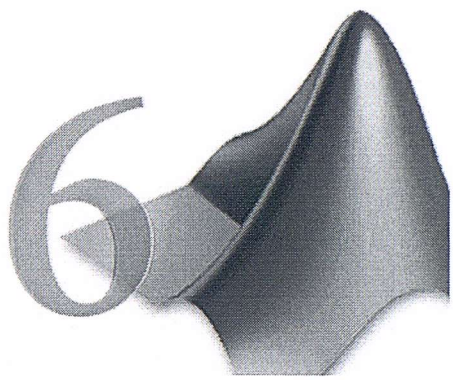
In this publication we have demonstrated a method for the monitoring the formation of quantum dots in continous real-time using confocal spectroscopy. The same confocal fluorescence spectrometer was also used to show single molecule detection cabaility of the CdSe nanocrystals in the solution state.

References

1. M.A Hines, and P.J. Guyot-Sionnest, *J. Phys. Chem.*, 1996, **100,** 468 - 471.
2. J.B. Edel, R. Fortt, J.C. de Mello and A.J. de Mello, *Chem. Commun.*, 2002, 1136-1137.
3. J.B. Edel, E. K. Hill, and A. J. de Mello, *Analyst,* 2001, **126,** 1953-1957.

Appendix 2

MATLAB®



Source code for programs written in Matlab

A2.1 SMD statistical analysis program

The *SmdAnal* program has the capability of importing an ascii file containing raw photon burst scans and performing a complete statistical analysis. I.e. threshold determination, Poisson recurrence time analysis, autocorrelation analysis, and the calculation of photon burst width distributions. The output is summarized in a text document and all graphical outputs are exported to tab delimited text files so that they can be plotted using other software packages such as Origin. The user adjustable parameter is as follows:

FileSeries = 'c:\4-001'	Name of the file series to import. All files should end in a '*.Asc' format and should follow the format -001,-002,-003 etc .
first = 1;	First file to import (e.g. – 001)
last = 90;	Last file to import (e.g. -090)
split = 10;	If there is a large amount of data to be analyzed it should be split up into groups. (e.g. analysis will be split up into groups of 10). If there is only one file to be analyzed (i.e. c:\burst-001) then *first*, *last*, and *split* would all be set to 1.
Rectangle = 15;	Defines the precision of the peak search algorithm. Use between 10 for large data sets (650 000 bins) and 50 for smaller data sets (16 000 bins)
delta = 1;	Typically set to 1. Change to speed up peak search (3 for 650 000 bins, 2 for 240 000, 1 for 120 000).
SearchPeak = 4;	Search for peaks >= value after threshold subtraction
fudge = 0.01;	Addition to the background threshold. Increase *fudge* to increase burst threshold (0-1).
tol = 1e-8;	Degree of convergence in LSA (0.1 – 1e-12). 1e-8 is typically sufficient.
tau = 500;	Number of autocorrelation points
startingB(1) = 1.97e-005;	Initial autocorrelation parameter (T_d)
startingB(2) = 3.21e-004;	Initial autocorrelation parameter (T_f)
startingB(3)=1	Initial autocorrelation parameter (R/d)
startingB(4)=3.12e-005;	Initial autocorrelation parameter (N)
startingB(5) = 2;	Initial autocorrelation parameter (Anol. Diffusion)
startingB(6)=10;	Initial autocorrelation parameter (Bkg Shift)
ub = [1;1;2;0.1;2.1;1e5];	Upper boundary for autocorrelation fit
lb = [0;0;0.5;0;1;0];	Lower boundary for autocorrelation fit

BWidthBins = 100;	Bin Width in Channels surrounding Local Maxima
WidthBkg = 0.8;	limiting width threshold factor 0-1. Typically set to 0.8.

```
% Program for the statistical analysis of SMD using CM
% Joshua B. Edel
% sub programs used 'pdist2' , 'autofn2', 'lclmax'

close all;
clear all;
warning off;
%%%%%%%%%%%%%%%%%%%% Parameters %%%%%%%%%%%%%%%%%%%%%%%%%%%%%%%%
FileSeries = 'e:\temp\qd-life\qd-001'; % all files should be in format *-001

first = 1; % first file
last = 1; % last file
split = 1; % split files into groups

Rectangle = 25; % Peak Search rectangle size
delta = 1; % 3 for 650 000 , 2 for 240 000 1 for 120 000 Peak search divide into sets ↙
 length(counts)/factor(mult)
SearchPeak = 7; % Search for peaks >= value after threshold subtraction
fudge = 0.2; % addition to the background threshold

tol = 1e-8; % Quality of fit 'TolX'
tau = 100; % autocorrelation points
StAuto = 1; % Start of autocorrelation fit
startingB(1) = 1.97e-005; startingB(2) = 3.21e-004; %Td , Tf     % autoFit
startingB(3)=1; startingB(4)=3.12e-005; startingB(5) = 2; % R/d, N, anol diff
startingB(6)=10; % bkg shift
ub = [1;1;2;0.1;2.1;1e5];
lb = [1e-10;1e-10;0.5;1e-10;1;0];

StPois = 1; %start of poisson recurrence time fit
EnPois = 0;
BWidthBins = 100; % Bin Width in Channels surrounding Local Maxima
WidthBkg = 0.8; % limiting width factor 0-1

%%%%%%%%%%%%%%%%%%%%%%%%%%%%%%%%%%%%%%%%%%%%%%%%%%%%%%%%%%%%%%%%%%
for i = 1:(last-first+1)/split
    start = first + i*split-split;
    numb = first + i*split-1;

[fid,time,counts,Size,MaxThreshBin,mult,FileSeriesb] = open(FileSeries,numb,delta,sta ↙
rt);

[thresh] = threshold(counts,fudge,Size,MaxThreshBin,tol,fid,FileSeriesb);

[FindTimeMax, BurstHeight,TotalPeaks,peaks] = peaklocation(counts, time, thresh,mult, ↙
Rectangle,SearchPeak,FileSeriesb,fid);

poisson(FindTimeMax,StPois,EnPois,time,TotalPeaks,fid,FileSeriesb);

```

```
47  autocor(time,counts,tau,tol,StAuto,Size,startingB,lb,ub,fid,FileSeriesb);
48
49  [BurstWidth,BwData] = distributions(BurstHeight,counts,thresh,peaks,SearchPeak,BWidth
    Bins,WidthBkg,Size,time,fid,FileSeriesb);
50
51  %%%%%%%%%%%%%%%%%%%%%%%%%%%%%%%%%%%%%%%%%%%%%%%%%%%%%%%%%%%%%%%%%%%%%%%%%%%%%%%%
52  fclose(fid); % writes data to word document
53
54  end
55  % TotalFiles = last-first+1;
56  % converge(FileSeriesb,TotalFiles,split,tau,time(2,1));
57
58
59  %  BW = BwData';
60  %  BwAvg = cumsum(BW);
61  %  BwAvg = BwAvg';
62  %  dlmwrite([FileSeries(1:end-3),'Bw.txt'],BwData,'\t');
63  %  dlmwrite([FileSeries(1:end-3),'BwAvg.txt'],BwAvg,'\t');
```

```
 1  function [fid, time, counts, Size, MaxThreshBin,mult,FileSeriesb] = open(FileSeriesRa ↙
    w,numb,delta,start)
 2
 3  %%%%%%%%%%%%%%%%%%%%%%%%%%%%%%%%%%%%%%%%%%%%%%%%%%%%%%%%%%%%%%%%%%%%%%%%%%%%%%%%%%%
 4  for i=start:numb
 5  FileSeries = FileSeriesRaw;
 6  a=10.^(2:-1:0)';
 7
 8  for k = 1:3;
 9      if (i >= a(k))
10      FileSeries = FileSeries(1:end-1);
11      end
12  end
13      file =[FileSeries int2str(i) '.Asc']; % import data
14      raw = load(file);
15      counts(:,i-start+1) = raw(:,2);
16  end
17
18
19  %%%%%%%%%%%%%%%%%%%%%%%%%%%%%%%%%%%%%%%%%%%%%%%%%%%%%%%%%%%%%%%%%%%%%%%%%%%%%%%%%%%
20  fid = fopen([FileSeriesRaw(1:end-3) int2str(numb) '.doc'],'w'); % Data saved to this ↙
    file
21  FileSeriesb = [FileSeries(1:end-1) int2str(numb)];
22
23  counts = reshape(counts,[],1);
24
25  fact = factor(length(counts));
26  mult = length(counts)/prod(fact(1:delta));
27
28  if(max(counts) > 100)
29      MaxThreshBin = 100;
30  else
31      MaxThreshBin = fix(max(counts)/2)*2;
32  end
33
34  timeStep = raw(2,1);
35  if  raw(2,1) == raw(3,1)
36      timeStep = timeStep/2;
37  end
38  % timeStep = 0.00002;
39
40  time = (0:timeStep:(timeStep*size(counts(:,1))-timeStep))';
41  %%%%%%%%%%%%%%%%%%%%%%%% End %%%%%%%%%%%%%%%%%%%%%%%%%%%%%%%%%%%%%%%%%%%%%%%%%%%%%%
42
43  %%%%%%%%%%%% Plot Data %%%%%%%%%%%%%%%%%%%%%%%%%%%%%%%%%%%%%%%%%%%%%%%%%%%%%%%%%%%%
44  fprintf(1,'Plot Data \n');
45  subplot(2,2,1);
46  plot(time,counts)
47  axis([time(1) time(end) 0 max(counts)+5]);
```

```
ylabel('Counts'); title('Recorded Data');

%Determine how many data points
Size =size(counts);
%%%%%%%%%%%%%%%%%%%%%%%%%%%%%%%%%%%%%%%%%%%%%%%%%%%%%%%%%%%%%%%%%%%%
fprintf(fid,'\n\n');
fprintf(fid,'File Name: %s\n',file);
fprintf(fid,'Dwell Time: %d\n',time(2,1));
fprintf(fid,'Number of Bins: %d\n',Size(1,1));

fprintf(fid,'\n');
fprintf(fid,'Initial Parameters \n');
fprintf(fid,'Bkg threshold Starting guess: %d\n',mean(counts));
```

```
 1  function [thresh] = threshold(counts,fudge,Size,MaxThreshBin,tol,fid,FileSeries)
 2
 3  %%%%%%%%%%%%%% Theshold Calculation %%%%%%%%%%%%%%%%%%%%%%%%
 4  startingA(1) = mean(counts); % Poisson Bkg Distribution Starting guess
 5
 6  fprintf(1,'Threshold Calculation \n');
 7  ThreshPoisHist = ((hist(counts,max(counts)+1))/Size(1))';
 8  ThreshPoisHist = ThreshPoisHist(1:MaxThreshBin);
 9  ThreshPoisHist1 = ThreshPoisHist(1:2:end);
10  ThreshPoisHist2 = ThreshPoisHist(2:2:end);
11  ThreshPoisHist = (ThreshPoisHist1 + ThreshPoisHist2);
12
13  bins = (0:2:(MaxThreshBin-1))';
14  % bins = (0:max(counts))';
15
16  subplot(2,2,2);
17  semilogy(bins,ThreshPoisHist,'x'); xlabel('Channel Count'); ylabel('Frequency'); titl↙
    e('Channel Count Distribution');
18
19  % Call fitting function
20
21  options=optimset('Display','Iter','TolX',tol,'MaxFunEvals',10000,'MaxIter',100000);
22  estimatesA = fminsearch('pdist2',startingA,options,bins,ThreshPoisHist);
23
24  PoisThreshFit =  ((exp(-estimatesA(1)+fudge)).*((estimatesA(1)+fudge).^(bins)));
25
26  % pr(1:max(counts+1))=0;
27  pr(1:(max(bins)/2+1))=0;
28  pro = pr';
29
30  % for i = 1:(max(counts)+1)
31
32  for i = 1:(max(bins)/2+1)
33  pro(i) = factorial(bins(i,1));
34  end
35
36  PoisThreshFitB = PoisThreshFit./pro;
37
38  hold on;
39  plot(bins(:,1),PoisThreshFitB(:,1),'r');
40  axis([0 MaxThreshBin/2 0.00001 1]);
41  %%%%%% check
42  % estimatesA(1)=10; % use only if poisson fit threshold doesn't work
43  thresh = estimatesA(1) + 3*sqrt(estimatesA(1)+fudge)+fudge;
44  text(20,0.3,'Threshold = '); text(20, 0.03, num2str(thresh));
45  %%%%%%%%%%%%%% End %%%%%%%%%%%%%%%%%%%%%%%%%%%%%%%%%%%%%%%%%%%%%%%%%%%%%%%%%%%%
46
47
48  fprintf(fid,'Addition to Bkg threshold: %d\n',fudge);
```

```
49  fprintf(fid,'Tolerence of fits: %d\n',tol);
50
51  fprintf(fid,'\n');
52  fprintf(fid,'Poisson Background Statistics \n');
53  fprintf(fid,'Background Threshold: %d\n',thresh);
54
55  dlmwrite([FileSeries(1:end),'Threshold.txt'],[ThreshPoisHist PoisThreshFitB],'\t');
56
57
58
59
```

```
1  function [FindTimeMax, BurstHeight,TotalPeaks,peaks] = peaklocation(counts, time, thr↙
   eshold,mult,Rectangle,SearchPeak,FileSeries,fid)
2
3  %%%%%%%%%%%%%%% Peak Location %%%%%%%%%%%%%%%%%%%%%%%%%%%%%%%%%%%%%%%%%%%
4  fprintf(1,'Locating Peaks \n');
5  SubData = counts - threshold;
6  lessZero = find(SubData <= 0);
7  SubData(lessZero) = 0;
8
9  subplot(2,2,3);
10 plot(time,SubData);xlabel('Time (s)'); ylabel('Counts');
11 axis([time(1) time(end) 0 max(counts)]);
12 hold on;
13
14 for m = 1:length(counts)/mult
15 peaks((m-1)*mult+1:mult*m,1) = lclmax(counts((m-1)*mult+1:mult*m),Rectangle);
16 end
17
18 FindTimeMax = time(peaks);
19 BurstHeight = counts(peaks);
20 BurstHeight = BurstHeight - threshold;
21 LessZero2 = find(BurstHeight >= SearchPeak);
22
23 TotalPeaks = size(LessZero2,1);
24 FindTimeMax = FindTimeMax(LessZero2);
25 BurstHeight = BurstHeight(LessZero2);
26
27 plot(FindTimeMax, BurstHeight, 'o'); title(['Number of Peaks = ',num2str(TotalPeaks)]↙
   );
28 % print([FileSeries '1.jpg'],'-djpeg');
29 %%%%%%%%%%%%%%% End %%%%%%%%%%%%%%%%%%%%%%%%%%%%%%%%%%%%%%%%%%%%%%%%%%%%
30 fprintf(fid,'Peak Location Rectangle size: %d\n',Rectangle);
31 fprintf(fid,'Search for Peaks greater than: %d\n',SearchPeak);
32
33 fprintf(fid,'\n');
34 fprintf(fid,'Total number of peaks: %d\n',TotalPeaks);
35 dlmwrite([FileSeries(1:end),'FindPeaks.txt'],[FindTimeMax BurstHeight],'\t');
36
37
```

```
 1  function [] = poisson(FindTimeMax,StPois,EnPois,time,TotalPeaks,fid,FileSeries)
 2
 3  %%%%%%%%%%%%%%% Poisson Analysis %%%%%%%%%%%%%%%%%%%%%%%%%%%%%%%%%%%%%%%%
 4  fprintf(1,'Poisson Analysis \n');
 5  recurrence = diff(FindTimeMax);
 6  HistRec = (hist(recurrence,20))';
 7  HistRecNonZero = find(HistRec>0);
 8  HistRec = HistRec(HistRecNonZero);
 9  Pt = (0:max(recurrence)/20:max(recurrence)-1/20*max(recurrence))';
10  figure(3)
11  subplot(3,1,1)
12  Pt = Pt(HistRecNonZero);
13  plot(Pt,HistRec,'o'); title('Poisson Analysis'); xlabel('time (s)'); ylabel('Frequenc↙
    y');
14  hold on;
15
16  PoisFit = polyfit(Pt(StPois:(end-EnPois)),log10(HistRec(StPois:(end-EnPois))),1);
17  PoisFitCurve = 10.^polyval(PoisFit,Pt(StPois:(end-EnPois)));
18  plot(Pt(StPois:(end-EnPois)),PoisFitCurve,'r');
19
20  subplot(3,1,2)
21  semilogy(Pt,HistRec,'o');
22  hold on;
23  semilogy(Pt(StPois:(end-EnPois)),PoisFitCurve,'r'); title(-1/PoisFit(1));
24  Tr = -1/PoisFit(1);, Freq = time(end)/TotalPeaks;
25
26  resB = (HistRec(StPois:(end-EnPois))-PoisFitCurve)./HistRec(StPois:(end-EnPois))*100;
27  subplot(3,1,3)
28  plot(Pt(StPois:(end-EnPois)),resB,'x');
29  axis([0 Pt(end) min(resB) max(resB)]);
30  ylabel('% error')
31  xlabel('Time (s)')
32
33  % print([FileSeries '3.jpg'],'-djpeg');
34  %%%%%%%%%%%%%%%% End %%%%%%%%%%%%%%%%%%%%%%%%%%%%%%%%%%%%%%%%%%%%%%%%%%%%
35  fprintf(fid,'recurrence time fit starting at point: %d\n',StPois);
36
37  fprintf(fid,'\n');
38  fprintf(fid,'Poisson Recurrence Time Statistics \n');
39  fprintf(fid,'Recurrence Time: %d\n',Tr);
40  fprintf(fid,'Frequency Time: %d\n',Freq);
41
42  dlmwrite([FileSeries(1:end),'Pois.txt'],[Pt(StPois:end-EnPois) HistRec(StPois:end-EnP↙
    ois) PoisFitCurve],'\t');
43
```

```
 1  function sse = autofn(params,Input,Actual_Output)
 2
 3  % Fitting Constants initial parameters
 4  lambda =params(1);
 5
 6  % fitting routine
 7  n =  ((exp(-lambda)).*(lambda.^Input));
 8  fitted_curve = n;
 9
10  pr(1:(max(Input))/2+1)=0;
11  pro = pr';
12
13  for ff = 1:((max(Input)/2)+1)
14  pro(ff) = factorial(Input(ff,1));
15  end
16
17  fitted_curve = n./pro;
18
19  % sum diff squared exp-theoretical
20  error_vector=fitted_curve - Actual_Output;
21  sse = sum(error_vector.^2);
22
```

```
function [] = autocor(time,counts,tau,tol,StAuto,Size,startingB,lb,ub,fid,FileSeries) ↙
;

%%%%%%%%%%%%%%% Autocorrelation Analysis %%%%%%%%%%%%%%%%%%%%%%%%%%%%%
fprintf(1,'Calculating Autocorrelation Function \n');
%Total Measurment time
TotalTime=Size*time(2);

%mean root square
rootmean=mean(counts);
rootmeansq = rootmean*rootmean;

 corr = xcorr(counts,counts,tau);

AutoCorTi = ((0:(tau-1))*time(2,1))';
auto = corr((tau+1):(2*tau),1);
auto =(auto/(rootmeansq*TotalTime(1)));

figure(2)
subplot(2,1,1)
semilogx(AutoCorTi,auto,'o');
ylabel('G(tau)'); xlabel('tau (s)'); title('Autocorrelation');
hold on;

% Call fitting function
options=optimset('Display','Iter','TolX',tol,'MaxFunEvals',10000,'MaxIter',10000,'Lar ↙
geScale','off');
AutoCorrVar = fmincon('autofn2',startingB,[],[],[],[],lb,ub,[],options,AutoCorTi(StAu ↙
to:end),auto(StAuto:end));

k = 1 + (AutoCorTi/AutoCorrVar(1)).^(2/AutoCorrVar(5));
l = 1 + (AutoCorrVar(3)*AutoCorrVar(3)*((AutoCorTi/AutoCorrVar(1)).^(2/AutoCorrVar(5) ↙
)));
sec = sqrt(l);
m = 1./(k.*sec);
AutoCorFit =1+ (1/(AutoCorrVar(4)))*(m.*exp(m.*(AutoCorTi/AutoCorrVar(2)).*(AutoCorTi ↙
/AutoCorrVar(2))))+AutoCorrVar(6);

semilogx(AutoCorTi(StAuto:end),AutoCorFit(StAuto:end),'r');

subplot(2,1,2)
resA = (auto-AutoCorFit)./auto*100;
subplot(2,1,2)
semilogx(AutoCorTi(StAuto:end),resA(StAuto:end),'x');
ylabel('% error')
xlabel('Time (s)')

% print([FileSeries '2.jpg'],'-djpeg');
%%%%%%%%%%%%%%%%%%% End %%%%%%%%%%%%%%%%%%%%%%%%%%%%%%%%%%%%%%%%%%%%%%%
```

```
45  fprintf(fid,'Number of autocorrelation points: %d\n',tau);
46  fprintf(fid,'Autocorrelation fit starting at point: %d\n',StAuto);
47  fprintf(fid,'Starting Parameters for autocorrelation fit Td, Tf, R/D, N, D": %d\n',st↙
    artingB);
48
49  fprintf(fid,'\n');
50  fprintf(fid,'Autocorrelation Statistics \n');
51  fprintf(fid,'Diffusion time: %d\n',AutoCorrVar(1));
52  fprintf(fid,'flow through time: %d\n',AutoCorrVar(2));
53  fprintf(fid,'Probe Width / depth: %d\n',AutoCorrVar(3));
54  fprintf(fid,'Normalization Constant: %d\n',AutoCorrVar(4));
55  fprintf(fid,'Anomalous Diffusion component: %d\n',AutoCorrVar(5));
56  fprintf(fid,'Bkg Shift: %d\n',AutoCorrVar(6));
57
58
59  dlmwrite([FileSeries(1:end),'AutoCor.txt'],[AutoCorTi auto AutoCorFit],'\t');
60
61
```

```
 1  function sse = autofn(params,Input,Actual_Output)
 2
 3  % Fitting Constants initial parameters
 4  diff_time = params(1); %diffusion time
 5  flow_time = params(2); %flow time
 6  rad_dep = params(3); % radius /depth
 7  % intent= params(4); %intensity
 8  % signo= params(5); % signal to noise
 9  numb= params(4);% number of molecules
10  block=params(5); % degree of blockage\
11  bkg = params(6); % bkg shift
12
13  % constraints
14  diff_time > 0;
15  flow_time >0;
16  rad_dep > 0;
17  block > 1;
18
19  % fitting routine
20  k = 1 + (Input./diff_time).^(2/block);
21  l = 1 + (rad_dep*rad_dep*((Input./diff_time).^(2/block)));
22  sec = sqrt(l);
23  m = 1./(k.*sec);
24  n =1+ (1/(numb))*(m.*exp(m.*(Input/flow_time).*(Input/flow_time)))+params(6);
25
26  fitted_curve = n;
27
28  % sum diff squared exp-theoretical
29  error_vector=fitted_curve - Actual_Output;
30  sse = sum(error_vector.^2);
```

```
function [BurstWidth,BwData] = distributions(BurstHeight,counts,threshold,peaks,Searc ↙
hPeak,BWidthBins,WidthBkg,Size,time,fid,FileSeries)

%%%%%%%%%%%%%%%% Burst Distribution Analysis %%%%%%%%%%%%%%%%%%%%%%
fprintf(1,'Burst Height Analysis \n');
BurstHeightHist = hist(BurstHeight,max(BurstHeight));
MeanHeight = mean(BurstHeight); StdHeight = std(BurstHeight);
RsdHeight = 100*StdHeight/MeanHeight;
figure(4)
subplot(2,2,1)
plot(BurstHeightHist,'x'); xlabel('Burst Height'); ylabel('Frequency');

%%%%%%%%%%%%%%%%%%%%%%
fprintf(1,'Burst Area Analysis \n');
% obtain local maxima location relative to raw data

PPP = peaks.*counts - threshold;
LocalMaxima = find(PPP >= SearchPeak);
CountsMinBin = counts((BWidthBins/2):(end - (BWidthBins/2)));
LocalMaxima2 = LocalMaxima(find((LocalMaxima > BWidthBins/2) & (LocalMaxima < ((Size( ↙
1,1) - BWidthBins/2)))));

% columns of peaks
 for i = 1:BWidthBins
    BwData(:,i) = counts(LocalMaxima2+i-BWidthBins/2);
 end

% obtain zeroes for below threshold value
for j=1:BWidthBins
    for i = 1:size(LocalMaxima2)
        if BwData(i,j) < WidthBkg*threshold
            BwData(i,j) = 0;
        end
    end
end

% get rid of all values to left and right of zero
for j = 1:(BWidthBins/2-1)
    for i = 1:size(LocalMaxima2)
        if BwData(i,j+BWidthBins/2) == 0
            BwData(i,j+BWidthBins/2+1) = 0;
        end
    end
end

for j = 1:(BWidthBins/2-2)
    for i = 1:size(LocalMaxima2)
        if BwData(i,BWidthBins/2-j) == 0
            BwData(i,BWidthBins/2-1-j) = 0;
```

```
48          end
49      end
50  end
51
52  BwData = BwData';
53
54  BurstArea = sum(BwData);
55  MeanArea = mean(BurstArea); StdArea = std(BurstArea);
56  BurstAreaHist = hist(BurstArea,max(BurstArea));
57  RsdArea = 100*StdArea/MeanArea;
58  subplot(2,2,2)
59  plot(BurstAreaHist,'x'); xlabel('Burst Area'); ylabel('Frequency');
60
61  %%%%%%%%%%%%%%%%%%%%%%%%%%%%
62  fprintf(1,'Burst Width Analysis \n');
63  for k = 1:size(LocalMaxima2)
64     BwTemp = size(find(BwData(:,k) > 0));
65     BurstWidth(k) = BwTemp(1,1);
66  end
67
68  BurstWidth = BurstWidth*time(2,1);
69  BurstWidthHist = hist(BurstWidth,max(BurstWidth)/time(2,1));
70  MeanWidth = mean(BurstWidth); StdWidth = std(BurstWidth);
71  RsdWidth = 100*StdWidth/MeanWidth;
72  subplot(2,2,3)
73  plot(time(2,1):time(2,1):length(BurstWidthHist)*time(2,1),BurstWidthHist,'x'); xlabel↙
    ('Burst Width (s)'); ylabel('Frequency');
74
75  subplot(2,2,4)
76  plot(counts(LocalMaxima2), (BurstArea)','x'); xlabel('Burst Heigth'); ylabel('Burst A↙
    rea');
77
78  % print([FileSeries '4.jpg'],'-djpeg');
79  %%%%%%%%%%%%%%%%%%%%%%%% End  %%%%%%%%%%%%%%%%%%%%%%%%%%%%%%%%%%%%%%%%%%%%
80  fprintf(fid,'Bin Widths Selected surrounding Local Maxima: %d\n',BWidthBins);
81  fprintf(fid,'Burst Width Bkg threshold value: %d\n',WidthBkg);
82
83  fprintf(fid,'\n');
84  fprintf(fid,'Burst Distribution Statistics \n');
85  fprintf(fid,'Mean Height: %d\n',MeanHeight);
86  fprintf(fid,'Standard Deviation in Height: %d\n',StdHeight);
87  fprintf(fid,'Relative Standard Deviation in Height: %d\n',RsdHeight);
88
89  fprintf(fid,'\n');
90  fprintf(fid,'Mean Area: %d\n',MeanArea);
91  fprintf(fid,'Standard Deviation in Area: %d\n',StdArea);
92  fprintf(fid,'Relative Standard Deviation in Area: %d\n',RsdArea);
93
94  fprintf(fid,'\n');
```

```
 95  fprintf(fid,'Mean Width: %d\n',MeanWidth);
 96  fprintf(fid,'Standard Deviation in Width: %d\n',StdWidth);
 97  fprintf(fid,'Relative Standard Deviation in Width: %d\n',RsdWidth);
 98
 99  dlmwrite([FileSeries(1:end),'BHH.txt'],[BurstHeightHist'],'\t');
100  dlmwrite([FileSeries(1:end),'BAH.txt'],[BurstAreaHist'],'\t');
101  dlmwrite([FileSeries(1:end),'BWH.txt'],[(time(2,1):time(2,1):length(BurstWidthHist)*t↙
     ime(2,1))' BurstWidthHist'],'\t');
102  dlmwrite([FileSeries(1:end),'WidthArea.txt'],[counts(LocalMaxima2) (BurstArea)'],'\t'↙
     );
103
```

A2.2 TCSPC fitting program (without a GUI)

The *TCSPC ascii* lifetime decay fitting program has the capability of importing an ascii file containing both the instrument response and the decay. The program can calculate lifetimes with up to 5 components. The output is summarized in a text document. Least squares fits and curves are exported to tab delimited text files so that they can be plotted using other software packages such as Origin. The user adjustable parameter is as follows:

file = 'e:\temp\ \BulkPro.txt';	Name of file to import. Should be in a *.txt tab delimited format.
TimePerChan = 0.006288;	Time per channel (ns).
tol = 1e-8;	Degree of convergence in LSA (0.1 – 1e-12). 1e-8 is typically sufficient.
StartTime = 10;	Initial channel to be used in fit
EndTime = 6000;	Initial channel to be used in fit
Amp = [5e-3 1e-2 0.1 0.1 0.1];	Initial amplitude guess (A1, A2,A3,A4,A5)
Life = [3.3 1 0.25 0.5 .1];	Initial lifetime guess (τ_1, τ_2, τ_3, τ_4, τ_5,)
InstCurveNum = 1;	Instrument response column number
DataCurveNum = 2;	Decay column number
components = 3;	Number of components to fit

Upper and lower boundary conditions for least squares fitting routine

AmpL = [0;0;0;0;0];	*AmpU = [1;1;1;1;1];*	amplitude
LifeL = [1;1;0.01;0.01;0.01];	*LifeU = [6;10;3;10;10];*	lifetime (ns)
TShiftL = [-0.1];	*TShiftU = [0.1];*	time shift (ns)
BackL = [-50;-50];	*BackU = [50;50];*	bkg shift (counts)

```
% Program for the Calculation of Lifetimes
% imported data should be tab delimited with 2 columns (inst resp and decay)

% Sub Routines: LifeFunc1com,LifeFunc2com,LifeFunc3com,MainRoutine,plots
% Joshua B. Edel

close all
clear;
warning off;
%%%%%%%%%%%%%%%%%%%% Parameters %%%%%%%%%%%%%%%%%%%%%%%%%%%%%%%%%%
file = 'c:\mex\234.txt'; % file location should be tab delimited
TimePerChan = 0.22489; % time per channel in ns
tol = 1e-6; % Quality of fit 'TolX'
StartTime = 50; %start chan; set to 1 for beginning
EndTime = 4096; %end chan; Actual end time is [EndTime*TimePerChan]
Amp = [0.08 0.03 0.01]; % initial amplitude guess
Life = [5 3 1]; % initial lifetime guess
InstCurveNum = 1; % column number of inst response
DataCurveNum = 2; % column number of decay
components = 1; % number of lifetime components to fit. max of 3

%%%%%%%%%%%%%%%%%%%   End %%%%%%%%%%%%%%%%%%%%%%%%%%%%%%%%%%%%%%%%

ExportData = MainRoutine(file,TimePerChan,tol,StartTime,EndTime,Amp,Life,InstCurveNum ↙
,DataCurveNum,components);

for i = 1:components
fid=fopen([file,'-data' int2str(i), 'com.Asc'],'wt');
fprintf(fid,[repmat('%f\t',1,4) '%f\n'],ExportData(:,:,i).');
fclose(fid);
end

```

```
function ExportData = MainRoutine(file,TimePerChan,tol,StartTime,EndTime,Amp,Life,InstCurveNum,DataCurveNum,components)

fid2 = fopen([file '-stats.doc'],'w'); % Data saved to this file
raw = load(file);

InstrumentResponse = raw(:,InstCurveNum); %Import Data Set
Data = raw(:,DataCurveNum); %Import Data Set
InstrumentResponse = InstrumentResponse/max(InstrumentResponse)*max(Data);

 if (EndTime > size(Data(:,1)))
     EndTime = size(Data(:,1));
 end

iback = -1*mean(InstrumentResponse(EndTime-100:EndTime))-1;
Dback = sqrt(mean(Data(EndTime-100:EndTime)));

TimeShift = 0; % shift in time variable

starting = [Amp Life iback Dback TimeShift]; starting =  starting';


 InstrumentResponse = InstrumentResponse(StartTime:EndTime);
 Data = Data(StartTime:EndTime);
 Time = (0:TimePerChan:(TimePerChan*size(Data)-TimePerChan))';

lb = [0;0;0;0;0;0;-inf;-inf;-inf];
ub = [1;1;1;inf;inf;inf;inf;inf;inf];


options=optimset('Display','Iter','LargeScale','on','TolX',tol,'MaxFunEvals',5000,'MaxIter',5000);

if components == 1
    %%%%%%%%%%%%% First Run
    FittedDecay = fmincon('lifeFunc1com',starting,[],[],[],[],lb,ub,[],options,Time,Data,InstrumentResponse);
    FittedDecay(2) = 0;FittedDecay(3) = 0;FittedDecay(5) = 0;FittedDecay(6) = 0;
    FittedDecays = [FittedDecay];

elseif components == 2
    %%%%%%%%%%%%% Second Run
    FittedDecay = fmincon('lifeFunc1com',starting,[],[],[],[],lb,ub,[],options,Time,Data,InstrumentResponse);
    FittedDecay(2) = 0;FittedDecay(3) = 0;FittedDecay(5) = 0;FittedDecay(6) = 0;

    starting2 = FittedDecay*1.2; starting2(2) = starting(2); starting2(3)=starting(3); starting2(5) = starting(5); starting2(6)=starting(6);
    FittedDecay2 = fmincon('lifeFunc2com',starting2,[],[],[],[],lb,ub,[],options,Time
```

```
,Data,InstrumentResponse);
45      FittedDecay2(3) = 0;FittedDecay2(6) = 0;
46      FittedDecays = [FittedDecay,FittedDecay2];
47
48  elseif components == 3
49      %%%%%%%%%%%% Third Run
50      FittedDecay = fmincon('lifeFunc1com',starting,[],[],[],[],lb,ub,[],options,Time,D↙
    ata,InstrumentResponse);
51      FittedDecay(2) = 0;FittedDecay(3) = 0;FittedDecay(5) = 0;FittedDecay(6) = 0;
52
53      starting2 = FittedDecay*1.2; starting2(2) = starting(2); starting2(3)=starting(3)↙
    ; starting2(5) = starting(5); starting2(6)=starting(6);
54      FittedDecay2 = fmincon('lifeFunc2com',starting2,[],[],[],[],lb,ub,[],options,Time↙
    ,Data,InstrumentResponse);
55      FittedDecay2(3) = 0;FittedDecay2(6) = 0;
56
57      starting3 = FittedDecay2*1.2; starting3(3) = starting(3); starting3(6)=starting(6↙
    );
58      FittedDecay3 = fmincon('lifeFunc3com',starting3,[],[],[],[],lb,ub,[],options,Time↙
    ,Data,InstrumentResponse);
59      FittedDecays = [FittedDecay,FittedDecay2,FittedDecay3];
60  end
61      %%%%%%%%%%%%%%%%%%%%%%%%%%%%% Fit Plot
62      %%%%%%%%%%%%%%%%%%%%%%%%%%%%% %%%%%%%%%%%%%%%%%%%%%%%%%%%%%%%%%%%%%%%%%%%%%%↙
    %%%%%%%%%%%%
63  for i = 1:components
64     ExportData(:,:,i) = plots(FittedDecays(:,i),Time,Data,InstrumentResponse,StartTime↙
    ,EndTime,fid2);
65  end
66
67  fclose(fid2);
68
69  % ExportData = [TimeForDecayb TotalDecayb InstRespForCalcb DataForCalcb Residb];
70
```

```
function RedChi = lifefn(params,Time,Data,InstrumentResponse)

Amp1 = params(1);
Life1 = params(4);
iback = params(7);
Dback = params(8);
TimeShift = params(9); % shift in time variable

TimeWithShift = Time + TimeShift;
InterpolateInstResp = interp1(Time,InstrumentResponse,TimeWithShift,'cubic');

TimeForDecay = Time;
InstRespForCalc = InterpolateInstResp +1+iback;

DataForCalc = Data + 1;

Decay1(1:size(Data(:,1))) = 0; Decay1 = Decay1';

for i = 1:(size(Data(:,1))-2)
Decay1(i+1) = ((Decay1(i,1)+Amp1*0.5*(InstRespForCalc(i+1,1)))*exp(-Time(2,1)/Life1)) ↙
...
    +0.5*Amp1*(InstRespForCalc(i+2,1));
end

TotalDecay = Decay1+Dback;
Resid = (1./sqrt(DataForCalc)).*(TotalDecay-DataForCalc);
ResidSq = Resid.^2;

RedChi = (sum(ResidSq))./size(Data(:,1)); RedChi = RedChi(1,1);

```

```
function RedChi = lifefn(params,Time,Data,InstrumentResponse)

Amp1 = params(1); Amp2 = params(2);
Life1 = params(4); Life2 = params(5);
iback = params(7);
Dback = params(8);
TimeShift = params(9); % shift in time variable

TimeWithShift = Time + TimeShift;
InterpolateInstResp = interp1(Time,InstrumentResponse,TimeWithShift,'cubic');

TimeForDecay = Time;
InstRespForCalc = InterpolateInstResp +1+iback;

DataForCalc = Data + 1;

Decay1(1:size(Data(:,1))) = 0; Decay1 = Decay1';
Decay2(1:size(Data(:,1))) = 0; Decay2 = Decay2';
Decay3(1:size(Data(:,1))) = 0; Decay3 = Decay3';

for i = 1:(size(Data(:,1))-2)
Decay1(i+1) = ((Decay1(i,1)+Amp1*0.5*(InstRespForCalc(i+1,1)))*exp(-Time(2,1)/Life1)) ...
    +0.5*Amp1*(InstRespForCalc(i+2,1));
end

for i = 1:(size(Data(:,1))-2)
Decay2(i+1) = ((Decay2(i,1)+Amp2*0.5*(InstRespForCalc(i+1,1)))*exp(-Time(2,1)/Life2)) ...
    +0.5*Amp2*(InstRespForCalc(i+2,1));
end

TotalDecay = Decay1+Decay2+Dback;
Resid = (1./sqrt(DataForCalc)).*(TotalDecay-DataForCalc);
ResidSq = Resid.^2;

RedChi = (sum(ResidSq))./size(Data(:,1)); RedChi = RedChi(1,1);

```

```
function RedChi = lifefn(params,Time,Data,InstrumentResponse)

Ampl = params(1); Amp2 = params(2); Amp3 = params(3);
Life1 = params(4); Life2 = params(5);Life3 = params(6);
iback = params(7);
Dback = params(8);
TimeShift = params(9); % shift in time variable

TimeWithShift = Time + TimeShift;
InterpolateInstResp = interp1(Time,InstrumentResponse,TimeWithShift,'cubic');

TimeForDecay = Time;
InstRespForCalc = InterpolateInstResp +1+iback;

DataForCalc = Data + 1;

Decay1(1:size(Data(:,1))) = 0; Decay1 = Decay1';
Decay2(1:size(Data(:,1))) = 0; Decay2 = Decay2';
Decay3(1:size(Data(:,1))) = 0; Decay3 = Decay3';

for i = 1:(size(Data(:,1))-2)
Decay1(i+1) = ((Decay1(i,1)+Amp1*0.5*(InstRespForCalc(i+1,1)))*exp(-Time(2,1)/Life1)) ↙
...
    +0.5*Amp1*(InstRespForCalc(i+2,1));
end

for i = 1:(size(Data(:,1))-2)
Decay2(i+1) = ((Decay2(i,1)+Amp2*0.5*(InstRespForCalc(i+1,1)))*exp(-Time(2,1)/Life2)) ↙
...
    +0.5*Amp2*(InstRespForCalc(i+2,1));
end

for i = 1:(size(Data(:,1))-2)
Decay3(i+1) = ((Decay3(i,1)+Amp3*0.5*(InstRespForCalc(i+1,1)))*exp(-Time(2,1)/Life3)) ↙
...
    +0.5*Amp3*(InstRespForCalc(i+2,1));
end

TotalDecay = Decay1+Decay2+Decay3+Dback;
Resid = (1./sqrt(DataForCalc)).*(TotalDecay-DataForCalc);
ResidSq = Resid.^2;

RedChi = (sum(ResidSq))./size(Data(:,1)); RedChi = RedChi(1,1);

```

```
function ExportData = plots(FittedDecay2,Time,Data,InstrumentResponse,StartTime,EndTime,fid2)

Amp1b = FittedDecay2(1); Amp2b = FittedDecay2(2); Amp3b = FittedDecay2(3);
Life1b = FittedDecay2(4); Life2b = FittedDecay2(5); Life3b = FittedDecay2(6);
ibackb = FittedDecay2(7);
Dbackb = FittedDecay2(8);
TimeShiftb = FittedDecay2(9); % shift in time variable

TimeWithShiftb = Time + TimeShiftb;
InterpolateInstRespb = interp1(Time,InstrumentResponse,TimeWithShiftb,'cubic');

TimeForDecayb = Time;
InstRespForCalcb = InterpolateInstRespb +1+ibackb;

DataForCalcb = Data + 1;

Decay1b(1:size(Data(:,1))) = 0; Decay1b = Decay1b';
Decay2b(1:size(Data(:,1))) = 0; Decay2b = Decay2b';
Decay3b(1:size(Data(:,1))) = 0; Decay3b = Decay3b';

for i = 1:(size(Data(:,1))-2)
Decay1b(i+1) = ((Decay1b(i,1)+Amp1b*0.5*(InstRespForCalcb(i+1,1)))*exp(-Time(2,1)/Life1b))...
    +0.5*Amp1b*(InstRespForCalcb(i+2,1));
end

for i = 1:(size(Data(:,1))-2)
Decay2b(i+1) = ((Decay2b(i,1)+Amp2b*0.5*(InstRespForCalcb(i+1,1)))*exp(-Time(2,1)/Life2b))...
    +0.5*Amp2b*(InstRespForCalcb(i+2,1));
end

for i = 1:(size(Data(:,1))-2)
Decay3b(i+1) = ((Decay3b(i,1)+Amp3b*0.5*(InstRespForCalcb(i+1,1)))*exp(-Time(2,1)/Life3b))...
    +0.5*Amp3b*(InstRespForCalcb(i+2,1));
end

TotalDecayb = Decay1b+Decay2b+Decay3b+Dbackb;
TotalDecayb = TotalDecayb(1:(size(Data)-1));
DataForCalcb = DataForCalcb(1:size(Data)-1);
TimeForDecayb = TimeForDecayb(1:size(Data)-1);
InstRespForCalcb = InstRespForCalcb(1:size(Data)-1);
Residb = (1./sqrt(DataForCalcb)).*(TotalDecayb-DataForCalcb);
ResidSqb = Residb.^2;
RedChib = (sum(ResidSqb))./EndTime(:,1); RedChib = RedChib(1,1);
ResDifSqb = (diff(Residb)).^2;
DWb = sum(ResDifSqb)/sum(ResidSqb);
```

```
46
47  figure;
48  subplot('Position',[0.1 0.40 0.8 0.55]);
49  semilogy(TimeForDecayb,TotalDecayb,'r');
50  hold on;
51  semilogy(TimeForDecayb,InstRespForCalcb);
52  semilogy(TimeForDecayb,DataForCalcb,'g');
53  ylabel('Counts');
54  axis tight;
55
56  subplot('Position',[0.1 0.1 0.8 0.2]);
57  plot(TimeForDecayb,Residb);
58  xlabel('Time (ns)');
59  ylabel('Residual');axis tight;
60
61  fprintf(fid2,'\n');
62  fprintf(fid2,'COMPONENT 1 \n');
63  fprintf(fid2,'  Lifetime: %d',Life1b);
64  fprintf(fid2,'  Amplitude: %d',Amp1b);
65  yield1b = 100*Amp1b*Life1b/(Amp1b*Life1b+Amp2b*Life2b+Amp3b*Life3b);
66  fprintf(fid2,'  yield: %d\n',yield1b);
67
68  fprintf(fid2,'\n');
69  fprintf(fid2,'COMPONENT 2 \n');
70  fprintf(fid2,'  Lifetime: %d',Life2b);
71  fprintf(fid2,'  Amplitude: %d',Amp2b);
72  yield2b = 100*Amp2b*Life2b/(Amp1b*Life1b+Amp2b*Life2b+Amp3b*Life3b);
73  fprintf(fid2,'  yield: %d\n',yield2b);
74
75  fprintf(fid2,'\n');
76  fprintf(fid2,'COMPONENT 3 \n');
77  fprintf(fid2,'  Lifetime: %d',Life3b);
78  fprintf(fid2,'  Amplitude: %d',Amp3b);
79  yield3b = 100*Amp3b*Life3b/(Amp1b*Life1b+Amp2b*Life2b+Amp3b*Life3b);
80  fprintf(fid2,'  yield: %d\n',yield3b);
81
82  fprintf(fid2,'\n');
83  AverageLifetimeb = yield1b*Life1b/100 + yield2b*Life2b/100+ yield3b*Life3b/100;
84  fprintf(fid2,'Average Lifetime: %d\n',AverageLifetimeb);
85  fprintf(fid2,'\n');
86
87  fprintf(fid2,'\n');
88  fprintf(fid2,'STATS \n');
89  fprintf(fid2,'Background Correction Intensity: %d\n',Dbackb);
90  fprintf(fid2,'Instrument Response Correction Intensity: %d\n',ibackb);
91  fprintf(fid2,'Shift in Instrument Response: %d\n',TimeShiftb);
92  fprintf(fid2,'Reduced Chi Sq: %d\n',RedChib);
93  fprintf(fid2,'Derb Wat: %d\n',DWb);
94
```

```
95  % fclose(fid2);
96
97  ExportData = [TimeForDecayb TotalDecayb InstRespForCalcb DataForCalcb Residb];
```

A2.3 Binning of time tagged scans

The *SMD* lifetime decay fitting program has the capability of importing a *.t3r file containing time tagged photon data. The program bins the data so that a photon burst scan can be extracted to a file. Once this is extracted the lifetime decay from all photon bursts can be determined using the program described in A2.2. SMD statistics can also be determined using the program described in A2.1. This program requires the peak searching function *lclmax* which was previously described. The user adjustable parameter is as follows:

file= 'e: cfp-cells\444.t3r';	Name of the file to import.
bin = 400e-6;	Defines dwell time for photon burst scan (s)
bkg = 40;	Searches for peaks above the 'bkg' threshold
toe = 10	Defines the precision of the peak search algorithm. Use between 10 for large data sets (650 000 bins) and 50 for smaller data sets (16 000 bins)

```
 1  close all;
 2  clear all;
 3
 4  [tt,ch]=readt3r('e:\temp\qd-life\qe6.t3r');
 5
 6  bin = 500e-6; % dwell time (s)
 7  bkg = 10; % bkg correction
 8  toe = 15; % search rectangle for toeplitz
 9
10  len=length(tt);
11  maxbin = len;
12  % form absolute time tags
13  t=0;
14  abstt=zeros(size(tt));
15  for i=2:len
16      delta = tt(i)-tt(i-1);
17      if( delta > 0)
18          t=t+delta;
19      else
20          t=t+1048576+delta; % negative or zero delta is the wrap around case
21      end;
22      abstt(i)=t*1e-7; % 100ns per tick
23  end;
24
25
26    abstt=abstt(1:maxbin);
27    counts(1:len) = 1; counts = counts(1:maxbin)';
28    raw = [abstt counts];
29
30  bin_index=floor(1+abstt/bin);
31  bin_counts=sparse(bin_index,1,counts);
32  m = full(bin_counts);
33
34  peaks = lclmax(m,toe);
35  PeakMaxLocation = find(peaks);
36  time = (0:bin:length(m)*bin-bin)';
37
38  TimeMax = time(PeakMaxLocation);
39
40  plot(time, m);
41  Data = [time m];
42  % fid=fopen('e:\temp\CFP-cells\testc-001.asc','wt');
43  % fprintf(fid,[repmat('%f\t',1,1) '%f\n'],Data.');
44  % fclose(fid);
45  hold on;
46
47  PeakMax = m(PeakMaxLocation);
48  PeakMaxTime = time(PeakMaxLocation);
49  PeakMaxTime=PeakMaxTime(PeakMax>bkg);
```

```
50  PeakMaxLocation = PeakMaxLocation(PeakMax>bkg);
51  PeakMax = PeakMax(PeakMax>bkg);
52
53
54  plot(PeakMaxTime,PeakMax,'o');
55  PeakGlobMax = max(m);
56  PeakNumber=1;
57  NumOfPeak = length(PeakMax);
58
59
60
61  %%%%%%%%%%% Decay at max
62   B = zeros(PeakGlobMax,NumOfPeak);
63   for j = 1:NumOfPeak
64      B(1:PeakMax(j),j) = ch(bin_index == PeakMaxLocation(j));
65  end
66
67  step = 0:1:4096;
68
69  C = hist(B,step);
70  C = C(2:end,:);
71  figure(2);
72  image(C,'CDataMapping','scaled'); colorbar;
73
74  D = C';
75  D = sum(D);
76  figure(3);
77  plot(D);
78  %%%%%%%%%%%%%%%%%%%%%%%%%%%%%%%%
79  aaa= PeakMaxLocation; bbb = diff(aaa);
80  bbb=bbb/2;bbb = floor(bbb);
81  ccc = aaa(1:length(aaa)-1) + bbb;
82
83  aaa = []; aaa(2:length(PeakMaxLocation)+1,1)= PeakMaxLocation; bbb = diff(aaa);
84  bbb=bbb/2;bbb = floor(bbb);
85  ddd = aaa(2:length(aaa)-1) - bbb(1:end-1);
86
87  for i = 1:length(ddd)
88  ggg(i,1) = sum(m(ddd(i):ccc(i)));
89  end
90
91  BB = zeros(max(ggg),NumOfPeak);
92   for j = 1:NumOfPeak-1
93      BB(1:ggg(j),j) = ch(bin_index >= ddd(j) & bin_index <= ccc(j));
94  end
95
96
97
98  E = hist(BB,step);
```

```
 99  E = E(2:end,:);
100  E = flipud(E);
101  figure(4);
102  image(E,'CDataMapping','scaled'); colorbar;
103
104  q =length(E(1,:))
105
106  fid=fopen('e:\temp\qd-life\single.txt','wt');
107  fprintf(fid,[repmat('%f\t',1,q-1) '%f\n'],E.');
108  fclose(fid);
109
110
111
112  F = E';
113  F = sum(F);
114  figure(5);
115  plot(F);
```

```
 1  function [ttag, chan] = readt3r(name);
 2  %[ttag, chan] = readt3r('name') reads a TimeHarp t3r mode file
 3  fid=fopen(name);
 4  fprintf(1,'\n');
 5
 6  %read text header
 7  ident = setstr(fread(fid, 16, 'char'));
 8  fprintf(1,'Ident: %s\n',ident);
 9  sw_ver = setstr(fread(fid, 6, 'char'));
10  fprintf(1,'Software version: %s\n',sw_ver);
11  hw_ver = setstr(fread(fid, 6, 'char'));
12  fprintf(1,'Hardware version: %s\n',hw_ver);
13  filetime = setstr(fread(fid, 18, 'char'));
14  fprintf(1,'File creation: %s\n',filetime);
15  crlf = setstr(fread(fid, 2, 'char'));
16  comment = setstr(fread(fid, 256, 'char'));
17  fprintf(1,'Comment: %s\n',comment);
18
19  %read binary header
20  channels = fread(fid, 1, 'long');
21  fprintf(1,'Channels: %d\n',channels);
22  curves = fread(fid, 1, 'long');
23  fprintf(1,'Curves: %d\n',curves);
24  active = fread(fid, 1, 'long');
25  fprintf(1,'Active: %d\n',active);
26  measmode = fread(fid, 1, 'long');
27  fprintf(1,'Measurement Mode: %d\n',measmode);
28  histmode = fread(fid, 1, 'long');
29  fprintf(1,'Histogramming Mode: %d\n',histmode);
30  range=fread(fid, 1, 'long');
31  fprintf(1,'Range: %d\n',range);
32  offset=fread(fid, 1, 'long');
33  fprintf(1,'Offset: %d\n',offset);
34  acqtime=fread(fid, 1, 'long');
35  fprintf(1,'Acqu. time: %d\n',acqtime);
36  displinlog=fread(fid, 1, 'long');
37  fprintf(1,'Disp lin/log: %d\n',displinlog);
38  disptfrom=fread(fid, 1, 'long');
39  fprintf(1,'Disp time from: %d\n',disptfrom);
40  disptto=fread(fid, 1, 'long');
41  fprintf(1,'Disp time to: %d\n',disptto);
42  dispcfrom=fread(fid, 1, 'long');
43  fprintf(1,'Disp counts from: %d\n',dispcfrom);
44  dispcto=fread(fid, 1, 'long');
45  fprintf(1,'Disp counts to: %d\n',dispcto);
46  cfdzerox=fread(fid, 1, 'long');
47  fprintf(1,'CFD zero cross: %d\n',cfdzerox);
48  cfddiscr=fread(fid, 1, 'long');
49  fprintf(1,'CFD discr min: %d\n',cfddiscr);
```

```
50  synclevel=fread(fid, 1, 'long');
51  fprintf(1,'SYNC level: %d\n',synclevel);
52  resolution=fread(fid, 1, 'float');
53  fprintf(1,'Resolution: %d\n',resolution);
54  macroclock=fread(fid, 1, 'long');
55  fprintf(1,'Macro clock: %d\n',macroclock);
56  tttrrecs=fread(fid, 1, 'ulong');
57  fprintf(1,'No of TTTR records: %d\n',tttrrecs);
58
59  %read all TTTR records
60  tttrdata=fread(fid, tttrrecs, 'ulong');
61
62  ttag=floor(tttrdata/4096);
63  chan=tttrdata-ttag*4096;
64
65  fprintf(1,'\n%d records loaded\n',length(tttrdata));
66
67  fclose(fid);
68
```

A2.4 MLE statistics program

The *MLE statistics* program compares photon bursts by using a maximum likelihood estimator. This program compares 2 sets of single particle burst scans with well defined average burst width distributions. The program requires a matrix containing single particle bursts with each column representing the counts from a single particle. An average photon burst distribution is also required. For trial data, this can be done by applying the following code to the end of the SMD analysis program (A2.1).

BW = BwData';	
BwAvg = cumsum(BW);	Matrix of photon bursts
BwAvg = BwAvg';	Average particle burst
dlmwrite([FileSeries(1:end-3),'Bw.txt'],BwData,'\t');	Writes the matrix to a file
dlmwrite([FileSeries(1:end-3),'BwAvg.txt'],BwAvg,'\t'); file	Writes the *BwAvg* to a

The user adjustable parameter in the *MLE Statistics* program is as follows:

BW = dlmread('e:\4-Bw.txt',';');	Imports 1st file containing matrix of photon bursts
BwAvg = dlmread('e\4-BwAvg.txt',';');	Imports average photon burst of 1st file
BW_b = dlmread('e:\5-Bw.txt',';');	Imports 2st file containing matrix of photon bursts
BwAvg_b = dlmread('e:\5-BwAvg.txt',';');	Imports average photon burst of 2nd file
mid = 50;	Row containing the maxima in the BW matrix (midpoint).
bin = 40;	Number of bins to analyze to the left and right of the midpoint.
tau = 100;	Number of autocorrelation points to analyze

```
clear all;
close all;
warning off;

%%%% i(1) 1100 nl; i(2) 1000 nl ........i(11) 100 nl



file = 'e:\temp\ProteinMLE\';
for i = 1:3
    w = dlmread([file int2str(i) '-Bw.txt'],';');
        q = w(:,1:200);
        Bw(:,:,i) =   q;

    x = dlmread([file int2str(i) '-BwAvg.txt'],';');
        r = x(:,end);
        BwAvg(:,i) = r;
end
%%%%%%%%%%%%%%%%%%%%%%%%%%%%%%%%%%%%%%%%%%%%%%%%%%%%%%%%
mid = 100;
bin = 99;
tau = 200;

for j = 1:2
for i = 1:2
[Diff C neg pos Prob Prob_2 A B] = ProbPeakFn(mid,bin,Bw(:,:,j),BwAvg(:,j),Bw(:,:,i), ↙
BwAvg(:,i));

Data = [Diff C A B];
fid=fopen([file int2str(j) '-' int2str(i) '-Data.Asc'],'wt');
fprintf(fid,[repmat('%f\t',1,3) '%f\n'],Data.');
fclose(fid);

Data2 = [Prob Prob_2];
fid=fopen([file int2str(j) '-' int2str(i) '-Data2.Asc'],'wt');
fprintf(fid,[repmat('%f\t',1,1) '%f\n'],Data2.');
fclose(fid);

DataB(:,i) = B;


end


fid=fopen([file int2str(j) '-' int2str(i) '-DataB.Asc'],'wt');
fprintf(fid,[repmat('%f\t',1,10) '%f\n'],DataB.');
fclose(fid);

end
```

```
49
50  figure(1); plot(Prob,'x'); hold on; plot(Prob_2,'or');
51  figure(2);
52  plot(C,'o');
```

```
function [Cb, C, neg, pos, Prob, Prob_2, A, B] = ProbPeakFn(mid,bin,BW_1,BwAvg_1,BW_2,BwAvg_2)

%%%%%%%%%%%%%%%%%%%%% Determine Probability %%%%%%%%%%%%%%%%%%%%%%%%%%%%%
AT = BwAvg_1(mid-bin:mid+bin); Prob = AT/sum(AT);
AT2 = BwAvg_2(mid-bin:mid+bin); Prob_2 = AT2/sum(AT2);
%%%%%%%%%%%%%%%%%%%%%%%%%MLE on peak shape probability%%%%%%%%%%%%%%%%%%%%%%%%%%%%
for i = 1:size(BW_1(1,:),2)
    Ia = BW_1(mid-bin:mid+bin,i).*log(BW_1(mid-bin:mid+bin,i)./(sum(BW_1(mid-bin:mid+bin,i))*Prob));
    Ia(isnan(Ia)) = 0; % Change NaN = 0
    Ia(isinf(Ia)) = 0; % Change inf = 0
    SumIa(:,i) = sum(Ia);
end
%%%%%%%%%%%%%%%%%%%%%%%%%%%%%%%%%%%%%%%%%%%%%%%%%%%%%%%%%%%%%%%%%%%%%%%%%%%%

for i = 1:size(BW_1(1,:),2)
    Ib = BW_1(mid-bin:mid+bin,i).*log(BW_1(mid-bin:mid+bin,i)./(sum(BW_1(mid-bin:mid+bin,i))*Prob_2));
    Ib(isnan(Ib)) = 0; % Change NaN = 0
    Ib(isinf(Ib)) = 0; % Change inf = 0
    SumIb(:,i) = sum(Ib);
end
%%%%%%%%%%%%%%%%%%%%%%%%%%%%%%%%%%%%%%%%%%%%%%%%%%%%%%%%%%%%%%%%%%%%%%%%%%%%
A = real(SumIa); A= A';
B = real(SumIb); B = B';
Cb = A - B;
C = A - B; C(C<0)=-1; C(C>0)=1;

neg = sum(C == -1);
pos = sum(C == 1);
%%%%%%%%%%%%%%%%%%%%%%%%%%%%%%%%%%%%%%%%%%%%%%%%%%%%%%%%%%%%%%%%%%%%%%%%%%%%
```

```
function [C2, Cq, negq, posq, Probq, Prob_2q, Aq, Bq] = ProbPeakFn(tau,BW_1,BwAvg_1,BW_2,BwAvg_2)

%%%%%%%%%%%%%%%%%%%%Autocorrelation of individual peaks%%%%%%%%%%%%%%%%%%%%%%%%
for i = 1:size(BW_1(1,:),2)
corr = xcorr(BW_1(:,i),BW_1(:,i),tau);
auto(:,i) = corr((tau+1):(2*tau),1);
end
auto(auto < 0) = 0;
autoavg = mean(auto')';

for i = 1:size(BW_2(1,:),2)
corr2 = xcorr(BW_2(:,i),BW_2(:,i),tau);
auto2(:,i) = corr2((tau+1):(2*tau),1);
end
auto2(auto2 < 0) = 0;
autoavg2 = mean(auto2')';
%%%%%%%%%%%%%%%%%%autocor probability%%%%%%%%%%%%%%
ATq = autoavg(1:tau,:); Probq = ATq/sum(ATq);
AT2q = autoavg2(1:tau,:); Prob_2q = AT2q/sum(AT2q);

%%%%%%%%%%%%%%%%%%%%MLE for autocor%%%%%%%%%%%%%%%%%%%%%%%%%%%%%%%%%%%%%%%%
for i = 1:size(auto(1,:),2)
    Iaq = auto(:,i).*log(auto(:,i)./(sum(auto(:,i))*Probq));
    Iaq(isnan(Iaq)) = 0; % Change NaN = 0
    Iaq(isinf(Iaq)) = 0; % Change inf = 0
    SumIaq(:,i) = sum(Iaq);
end
%%%%%%%%%%%%%%%%%%%%%%%%%%%%%%%%%%%%%%%%%%%%%%%%%%%%%%%%%%%%%%%%%%%%%%%%%%%
for i = 1:size(auto(1,:),2)
    Ibq = auto(:,i).*log(auto(:,i)./(sum(auto(:,i))*Prob_2q));
    Ibq(isnan(Ibq)) = 0; % Change NaN = 0
    Ibq(isinf(Ibq)) = 0; % Change inf = 0
    SumIbq(:,i) = sum(Ibq);
end
%%%%%%%%%%%%%%%%%%%%%%%%%%%%%%%%%%%%%%%%%%%%%%%%%%%%%%%%%%%%%%%%%%%%%%%%%%%

Aq = real(SumIaq); Aq= Aq';
Bq = real(SumIbq); Bq = Bq';
C2 = Aq - Bq;
Cq = Aq - Bq; Cq(Cq<0)=-1; Cq(Cq>0)=1;

negq = sum(Cq == -1);
posq = sum(Cq == 1);
```

A2.5 SMD Monte Carlo simulation

The *SMD monte carlo simulation* has the capability of simulation a photon burst scan for single molecules or particles confined within micro or nanofluidic channels. The output from this program can further be analyzed using the program described in section A2.1 in order to extract SMD statistics. Only the fundamental code is shown in this section, further modifications including the inclusion of collection and excitation efficiency functions, photobleaching effects will not be described. The user adjustable parameter is as follows:

P0 = 1.29e1;	Laser power (W);
lambda = 0.488;	Laser wavelength (mum)
planck = 6.6262e-34;	Planck's constant in SI
lightspeed = 2.9979e14;	speed of light in mum/s
v = 500;	linear flow velocity in mum/sec
D = 80;	diffusion constant in mum^2/s
dt = 50e-6;	time step in s
xfield = [-8 8];	Chip boundary (direction of flow(
yfield = [-4 4];	Chip boundary (width)
zfield = [-1 1];	Chip boundary (depth)
runs = 200;	Number of single molecules flowing through microfluidic channel.
res = 10;	Resolution (can range from 5 – 20).

```
% function [sims] = smdMCxyz

close all;
clear all;
warning off;

P0 = 1.29e2;
lambda = 0.488;
w0 = lambda*1600/pi/1.52/1500;
noise = 5;

planck = 6.6262e-34; % Planck's constant in SI
lightspeed = 2.9979e14; % speed of light in mum/s
v = 300; % molecule's flow velocity in mum/sec

D = 10; % diffusion constant in mum^2/s
dt = 500e-6; % time step in s
xfield = [-5 5]; %
yfield = [-8 8];
zfield = [-1 1]; % vertical extension of considered detection volume
N = ceil(2*xfield(2)/v/dt); % total number of time steps per simulation

runs = 200;
res = 15;

for i = 1:10

simul = MCfunc(lambda,P0,v,w0,D,dt,N,runs,xfield,yfield,zfield,res);
simul = simul + noise*rand(length(simul),1);

sims = [(0:dt:size(simul(:,1))*dt-dt)' simul];
file =['e:\temp\test\flow3000-00' int2str(i) '.Asc'];
% dlmwrite(file,sims,' ');

fid=fopen(file,'wt');
fprintf(fid,[repmat('%f\t',1,1) '%f\n'],sims.');
fclose(fid);

end

plot(sims(:,1),sims(:,2));

```

```
 1  function simul = MCfunc(lambda,P0,v,w0,D,dt,N,runs,xfield,yfield,zfield,res)
 2
 3  dx = lambda/res; dz = dx; dy = dx;
 4  xv = xfield(1) + (0.5:(xfield(2)-xfield(1))/dx)*dx;
 5  yv = yfield(1) + (0.5:(yfield(2)-yfield(1))/dy)*dy;
 6
 7  if length(zfield)>1
 8      zv = zfield(1) + (0.5:(zfield(2)-zfield(1))/dz)*dz;
 9  else
10      zv = zfield;
11  end
12
13  [xl, yl, zl] = ndgrid(xv, yv, zv);
14
15  w=w0*(1+(lambda*zl./(pi*w0^2)).^2).^0.5;
16  l=2*P0./(pi*w.^2);
17  Intensity = l.*exp(-2*(xl.^2+yl.^2)./w.^2);
18
19  xi=sqrt(2*D*dt);
20  dx = xl(2,1,1)-xl(1,1,1);
21  dy = yl(1,2,1)-yl(1,1,1);
22  dz = zl(1,1,2)-zl(1,1,1);
23  nx = size(xl,1);
24  ny = size(yl,2);
25  nz = size(zl,3);
26
27  for k=1:runs
28      % random variable dr
29      % with diffusion:
30      x = xi*randn(1,N) + v*dt;
31      y = xi*randn(1,N);
32      z = xi*randn(1,N);
33      % initial position
34      x(1) = -xfield(2);
35      y(1) = yfield(2)*(2*rand-1);
36      z(1) = zfield(1) + rand*diff(zfield);
37      % path calculation
38      x = cumsum(x);
39      y = cumsum(y);
40      z = cumsum(z);
41      x = round((x-xl(1,1))/dx);
42      y = round((y-yl(1,1))/dy);
43      z = round((z - zl(1,1))/dz);
44
45      x(x<1) = 1;
46      x(x>nx) = nx;
47      y(y<1) = 1;
48      y(y>ny) = ny;
49      z(z<1) = 1;
```

```
50      z(z>nz) = nz;
51
52      path = Intensity(sub2ind([nx ny nz],x,y,z));
53      fluo(:,k) = path';
54  end
55
56  simul = reshape(fluo,[],1);
```

A2.6 Hydrodynamic focussing simulations

This hydrodynamic focussing simulation calculates the number of particles which diffuse outside of a hydrodynamically focussed analyte stream within a microfluidic channel. The user adjustable parameter is as follows:

k = 1.38066e-23;	Boltzman eqaution
T = 295;	Temperature
Viscosity = 0.000891;	Viscosity (kg/m/s)
r = 1e-9;	Particle radius (m)
Density = 1;	Density (g/cm3)
Length = 16;	Micorchannel length (mm)
ChanWidth = 60;	Channel Width (μm)
depth = 30;	Channel Depth (μm)
foc = 10;	Focussing width (μm)
VolFlow = [0.01];	Volumetric flow velocity (ul/min)

```
clear all;
close all;

%%%%%%%%%%%%%%%%%%%%%% parameters %%%%%%%%%%%%%%%%%%%%%%%%%%%%%%%%
k = 1.38066e-23; %boltzman
T = 295; % temperature
Viscosity = 0.000891; % kg/m/s water = 0.000891
r = 1e-9; % particle radius
Density = 1; % g/cm3 water = 1

Length = 16; % chip Length mm
ChanWidth = 60;
depth = 30; % um
foc = 10; % analyte focused width
points = 1; % random points per step size
pre0 = 50; % points before 0 on x axis

VolFlow = [0.01 0.1 1 5]; % ul/min
LengthDown = 0.0:0.02:Length; % chip Length dimensions

%%%%%%%%%%%%%%%%%%%%%%%%%%%%%%%%%%

DiffCoef = (k*T)./(6*pi*Viscosity*r); % diffusion m2/s
LinVeloc = VolFlow./ChanWidth/depth/60*1e6; % mm/s
%%%%%%%% % particles lost %%%%%%%%%%%%%%%%%%%

[LD,LV] = meshgrid(LengthDown, LinVeloc);

ti = LD./LV; % Time to go given Length down channel
Wi = 1e6*(2*ti.*DiffCoef).^0.5; %ms Diff time across foc width

WidthDiff = Wi/2 + foc;
WidthDiff(WidthDiff > ChanWidth) = ChanWidth;

Loss = (WidthDiff-foc)./WidthDiff*100;
Loss = Loss';
LengthDown=LengthDown';
plot(LengthDown,Loss,'o');
xlabel('Position down Stream (mm)');
ylabel('Percent of particles lost');

%%%%%%%%%%%%%%%%%%%%%%%%%%%%%%%%
for j= 1:length(VolFlow)
figure
aaa = WidthDiff(j,:);
bbb = LengthDown';
x=[];
m=1;

```

```
50  for i = 1:length(LengthDown)
51      a = -aaa(1,i)/2; b = aaa(1,i)/2;
52      x(:,m) = a+(b-a)*rand(points,1);
53      m=m+1;
54  end
55  c = -foc/2; d = foc/2;
56       y = c+(d-c)*rand(points,pre0);
57  xx=[y x];
58
59  upper = length(LengthDown)-1;
60  yy = -pre0*Length/upper:Length/upper:Length;
61  %
62  plot(yy,xx','ro','MarkerEdgeColor','k','MarkerFaceColor','c', 'MarkerSize',1.5);hold ↙
    on;
63  text(10,37,['Particle size: ' num2str(r*1e9) ' nm']);
64  text(10,33,['Flow rate: ' num2str(VolFlow(j)) ' \mul/min']);
65
66  top(1:length(yy)) = ChanWidth/2;
67  bottom(1:length(yy)) = -ChanWidth/2;
68  plot(yy,top,'--g');
69  plot(yy,bottom,'--g');
70
71  focTop(1:length(yy)) = foc/2;
72  focBottom(1:length(yy)) = -foc/2;
73  plot(yy,focTop,'--b');
74  plot(yy,focBottom,'--b');
75
76  xlabel('Channel Length (mm)'); ylabel('Channel width (\mum)');
77  axis([-0.55,16,-40,40]);
78
79  horiz = -40:0.1:40;
80  plot(0,horiz,'r');
81
82  % Export = [yy' x' top' bottom' focTop' focBottom'];
83
84  % fid=fopen(['e:\temp\foc\' int2str(foc) 'j' int2str(j) '.txt'],'wt');
85  % fprintf(fid,[repmat('%f\t',1,9) '%f\n'],Export.');
86  % fclose(fid);
87
88  end
```

List of publications

1) **Edel, J. B.**; de Mello, A. J. "Hydrodynamic Focusing in Microstructures for Improved Single Molecule Detection Efficiencies Using Confocal Spectroscopy." *Analytical Chemistry* **2004** (Submitted).

2) **Edel, J. B.**; Beard, N. P.; de Mello, A.J. "Thin-Film Polymer Light Emitting Diodes as Integrated Excitation Sources for Microfabricated Capillary Electrophoresis." *Lab on a Chip* **2004** (Accepted).

3) **Edel, J. B.**; Leung, S.A.; de Mello, A. J. "Continuous Real-time Bubble Monitoring in Microchannels Using Refractive Index Detection." *Measurement Science and Technology* **2004** (15): 290-296.

4) **Edel, J. B.**; Krishnadasan, S.; de Mello J.C.; de Mello A.J. "Continuous real-time monitoring of quantum dot synthesis within microfluidic reactors", *Proceedings of the 7th International Conference on Micro Total Analysis Systems* **2003** pp. 673 – 676.

5) **Edel, J. B.**; Krishnadasan, S.; cao-Romero, J. T.; Vilar R.; de Mello J.C.; de Mello A.J. "Controlled Synthesis of Compound Semiconductor Nanoparticles Using Microfluidic Reactors." *Transducers* **2003** (4B1.1): 1730-1733.

6) **Edel, J. B.**; de Mello, A. J. "Determination of Single Particle Flow Velocities in Microchannels using Maximum Likelihood Estimator." *Physical Chemistry Chemical Physics* **2003** (5): 3973-3978.

7) **Edel, J. B.**; de Mello, A. J. "Single Particle Confocal Fluorescence Spectroscopy in Microchannels: Dependence of Burst Width and Burst Area Distributions on Particle Size and Flow Rate." *Analytical Sciences* **2003** (19): 1065-1069.

8) de Mello, A. J.; **Edel, J. B.**; Hill, E. K. Single Molecule Detection in Liquids. *Encyclopedia of Modern Optics, Elsevier Science* **2003** (In press).

9) **Edel, J. B.**; de Mello, A. J.; de Mello, J. C. "Solution-phase Electroluminescence." *Chemical Communications* **2002** (17): 1954-1955.

10) **Edel, J. B.**; de Mello, A. J. "Velocity Measurement of Particulate Flow in Microfluidic Channels Using Confocal Spectroscopy" *Proceedings of the Imperial College postgraduate symposium* **2002** pp. 25.

11) **Edel, J. B.**; de Mello, A. J.; de Mello., J. C. "Controlled Quantum Dot Synthesis Within Microfluidic Circuits", *Proceedings of the 6th International Conference on Micro Total Analysis Systems* **2002** pp. 772- 774.

12) **Edel, J. B.**; Fortt, R.; de Mello, A. J. "Microfluidic Routes to the Controlled Production of Nanoparticles." *Chemical Communications* **2002** (10): 1136-1137.

13) **Edel, J. B.**; Hill, E. K.; de Mello, A. J. "Velocity Measurement of Particulate Flow in Microfluidic Channels Using Single Point Confocal Fluorescence Detection." *Analyst* **2001** 126 (11): 1953-1957.